Light-Induced Charge-Accumulation in Molecular Systems with Multi-Electron Donors and Acceptors

Inauguraldissertation

zur Erlangung der Würde eines Doktors der Philosophie

vorgelegt der Philosophisch-Naturwissenschaftlichen Fakultät

der Universität Basel

von

Michael Skaisgirski

aus Freiburg i. Br., Deutschland

Basel, 2018

Genehmigt von der Philosophisch-Naturwissenschaftlichen Fakultät auf Antrag von

Fakultätsverantwortlicher/Dissertationsleiter: Prof. Dr. Oliver S. Wenger
Korreferent: Prof. Dr. Marcel Mayor

Basel, den 16.10.2018

Prof. Dr. Martin Spiess

We've all got both light and dark inside us. What matters is the part we choose to act on. That's who we really are.

Harry Potter and the Order of the Phoenix

Angelika

und meinen Eltern

Acknowledgements

I cordially thank **Prof. Dr. Oliver S. Wenger** for giving me the opportunity to do my PhD thesis under his supervision. Thank you for the interesting research projects I could work on, thank you for all the guidance and encouragement during these four years of my PhD and thank you for always having an open door whenever help was needed. I could not have wished for a better supervisor.

Special thanks are given to **Prof. Dr. Marcel Mayor** who kindly agreed to co-examine this thesis.

Prof. Dr. Christof Sparr is sincerely thanked for chairing my examination.

Dr. Heinz Nadig and **Dr. Michael Pfeffer** are thanked for measuring high resolution mass spectra, **Sylvie Mittelheisser** is thanked for measuring the elemental analyses presented in this thesis.

Many thanks are given to **Markus Hauri**, **Oliver Ilg** and the whole **Werkstatt-Team** for keeping the department and the daily lab-work run as smoothly as possible. Thanks also go to **Brigitte Howald** and **Beatrice Erismann** for their support in all administrative and organizational matters.

Furthermore, I would like to thank all past and present members of the **AK Wenger** for the relaxed and cooperative working atmosphere which made it a pleasure not only to work in this group, but also to participate in the events outside the lab.

Special thanks go to:

Martin, **Chris** and **Mirj** for their helpful input while proof-reading this thesis,

Xingwei, **Martin**, **Chris** and **Christoph** for the helpful discussions on several topics, for the optimization of new project ideas and for their support in various measurements,

Hauke and **Svenja** for the good cooperation in organizing the Pharmapraktikum over several semesters,

the whole Lab 302, namely **Svenja**, **Julia**, **Hauke** and **Andrea** for the good time we had together, for all the joking, for the conversations on various topics and for the joint problem solving in the everyday lab-work,

Xingwei and **Mirj** for all the NCCR-related events we attended together,

Mirj and **Svenja** for organizing BBQs, game nights, group fondues and other group-related events,

and of course, all the people who were not mentioned yet (**Patrick**, **Sabine**, **Lucius**, **Jakob**, **Tobias**, **Fabienne**, **Felix**), but who helped making the coffee breaks, rounds of card games and Apéros more fun.

I would like to thank **Leon**, **Lisa**, **Marco**, **Rut**, **Dominik** and **Benny** for the great time we had together during our Bachelor and Master studies in Freiburg. Thanks to the support of one another, we will all have our PhD soon. And Rut, it is your task to organize the Party-Straba next year...

I deeply want to thank **Angelika** for her love and the never-ending support during all those years. You know me since I started studying and we went through all the ups and downs of being a chemist together, I could not have asked for more.

Last, but most important, I would like to thank **my family**. You have supported me during all these years, always had an open door when problems arose and strengthened my decisions made. Thank you for always being there for me!

Abstract

To date, the world's population mainly relies on fossil fuels for covering its daily energy need. However, not only is the mining of oil, natural gas and coal demanding, but the combustion of these fossil fuels also leads to the release of gases that are harmful to human health, or contribute to global warming. A global shift from fossil fuels to 'solar fuels' is therefore highly desirable. The conversion of solar energy into usable chemical fuels, however, is complicated - a central challenge being the accumulation of several redox equivalents to catalyze multi-electron reactions. This thesis therefore addresses the aspect of light-driven charge-accumulation in molecular systems.

In the first project (Chapter 3), accumulation of two electrons on a triad consisting of a central naphthalene diimide (NDI) moiety flanked by two $[Ru(bpy)_3]^{2+}$ photosensitizers was investigated. Under continuous irradiation with visible light, two electrons were successfully accumulated on NDI in the presence of a sacrificial electron donor. When the sacrificial donor was replaced with two covalently connected triarylamine electron donors, however, only a singly charge-separated state could be observed in the pentad. The pathways leading to charge-accumulation in case of the triad and the processes preventing the accumulation of charges in the pentad were studied in detail.

In the second project (Chapter 4), the impact of charge-accumulation on the catalytic process for BNA^+ (an analog of $NAD(P)^+$) reduction was studied. Experiments with a multi-component system as well as with covalently connected molecular systems were performed. Analysis of these measurements revealed that prior charge-accumulation does not lead to an accelerated BNAH formation rate and that the predominant reaction path most likely relies on a disproportionation of the intermediate Rh^{II} species.

In the third project (Chapter 5), the problems preventing charge-accumulation on the NDI pentad in the first project were addressed. A new concept was developed based on electron donor and acceptor moieties with potential inversion to increase the driving force for the transfer of the second electron. In addition, intermediate electron donors and acceptors were incorporated to establish a redox gradient in analogy to the electron transfer paths in natural photosynthesis. This redox gradient is expected to promote productive electron transfer while the increased spatial separation of terminal donor and acceptor moiety is expected to significantly decrease back-electron transfer. While the successful synthesis of this pentad is still pending, the individual donor and acceptor moieties were examined. A donor triad was synthesized, which upon excitation, showed rapid excited-state quenching by the intermediate electron donor and rapid subsequent

hole transfer from the intermediate to the terminal electron donor. The lifetime of this charge-separated state is rather long and therefore shows that back-electron transfer in the triad is significantly retarded by the intermediate electron donor. The overall concept of this pentad is therefore highly promising and could provide the basis for a new generation of charge-accumulative systems.

Contents

Abbreviations

A_0	chlorophyll A_0
A_1	phylloquinone
Ac	acetate
AQ	9,10-anthraquinone
ATP	adenosine triphosphate
BNA^+	1-benzyl nicotinamide
Bpin	pinacol boronic ester
bpy	2,2'-bipyridine
CAT	catalyst
Cp*	1,2,3,4,5-pentamethylcyclopentadiene
CV	cyclic voltammetry
Cyt	cytochrome
δ	chemical shift
dba	dibenzylideneacetone
DCM	dichloromethane
DMF	N,N'-dimethylformamide
DMSO	dimethylsulfoxide
ε	extinction coefficient
e	elementary charge
EA	electron acceptor
ED	electron donor
ESI	electrospray ionization
ET	electron transfer
Et_2O	diethyl ether
EtOAc	ethyl acetate
EtOH	ethanol
exTTF	9,10-di(1,3-dithiol-2-ylidene)-9,10-dihydroanthracene
Fc	ferrocene
FD	ferredoxin
FeS	iron-sulfur cluster
FMN	fluoren-9-ylidene malononitrile
FNR	ferredoxin-NADP-reductase
FO	9-fluorenone

ΔG	free energy
GCE	glassy carbon electrode
HRMS	high-resolution mass spectrometry
hxy	*p*-(di-*n*-hexyl)phenyl
iEA	intermediate electron acceptor
iED	intermediate electron donor
IR	infrared
M	molar, $mol \cdot L^{-1}$
m/z	mass per charge
MALDI	matrix-assisted laser desorption/ionization
MCET	metal ion-coupled electron transfer
MeCN	acetonitrile
MeOH	methanol
MHz	megahertz
MLCT	metal-to-ligand charge transfer
MS	mass spectrometry
Mtoe	million tons of oil equivalents
MV^{2+}	methyl viologen
$NAD(P)^{+}$	nicotinamide adenine dinucleotide (phosphate)
NBS	*N*-bromosuccinimide
nBu	*n*-butyl
NCCR	national center of competence in research
NDI	naphthalene diimide
NIR	near-infrared
NMR	nuclear magnetic resonance
OEC	oxygen evolving complex
OTA	oligo-triarylamine
OTf	triflate
p	para
PC	plastocyanine
PCET	proton-coupled electron transfer
PDI	perylene diimide
pheo	pheophytin
PhSSPh	dibenzo dithiin
Por	porphyrin
PPh_3	triphenylphosphine
ppm	parts per million

PQ	plastoquinone
PS	photosensitizer
PS I / PS II	photosystem I / II
PTZ	10-(4-methoxyphenyl) phenothiazine
RT	room temperature
SCE	saturated calomel electrode
sD	sacrificial donor
SEC	spectro-electrochemistry
TAA	triarylamine
TATPQ	tetraazatetrapyrido pentacene quinone
TBA	tetra-*n*-butylammonium
$TBAPF_6$	tetra-*n*-butylammonium hexafluorophosphate
^{t}Bu	tert-butyl
TCAQ	11,11,12,12-tetracyano-9,10-anthraquinodimethane
TCEP	tris(2-carboxyethyl) phosphine
TEA	triethylamine
TEOA	triethanolamine
THF	tetrahydrofuran
TMS	trimethylsilyl
Tyr_Z	tyrosine Z
UV	ultraviolet
Vis	visible
xy	*p*-xylene
ZnPor	zinc porphyrin

1 General Introduction

The availability of a stable energy supply plays a crucial role for humanity. It is believed that the rise of *Homo erectus* from its more primitive ancestors was boosted by its ability to tame fire, allowing it to colonize colder environments and protecting it from predators.[1] From these early days on, the dependence of humankind on energy increased strongly. Nowadays, a stable supply of energy for electricity, mobility, heating, communication and fabrication is required for our daily life. To date, most of the required energy is generated by the combustion of coal, oil and natural gas. In 2015, the world's total energy need amounted to 13'647 Mtoe (million tons of oil equivalents) which corresponds to roughly 18.1 TW.[2] Its composition can be seen in Figure 1.1.

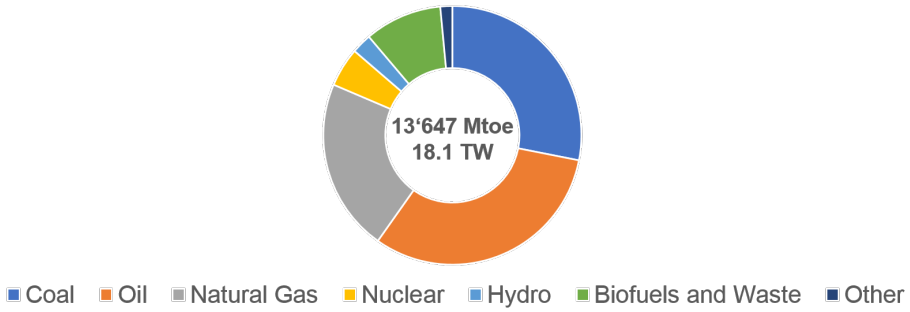

Figure 1.1: Contributions of the different energy sources to the world's energy demand in 2015.[2]

While the total fuel consumption in Europe and North America is predicted to slightly decrease over the next years, the world's global energy need is growing.[3] A prediction of the changes in primary energy demand by 2040 is shown in Figure 1.2.

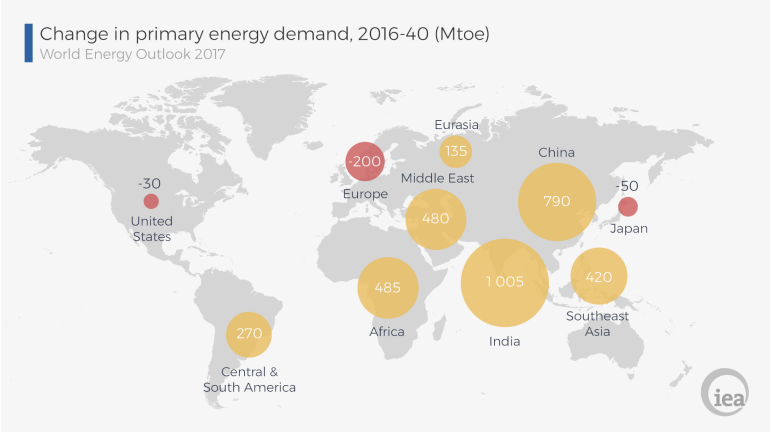

Figure 1.2: Predicted change in primary energy demand from 2016 to 2040. Values are given in Mtoe (million tons of oil equivalents). Figure from World Energy Outlook 2017.[3]

With the global energy demand ever-expanding, a potential problem arises. Today's main energy sources coal, oil and natural gas are finite and natural deposits become more difficult to exploit. In addition, their combustion releases greenhouse gases such as CO_2, which contribute to global warming.[4] A systemic switch from fossil fuels to alternative energy sources is therefore highly desirable. A potential infinite energy source is sunlight, which provides the surface of the earth with roughly 120'000 TW of energy.[5, 6] If only 0.015% of this energy could be converted into solar fuels, it would have been enough to cover the world's global energy needs as of 2015.

A blueprint for the successful conversion of sunlight into solar fuels can be found in nature. In natural photosynthesis, water-splitting results in O_2 formation, while the released electrons and protons are subsequently used to reduce CO_2 into energy-rich carbohydrates.[7] If a similar artificial mechanism could be established using sunlight to produce high-energy products such as H_2, CH_4 or methanol, a smart way to substitute the finite fossil fuels on a large scale could be found.

However, the processes behind natural photosynthesis are rather complex and a molecular system that could mimic the natural mechanism would need to be comprised of several customized modules. An exemplary design of such a molecular system is shown in Figure 1.3.[8]

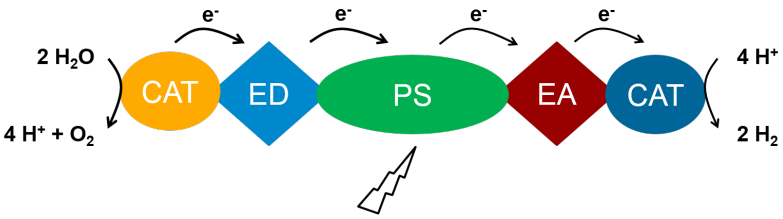

Figure 1.3: Schematic representation of a molecular system mimicking natural photosynthesis.

In Figure 1.3, five components are shown that are necessary to mimic natural photosynthesis. In the center of such a molecular system, a module for the absorption of visible light (photosensitizer, PS) is located. The energy from the absorbed photon is then employed to induce charge-separation yielding a positively charged electron donor (ED) and a negatively charged electron acceptor (EA). The formation of a charge-separated state, however, is not sufficient to perform water-splitting and CO_2 reduction, as these reactions require several electrons or positive charges (holes) to proceed. Therefore, catalytic modules (CAT) for the accumulation of several electrons or holes need to be present that ensure enough charges are available for the multi-electron reactions to proceed.

While a lot of research has been done regarding charge-separation following the excitation of a photosensitizer, the accumulation of electrons and holes in molecular systems is far less explored and only a few molecular systems are reported to exhibit charge-accumulation. However, charge-accumulation is a crucial point in natural and artificial photosynthesis. This work will therefore focus on the aspect of light-induced charge-accumulation.

In the following chapter, a short overview of the essential reaction steps in natural photosynthesis is given. Subsequently, the basics of accumulative electron-transfer reactions in molecular systems and the hence resulting difficulties are addressed. Finally, selected examples of systems undergoing light-induced charge-accumulation are presented.

2 Theoretical Background and Motivation

2.1 Natural Photosynthesis

Natural photosynthesis describes the solar-energy-driven process of water oxidation and the associated reduction of CO_2 into carbohydrates as given in the reaction equation:[9]

$$6\,CO_2 + 6\,H_2O \rightarrow C_6H_{12}O_6 + 6\,O_2$$

This process takes place in plants, algae and cyanobacteria and consists of a sophisticated process of light absorption, charge-separation, electron-transfer and charge-accumulation steps interlinked with each other to perform multi-electron catalysis. The key complexes involved herein are light-harvesting antenna molecules, ATP synthase, cytochrome b_6f and photosystems I and II (PS I / PS II).

In the catalytic system, PS I and II play a crucial role. Upon consecutive absorption of four photons by PS II, four electrons and four protons are extracted from water, yielding O_2 as a waste product. Each extracted electron is transported to PS I, and, upon excitation of PS I, further transferred to ferredoxin. Consequently, for the successful transfer of the four electrons, four additional photons are needed. The extracted electrons are then used to reduce $NADP^+$ to NADPH. Meanwhile, the extracted protons are used to develop a proton gradient by cytochrome b_6f, which is then employed by ATP synthase for the synthesis of ATP. All these electron and proton transfer steps require energy in the form of visible light to proceed and are therefore called light reactions. In the subsequent Calvin cycle, the formed NADPH and ATP molecules are then used to reduce fixated CO_2 to build up carbohydrates. This process is independent of light and is therefore called dark reaction.[9–11]

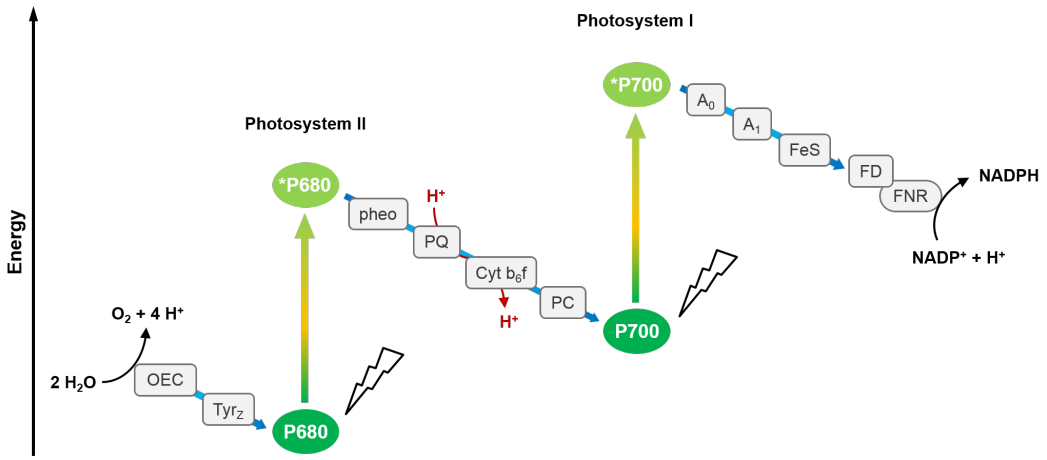

Figure 2.1: Simplified Z-scheme representation of the light-dependent reactions in PS II and PS I.

The Z-scheme (Figure 2.1) represents a more detailed view of the electron-transfer pathways in the light reactions of natural photosynthesis.[7, 12–14] Both PS II and PS I consist of central chlorophyll dimers which are called P680 and P700. Upon absorption of a photon by P680, an electron is transferred to pheophytin (pheo) and a redox gradient leads to electron transfer via plastoquinone (PQ), cytochrome b_6f (Cyt b_6f) and plastocyanine (PC) to photosystem I. Upon excitation of the chlorophyll dimer P700 in PS I, a second electron-transfer cascade is initiated transferring the electron via chlorophyll A_0, phylloquinone A_1 and a sequence of iron-sulfur clusters (FeS) to ferredoxin (FD). Ferredoxin can then bind to ferredoxin-NADP-reductase (FNR) which promotes the reduction of $NAPD^+$ to NADPH. NADPH hereby represents the final product of this electron transfer pathway.

On the other side of the Z-scheme, the oxidized P680 is re-reduced by tyrosine Z (Tyr_Z), accompanied by a transfer of the phenolic proton to nearby histidine His190. The hereby formed tyrosyl radical is a strong oxidant which can abstract an electron from the oxygen-evolving complex (OEC). Upon four iterations of the above described electron transfer pathway, four electrons and four protons are released from the OEC. The oxidized OEC can then catalyze water-splitting leading to the release of molecular oxygen.

The structure of the OEC was found to be a rather unique $CaMn_4O_5$-cluster.[15, 16] During natural photosynthesis, the central $CaMn_4O_5$ motif passes through five different states which were first described by Kok and co-workers.[17] A more detailed study on the different states was performed by Dau and Hauman and consequential an extended reaction cycle was proposed which is shown in Figure 2.2.[7, 18, 19]

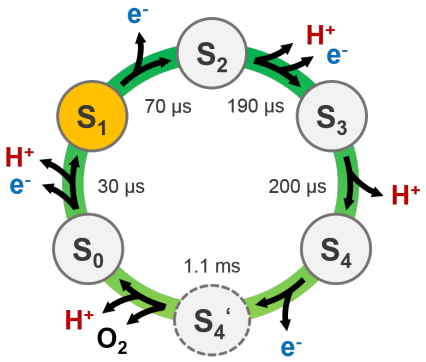

Figure 2.2: Extended water oxidation cycle as proposed by Dau and Hauman. A series of light-induced electron and proton releases leads to different oxidation states in the $CaMn_4O_5$ cluster resulting in a hypothetical S_4' state which catalyzes the oxidation of H_2O to O_2. The catalytic cycle starts with the dark-stable resting state S_1 and requires four photons for one full rotation.

The catalytic cycle shown in Figure 2.2 starts with the dark-stable resting state S_1, which upon excitation of PS II, releases the first electron. The second photon then leads to the oxidation of S_2 combined with the release of a proton. The third photon then leads to a reaction cascade releasing a proton to form S_4 and subsequently the release of the third electron yields the hypothetical S_4' state which leads to the combined release of O_2 and a proton. With the fourth photon, the S_0 state releases the fourth proton and electron and restores the S_1 resting state. While the release of four electrons and four protons during this cycle is certain, neither the exact molecular mechanism of this cycle nor the details of the O-O-bond forming process are known to date.[12, 19]

In summary, natural photosynthesis consists of a well-balanced cascade of electron and proton transfer pathways driven by the absorption of multiple photons. With each excitation of the P680 and P700 photosensitizers, one electron from the OEC is transferred to ferredoxin via a sophisticated redox gradient. Ferredoxin NADP reductase then uses the electrons to reduce $NADP^+$ to the energy-rich NADPH. Upon four subsequent cycles, four holes are accumulated on the OEC, which can then oxidize water to molecular oxygen. Due to the multitude of complexes involved in the general process, the reaction centers for water oxidation and $NADP^+$ reduction are spatially separated by a membrane and therefore oxidative and reductive processes do not interfere with one another.

2.2 Accumulative Electron Transfer

In Chapter 1, the importance of light-driven fuel generation was introduced. However, the design of appropriate molecular systems is challenging, as the generation of solar fuels requires several redox equivalents to proceed:

$$2\,H^+ + 2\,e^- \rightarrow H_2$$
$$2\,H_2O \rightarrow O_2 + 4\,H^+ + 4\,e^-$$
$$CO_2 + 6\,H^+ + 6\,e^- \rightarrow CH_3OH + H_2O$$
$$CO_2 + 8\,H^+ + 8\,e^- \rightarrow CH_4 + 2\,H_2O$$

On a molecular level, the absorption of a photon by the photosensitizer leads to charge-separation. The generated electron-hole pair, however, cannot perform the above listed multi-electron reactions. Therefore, the accumulation of electrons or holes is a prerequisite for the successful generation of solar fuels.

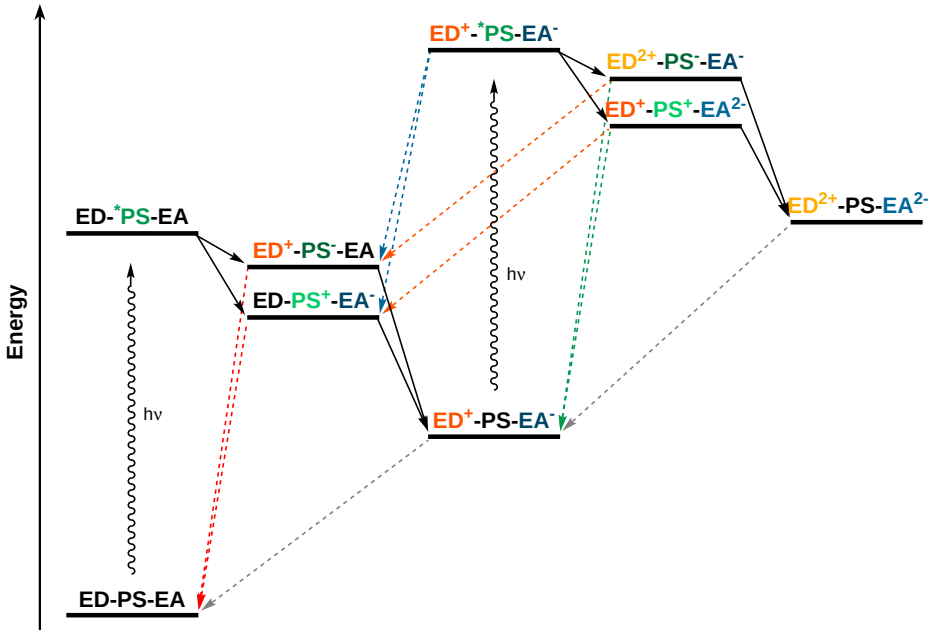

Scheme 2.1: Exemplary depiction of the electron transfer pathways in an ED-PS-EA triad leading to charge-accumulation (solid arrows) and the decay pathways counteracting the charge-accumulation process (dashed arrows).

The energy scheme in Scheme 2.1 shows the electron-transfer pathways for an ED-PS-EA triad.[8] Upon excitation of the photosensitizer (PS), a first electron transfer takes place, either from the electron donor (ED) to the excited PS (reductive excited state quenching, yielding ED^+-PS^--EA) or from the excited PS to the electron acceptor (EA, oxidative excited state quenching, yielding ED-PS^+-EA^-). These primary charge-separated states

can either recombine (red dashed arrows) to the ground state of the molecule or can undergo productive electron transfer, yielding the charge-separated state ED^{+}-PS-EA^{-}.

If the lifetime of the singly charge-separated state is long enough, a second excitation of the photosensitizer is possible. In the ED^{+}-*PS-EA^{-} state, again reductive or oxidative quenching of the photosensitizer by ED^{+} or EA^{-} is possible. However, with already a hole on the ED, the ED^{+} state competes with the EA^{-} moiety for the electron of the excited photosensitizer. The same is true for EA^{-} and ED^{+} which compete for reductive quenching of the *PS moiety. According to which electron transfer dominates, either the secondary charge-separated states ED^{2+}-PS^{-}-EA^{-} or ED^{+}-PS^{+}-EA^{2-} result or the triad returns to the primary charge-separated states EA^{+}-PS^{-}-EA or EA-PS^{+}-EA^{-} (blue dashed arrows).

If productive electron transfer prevails and the secondary charge-separated states ED^{2+}-PS^{-}-EA^{-} or ED^{+}-PS^{+}-EA^{2-} are formed, it takes another electron-transfer step to form the desired charge-accumulated ED^{2+}-PS-EA^{2-} state. However, unproductive electron transfer at this stage can also lead back to the singly charge-separated state (green dashed arrows) or to a primary charge-separated state (orange dashed arrows).

The overall electron-transfer processes depicted in Scheme 2.1 emphasize why charge-accumulation in molecular systems is not a commonly observed phenomenon. In the above sketched accumulation of two electrons and two holes, a multitude of decay pathways exist which can counteract the charge-accumulation process. When it comes to the accumulation of more charges, the increase in decay pathways further hampers the formation of the final charge-accumulated state. It therefore needs a good combination of productive electron-transfer reactions, suppressed back-electron transfer and suitable lifetimes of the major charge-separated states to obtain charge-accumulation in a system that can then subsequently catalyze multi-electron reactions.

2.3 Evolution of Charge-Accumulative Systems

In section 2.1, the fundamental mechanism of natural photosynthesis was sketched. An artificial system being able to mimic this mechanism therefore needs to copy the single components of natural photosynthesis. These are a photosensitizer for effective light absorption, which then induces charge-separation leading to a reduced electron acceptor and an oxidized electron donor. Subsequent redox gradients need to be established that allow electron transport from the terminal electron donor to the terminal electron acceptor. These terminal donor and acceptor moieties need to be able to undergo charge-accumulation while a spatial separation between reductive and oxidative catalytic site is needed to prevent undesired back-electron transfer.

A molecular system mimicking all these features of natural photosynthesis is not easy to realize. Therefore, much research has been dedicated in studying the different components for such an artificial system. Molecular systems that indeed can undergo light-induced charge-accumulation are scarce and often show serious drawbacks for the potential use in artificial photosynthesis. On the following pages, a selection of molecular systems are presented which demonstrate the developments on the topic of light-induced charge-accumulation over time.

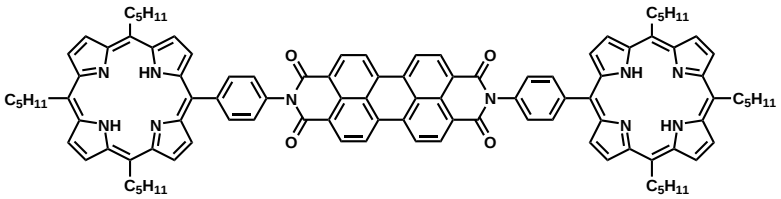

Figure 2.3: Structure of the Por-PDI-Por triad examined by Wasielewski *et al.*[20] Upon excitation, a short-lived doubly charge-separated state is formed.

A first example for charge-accumulation dates to 1992.[20] Wasielewski and co-workers presented a molecular system consisting of a central perylene diimide (PDI) acceptor moiety flanked by two free-base porphyrin (Por) photosensitizers (see Figure 2.3). Upon excitation of the porphyrin moieties at 585 nm, successive electron transfer from the porphyrins to PDI can be observed leading to the formation of PDI^{2-}. The doubly reduced state of PDI was found to have a rather short lifetime of 5 ns, which however is still longer than the lifetime of the singly charge-separated state (~120 ps).

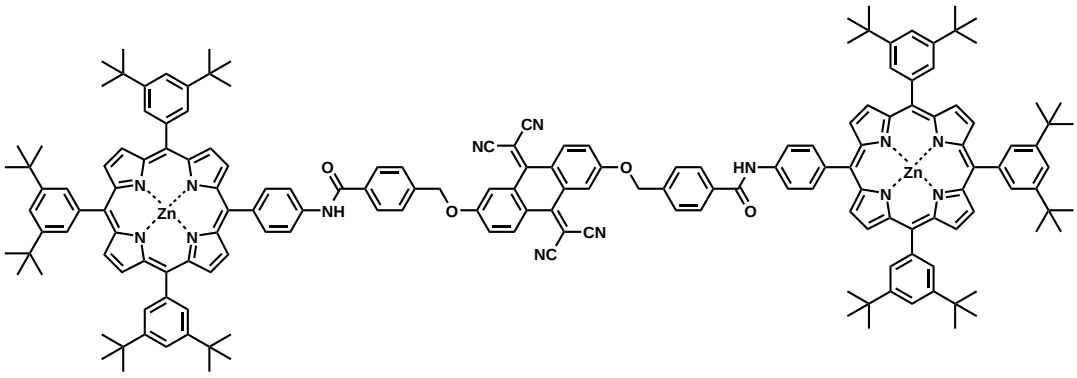

Figure 2.4: Structure of the ZnPor-TCAQ-ZnPor triad examined by Imahori and Sakata.[21] Upon excitation, a short-lived doubly charge-separated state is reported to be formed.

A very similar approach as the one of Wasielewski *et al.* was pursued by Imahori and Sakata in 1998.[21] The investigated system consists of the central two-electron acceptor tetracyano anthraquinodimethane (TCAQ) which is flanked by two zinc porphyrin photosensitizers (ZnPor). Upon consecutive excitation of both ZnPor photosensitizers with a two-pulse laser setup, the authors report the formation of $TCAQ^{2-}$ with a charge-accumulated state lifetime of approximately 1 ns. The formation of the singly and doubly reduced species is hereby quantified by the time constants for the formation and the decay of the absorption band at 610 or 620 nm. The underlying assumption is that both the $TCAQ^{-}$ and $TCAQ^{2-}$ absorption bands are centered at a very similar wavelength. However, literature reports[22, 23] as well as this thesis (Chapter 5) show that while the absorption of $TCAQ^{-}$ is centered around 600 nm, the absorption band of $TCAQ^{2-}$ is centered around 540 nm.

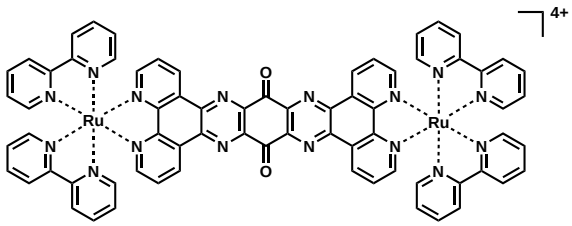

Figure 2.5: Structure of the Ru-TATPQ-Ru triad examined by MacDonnell *et al.*[24, 25] Upon excitation, four electrons and four protons can be accumulated when using a sacrificial electron donor.

In 2002, the first accumulation of four electrons (in combination with four protons) on a molecular system was reported by MacDonnell *et al.*[24, 25] In a dinuclear ruthenium complex bearing a central tetraazatetrapyrido pentacene quinone (TATPQ) moiety as

electron acceptor, four electrons were consecutively accumulated on TATPQ in a steady-state irradiation experiment. Upon excitation of one of the ruthenium photosensitizers, an electron is transferred to TATPQ. The positive charge on the ruthenium sensitizer is then subsequently compensated by the sacrificial electron donor triethylamine (TEA) which prevents back-electron transfer from the singly reduced TATPQ moiety. The reduced acceptor is subsequently protonated (proton released from oxidized TEA) which in sum corresponds to the uptake of a hydrogen atom. Four iterations then lead to the successful accumulation of four electrons and four protons on TATPQ.

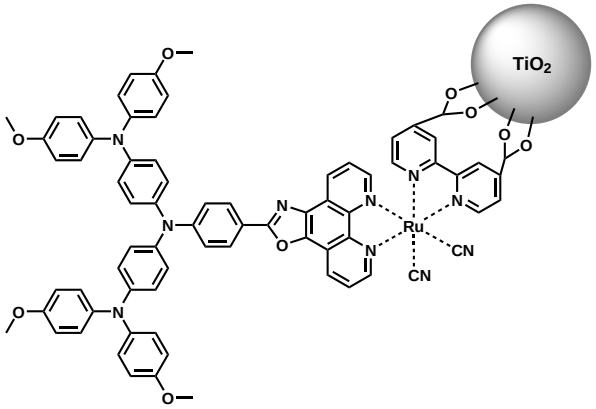

Figure 2.6: Structure of the OTA-Ru-TiO_2 triad examined by Hammarström *et al.*[26, 27] Upon excitation, two electrons are injected into the TiO_2 nanoparticle leading to the accumulation of two holes on OTA.

Another approach for charge-accumulation was pursued by Hammarström and co-workers in 2010.[26, 27] A TiO_2 nanoparticle was used as an electron acceptor which was combined with a ruthenium photosensitizer and an oligo-triarylamine (OTA) two-electron donor. The use of a TiO_2 nanoparticle offers the advantage of having fast electron injection into the nanoparticle, while the resulting decoupling of electrons and holes retards charge-recombination reactions. The first laser pulse therefore leads to the formation of OTA^+, while OTA^{2+} is formed with the second laser pulse. Both singly and doubly charge-separated states have a lifetime of 10 µs, the transport kinetics in TiO_2 being the rate-determining step in charge-recombination.

While the four above introduced systems are cleverly designed to allow for charge-accumulation, they all exhibit their own specific disadvantages for the aim of artificial photosynthesis. Wasielewski (and Imahori) could accumulate two electrons on an acceptor. However, the lifetime of the charge-accumulated state was too short to perform catalytic reactions. The system of MacDonnell shows a long lifetime of the charge-accumulated state; however, the use of sacrificial reagents is not compatible with the sustainable production of solar fuels. The use of a TiO_2 nanoparticle by Hammarström led to a fast

electron injection into TiO_2 and hence facilitated accumulation of two holes on OTA. However, TiO_2 in contrast to a purely molecular system offers no distinct reduced states and fast electron abstraction is not possible.

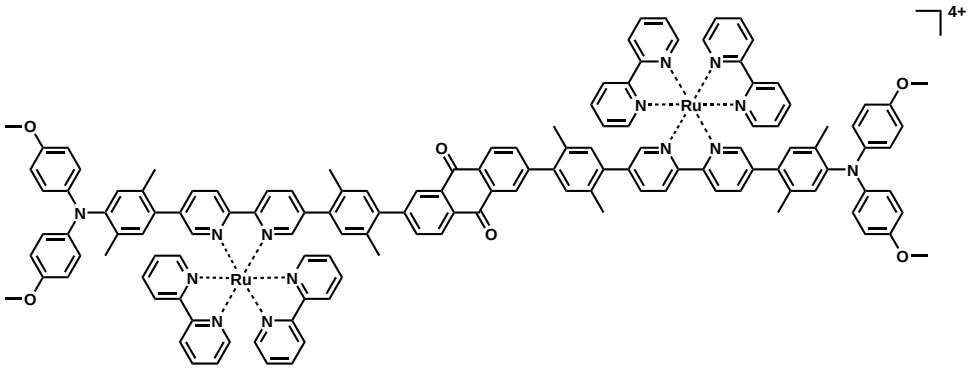

Figure 2.7: Structure of the TAA-Ru-AQ-Ru-TAA pentad investigated by Wenger and co-workers.[28] Upon excitation, one electron from each TAA donor is transferred to AQ, yielding a doubly reduced acceptor.

In 2016, a purely molecular pentad was examined in our group, being composed of a central anthraquinone (AQ) acceptor being flanked by two ruthenium photosensitizers and two triarylamine (TAA) electron donors.[28] Upon excitation of the photosensitizers, electron transfer from the TAA donors to AQ could be observed. The hereby formed charge-accumulated state exhibited an impressive lifetime of 870 ns, which could still be increased to 4.7 µs upon addition of *p*-toluenesulfonic acid[29] and even to the millisecond regime by exploiting metal ion-coupled electron transfer (MCET).[30] A downside of the pentad however is the rather small amount of charge-accumulated product formed, as only a fraction of the singly charge-separated states could be converted to the doubly charge-separated state within the laser pulse duration. This finding is mainly attributed to a reduced driving-force for the accumulation of the second electron as well as unproductive excited state quenching by TAA^+ and AQ^-.

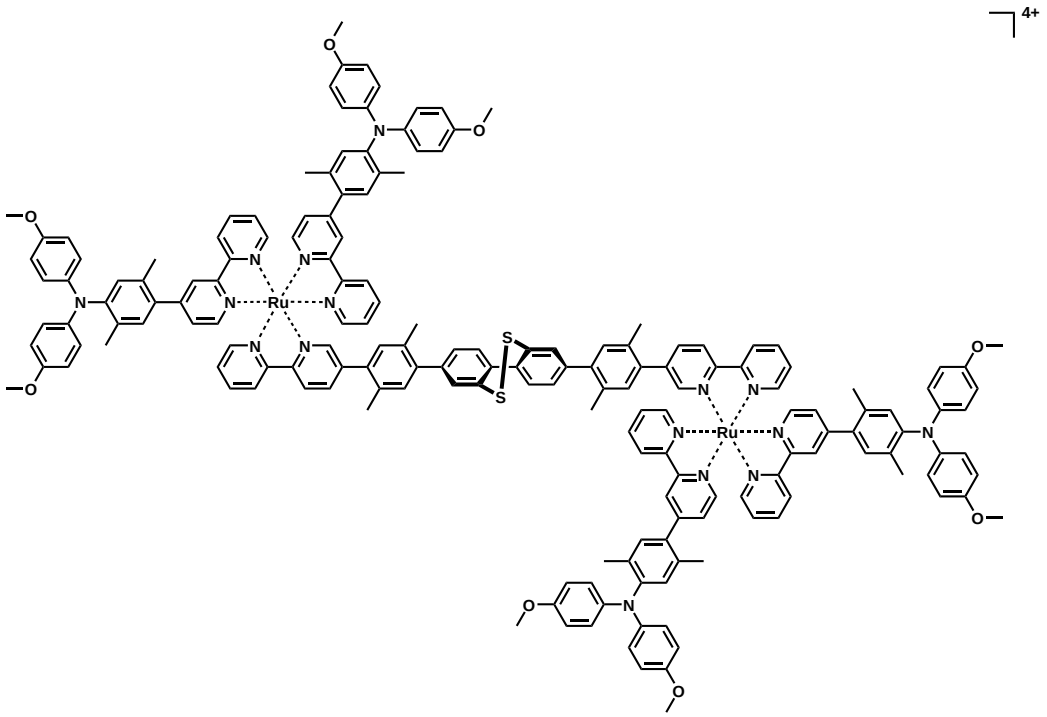

Figure 2.8: Structure of the $(TAA)_2$-Ru-PhSSPh-Ru-$(TAA)_2$ heptad investigated by Wenger and co-workers.[31] Upon excitation, two electrons from two TAA donors are transferred to PhSSPh, yielding a doubly reduced acceptor.

The problem of the reduced driving force for the second electron-transfer step was addressed by our group in 2018.[31] In the central position of the $(TAA)_2$-Ru-PhSSPh-Ru-$(TAA)_2$ heptad, dibenzo dithiin (PhSSPh) was used as a two-electron acceptor. In contrast to the previously used acceptors such as AQ, the reduction potentials of PhSSPh are inverted, meaning that the second reduction occurs more easily than the first. Excitation of both ruthenium photosensitizers then leads to the formation of doubly reduced PhSSPh and two oxidized TAA donor moieties. The hereby generated charge-accumulated state exhibits a lifetime of 66 ns, which upon protonation with *p*-toluenesulfonic acid can be drastically increased.

With an extended lifetime of the charge-accumulated state and increased driving force for the second electron-transfer step being obtained in these two systems, the next step now is the realization of a purely molecular system which can accumulate both electrons and holes in analogy to natural photosynthesis. This concept is approached in Chapter 5 of this thesis.

3 Studies of Charge-Accumulation: NDI as Two-Electron Acceptor

The idea of examining charge-accumulation on naphthalene diimide (NDI) arose from its favorable electrochemical and optical spectroscopic properties: NDI is a two-electron acceptor with reduction potentials of -0.5 V and -1.0 V vs. SCE.[32–34] Neutral, singly and doubly reduced states exhibit different absorption signatures[32] and therefore allow for clear differentiation of the observed (reduced) states. While the synthesis and modification of NDIs is well established and NDIs are used for several applications,[35–38] light-induced charge-accumulation on NDI has not been reported. In recent years, efforts to achieve charge-accumulation on NDI in molecular systems were made that either yielded a mixed-valence singly charge-separated state,[39] a (long-lived) singly charge-separated state[40–42] or a singly charge-separated state with two distinct charge-recombination lifetimes.[43] Charge-accumulation could not be achieved in any of these systems.

In this project, charge-accumulation in a Ru-NDI-Ru triad was achieved with triethylamine (TEA) as a sacrificial electron donor. In a related pentad, two triarylamine (TAA) electron donor moieties (replacing the role of TEA in the triad) were covalently linked to the $[Ru(bpy)_3]^{2+}$photosensitizers. In this pentad, charge-separation could be observed upon excitation, but two-pulse experiments did not lead to charge-accumulation. The reasons for this lie in the significantly reduced driving force for the second electron transfer to NDI^- and energetically more favorable excited state quenching by NDI^- or TAA^+. Details of the charge-accumulation and separation processes occurring in the triad and pentad can be found in the published paper presented on the following pages. A new concept to overcome the disadvantages observed with the NDI pentad will be presented in Chapter 5.

In 2017, a few months after this project was published, a paper was released by Aukauloo and co-workers where the authors were able to achieve charge-accumulation on NDI using the reversible external electron donor ascorbate.[44] In a fully covalently linked system, charge-accumulation on NDI is still pending.

Inorganic Chemistry

Article

pubs.acs.org/IC

Electron Accumulation on Naphthalene Diimide Photosensitized by [Ru(2,2′-Bipyridine)$_3$]$^{2+}$

Michael Skaisgirski, Xingwei Guo, and Oliver S. Wenger*

Department of Chemistry, University of Basel, St. Johanns-Ring 19, 4056 Basel, Switzerland

Supporting Information

ABSTRACT: In a molecular triad comprised of a central naphthalene diimide (NDI) unit flanked by two [Ru(bpy)$_3$]$^{2+}$ (bpy = 2,2′-bipyridine) sensitizers, NDI^{2-} is formed after irradiation with visible light in deaerated CH_3CN in the presence of excess triethylamine. The mechanism for this electron accumulation involves a combination of photoinduced and thermal elementary steps. In a structurally related molecular pentad with two peripheral triarylamine (TAA) electron donors attached covalently to a central [Ru(bpy)$_3$]$^{2+}$-NDI-[Ru(bpy)$_3$]$^{2+}$ core but no sacrificial reagents present, photoexcitation only leads to NDI$^-$ (and TAA$^+$), whereas NDI^{2-} is unattainable due to rapid electron transfer events counteracting charge accumulation. For solar energy conversion, this finding means that fully integrated systems with covalently linked photosensitizers and catalysts are not necessarily superior to multicomponent systems, because the fully integrated systems can suffer from rapid undesired electron transfer events that impede multielectron reactions on the catalyst.

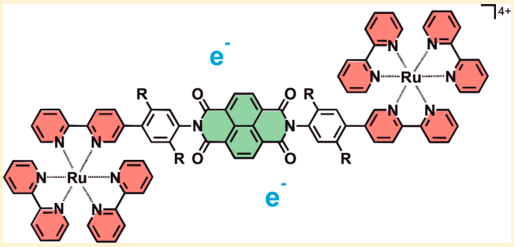

INTRODUCTION

To perform multielectron redox chemistry using visible light as an energy input, it is desirable to understand the basic principles of the photodriven accumulation of redox equivalents.[1,2] Many prior studies employed sacrificial reagents to generate solar fuels using various molecular catalysts, but often the focus was mainly on product formation rather than on understanding the key elementary step of charge accumulation.[3−15] Photosensitizers and catalysts are often attached covalently to each other, but in some cases the resulting fully integrated assemblies do not exhibit strongly improved properties compared to multicomponent systems in which there are no covalent linkages between individual components or reactants. Against this background, we became interested in performing a direct comparison of light-induced charge accumulation in multicomponent and unimolecular systems with particular focus on mechanistic aspects.

Several prior studies concentrated specifically on the phenomenon of light-driven charge accumulation in artificial molecular systems, as highlighted in three recent reviews.[16−18] Many of the studied systems relied on sacrificial reagents,[19−29] but newer systems (as well as a few older ones) exhibit intramolecular charge accumulation in absence of sacrificial substances.[30−35] Nevertheless, compared to the ordinary photoinduced transfer of single electrons, light-induced charge accumulation is still poorly explored, for example, because multiple photons are usually required to drive multiple electron transfers, and because there can be many processes that counteract charge accumulation after primary charge separation.

In this work, we explored triad **I** and pentad **II** (Scheme 1) with a view to obtaining doubly reduced naphthalene diimide (NDI^{2-}) after excitation of the covalently attached [Ru(bpy)$_3$]$^{2+}$ (bpy = 2,2′-bipyridine) photosensitizers with visible light. NDI is well-suited for studies with UV−vis spectroscopy, because its neutral, singly, and doubly reduced forms exhibit diagnostic, easily distinguishable signatures.[36] We aimed to explore how charge accumulation on NDI can be achieved with a standard photosensitizer such as [Ru(bpy)$_3$]$^{2+}$, to understand its mechanisms in detail, and to obtain insight into the factors limiting its overall efficiency. Through direct comparison of triad **I** (which requires sacrificial electron donors) and pentad **II** (which has covalently attached donors), we aimed to identify advantages and disadvantages of multicomponent versus fully integrated (covalently linked) systems for photoinduced charge accumulation, and more generally, for artificial photosynthesis relying on multielectron chemistry.

RESULTS AND DISCUSSION

Syntheses and characterization data of triad **I** and pentad **II** are reported in the Supporting Information. Both compounds have the [Ru(bpy)$_3$]$^{2+}$-NDI-[Ru(bpy)$_3$]$^{2+}$ core motif in common but with different connectivity between subunits. This is owing to synthetic challenges faced in the course of attempts to make a pentad that is structurally strictly analogous to triad **I** (i.e., with 5,5′- instead of 4,4′-substituted bpy units). This structural difference is expected to entail significantly stronger electronic communication between subunits in the pentad, because

Received: October 11, 2016
Published: February 23, 2017

DOI: 10.1021/acs.inorgchem.6b02446
Inorg. Chem. 2017, 56, 2432−2439

Scheme 1. Molecular Structures of Triad I and Pentad II

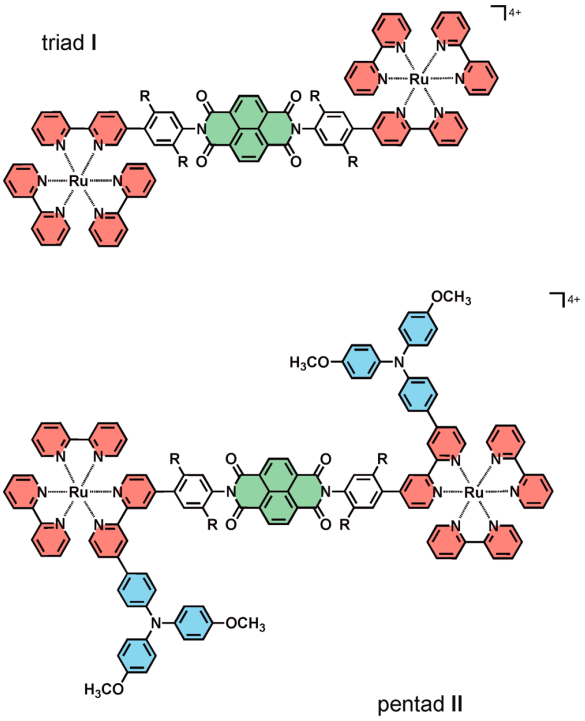

electronic coupling across the 4- and 4′-positions of bpy is usually stronger than across its 5- and 5′-positions.[37,38]

The cyclic voltammograms of **I** and **II** are essentially a superposition of the individual voltammograms of their subcomponents (Supporting Information, Figures S1 and S2). The first two reductions are NDI-based, whereas $[Ru(bpy)_3]^{2+}$-localized reductions appear at more negative potentials (Table 1).

Table 1. Redox Potentials of the Individual Components of Triad I and Pentad II in CH_3CN at 25 °C

	triad **I**		pentad **II**	
redox couple	$E_{1/2}$[a] [V]	$E_{p,a} - E_{p,c}$ [mV]	$E_{1/2}$[a] [V]	$E_{p,a} - E_{p,c}$ [mV]
TAA^+/TAA			0.38	103
NDI/NDI^-	−0.83	82	−0.89	70
NDI^-/NDI^{2-}	−1.33	60	−1.34	65
bpy/bpy^-	−1.53	99	−1.72	112

[a] $E_{1/2}$ in volts versus Fc^+/Fc. $E_{p,a} - E_{p,c}$ (in mV) is the difference in anodic and cathodic peak potentials.

UV−vis spectra of **I** and **II** in CH_3CN exhibit the typical MLCT absorptions of the $[Ru(bpy)_3]^{2+}$ chromophores and $\pi-\pi^*$ transitions on bpy, NDI, and TAA at shorter wavelengths (Supporting Information, Figure S3). Selective excitation of the $[Ru(bpy)_3]^{2+}$ chromophore in the visible spectral range is readily possible, but given the direct attachment of *p*-phenylene substituents to one of its bpy ligands, consideration of the ruthenium chromophore as an isolated $[Ru(bpy)_3]^{2+}$ complex is a somewhat crude (but for our purposes nevertheless sufficient) approximation.[39]

Charge accumulation studies were performed on 1.7×10^{-5} M solutions of **I** in deaerated CH_3CN containing various concentrations of triethylamine (Et_3N) or tetra-*n*-butylammonium 5,6-isopropylidene ascorbate (TBA^+ $iASc^-$). Continuous irradiation at 410 nm with a flux of $(3.22 \pm 0.14) \times 10^{16}$ photons per second occurred in a commercial spectrofluorimeter over several minutes (see Supporting Information for details). In presence of 0.5 M Et_3N, the spectral changes shown in Figure 1a appear in the course of the first 30 s of photo-irradiation.

Comparison with the UV−vis difference spectrum obtained from an experiment in which the NDI unit of **I** in dry tetrahydrofuran (THF) was reduced to NDI^- with benzophenone radical anion (Figure 1b) shows that the main photochemical reduction product after 30 s is NDI^-, while $[Ru(bpy)_3]^{2+}$ must be in its initial (ground) state. Continued irradiation for another 690 s under the same conditions then induces the spectral changes shown in Figure 1c. The final spectrum is compatible with the formation of NDI^{2-}, as the comparison with the difference spectrum obtained after chemical reduction of the NDI unit of **I** to NDI^{2-} in THF (Figure 1d) shows. From the difference spectra, it becomes evident why 410 nm was chosen for excitation: At this wavelength the changes in optical density in the course of the conversion of NDI to NDI^- and finally NDI^{2-} are comparatively small, and it remains possible to excite relatively selectively into the $[Ru(bpy)_3]^{2+}$ chromophore. Direct excitation into NDI^- or NDI^{2-} could potentially induce energy-wasting electron transfer events (see below).[17,31,40,41]

From the difference spectra in Figure 1a,c the proportions of NDI^0, NDI^-, and NDI^{2-} at different irradiation times can be determined. The resulting speciation curves (Figure 2) indicate that in the presence of 0.5 M Et_3N the population of NDI^- maximizes at ca. 30 s, and after 720 s the formation of NDI^{2-} is essentially complete. When using 0.25 M Et_3N the kinetics are similar, but with 0.1 M Et_3N they are markedly slower (Supporting Information, Figures S4 and S5). These irradiation times are obviously dependent on triad concentration and irradiation flux, and consequently it is more meaningful to report quantum yields. In the first few seconds of the conversion of NDI^0 to NDI^-, as well as in the conversion of NDI^- to NDI^{2-}, the growth of the new absorption signals is approximately linear, and we used these (short) time regimes to estimate the quantum yields (ϕ) in Table 2. The key observation is that the conversion of NDI^- to NDI^{2-} has a markedly lower quantum yield than the formation of NDI^- from NDI^0. Not surprisingly, the electron-accumulating step is therefore the more difficult one to accomplish.

Mechanistic insight comes from transient absorption spectroscopy and luminescence quenching experiments. Excitation of triad **I** at 532 nm in deaerated CH_3CN in absence of Et_3N induces intramolecular electron transfer from photoexcited $[Ru(bpy)_3]^{2+}$ to NDI (Supporting Information, Figure S6) with a time constant of 300 ps (Supporting Information, Figure S7a). Subsequently, thermal charge recombination, that is, electron transfer from NDI^- to $[Ru(bpy)_3]^{3+}$, takes place with a time constant of ~20 ns (Supporting Information, Figure S7b). For ^{3}MLCT excited-state quenching of $[Ru(bpy)_3]^{2+}$ by Et_3N an upper rate limit of 1×10^6 M^{-1} s^{-1} has been estimated in prior studies;[42] hence, at a concentration of 0.5 M Et_3N, the pseudo-first-order rate constant for electron transfer from Et_3N to photoexcited $[Ru(bpy)_3]^{2+}$ is less than 5×10^5 s^{-1}. This is more than 6600 times slower than intramolecular photoinduced electron transfer to NDI in triad **I**, and consequently it seems clear that the dominant reaction pathway for the

DOI: 10.1021/acs.inorgchem.6b02446
Inorg. Chem. 2017, 56, 2432−2439

Inorganic Chemistry Article

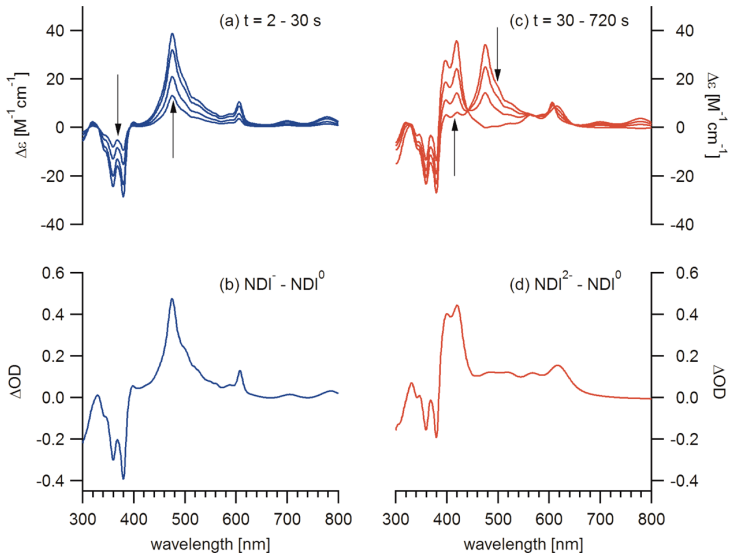

Figure 1. (a) UV−vis difference spectra measured on a 1.7×10^{-5} M solution of triad **I** in deaerated CH_3CN containing 0.5 M Et_3N. Irradiation occurred with a flux of $(3.22 \pm 0.14) \times 10^{16}$ photons per second at 410 nm over time intervals ranging from 2 to 30 s. The spectrum measured at t = 0 s served as a baseline. (b) UV−vis difference spectrum obtained after chemical reduction of the NDI unit in triad **I** to NDI^-, using benzophenone radical anion in THF as a chemical reductant. The spectrum of the triad prior to reduction served as a baseline. (c) UV−vis difference spectra of the same solution as in (a) measured after irradiation times between 30 and 720 s. (d) UV−vis difference spectrum obtained after reduction of NDI in triad **I** to NDI^{2-} using benzophenone radical anion in THF; the spectrum measured prior to adding the chemical reductant served as a baseline.

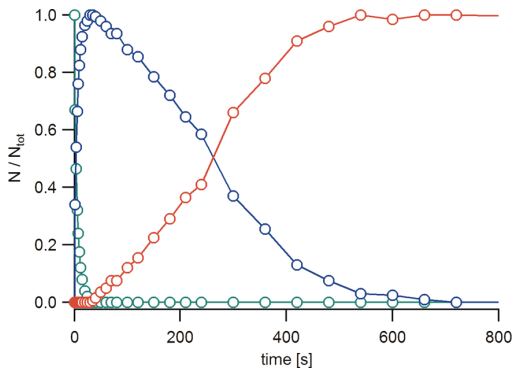

Figure 2. Relative proportions (molar fractions) of NDI (green), NDI^- (blue), and NDI^{2-} (red) present in triad **I** after different irradiation times. The flux used for excitation at 410 nm was $(3.22 \pm 0.14) \times 10^{16}$ photons per second, and the sample contained 3.4×10^{-8} mol of triad **I**. This corresponds to roughly two photons per molecule per second. Some of the quantum yields reported in Table 2 were extracted from this data.

Table 2. Quantum Yields for Formation of NDI^- and NDI^{2-} when Irradiating Triad I at 410 nm in Deaerated CH_3CN at 25 °C in the Presence of Different Concentrations of Et_3N[a]

$[Et_3N]$, M	ϕ (NDI → NDI^-)	ϕ (NDI^- → NDI^{2-})
0.10	0.061	0.000 26
0.25	0.079	0.001 41
0.50	0.107	0.001 50

[a]The experimental uncertainties are ~20%.

formation of NDI^- in the presence of Et_3N involves the sequence of intra- and intermolecular electron transfer steps shown in Scheme 2a (process (i) rather than process (ii)).

Following the intramolecular step leading to $[Ru(bpy)_3]^{3+}$ and NDI^-, regeneration of $[Ru(bpy)_3]^{2+}$ by Et_3N is in competition with intramolecular thermal charge recombination. For the reaction between $[Ru(bpy)_3]^{3+}$ and triethanolamine a rate constant of 1.67×10^7 M^{-1} s^{-1} has been reported.[43] Assuming that the reaction with Et_3N is similarly rapid, one expects a pseudo-first-order rate constant of $\sim 8 \times 10^6$ s^{-1} at an Et_3N concentration of 0.5 M. Since the rate constant for intramolecular charge recombination between $[Ru(bpy)_3]^{3+}$ and NDI^- is $\sim 5 \times 10^7$ s^{-1} (time constant of ~20 ns, see above), the bimolecular reaction between $[Ru(bpy)_3]^{3+}$ and Et_3N is comparatively slow. This explains why the quantum yields for the formation of NDI^- under the steady-state irradiation conditions are limited to values in the range of 0.061−0.107 (Table 2).

The mechanism leading from NDI^- to NDI^{2-} is more difficult to identify. Spontaneous thermal disproportionation of NDI^- to NDI^{2-} and NDI^0 is not possible, because it is exergonic by 0.4 eV based on the redox potentials for triad **I** (Table 1). When a deaerated solution of triad **I** in which NDI^- has been formed photochemically with Et_3N is left standing in the dark, NDI^{2-} is not formed (Supporting Information, Figure S8a), indicating that further light input is required for the electron-accumulating step. Reductive quenching of ^{3}MLCT-excited $[Ru(bpy)_3]^{2+}$ by Et_3N (process (vi) in Scheme 2b) is slow ($<5 \times 10^5$ s^{-1} at 0.5 M, see above), and intramolecular electron transfer to NDI^- (process (v) in Scheme 2b) is energetically uphill by 0.14 eV based on the potentials in Table 1. Moreover, intramolecular reductive ^{3}MLCT quenching by NDI^- (process (iv) in Scheme 2b) is exergonic by 1.4 eV. Given its high driving force, this undesired charge shift event is likely to represent the dominant reaction channel after absorption of a photon by triads in which NDI^- is present. This process is expected to be followed by intramolecular thermal charge shift from $[Ru(bpy)_3]^+$ to NDI^0, and the net

DOI: 10.1021/acs.inorgchem.6b02446
Inorg. Chem. 2017, 56, 2432−2439

Scheme 2. Reaction Pathways Leading to Electron Accumulation in Triad I in the Presence of Excess Et_3N[a]

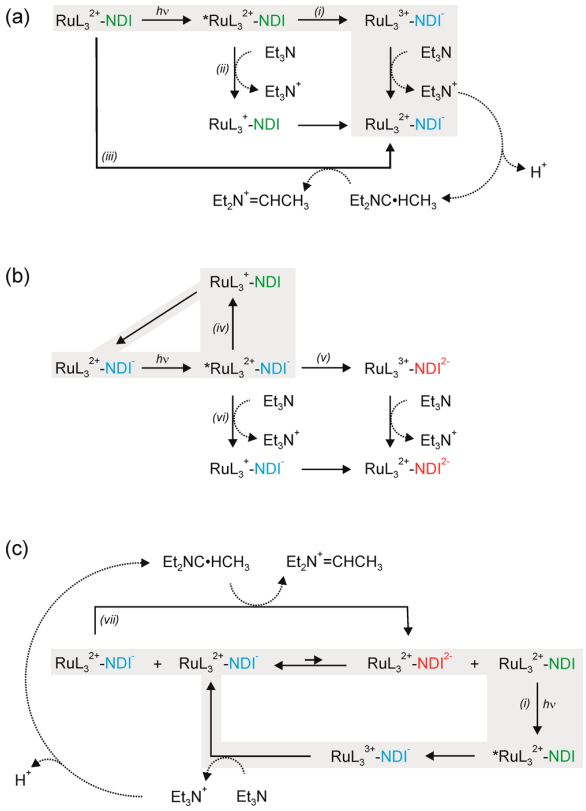

[a]Only one of the two photosensitizers (RuL_3^{2+}) of the triad is indicated for brevity. Gray shaded areas mark the most important pathways. (a) Sequence of reaction steps leading to the formation of NDI^-. (b) Unproductive electron transfer events leading to light absorption but no net photochemistry. (c) Displacement of the (unfavorable) disproportionation equilibrium through continuous removal of NDI^0 and further formation of NDI^{2-} through a thermal reaction with a carbon-centered radical resulting from the decomposition of oxidized Et_3N.

result is the initial $[Ru(bpy)_3]^{2+}/NDI^-$ couple, but a photon has been consumed (gray shaded area in Scheme 2b). In view of all these pitfalls, the very low quantum yields for the electron-accumulating step (Table 2) become understandable.

After oxidation, Et_3N is known to deprotonate to form the highly reactive $Et_2NC{\cdot}{=}CH_3$ radical, which is able to reduce $[Ru(bpy)_3]^{2+}$ to $[Ru(bpy)_3]^{+}$ in the ground state, that is, in a dark reaction.[44−47] However, as noted above, the formation of NDI^{2-} from NDI^- does not proceed in absence of light (Supporting Information, Figure S8a), and it seems likely that the $Et_2NC{\cdot}{=}CH_3$ radicals react rapidly after they are formed. Presumably, they contribute to the formation of NDI^- already in the course of initial photo-irradiation (Figure 1a), as illustrated in Scheme 2a (process (iii)).

As noted above, spontaneous disproportionation of NDI^- can be excluded on thermodynamic grounds, but this disproportionation equilibrium can be shifted to the product side by constant removal of NDI^0 (Scheme 2c). When the solution contains largely NDI^- (i.e., after 30 s in Figure 1a), a residual concentration of $\sim 1 \times 10^{-8}$ M^{-1} of NDI^0 is expected in a solution containing an initial triad concentration of 1.7×10^{-5} M (based on a disproportionation constant of 1.7×10^{-7} obtained from the redox potentials in Table 1). Prolonged irradiation will eventually bring even this small residual amount of NDI^0 to reaction with Et_3N to afford NDI^-, and with NDI^0 being continuously consumed, more and more NDI^{2-} is formed (gray shaded area in Scheme 2c), also by the reaction of newly produced $Et_2NC{\cdot}{=}CH_3$ radicals (process (vii) in Scheme 2c).[44−47] It seems plausible that this thermal overall process (which, however, clearly relies on further light input) is in fact the main electron-accumulating step, particularly in view of the fact that excitation of $[Ru(bpy)_3]^{2+}$ in triads containing NDI^- predominantly induces an unproductive sequence of photo-induced and thermal (intramolecular) charge shift reactions (gray shaded area in Scheme 2b).

With ascorbate as an electron source instead of Et_3N, electron accumulation on NDI is not possible. For solubility reasons, we used tetra-*n*-butylammonium 5,6-isopropylidene ascorbate as a donor and deaerated methanol for steady-state photo-irradiation of triad **I** at 410 nm,[48] but in this experiment not even NDI^- is formed in substantial amounts (Supporting Information, Figure S8b). Transient absorption studies demonstrate why: Once NDI^- is formed (Supporting Information, Figures S9 and S10), it recombines with ascorbate oxidation products on a time scale of ~10 ms (Supporting Information, Figure S11). In view of the fact that ascorbate acts as a nonsacrificial quencher for ^{3}MLCT-excited $[Ru(2,2'\text{-bipyrazine})_3]^{2+}$,[49] this finding is not too surprising.

In a separate experiment, we photo-irradiated a three-component mixture containing 1.7×10^{-5} M of an NDI reference molecule, 2 equiv of $[Ru(bpy)_3]^{2+}$, and 0.5 M Et_3N in deaerated CH_3CN but were unable to observe charge accumulation on NDI in this case, possibly due to low cage escape yields (see Supporting Information for details). The quantum yield for formation of NDI^- in this case was 0.070.

Pentad **II** has covalently attached TAA donors, and we hoped to achieve entirely intramolecular photoinduced electron accumulation in this case, similar to what we recently observed in a structurally related system with anthraquinone as a two-electron acceptor.[35] Excitation of a 1.5×10^{-5} M solution of pentad **II** at 532 nm with laser pulses of ~10 ns duration leads to the transient absorption spectrum in Figure 3. The transient

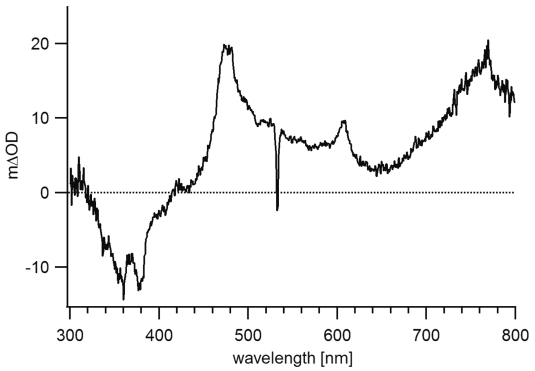

Figure 3. Transient absorption spectrum recorded from a 1.5×10^{-5} M solution of pentad **II** in deaerated CH_3CN. The sample was excited at 532 nm with laser pulses of ~10 ns duration, and detection occurred by time integration over 200 ns immediately after excitation. The spike at 532 nm is due to laser stray light.

DOI: 10.1021/acs.inorgchem.6b02446
Inorg. Chem. 2017, 56, 2432−2439

absorption bands at 477 and 606 nm signal the formation of NDI^{-} (Supporting Information, Figure S12, Figure 1b), while the bleaches at 355 and 380 nm mark the disappearance of NDI^{0} (Supporting Information, Figure S3).[36] The band at 765 nm is diagnostic for TAA^{+} (Supporting Information, Figure S13).[50−52]

The transient absorption signals at 480 and 770 nm form with an instrumentally limited time constant of 30 ps (Supporting Information, Figure S14). They decay in single exponential manner with the same time constant as the bleach at 360 nm recovers (Figure 4), indicating that (intramolecular)

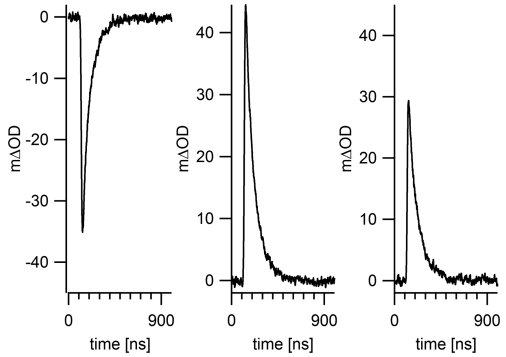

Figure 4. Temporal evolution of the transient absorption signals at (a) 360, (b) 480, and (c) 770 nm in the spectrum from Figure 3.

thermal charge recombination between NDI^{-} and TAA^{+} occurs with a time constant of 120 ns in deaerated CH_3CN at 25 °C. On the basis of the chemical reduction data in Figure 1d and based on prior studies,[36] one would expect NDI^{2-} to exhibit characteristic absorption bands at 400, 420, and 615 nm, and we searched carefully for such bands up to very high excitation pulse energies (~30 mJ). Because of the two-photon nature of the electron accumulation process,[35] the quantity of NDI^{2-} potentially produced is expected to be very low. For example, in a scenario in which 10% of all pentads are promoted to the NDI^{-}/TAA^{+} charge-separated state, only ~1% can be expected to be further promoted to a state in which NDI^{2-} is flanked by two TAA^{+} units.[31] We were unable to detect any signals attributable to NDI^{2-}, even when using a sequence of two excitation pulses (first pulse at 532 nm, 30 mJ; second pulse at 430 nm with a time delay of 50 ns, 21 mJ) in a so-called two-color pump−pump probe experiment (Supporting Information, Figure S15). The second excitation pulse at 430 nm seemed advantageous over excitation with two photons at 532 nm within a single pulse, because at 430 nm secondary excitation occurs predominantly into the MLCT absorption band of $[Ru(bpy)_3]^{2+}$, whereas at 532 nm $[Ru(bpy)_3]^{2+}$ only absorbs weakly, and there is also some NDI^{-} absorption. (Excitation of NDI^{-} could potentially trigger energy-wasting charge recombination reactions,[56] but we estimate that under the conditions used in our experiment the absorbance of photogenerated NDI^{-} at 532 nm is ~36 times weaker than that of $[Ru(bpy)_3]^{2+}$; hence, direct excitation of NDI^{-} is expected to be a minor deactivation pathway).

Even successful secondary excitation of $[Ru(bpy)_3]^{2+}$ can trigger unwanted electron-transfer reactions, in particular, either reductive excited-state quenching by NDI^{-} or oxidative quenching by TAA^{+}. Both of these processes have significantly higher driving force than the desired charge accumulation step leading to NDI^{2-} and two TAA^{+} units. These types of energy-wasting photoinduced charge recombination processes seem to be generally the most difficult ones to avoid when aiming at

Scheme 3. Reaction Pathways Relevant for Electron Accumulation[a]

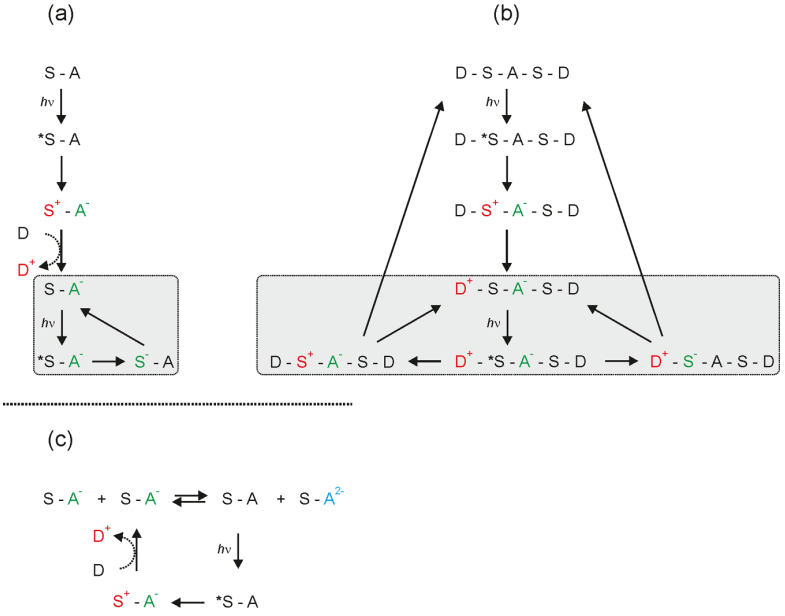

[a]In (a) sensitizer-acceptor dyads, and (b) in donor-sensitizer-acceptor-sensitizer-donor pentads. The grey shaded areas mark unproductive yet important electron transfer sequences competing with the electron-accumulating step. (c) Shift of a disproportionation equilibrium through constant removal of the starting material via continuous photoexcitation as a key pathway to charge accumulation.

DOI: 10.1021/acs.inorgchem.6b02446
Inorg. Chem. 2017, 56, 2432−2439

photoinduced charge accumulation,[31,40,41] and in this regard, multicomponent systems are advantageous compared to fully integrated, covalently linked systems. This is not only because of the large excess of sacrificial reagents in multicomponent systems but also because the primary oxidation and reduction products can diffuse away from each other, and when absorption of a second photon then takes place, the photoinduced charge recombination events discussed above are far less probable. Furthermore, in multicomponent systems the primary charge-separated state (here comprised of NDI^{-} and oxidized Et_3N in the case of **I**) is usually much longer-lived than in covalently connected systems (120 ns for NDI^{-} and TAA^{+} in pentad **II**), giving access to the disproportionation chemistry discussed above (Scheme 2c).

Attempts to favor the formation of NDI^{2-} by metal-ion coupled electron transfer (MCET) through addition of the strong Lewis acid Sc^{3+} (50 mM $Sc(OTf)_3$) were unsuccessful.[26,53,54]

Finally, we note that the ^{3}MLCT excited state of pentad **II** can in principle be quenched by energy transfer to TAA^{+} or NDI^{-}. Both radical species have absorptions at wavelengths below 600 nm (Figure 1b, Supporting Information, Figures S12 and S13), indicating that they both have excited states that are energetically below the lowest ^{3}MLCT state of $[Ru(bpy)_3]^{2+}$. The NDI^{-} and TAA^{+} are doublet species, and it remains to be explored how spin selection rules affect the efficiency of energy transfer in such a case.[55]

SUMMARY AND CONCLUSIONS

Triad **I** is symmetrical with two photosensitizer units for ease of synthesis, but in principle it is functionally analogous to simple sensitizer-acceptor (S-A) dyads. Photoreduction of the NDI unit by one electron in triad **I** is readily possible by the sequence of intra- and intermolecular electron transfer events outlined in Scheme 3a, leading ultimately to the $S\text{-}A^{-}$ form. Further excitation of the latter principally induces reductive excited-state quenching of the sensitizer by A^{-}, because the latter is a strong donor, and the excited sensitizer is a potent acceptor. The resulting $S^{-}\text{-}A$ form subsequently reverts spontaneously to the $S\text{-}A^{-}$ form via intramolecular thermal reverse electron transfer (gray shaded area in Scheme 3a). This unproductive (but energy-consuming) sequence of reactions is generally problematic in charge accumulation processes,[17,31,40,41,56] unless A^{-} is rendered less reducing, for example, through protonation in an overall proton-coupled electron transfer (PCET) reaction.[57−59]

In triad **I**, formation of the $S\text{-}A^{2-}$ form is only possible thanks to the displacement of the (unfavorable) disproportionation equilibrium in Scheme 3c. Importantly, this thermal reaction requires further light input for continuous removal of the S-A starting material and the concomitant formation of the charge-accumulated $S\text{-}A^{2-}$ species. This reaction pathway is only viable with sacrificial donors such as Et_3N but not with reversible donors such as ascorbate. In cases in which the disproportionation of A^{-} to A and A^{2-} is thermodynamically favored, no further light input is evidently necessary. This should be the case, for example, in various benzoquinone derivatives.[60,61]

In donor-sensitizer-acceptor-sensitizer-donor pentad **II**, the primary charge-separated state ($D^{+}\text{-}S\text{-}A^{-}\text{-}S\text{-}A$) has a comparatively short lifetime (120 ns), and this makes bimolecular disproportionation ineffective. Further excitation of the primary charge-separated species predominantly induces the unproductive electron transfer events shown in the gray shaded area of Scheme 3b: The excited state of the sensitizer (*S) is quenched either reductively by A^{-} or oxidatively by D^{+}. Again, PCET would be helpful to make A^{-} less reducing through protonation (see above) and to make D^{+} less oxidizing through deprotonation. Phenols would be an interesting choice as one-electron donors, because they usually undergo deprotonation in the course of oxidation.[62−69]

Our direct comparison of a multicomponent system (triad **I** with sacrificial donors) and a fully integrated compound (pentad **II** with covalently attached reversible donors) illustrates possible reaction pathways leading to electron accumulation and counteracting processes in both types of approaches. Our study demonstrates that, for applications aiming at multielectron (photo)redox reactions, the covalent linkage of photosensitizers and catalytic reaction centers introduces significant challenges with regard to avoiding unproductive (but energy-consuming) electron-transfer reactions upon sequential absorption of two (or more) photons. These unproductive electron transfers could presumably be decelerated significantly with suitable PCET photochemistry,[70−74] leading ultimately to the accumulation of redox equivalents rather than the accumulation of charge, similar to what is observed in the oxygen-evolving complex of photosystem II.[75,76]

ASSOCIATED CONTENT

Supporting Information

The Supporting Information is available free of charge on the ACS Publications website at DOI: 10.1021/acs.inorgchem.6b02446.

Synthesis protocols, product characterization data, electrochemical data, and optical spectroscopic data (PDF)

AUTHOR INFORMATION

Corresponding Author

*E-mail: oliver.wenger@unibas.ch.

ORCID

Oliver S. Wenger: 0000-0002-0739-0553

Author Contributions

The manuscript was written through contributions of all authors. All authors have given approval to the final version of the manuscript.

Funding

Swiss National Science Foundation (NCCR Molecular Systems Engineering, R′Equip Grant No. 206021_157687/1).

Notes

The authors declare no competing financial interest.

ACKNOWLEDGMENTS

This work was funded by the Swiss National Science Foundation through the NCCR Molecular Systems Engineering and through the R′Equip program (Grant No. 206021_157687/1).

REFERENCES

(1) Meyer, T. J. Chemical Approaches to Artificial Photosynthesis. *Acc. Chem. Res.* **1989**, *22*, 163−170.

(2) Gray, H. B.; Maverick, A. W. Solar Chemistry of Metal Complexes. *Science* **1981**, *214*, 1201−1205.

DOI: 10.1021/acs.inorgchem.6b02446
Inorg. Chem. 2017, 56, 2432−2439

(3) Artero, V.; Chavarot-Kerlidou, M.; Fontecave, M. Splitting Water with Cobalt. *Angew. Chem., Int. Ed.* **2011**, *50*, 7238−7266.
(4) Du, P. W.; Eisenberg, R. Catalysts Made of Earth-Abundant Elements (Co, Ni, Fe) for Water Splitting: Recent Progress and Future Challenges. *Energy Environ. Sci.* **2012**, *5*, 6012−6021.
(5) Dempsey, J. L.; Brunschwig, B. S.; Winkler, J. R.; Gray, H. B. Hydrogen Evolution Catalyzed by Cobaloximes. *Acc. Chem. Res.* **2009**, *42*, 1995−2004.
(6) Boston, D. J.; Xu, C. D.; Armstrong, D. W.; MacDonnell, F. M. Photochemical Reduction of Carbon Dioxide to Methanol and Formate in a Homogeneous System with Pyridinium Catalysts. *J. Am. Chem. Soc.* **2013**, *135*, 16252−16255.
(7) Kobayashi, M.; Masaoka, S.; Sakai, K. Photoinduced Hydrogen Evolution from Water by a Simple Platinum(II) Terpyridine Derivative: A Z-Scheme Photosynthesis. *Angew. Chem., Int. Ed.* **2012**, *51*, 7431−7434.
(8) Goy, R.; Bertini, L.; Görls, H.; De Gioia, L.; Talarmin, J.; Zampella, G.; Schollhammer, P.; Weigand, W. Silicon-Heteroaromatic FeFe Hydrogenase Model Complexes: Insight into Protonation, Electrochemical Properties, and Molecular Structures. *Chem. - Eur. J.* **2015**, *21*, 5061−5073.
(9) Petermann, L.; Staehle, R.; Pfeifer, M.; Reichardt, C.; Sorsche, D.; Wächtler, M.; Popp, J.; Dietzek, B.; Rau, S. Oxygen-Dependent Photocatalytic Water Reduction with a Ruthenium(imidazolium) Chromophore and a Cobaloxime Catalyst. *Chem. - Eur. J.* **2016**, *22*, 8240−8253.
(10) Herrero, C.; Lassalle-Kaiser, B.; Leibl, W.; Rutherford, A. W.; Aukauloo, A. Artificial Systems Related to Light Driven Electron Transfer Processes in PSII. *Coord. Chem. Rev.* **2008**, *252*, 456−468.
(11) Windle, C. D.; Perutz, R. N. Advances in Molecular Photocatalytic and Electrocatalytic CO_2 Reduction. *Coord. Chem. Rev.* **2012**, *256*, 2562−2570.
(12) Luo, S. P.; Mejia, E.; Friedrich, A.; Pazidis, A.; Junge, H.; Surkus, A. E.; Jackstell, R.; Denurra, S.; Gladiali, S.; Lochbrunner, S.; Beller, M. Photocatalytic Water Reduction with Copper-Based Photosensitizers: A Noble-Metal-Free System. *Angew. Chem., Int. Ed.* **2013**, *52*, 419−423.
(13) Pan, Q.; Freitag, L.; Kowacs, T.; Falgenhauer, J. C.; Korterik, J. P.; Schlettwein, D.; Browne, W. R.; Pryce, M. T.; Rau, S.; Gonzalez, L.; Vos, J. G.; Huijser, A. Peripheral Ligands as Electron Storage Reservoirs and Their Role in Enhancement of Photocatalytic Hydrogen Generation. *Chem. Commun.* **2016**, *52*, 9371−9374.
(14) Kowacs, T.; O'Reilly, L.; Pan, Q.; Huijser, A.; Lang, P.; Rau, S.; Browne, W. R.; Pryce, M. T.; Vos, J. G. Subtle Changes to Peripheral Ligands Enable High Turnover Numbers for Photocatalytic Hydrogen Generation with Supramolecular Photocatalysts. *Inorg. Chem.* **2016**, *55*, 2685−2690.
(15) Shan, B.; Schmehl, R. Photochemical Generation of Strong One-Electron Reductants via Light-Induced Electron Transfer with Reversible Donors Followed by Cross Reaction with Sacrificial Donors. *J. Phys. Chem. A* **2014**, *118*, 10400−10406.
(16) Pellegrin, Y.; Odobel, F. Molecular Devices Featuring Sequential Photoinduced Charge Separations for the Storage of Multiple Redox Equivalents. *Coord. Chem. Rev.* **2011**, *255*, 2578−2593.
(17) Hammarström, L. Accumulative Charge Separation for Solar Fuels Production: Coupling Light-Induced Single Electron Transfer to Multielectron Catalysis. *Acc. Chem. Res.* **2015**, *48*, 840−850.
(18) Bonn, A. G.; Wenger, O. S. Photoinduced Charge Accumulation in Molecular Systems. *Chimia* **2015**, *69*, 17−21.
(19) Konduri, R.; Ye, H. W.; MacDonnell, F. M.; Serroni, S.; Campagna, S.; Rajeshwar, K. Ruthenium Photocatalysts Capable of Reversibly Storing up to Four Electrons in a Single Acceptor Ligand: A Step Closer to Artificial Photosynthesis. *Angew. Chem., Int. Ed.* **2002**, *41*, 3185−3187.
(20) Konduri, R.; de Tacconi, N. R.; Rajeshwar, K.; MacDonnell, F. M. Multielectron Photoreduction of a Bridged Ruthenium Dimer, $[(phen)_2Ru(tatpp)Ru(phen)_2][PF_6]_4$: Aqueous Reactivity and Chemical and Spectroelectrochemical Identification of the Photoproducts. *J. Am. Chem. Soc.* **2004**, *126*, 11621−11629.
(21) Wouters, K. L.; de Tacconi, N. R.; Konduri, R.; Lezna, R. O.; MacDonnell, F. M. Driving Multi-Electron Reactions with Photons: Dinuclear Ruthenium Complexes Capable of Stepwise and Concerted Multi-Electron Reduction. *Photosynth. Res.* **2006**, *87*, 41−55.
(22) Rangan, K.; Arachchige, S. M.; Brown, J. R.; Brewer, K. J. Solar Energy Conversion Using Photochemical Molecular Devices: Photocatalytic Hydrogen Production from Water Using Mixed-Metal Supramolecular Complexes. *Energy Environ. Sci.* **2009**, *2*, 410−419.
(23) Molnar, S. M.; Nallas, G.; Bridgewater, J. S.; Brewer, K. J. Photoinitiated Electron Collection in a Mixed-Metal Trimetallic Complex of the Form $\{[(bpy)_2Ru(dpb)_2Ir]_2IrCl_2\}$ (bpy = 2,2′-Bipyridine and dpb = 2,3-Bis(2-pyridyl)benzoquinoxaline. *J. Am. Chem. Soc.* **1994**, *116*, 5206−5210.
(24) Matt, B.; Fize, J.; Moussa, J.; Amouri, H.; Pereira, A.; Artero, V.; Izzet, G.; Proust, A. Charge Photo-Accumulation and Photocatalytic Hydrogen Evolution under Visible Light at an Iridium(III)-Photosensitized Polyoxotungstate. *Energy Environ. Sci.* **2013**, *6*, 1504−1508.
(25) Polyansky, D.; Cabelli, D.; Muckerman, J. T.; Fujita, E.; Koizumi, T.; Fukushima, T.; Wada, T.; Tanaka, K. Photochemical and Radiolytic Production of an Organic Hydride Donor with a Ru(II) Complex Containing an NAD^+ Model Ligand. *Angew. Chem., Int. Ed.* **2007**, *46*, 4169−4172.
(26) Bonn, A. G.; Wenger, O. S. Photoinduced Charge Accumulation by Metal Ion-Coupled Electron Transfer. *Phys. Chem. Chem. Phys.* **2015**, *17*, 24001−24010.
(27) Knör, G.; Vogler, A.; Roffia, S.; Paolucci, F.; Balzani, V. Switchable Photoreduction Pathways of Antimony(V) Tetraphenylporphyrin. A Potential Multielectron Transfer Photosensitizer. *Chem. Commun.* **1996**, 1643−1644.
(28) Elliott, K. J.; Harriman, A.; Le Pleux, L.; Pellegrin, Y.; Blart, E.; Mayer, C. R.; Odobel, F. A Porphyrin-Polyoxometallate Bio-Inspired Mimic for Artificial Photosynthesis. *Phys. Chem. Chem. Phys.* **2009**, *11*, 8767−8773.
(29) Kitamoto, K.; Ogawa, M.; Ajayakumar, G.; Masaoka, S.; Kraatz, H. B.; Sakai, K. Molecular Photo-Charge-Separators Enabling Single-Pigment-Driven Multi-Electron Transfer and Storage Leading to H_2 Evolution From Water. *Inorg. Chem. Front.* **2016**, *3*, 671−680.
(30) Karlsson, S.; Boixel, J.; Pellegrin, Y.; Blart, E.; Becker, H. C.; Odobel, F.; Hammarström, L. Accumulative Electron Transfer: Multiple Charge Separation in Artificial Photosynthesis. *Faraday Discuss.* **2012**, *155*, 233−252.
(31) Karlsson, S.; Boixel, J.; Pellegrin, Y.; Blart, E.; Becker, H. C.; Odobel, F.; Hammarström, L. Accumulative Charge Separation Inspired by Photosynthesis. *J. Am. Chem. Soc.* **2010**, *132*, 17977−17979.
(32) O'Neil, M. P.; Niemczyk, M. P.; Svec, W. A.; Gosztola, D.; Gaines, G. L.; Wasielewski, M. R. Picosecond Optical Switching Based on Biphotonic Excitation of an Electron Donor-Acceptor-Donor Molecule. *Science* **1992**, *257*, 63−65.
(33) Imahori, H.; Hasegawa, M.; Taniguchi, S.; Aoki, M.; Okada, T.; Sakata, Y. Synthesis and Photophysical Properties of Porphyrin-Tetracyanoanthraquinodimethane-Porphyrin Triad: Photon-Dependent Molecular Switching. *Chem. Lett.* **1998**, *27*, 721−722.
(34) Ghaddar, T. H.; Wishart, J. F.; Thompson, D. W.; Whitesell, J. K.; Fox, M. A. A Dendrimer-Based Electron Antenna: Paired Electron-Transfer Reactions in Dendrimers With a 4,4′-Bipyridine Core and Naphthalene Peripheral Groups. *J. Am. Chem. Soc.* **2002**, *124*, 8285−8289.
(35) Orazietti, M.; Kuss-Petermann, M.; Hamm, P.; Wenger, O. S. Light-Driven Electron Accumulation in a Molecular Pentad. *Angew. Chem., Int. Ed.* **2016**, *55*, 9407−9410.
(36) Gosztola, D.; Niemczyk, M. P.; Svec, W.; Lukas, A. S.; Wasielewski, M. R. Excited Doublet States of Electrochemically Generated Aromatic Imide and Diimide Radical Anions. *J. Phys. Chem. A* **2000**, *104*, 6545−6551.
(37) Büldt, L. A.; Prescimone, A.; Neuburger, M.; Wenger, O. S. Photoredox Properties of Homoleptic d^6 Metal Complexes With the Electron-Rich 4,4′,5,5′-Tetramethoxy-2,2′-Bipyridine Ligand. *Eur. J. Inorg. Chem.* **2015**, *2015*, 4666−4677.

DOI: 10.1021/acs.inorgchem.6b02446
Inorg. Chem. 2017, 56, 2432−2439

(38) Lever, A. B. P. Electrochemical Parametrization of Metal-Complex Redox Potentials, Using the Ruthenium(III)/Ruthenium(II) Couple to Generate a Ligand Electrochemical Series. *Inorg. Chem.* **1990**, *29*, 1271−1285.
(39) Kuss-Petermann, M.; Wenger, O. S. Electron Transfer Rate Maxima at Large Donor-Acceptor Distances. *J. Am. Chem. Soc.* **2016**, *138*, 1349−1358.
(40) Bonn, A. G.; Neuburger, M.; Wenger, O. S. Photoinduced Electron Transfer in Rhenium(I)-Oligotriarylamine Molecules. *Inorg. Chem.* **2014**, *53*, 11075−11085.
(41) Bonn, A. G.; Yushchenko, O.; Vauthey, E.; Wenger, O. S. Photoinduced Electron Transfer in an Anthraquinone-Ru(bpy)$_3^{2+}$-Oligotriarylamine-Ru(bpy)$_3^{2+}$-Anthraquinone Pentad. *Inorg. Chem.* **2016**, *55*, 2894−2899.
(42) Hoffman, M. Z.; Bolletta, F.; Moggi, L.; Hug, G. L. Rate Constants for the Quenching of Excited-States of Metal-Complexes in Fluid Solution. *J. Phys. Chem. Ref. Data* **1989**, *18*, 219−544.
(43) Suzuki, M.; Waraksa, C. C.; Mallouk, T. E.; Nakayama, H.; Hanabusa, K. Enhanced Photocatalytic Reduction of Methyl Viologen by Self-Assembling Ruthenium(II)poly(pyridyl) Complexes with L-Lysine Containing Side Chains. *J. Phys. Chem. B* **2002**, *106*, 4227−4231.
(44) Delaive, P. J.; Foreman, T. K.; Giannotti, C.; Whitten, D. G. Photoinduced Electron-Transfer Reactions of Transition-Metal Complexes with Amines - Mechanistic Studies of Alternate Pathways to Back Electron-Transfer. *J. Am. Chem. Soc.* **1980**, *102*, 5627−5631.
(45) Summers, P. A.; Dawson, J.; Ghiotto, F.; Hanson-Heine, M. W. D.; Vuong, K. Q.; Stephen Davies, E.; Sun, X. Z.; Besley, N. A.; McMaster, J.; George, M. W.; Schröder, M. Photochemical Dihydrogen Production Using an Analogue of the Active Site of NiFe Hydrogenase. *Inorg. Chem.* **2014**, *53*, 4430−4439.
(46) Cohen, S. G.; Parola, A.; Parsons, G. H. Photoreduction by Amines. *Chem. Rev.* **1973**, *73*, 141−161.
(47) Probst, B.; Rodenberg, A.; Guttentag, M.; Hamm, P.; Alberto, R. A Highly Stable Rhenium-Cobalt System for Photocatalytic H_2 Production: Unraveling the Performance-Limiting Steps. *Inorg. Chem.* **2010**, *49*, 6453−6460.
(48) Zhu, X. Q.; Mu, Y. Y.; Li, X. T. What Are the Differences between Ascorbic Acid and NADH as Hydride and Electron Sources in Vivo on Thermodynamics, Kinetics, and Mechanism? *J. Phys. Chem. B* **2011**, *115*, 14794−14811.
(49) Neshvad, G.; Hoffman, M. Z. Reductive Quenching of the Luminescent Excited-State of Tris(2,2′-Bipyrazine)ruthenium(2+) Ion in Aqueous Solution. *J. Phys. Chem.* **1989**, *93*, 2445−2452.
(50) Lambert, C.; Nöll, G. The Class II/III Transition in Triarylamine Redox Systems. *J. Am. Chem. Soc.* **1999**, *121*, 8434−8442.
(51) Sreenath, K.; Thomas, T. G.; Gopidas, K. R. Cu(II) Mediated Generation and Spectroscopic Study of the Tris(4-anisyl)amine Radical Cation and Dication. Unusually Shielded Chemical Shifts in the Dication. *Org. Lett.* **2011**, *13*, 1134−1137.
(52) Hankache, J.; Wenger, O. S. Microsecond Charge Recombination in a Linear Triarylamine-Ru(bpy)$_3^{2+}$-Anthraquinone Triad. *Chem. Commun.* **2011**, *47*, 10145−10147.
(53) Fukuzumi, S.; Ohkubo, K.; Morimoto, Y. Mechanisms of Metal Ion-Coupled Electron Transfer. *Phys. Chem. Chem. Phys.* **2012**, *14*, 8472−8484.
(54) Okamoto, K.; Mori, Y.; Yamada, H.; Imahori, H.; Fukuzumi, S. Effects of Metal Ions on Photoinduced Electron Transfer in Zinc Porphyrin-Naphthalenediimide Linked Systems. *Chem. - Eur. J.* **2004**, *10*, 474−483.
(55) Guo, D.; Knight, T. E.; McCusker, J. K. Angular Momentum Conservation in Dipolar Energy Transfer. *Science* **2011**, *334*, 1684−1687.
(56) Kuss-Petermann, M.; Wenger, O. S. Pump-Pump-Probe Spectroscopy of a Molecular Triad Monitoring Detrimental Processes for Photoinduced Charge Accumulation. *Helv. Chim. Acta* **2017**, *100*, e1600283.
(57) Mayer, J. M. Proton-Coupled Electron Transfer: A Reaction Chemist's View. *Annu. Rev. Phys. Chem.* **2004**, *55*, 363−390.
(58) Hankache, J.; Wenger, O. S. Large Increase of the Lifetime of a Charge-Separated State in a Molecular Triad Induced by Hydrogen-Bonding Solvent. *Chem. - Eur. J.* **2012**, *18*, 6443−6447.
(59) Hankache, J.; Niemi, M.; Lemmetyinen, H.; Wenger, O. S. Hydrogen-Bonding Effects on the Formation and Lifetimes of Charge-Separated States in Molecular Triads. *J. Phys. Chem. A* **2012**, *116*, 8159−8168.
(60) Quan, M.; Sanchez, D.; Wasylkiw, M. F.; Smith, D. K. Voltammetry of Quinones in Unbuffered Aqueous Solution: Reassessing the Roles of Proton Transfer and Hydrogen Bonding in the Aqueous Electrochemistry of Quinones. *J. Am. Chem. Soc.* **2007**, *129*, 12847−12856.
(61) Warren, J. J.; Tronic, T. A.; Mayer, J. M. Thermochemistry of Proton-Coupled Electron Transfer Reagents and its Implications. *Chem. Rev.* **2010**, *110*, 6961−7001.
(62) Markle, T. F.; Mayer, J. M. Concerted Proton-Electron Transfer in Pyridylphenols: The Importance of the Hydrogen Bond. *Angew. Chem., Int. Ed.* **2008**, *47*, 738−740.
(63) Rhile, I. J.; Markle, T. F.; Nagao, H.; DiPasquale, A. G.; Lam, O. P.; Lockwood, M. A.; Rotter, K.; Mayer, J. M. Concerted Proton-Electron Transfer in the Oxidation of Hydrogen-Bonded Phenols. *J. Am. Chem. Soc.* **2006**, *128*, 6075−6088.
(64) Costentin, C.; Robert, M.; Savéant, J.-M. Concerted Proton-Electron Transfers: Electrochemical and Related Approaches. *Acc. Chem. Res.* **2010**, *43*, 1019−1029.
(65) Bronner, C.; Wenger, O. S. Kinetic Isotope Effects in Reductive Excited-State Quenching of Ru(2,2′-bipyrazine)$_3^{2+}$ by Phenols. *J. Phys. Chem. Lett.* **2012**, *3*, 70−74.
(66) Nomrowski, J.; Wenger, O. S. Photoinduced PCET in Ruthenium-Phenol Systems: Thermodynamic Equivalence of Uni- and Bidirectional Reactions. *Inorg. Chem.* **2015**, *54*, 3680−3687.
(67) Moore, G. F.; Hambourger, M.; Gervaldo, M.; Poluektov, O. G.; Rajh, T.; Gust, D.; Moore, T. A.; Moore, A. L. A Bioinspired Construct that Mimics the Proton Coupled Electron Transfer between P680$^{\bullet+}$ and the Tyr$_z$-His$_{190}$ Pair of Photosystem II. *J. Am. Chem. Soc.* **2008**, *130*, 10466−10467.
(68) Chen, J.; Kuss-Petermann, M.; Wenger, O. S. Distance Dependence of Bidirectional Concerted Proton-Electron Transfer in Phenol-Ru(2,2′-bipyridine)$_3^{2+}$ Dyads. *Chem. - Eur. J.* **2014**, *20*, 4098−4104.
(69) Lachaud, T.; Quaranta, A.; Pellegrin, Y.; Dorlet, P.; Charlot, M. F.; Un, S.; Leibl, W.; Aukauloo, A. A Biomimetic Model of the Electron Transfer between P-680 and the Tyr$_Z$-His$_{190}$ Pair of PSII. *Angew. Chem., Int. Ed.* **2005**, *44*, 1536−1540.
(70) Wenger, O. S. Proton-Coupled Electron Transfer with Photoexcited Metal Complexes. *Acc. Chem. Res.* **2013**, *46*, 1517−1526.
(71) Wenger, O. S. Proton-Coupled Electron Transfer with Photoexcited Ruthenium(II), Rhenium(I), and Iridium(III) Complexes. *Coord. Chem. Rev.* **2015**, *282*, 150−158.
(72) Eisenhart, T. T.; Dempsey, J. L. Photo-induced Proton-Coupled Electron Transfer Reactions of Acridine Orange: Comprehensive Spectral and Kinetics Analysis. *J. Am. Chem. Soc.* **2014**, *136*, 12221−12224.
(73) Concepcion, J. J.; Brennaman, M. K.; Deyton, J. R.; Lebedeva, N. V.; Forbes, M. D. E.; Papanikolas, J. M.; Meyer, T. J. Excited-State Quenching by Proton-Coupled Electron Transfer. *J. Am. Chem. Soc.* **2007**, *129*, 6968−6969.
(74) Bronner, C.; Wenger, O. S. Long-Range Proton-Coupled Electron Transfer in Phenol-Ru(2,2′-Bipyrazine)$_3^{2+}$ Dyads. *Phys. Chem. Chem. Phys.* **2014**, *16*, 3617−3622.
(75) Sproviero, E. M.; Gascon, J. A.; McEvoy, J. P.; Brudvig, G. W.; Batista, V. S. Quantum Mechanics/Molecular Mechanics Study of the Catalytic Cycle of Water Splitting in Photosystem II. *J. Am. Chem. Soc.* **2008**, *130*, 3428−3442.
(76) Sartorel, A.; Bonchio, M.; Campagna, S.; Scandola, F. Tetrametallic Molecular Catalysts for Photochemical Water Oxidation. *Chem. Soc. Rev.* **2013**, *42*, 2262−2280.

DOI: 10.1021/acs.inorgchem.6b02446
Inorg. Chem. 2017, 56, 2432−2439

4 Studies of Light-Induced Catalysis: Using Electron-Accumulation to Perform Two-Electron Catalysis

In the previous chapter, the accumulation of two electrons on a central naphthalene diimide (NDI) acceptor moiety could be achieved with the use of the sacrificial electron donor triethylamine (TEA). If kept under inert atmosphere, the charge-accumulated state was stable for several hours. Based on this finding, the idea arose to utilize the accumulated electrons to perform two-electron catalytic reductions.

In the context of the involvement of our group in the research cluster NCCR Molecular Systems Engineering,[45] a re-usable fuel was needed to power biochemical reactions occurring in the projected concept of a molecular factory. An appropriate fuel was found in nicotinamide adenine dinucleotide (phosphate) ($NAD(P)^+$), a molecule well known in biochemistry which in its reduced form (NAD(P)H) is a strong reductant and serves as an energy source for several enzymatic reactions.[46–49] NAD(P)H is a hydride donor and after its oxidation in a biochemical reaction, two electrons in combination with a proton are needed to regenerate its energy-rich state.[48, 50–52] To obtain exclusive 1,4-reduction on $NAD(P)^+$, a selective hydride transfer mediator is needed to generate the bioactive species.[48, 53–56] A suitable and commonly used mediator for this reaction is the complex [RhBpyCp*Cl]Cl which can undergo reduction from Rh^{III} to Rh^{I} and upon subsequent protonation leads to a hydride transfer reagent.[48, 49, 52, 53, 57–65] In the experiments described in this chapter, the $NAD(P)^+$ chemical analogue 1-benzyl nicotinamide (BNA^+) was used for simplicity.[66, 67] The structures of the Ru-NDI-Ru triad, the [RhBpyCp*Cl]Cl complex, of BNA^+ and of $NAD(P)^+$ are presented in Figure 4.1.

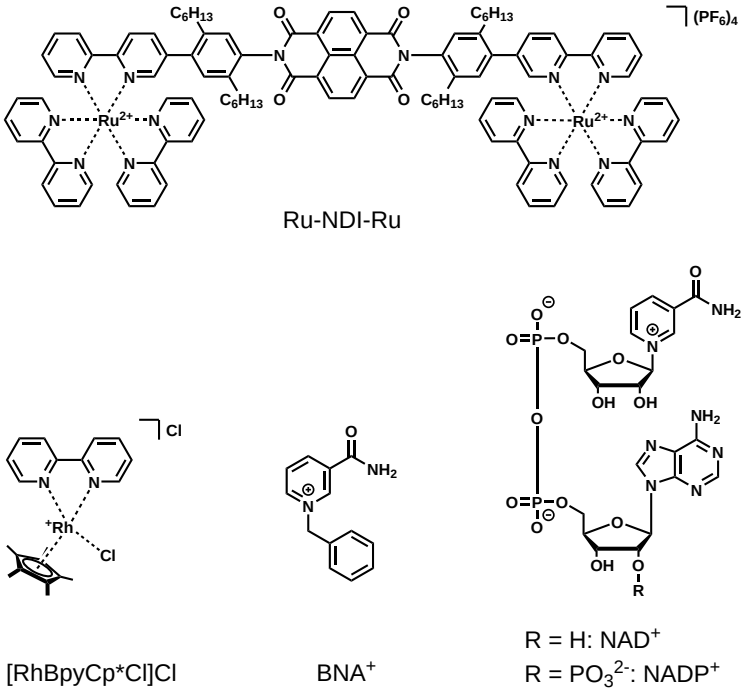

Figure 4.1: Molecular structures of the Ru-NDI-Ru triad, the [RhBpyCp*Cl]Cl co-catalyst, of BNA^+ and of $NAD(P)^+$.

4.1 The Ru-NDI-Ru Triad in an Intermolecular Reaction Cascade for BNA^+ Reduction

Steady-state Catalysis

For primary tests, reaction conditions in analogy to the ones used by Knör and co-workers[68] and Rau and co-workers[69] were chosen. The proposed reaction mechanism of the BNA^+ reduction is depicted in Scheme 4.1.

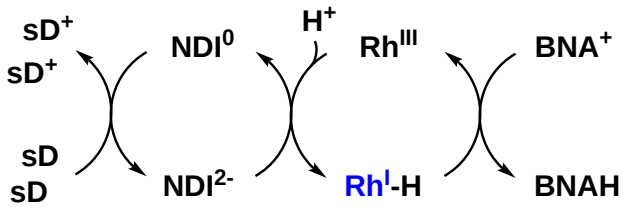

Scheme 4.1: Proposed reaction mechanism following excitation of the Ru-NDI-Ru triad leading to the reduction of BNA^+ to BNAH (sD: sacrificial electron donor).

In analogy to the experiments in Chapter 3, an excitation wavelength of 410 nm was chosen due to the NDI^- anion not exhibiting any absorption at this wavelength while the $[Ru(bpy)_3]^{2+}$ photosensitizer can still be sufficiently excited. Following the excitation

of the Ru-NDI-Ru triad, the accumulation of two electrons on the NDI acceptor is expected. The two electrons are then transferred onto the Rh co-catalyst, which undergoes protonation and subsequently reduces BNA^+ to BNAH.

In the following experiments, a 1:1 solvent mixture of MeCN and H_2O was used to ensure the solubility of all involved species. The result of the corresponding steady-state irradiation experiment can be seen in Figure 4.2.

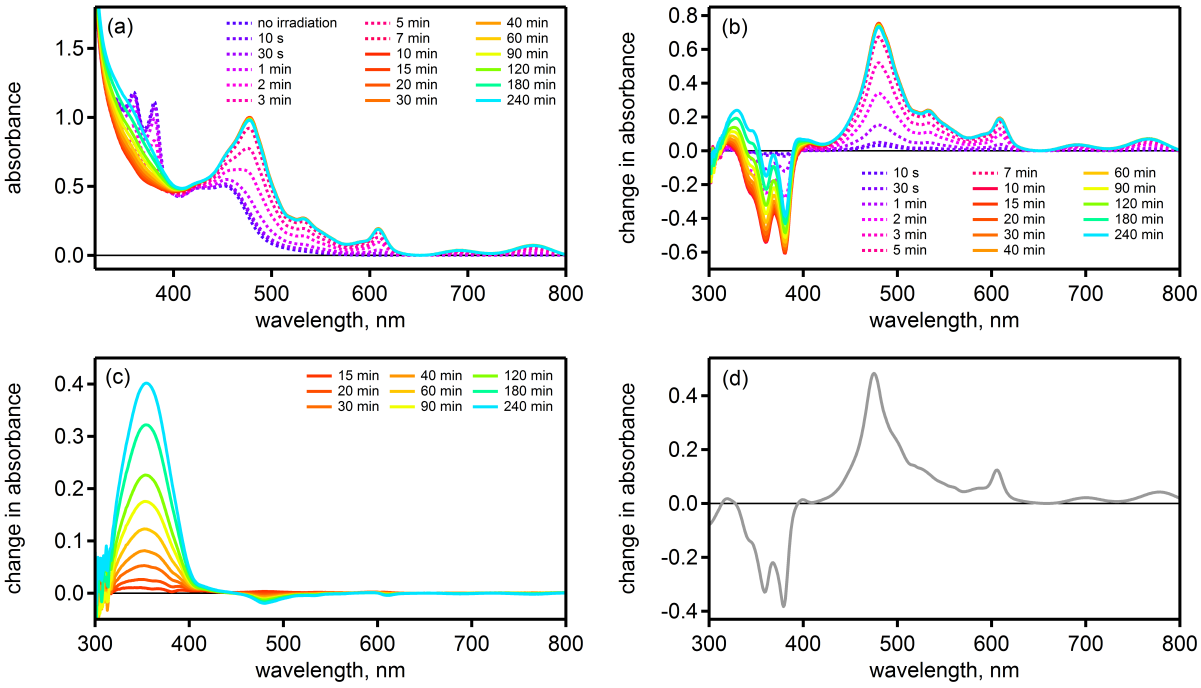

Figure 4.2: UV-Vis spectral changes upon steady-state irradiation of the catalytic mixture for BNAH generation. The sample contained the following components: triethanolamine (TEOA, 0.5 M) as sacrificial electron donor, a NaH_2PO_4/Na_2HPO_4 buffer system at pH 8.65, the Ru-NDI-Ru triad ($1.6 \cdot 10^{-5}$ M), the [RhBpyCp*Cl]Cl co-catalyst ($1.6 \cdot 10^{-4}$ M) and BNA^+Cl^- (1 mM) in a 1:1 mixture of MeCN and H_2O. The sample was de-oxygenated under exclusion of light and then irradiated at 410 nm. (a) UV-Vis absorption spectra measured after the time intervals given in the legend. (b) Difference spectra constructed by subtracting the ground state absorption spectrum prior to irradiation from the spectra measured after each time interval. (c) Difference spectra highlighting the formation of the absorption band at 355 nm. Spectra were constructed by subtracting the absorption spectrum measured after 10 minutes from the subsequently measured spectra. (d) Difference spectrum of NDI^- for comparison. Spectrum was taken from the chemical reduction experiment in Chapter 3.

In the steady-state irradiation experiment shown in Figure 4.2, growing absorption bands at 480, 610, 695 and 770 nm can be seen forming in the first 10 minutes (see Figure 4.2a and b, dashed lines). These absorption bands perfectly match with the spectral features of NDI^- as seen in Figure 4.2d and therefore show the formation of the singly reduced

NDI moiety. After 10 minutes of irradiation, the amount of $NDI^{\cdot-}$ remains at a constant level and a new absorption band located between 300 and 400 nm forms. This absorption band centered around 355 nm (see Figure 4.2c) can be either attributed to the formation of BNAH as reported in the literature[49, 68] or to the formation of a $(BNA)_2$ dimer formed by reaction of two $BNA^{\cdot}$ radical species.[70, 71]

Control Experiments

With this outcome, control experiments were performed to examine the necessity of the different components in the BNA^+ reduction process.

CONTROL1 - Removal of the [RhBpyCp*Cl]Cl co-catalyst

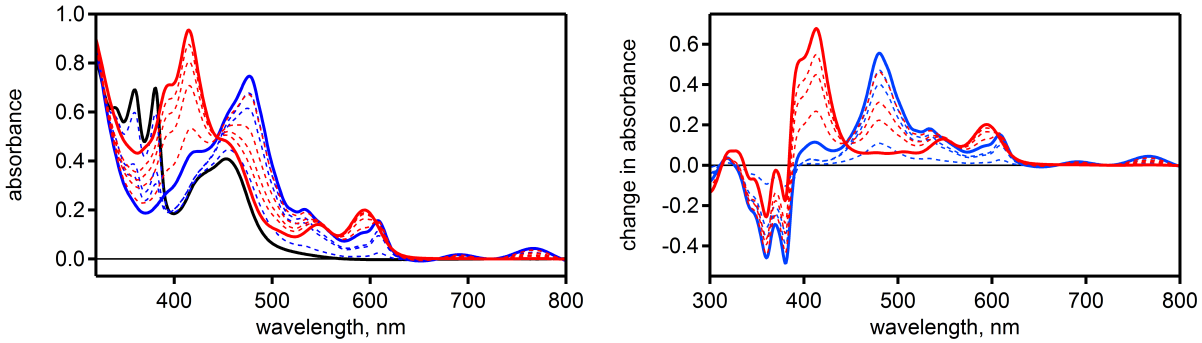

Figure 4.3: UV-Vis spectral changes upon steady-state irradiation of the catalytic mixture without the [RhBpyCp*Cl]Cl co-catalyst (***CONTROL1***). The control sample contained the following components: triethanolamine (TEOA, 0.5 M) as sacrificial electron donor, a NaH_2PO_4/Na_2HPO_4 buffer system at pH 8.65, the Ru-NDI-Ru triad ($1.6 \cdot 10^{-5}$ M) and BNA^+Cl^- (1 mM) in a 1:1 mixture of MeCN and H_2O. The sample was de-oxygenated under exclusion of light and then irradiated at 410 nm in the same time intervals as in the main experiment. For clarity reasons, the spectra only show a selection of traces. ***Left:*** UV-Vis absorption spectra. Black trace represents the ground state absorption spectrum, blue traces indicate $NDI^{\cdot-}$ formation (within the first 10 minutes) and red traces show the spectral changes associated with the NDI^{2-} formation. ***Right:*** Difference spectra constructed by subtraction of the ground state absorption spectrum from the subsequently measured spectra.

Upon exclusion of the [RhBpyCp*Cl]Cl co-catalyst, no formation of the absorption band around 355 nm could be observed. Instead, the recorded absorption spectra first show the formation of $NDI^{\cdot-}$ (blue traces) followed then by the formation of NDI^{2-}(red traces), very similar to the experiments in Chapter 3. This observation illustrates the importance of the Rh co-catalyst as direct electron transfer from NDI^{2-} to BNA^+ does not occur.

CONTROL2 - Removal of the Ru-NDI-Ru Triad

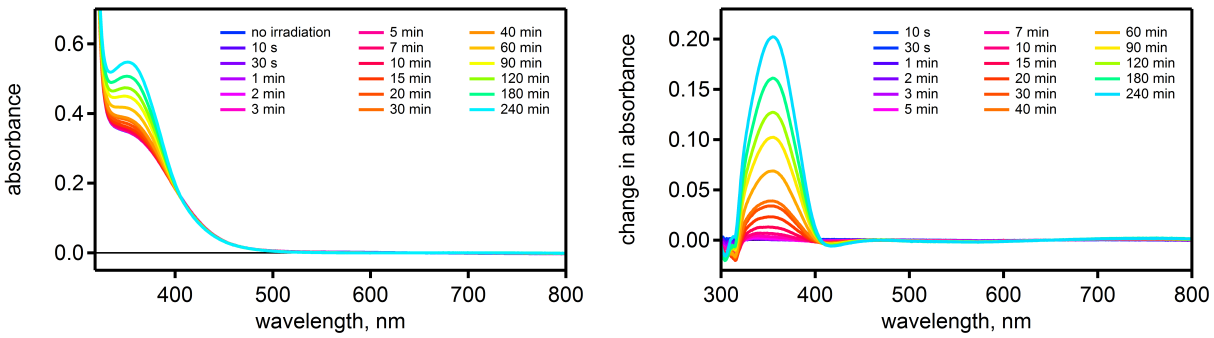

Figure 4.4: UV-Vis spectral changes upon steady-state irradiation of the catalytic mixture without the Ru-NDI-Ru triad (***CONTROL2***). The control sample contained the following components: triethanolamine (TEOA, 0.5 M) as sacrificial electron donor, a NaH_2PO_4/Na_2HPO_4 buffer system at pH 8.65, the [RhBpyCp*Cl]Cl co-catalyst ($1.6 \cdot 10^{-4}$ M) and BNA^+Cl^- (1 mM) in a 1:1 mixture of MeCN and H_2O. The sample was de-oxygenated under exclusion of light and then irradiated at 410 nm. ***Left:*** UV-Vis absorption spectra measured after different time intervals as given in the legend. ***Right:*** Difference spectra highlighting the formation of the absorption band at 355 nm. Spectra were constructed by subtraction of the ground state absorption spectrum before irradiation from the subsequently measured spectra.

Upon exclusion of the Ru-NDI-Ru triad, however, an absorption band at 355 nm can be seen forming (see Figure 4.4). The formation of the 355 nm band in this control experiment (absorbance change of $\Delta = 0.2$ in 240 min) is less effective than in the original experiment (absorbance change of $\Delta = 0.4$ in 240 min) but nevertheless notable. It appears that the absorption of the [RhBpyCp*Cl]Cl co-catalyst at 410 nm is sufficient to trigger the BNA^+ reduction process. The overall procedure for this is not quite clear because the Rh co-catalyst needs to undergo a two-electron reduction following excitation to form BNAH. A possible pathway lies in the disproportionation of two Rh^{II} species to Rh^{III} and Rh^{I}, which is reported in the literature[61, 72–74] and might be responsible for the observed BNAH formation.

Another potential pathway leading to BNA^+ reduction could be the absorption of light by BNA^+ itself, therefore acting as chromophore and electron acceptor at the same time. But as the ground state absorption spectrum of BNA^+ does not show any absorption above 320 nm, this possibility is excluded.[75]

The formation of the $(BNA)_2$ dimer in this experiment can also be excluded, as this reaction would require a one-electron transfer from Rh^{II} to BNA^+ which is energetically uphill ($\Delta G_{ET} = +0.34$ eV).[1] Additionally, the Rh^{II} species is coordinatively unstable

[1] The corresponding calculation is presented in the appendix.

and rapidly disproportionates into Rh^{I} and Rh^{III}.[76] A one-electron transfer process, and consequently the formation of the $(BNA)_2$ dimer, is therefore unlikely.

CONTROL3 - Replacement of the Ru-NDI-Ru Triad with $[Ru(bpy)_3]^{2+}$

With the observations upon removal of the Ru-NDI-Ru triad, the general question arose if the accumulation of two electrons is actually required for the BNA^+ reduction process. Therefore, a third control experiment was conducted where the Ru-NDI-Ru triad was replaced with the one-electron reductant $[Ru(bpy)_3]^{2+}$. To ensure comparability, the concentration of the $[Ru(bpy)_3]^{2+}$ photosensitizer was chosen to be twice the concentration of the Ru-NDI-Ru triad to make sure that the total amount of $[Ru(bpy)_3]^{2+}$ photosensitizer in both samples was equivalent. The sample was irradiated for the same time intervals as the samples before and the result of the control experiment can be seen in Figure 4.5.

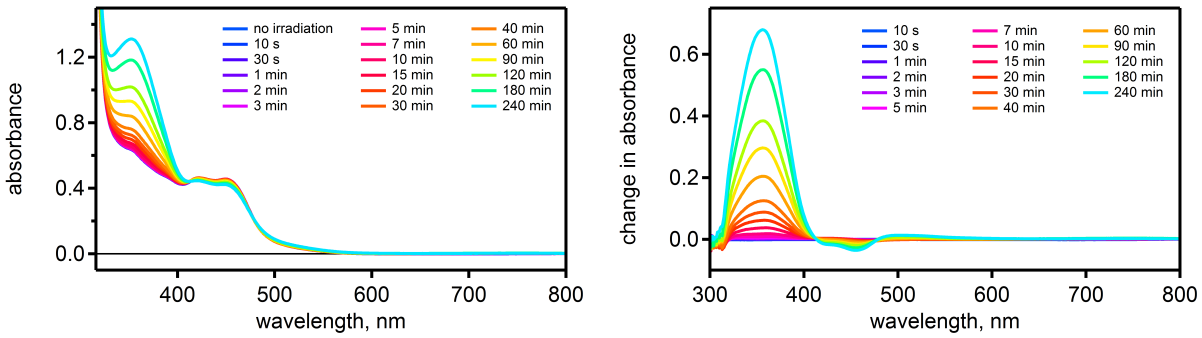

Figure 4.5: UV-Vis spectral changes upon steady-state irradiation of the catalytic mixture where the Ru-NDI-Ru triad is replaced by the $[Ru(bpy)_3]^{2+}$ photosensitizer (***CONTROL3***). The control sample contained the following components: $[Ru(bpy)_3](PF_6)_2$ ($3.2{\cdot}10^{-5}$ M), triethanolamine (TEOA, 0.5 M) as sacrificial electron donor, a NaH_2PO_4/Na_2HPO_4 buffer system at pH 8.65, the [RhBpyCp*Cl]Cl co-catalyst ($1.6{\cdot}10^{-4}$ M) and BNA^+Cl^- (1 mM) in a 1:1 mixture of MeCN and H_2O. The sample was de-oxygenated under exclusion of light and then irradiated at 410 nm. ***Left:*** UV-Vis absorption spectra measured after different time intervals as given in the legend. ***Right:*** Difference spectra highlighting the formation of the absorption band at 355 nm. Spectra were constructed by subtraction of the ground state absorption spectrum before irradiation from the subsequently measured spectra.

As the control measurement shows, upon irradiation at 410 nm an intense band centered around 355 nm forms which can be attributed to the formation of BNAH[49, 68] or $(BNA)_2$.[70, 71] Over a period of 240 minutes, at the wavelength of 355 nm an increase in absorbance of $\Delta = 0.7$ is monitored. This is much higher than in the control experiment without photosensitizer (absorbance change of $\Delta = 0.2$ in ***CONTROL2***, Figure 4.4), but also significantly higher than the absorbance change of $\Delta = 0.4$ induced by the Ru-NDI-Ru triad (Figure 4.2). Again, a potential disproportionation of two Rh^{II} species

	Potential	Remarks
E ($Ru^{*II/I}$)[77] =	0.77 V	in MeCN
E ($Ru^{III/*II}$)[77] =	-0.81 V	in MeCN
E ($Ru^{II/I}$)[77] =	-1.33 V	in MeCN
E ($Ru^{III/II}$)[77] =	1.29 V	in MeCN
E ($BNA^{+/0}$)[75, 78] =	-1.08 V	in MeCN
E ($BNAH^{+/0}$)[79] =	0.57 V	in MeCN
E ($Rh^{III/I}$)[56, 80] =	-0.74 V	in H_2O, potential describes a two-electron reduction
E ($TEOA^{+/0}$)[81] =	0.69 V	in H_2O, potential by averaging the literature values
E ($NDI^{0/-}$)[82] =	-0.45 V	in MeCN, from Ru-NDI-Ru triad
E ($NDI^{-/2-}$)[82] =	-0.95 V	in MeCN, from Ru-NDI-Ru triad

Table 4.1: Reduction and oxidation potentials of the different species involved in the BNA^+ reduction process. Potentials are taken from the literature as cited and reported vs. SCE.

formed after primary electron transfer from $[Ru(bpy)_3]^+$ is considered as a potential pathway leading to the formation of BNAH.[61, 72–74] However, the formation of the $(BNA)_2$ dimer following the one-electron reduction of BNA^+ under the reaction conditions is also feasible.

To gain insight into the potential reaction paths following excitation of the photosensitizer, the driving-forces for the different electron-transfer steps were estimated. The associated calculations are presented in the appendix and were performed with the reduction and oxidation potentials shown in Table 4.1.

Following excitation of the $[Ru(bpy)_3]^{2+}$ photosensitizer, several reaction paths are available to the different components in the steady-state experiment. For clarity reasons, the potential electron-transfer paths are separated in three groups: electron transfer from NDI^- or NDI^{2-} to Rh^{III} and BNA^+ (Scheme 4.2), electron transfer from excited $[Ru(bpy)_3]^{2+}$ to Rh^{III} (Scheme 4.3) and electron transfer from excited $[Ru(bpy)_3]^{2+}$ to BNA^+ (Scheme 4.4).

Scheme 4.2 shows the potential reaction pathways following the successful formation of NDI^- or NDI^{2-} as described in Chapter 3. As seen in the energy scheme, the oxidation potential of NDI^- is not sufficient to reduce either Rh^{III} to Rh^{II} or BNA^+ to $BNA^{\cdot}$. This finding is in accordance with the experiment shown in Figure 4.2 where primary formation of NDI^- can be observed and the absorption band at 355 nm only forms after a constant concentration of NDI^- has been reached.

NDI^{2-}, however, is energetically able to reduce Rh^{III} to Rh^{II} with a driving force of ΔG_{ET} = -0.21 eV. As the Rh^{III} reduction potential was reported for a two-electron process, the potential for the second electron transfer from Rh^{II} to Rh^{I} must be the same or even less negative. Depending on this potential, Rh^{I} could be formed by subsequent

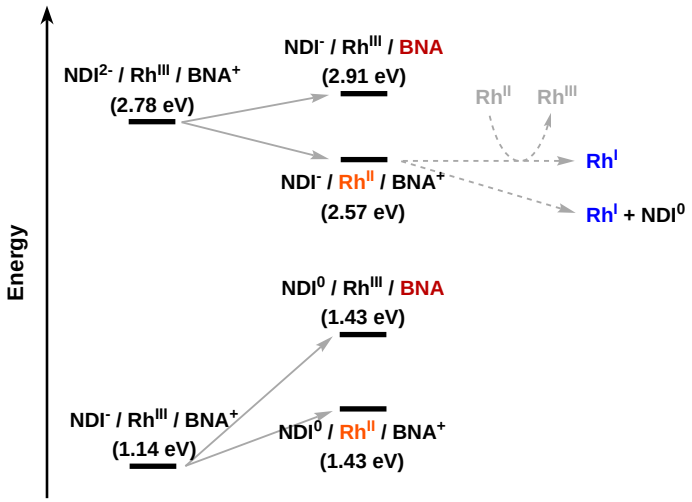

Scheme 4.2: Potential electron-transfer paths originating from NDI^- or NDI^{2-}.

electron transfer from NDI^-. If the energetics for the electron transfer from NDI^- are not promotive, then a disproportionation process of two Rh^{II} species could also lead to the formation of Rh^I. Upon protonation of the Rh^I species, the reduction of BNA^+ to BNAH can occur.

Regarding the electron transfer from NDI^{2-} to BNA^+, the reaction is energetically uphill (ΔG_{ET} = +0.13 eV) and therefore unlikely to occur. In addition, the electron transfer from Rh^{II} to BNA^+ is also energetically hindered (ΔG_{ET} = +0.34 eV).

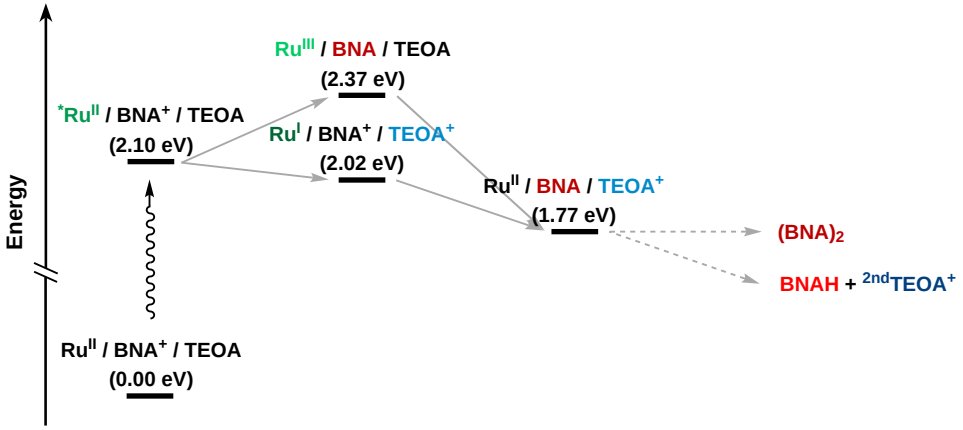

Scheme 4.3: Potential electron-transfer paths originating from $^*[Ru(bpy)_3]^{2+}$ and BNA^+.

Scheme 4.3 shows the potential reaction pathways of excited $[Ru(bpy)_3]^{2+}$ with BNA^+. While the direct electron transfer from $^*[Ru(bpy)_3]^{2+}$ to BNA^+ is energetically uphill by ΔG_{ET} = +0.27 eV, the primary excited state quenching by TEOA (ΔG_{ET} = -0.08 eV) and the subsequent electron transfer from Ru^I to BNA^+ (ΔG_{ET} = -0.25 eV) is energetically possible. The formed $BNA^{\cdot}$ radical can then dimerize yielding the unintended $(BNA)_2$ dimer. However, the $TEOA^{\cdot+}$ radical cation formed after the primary electron transfer to

$^{*}[Ru(bpy)_3]^{2+}$ can undergo deprotonation, yielding the TEOA$^{\cdot}$ radical which is a strong reducing agent.[83–85] The TEOA$^{\cdot}$ radical could therefore perform a second reduction on BNA$^{\cdot}$ yielding BNA^{-}. If the reduction took place at the right position, then the desired product 1,4-BNAH would form after protonation.

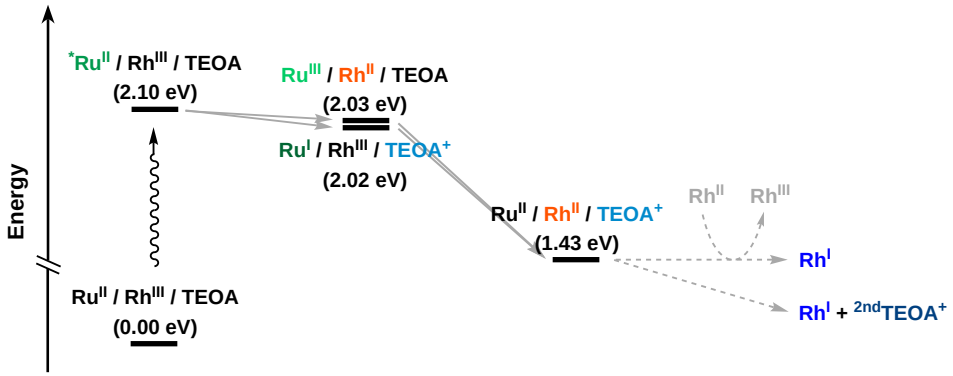

Scheme 4.4: Potential electron-transfer paths originating from $^{*}[Ru(bpy)_3]^{2+}$ and Rh^{III}.

In Scheme 4.4, the potential reaction pathways of excited $[Ru(bpy)_3]^{2+}$ with Rh^{III} can be seen. Here, both the oxidative quenching of $^{*}[Ru(bpy)_3]^{2+}$ by Rh^{III} (ΔG_{ET} = -0.07 eV) as well as the reductive quenching of $^{*}[Ru(bpy)_3]^{2+}$ by TEOA (ΔG_{ET} = -0.08 eV) exhibit a similar driving force. The next electron-transfer step then leads to the formation of Rh^{II} and $TEOA^{+}$. As Rh^{II} is coordinatively unstable, rapid disproportionation of two Rh^{II} species is likely to occur leading to the formation of Rh^{I}.[76] However, deprotonation of the $TEOA^{+}$ radical can also lead to the formation of a highly reducing species that can reduce Rh^{II} to Rh^{I}. In both cases, the formed Rh^{I} species can catalyze the reduction of BNA^{+} to BNAH upon protonation.

From the energy schemes shown above it becomes obvious that several reaction pathways exist that can contribute to the reduction of BNA^{+}. The accumulation of two electrons on an acceptor unit is not a necessity, as electron transfer from $^{*}[Ru(bpy)_3]^{2+}$ to Rh^{III} is also energetically possible. The formed Rh^{II} species then rapidly disproportionates, yielding the reactive Rh^{I} species that can catalyze the reduction of BNA^{+} to BNAH. However, reductive excited-state quenching by TEOA and subsequent electron transfer from Ru^{I} to BNA^{+} can also result in the formation of BNA$^{\cdot}$, which can then dimerize to yield the unwanted side product $(BNA)_2$. The energetics for the formation of BNA$^{\cdot}$ by electron transfer from Ru^{I} (ΔG_{ET} = -0.25 eV) are not as favorable as for the reduction of Rh^{III} by Ru^{I} (ΔG_{ET} = -0.59 eV), however, the concentration of BNA^{+} in the reaction mixture is six times higher than that of the Rh co-catalyst, which is likely to make both reactions paths competitive.

The addition of NDI as a two-electron acceptor in the BNA^{+} reduction process has its advantages and disadvantages. If electron transfer takes place from NDI^{2-}, then the for-

mation of Rh^{II} and consequently the formation of BNAH is energetically favored. Electron transfer from NDI^{2-} to BNA^{+}, in contrast, is energetically uphill and therefore the formation of the undesired $(BNA)_2$ dimer is energetically hindered. However, the preceding formation of NDI^{2-} retards the general catalytic process, as reductive excited state quenching by NDI^{-} (with a driving force of ΔG_{ET} = -1.28 eV) is a dominant reaction in the charge-accumulative process of the Ru-NDI-Ru triad, as discussed in Chapter 3. The favored formation of BNAH over $(BNA)_2$ would therefore be accompanied by a decreased reaction rate.

However, if the general reaction path in the Ru-NDI-Ru triad proceeds via a Ru^{I} species and not via NDI^{2-}, then the addition of the NDI acceptor moiety is counter-productive as a lot of excitation energy is lost in unproductive excited state quenching by NDI^{-}. The isolated $[Ru(bpy)_3]^{2+}$ photosensitizer would then be of advantage as no unproductive intramolecular excited state quenching would be possible and excited $[Ru(bpy)_3]^{2+}$ would solely be quenched by TEOA leading to $[Ru(bpy)_3]^{+}$. The formed Ru^{I} species, however, could lead both to the reduction of Rh^{III} as well as to the reduction of BNA^{+}. Therefore, a mixture of BNAH (formed by disproportionation of Rh^{II}) and $(BNA)_2$ (formed by dimerization of two $BNA^{\cdot}$ radicals) is expected to be formed, their ratio being defined by the kinetics of the electron-transfer process.

Summary

In the catalytic experiment with the Ru-NDI-Ru triad, the formation of the NDI^{-} spectral features could first be observed, followed by the formation of an absorption band around 355 nm. This absorption band can either be attributed to the formation of BNAH or to the formation of a $(BNA)_2$ dimer. The [RhBpyCp*Cl]Cl co-catalyst hereby proved to be essential, as no 355 nm absorption band forms if the Rh co-catalyst is removed from the reaction mixture. Instead, the accumulation of NDI^{-} followed by the accumulation of NDI^{2-} could be detected.

If the Ru-NDI-Ru triad is removed from the reaction mixture, however, the 355 nm absorption band is still formed, but to a lesser extent. This finding was explained with the [RhBpyCp*Cl]Cl co-catalyst also absorbing at the excitation wavelength of 410 nm, resulting in the formation of a Rh^{II} species that rapidly disproportionates to Rh^{III} and Rh^{I}, the latter being able to catalyze the reduction of BNA^{+} to BNAH. As electron transfer from Rh^{II} to BNA^{+} is endergonic, the formation of a $BNA^{\cdot}$ radical and the subsequent formation of the $(BNA)_2$ dimer was excluded. Therefore, the absorption band at 355 nm is most likely exclusively caused by the formed BNAH.

When the Ru-NDI-Ru triad from the initial experiment is replaced by $[Ru(bpy)_3]^{2+}$, an

interesting observation can be made. The absorption band around 355 nm grows faster ($\Delta = 0.7$) compared to the experiment with the Ru-NDI-Ru triad ($\Delta = 0.4$) over the same time period. In principle, the absorption band at 355 nm can be ascribed to BNAH as well as $(BNA)_2$ because both precursor species can be formed by exergonic electron transfer from Ru^{I}. However, the control experiment without the Rh co-catalyst showed that electron transfer from Ru^{I} in the Ru-NDI-Ru triad led to the formation of NDI^{2-} while the formation of $BNA^{\cdot}$ and therefore $(BNA)_2$ was not observed. This indicates that, while electron transfer from Ru^{I} to BNA^{+} is an exergonic process, electron transfer from Ru^{I} to Rh^{III} dominates and therefore BNAH is formed as the main product.

Transferring this interpretation to the initial experiment implies that also in the experiment with the Ru-NDI-Ru triad, BNAH is formed as the main product. However, the reaction path most probably takes place via a Ru^{I} species and not via NDI^{2-}. Therefore, the addition of an acceptor unit in this intermolecular approach does not accelerate the BNAH formation. In contrast, excited state quenching by NDI^{-} consumes a lot of the excitation energy and therefore decreases the BNAH formation rate compared to using $[Ru(bpy)_3]^{2+}$ as photosensitizer.

4.2 Optimizing the BNA^+ Reduction Process by Covalent Linkage

In the previous section, BNAH generation from BNA^+ was achieved, mainly based on Rh^{III} reduction to Rh^{II} and subsequent disproportionation of two Rh^{II} complexes leading to Rh^{III} and Rh^{I}. Upon protonation, the Rh^{I} species can then transfer a hydride and therefore reduce BNA^+ to BNAH. The reaction pathway heavily relies on a cascade of single electron-transfer steps and a crucial disproportionation reaction between two Rh^{II} complexes as sketched in Scheme 4.5.

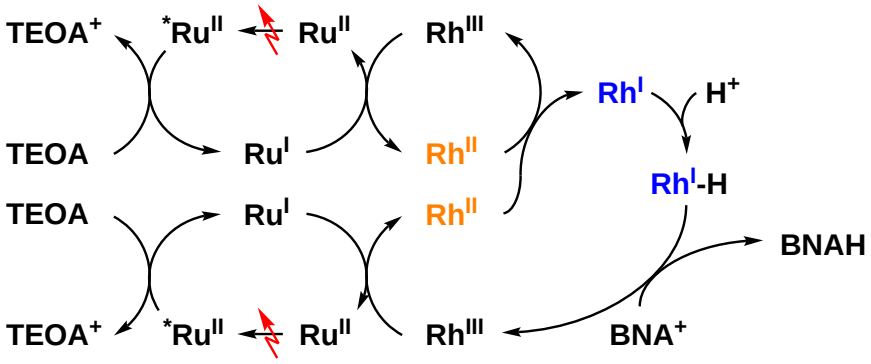

Scheme 4.5: Schematic representation of the electron (and proton) transfer steps necessary to reduce BNA^+ to BNAH in the experimental setup used in the previous section. Red flashes indicate the excitation of the $[Ru(bpy)_3]^{2+}$ photosensitizers, yellow color highlights the two Rh^{II} species that need to disproportionate to form the Rh^{I}-complex (blue) which upon protonation then reduces BNA^+ to BNAH. Please note that in each encounter one electron is transferred.

As can be observed in Scheme 4.5, several molecular encounters are necessary to lead to the formation of BNAH. The reaction rate therefore depends on the concentration of each involved species, their diffusion coefficients, and the encounter of the proper molecules to drive the reaction in the intended direction. This multitude of encounters retards the BNA^+ reduction process and leads to the long reaction times seen in the previous experiments.

To overcome the retardation from intermolecular electron-transfer reactions, an intramolecular approach was considered. This approach involved the covalent linkage of photosensitizer, electron storage moiety and co-catalyst to eliminate the intermolecular electron-transfer steps necessary. By this, two electrons can be transferred simultaneously without the need of different molecules to encounter. With these requirements in mind, two molecules were designed, which are depicted in Figure 4.6.

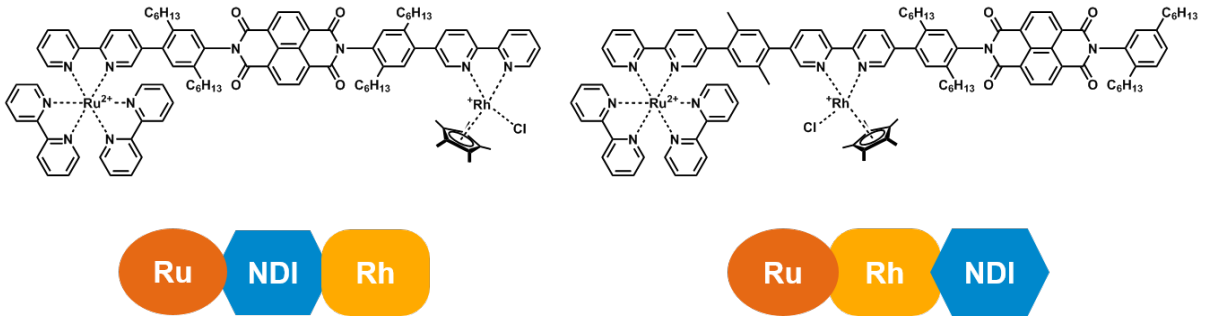

Figure 4.6: Structures of the molecular triads designed to accelerate BNA^+ reduction (top) and their corresponding schematic depictions (below).

Both triads shown in Figure 4.6 are composed of the same molecular moieties: $[Ru(bpy)_3]^{2+}$ photosensitizer, NDI electron acceptor and Rh co-catalyst. Their disposition, however, is different. In the triads, the structural motifs are as follows: Ru-NDI-Rh (left triad) and Ru-Rh-NDI (right triad). Upon excitation, both triads are expected to undergo similar procedures as illustrated in Figure 4.7: The excited $[Ru(bpy)_3]^{2+}$ photosensitizer is reductively quenched by TEOA and subsequently transfers an electron to the NDI acceptor (light green arrows). Upon second excitation of the $[Ru(bpy)_3]^{2+}$ photosensitizer and reductive quenching of the excited state by TEOA, the second electron is transferred to the Rh co-catalyst. At the same time, the stored electron on the NDI acceptor also transfers to the Rh co-catalyst, which in combination then leads to a two-electron reduction of the Rh co-catalyst (dark green arrows). The Rh^I species formed is then able to reduce BNA^+ to BNAH. With this approach, direct double-reduction of the Rh co-catalyst could be possible, which would bypass the Rh^{II} disproportionation mechanism determined before.

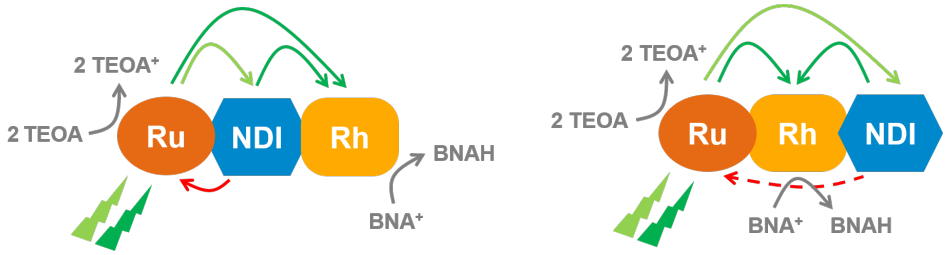

Figure 4.7: Schematic representation of the electron movements following first (light green) and second (dark green) excitation of the $[Ru(bpy)_3]^{2+}$ photosensitizer. Ru-NDI-Rh triad shown on the left side, Ru-Rh-NDI triad shown on the right.

The difference between the two triads is found in the position of the NDI acceptor. In the Ru-NDI-Rh triad (left side of Figure 4.7), the NDI moiety is in direct proximity to the $[Ru(bpy)_3]^{2+}$ photosensitizer. While this configuration ensures good electron transfer rates from $[Ru(bpy)_3]^{+}$ to NDI, the formed NDI^- is also quite likely to quench the re-excited $[Ru(bpy)_3]^{2+}$ photosensitizer as indicated by the red arrow. As seen in the pre-

vious experiments, reductive excited state quenching by NDI^- can annihilate a lot of the excitation energy. To prevent this from happening, the second triad Ru-Rh-NDI (right side of Figure 4.7) was designed. Here, the distance between photosensitizer and electron acceptor moiety is distinctly larger. This will likely retard the primary electron transfer from $[Ru(bpy)_3]^+$ to NDI, but it should retard the back-electron transfer from NDI^- to re-excited $[Ru(bpy)_3]^{2+}$ (indicated by the dashed red arrow) to a greater extent. With this modification, the loss of excitation energy should be minimized and the BNA^+ reduction process should be accelerated.

An uncertainty with these triads still lies in the second reduction potential of the Rh^{III} to Rh^I reduction. The reduction potential $E_{Rh^{III/I}}$ = -0.74 V vs. SCE describes a two-electron reduction including the uptake of a proton. While the first reduction potential certainly is at the given potential, the second reduction potential could be considerably shifted to less negative values, allowing electron transfer from NDI^-.

Steady-state Catalysis

To test the efficiency of BNA^+ reduction for the two triads versus the Ru-NDI-Ru triad or $[Ru(bpy)_3]^{2+}$, continuous irradiation experiments were conducted, again in analogy to experiments performed in the literature.[68, 69] In contrast to the experiments in the previous section, the experiments here were performed at a scale appropriate for analysis by NMR spectroscopy to better quantify the amount of BNAH formed within a specific time interval. Additionally, irradiation occurred at 455 nm to effectively coincide with the $[Ru(bpy)_3]^{2+}$ MLCT absorption band and at the same time minimize the absorption of the [RhBpyCp*Cl]Cl co-catalyst. All solutions were de-oxygenated prior to irradiation and the NMR tubes were sealed with a septum to exclude oxygen intrusion.

Catalysis with Triethanolamine as Electron Donor

For the steady-state irradiation experiments on a scale appropriate for analysis by NMR spectroscopy, a sample volume of 0.7 mL was used for each individual assay. Each sample contained BNACl ($2.3 \cdot 10^{-5}$ mol, 0.033 M) and 2 mol-% of the corresponding catalyst(s). The solvent was comprised of a NaH_2PO_4/Na_2HPO_4 buffer (0.1 M) dissolved in a 1:1 mixture of H_2O and MeCN and containing triethanolamine (0.5 M) as sacrificial electron donor.

To allow for accurate determination of the BNAH amount formed, the integral of the inherent solvent peak was set to 100. The new formed integrals of BNAH at 7.3 ppm and 5.7 ppm were then used to identify the relative amount of BNAH formed at a specific point in time.[68, 86, 87]

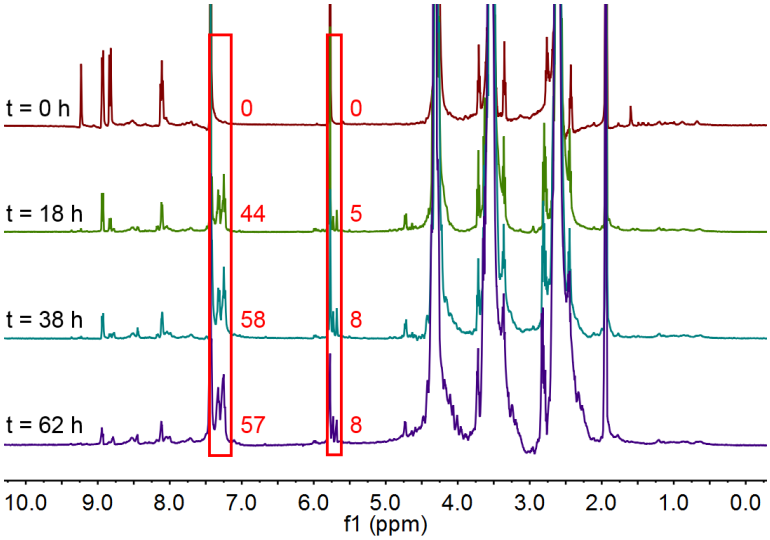

Figure 4.8: Sample A: continuous irradiation experiment for BNA^+ reduction with the Ru-NDI-Ru triad and the [RhBpyCp*Cl]Cl co-catalyst. NMR spectra were measured prior to excitation and after 18, 38 and 62 h of total irradiation time.

Having a look at the BNAH formation process catalyzed by Ru-NDI-Ru / [RhBpyCp*Cl]Cl (sample A, Figure 4.8), an integral of 44 can be observed after 18 h, increasing to 58 (38 h) and 57 (62 h), indicating that the reaction reached a stable plateau after approx. 38 h.

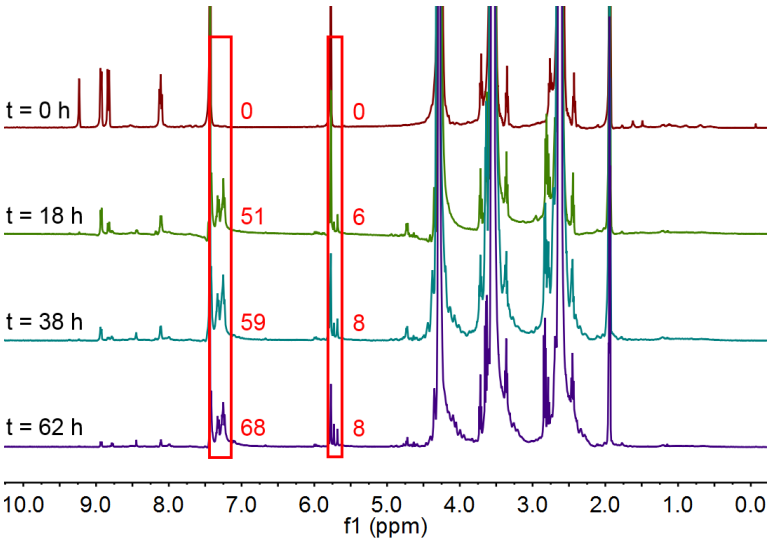

Figure 4.9: Sample B: continuous irradiation experiment for BNA^+ reduction with the Ru-NDI-Rh triad. NMR spectra were measured prior to excitation and after 18, 38 and 62 h of total irradiation time.

For the Ru-NDI-Rh catalysis (sample B, Figure 4.9), an integral of 51 can be determined after 18 h, increasing to 59 (38 h) and 68 (62 h). In this experiment, the plateau concentration seems to be higher than in sample A, however, the overall BNAH formation

rate is not dramatically increased. This is somewhat expected, as a significant part of the excitation energy is still expected to be consumed by reductive excited state quenching by NDI^{-}.

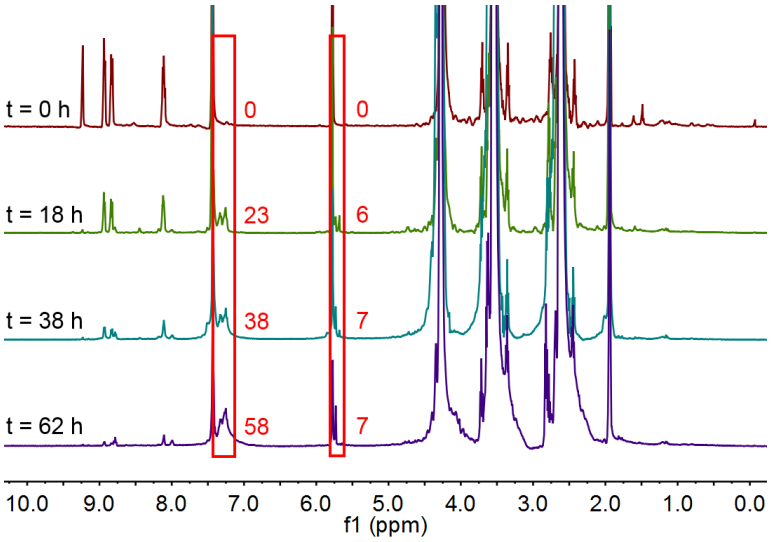

Figure 4.10: Sample C: continuous irradiation experiment for BNA^{+} reduction with the Ru-Rh-NDI triad. NMR spectra were measured prior to excitation and after 18, 38 and 62 h of total irradiation time.

The Ru-Rh-NDI catalysis (sample C, Figure 4.10), however, shows an unexpected outcome: after 18 h, an integral of 23 can be observed, increasing to 38 (38 h) and 58 (62 h). This is the slowest BNAH formation rate among the three catalysts and stands in contrast with the original expectations. The amount of BNAH formed after 18 h through catalysis with the Ru-Rh-NDI triad amounts to only 50% compared with the intermolecular approach (sample A). It takes 62 h for the Ru-Rh-NDI triad to reach the same amount of BNAH formed as in sample A after 38 h.

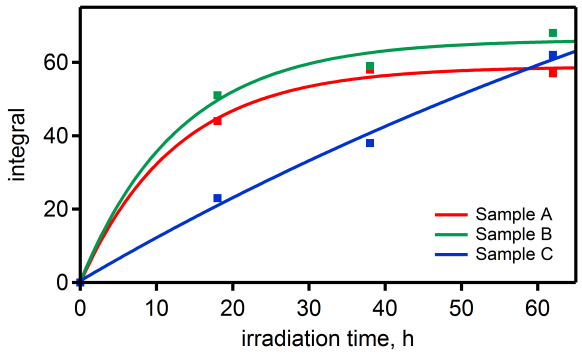

Figure 4.11: Plot of the determined integrals at 7.3 ppm versus irradiation time for sample A (red), sample B (green) and sample C (blue) to illustrate the kinetics of the BNAH formation process. Data points were fitted with an exponential function.

Figure 4.11 gives a summary of the NMR experiments performed above. While samples A and B exhibit similar kinetics for the formation of BNAH, the increase of the integral at 7.3 ppm is retarded in sample C. With the Ru-Rh-NDI catalyst (sample C), it takes significantly more time to obtain the same amount of BNAH as in samples A and B. The hypothesized acceleration of the BNAH formation rate by covalent linkage, however, is not observable.

In conclusion, the experiments described above show an unexpected outcome. The intermolecular pathway (sample A) which should have a significantly reduced reaction rate compared to the covalently linked triads proved to be rather effective. The Ru-NDI-Rh triad (sample B) did show an increased reaction rate (approx. 15% more BNAH formed in the same time period compared to sample A), but the gain in reaction speed did not heavily increase as hypothesized. In the case of the Ru-Rh-NDI triad (sample C), the results were even worse: the triad that was expected to be most effective in BNA^+ reduction exhibited the lowest performance with BNAH formation rates of only 65% after 38 h compared to the BNAH formation rate with the intermolecular system (sample A).

Reflecting on these results, the question arose if the BNAH formation process indeed follows the two-electron route that was sketched in Figure 4.7 or if the sacrificial electron donor TEOA did not provide a shortcut for the BNA^+ reduction process. As described in the NDI charge-accumulation paper (Chapter 3) for TEA, TEA upon primary electron donation forms a radical. This radical is likely to deprotonate and the resulting radical is a strong reducing agent.[83, 84, 88, 89] The same mechanism applies for TEOA as well. As soon as the first electron is donated, the TEOA radical cation deprotonates and subsequently can transfer a second electron.[81, 85] This could lead to a doubly reduced Rh-species that could reduce BNA^+ to BNAH without intermediate electron storage on NDI being necessary. According to this mechanism, the overall reaction rates in samples A, B and C should be in the same order of magnitude. To verify this hypothesis, a purely one-electron donor was used for the following experiments. These experiments are described in the next section.

Catalysis with Ascorbate (and TCEP) as Electron Donor

Due to TEOA being a possible two-electron donor in the BNA^+ reduction studies, a purely one-electron donor was needed. Ascorbate is such a one-electron donor[90, 91] which was already used in Chapter 3. Therefore, the same reaction conditions were chosen as in the previous experiments, the only difference being ascorbate replacing TEOA: sample volume 0.7 mL, solvent 1:1 mixture of H_2O and MeCN, NaH_2PO_4/Na_2HPO_4 buffer (0.1 M), sodium ascorbate (0.1 M), BNACl ($2.3 \cdot 10^{-5}$ mol, 0.033 M) and 2 mol-% of the corresponding catalyst(s). The samples were irradiated at 455 nm and NMR spectra

measured prior to excitation, after 20 minutes, after 14 hours and after 39 hours. In these NMR spectra, however, no new peaks were formed over time and no indication of BNAH formation could be found. As in the charge-accumulation on NDI project, the problem lies in the reversibility of the electron donation process of ascorbate. Oxidized ascorbate is a good electron acceptor and therefore back-electron transfer from the reduced catalyst to oxidized ascorbate is probable. Additionally, potentially formed BNAH is also a good reductant, leading to the reduction of oxidized ascorbate. In the overall picture, no lasting electron transfer from ascorbate takes place and because of this, no catalytic activity can be detected.

To address the problem of back-electron transfer to oxidized ascorbate, the addition of an additional electron donor was considered. The appropriate electron donor was found in a publication of the Alberto group: tris(2-carboxyethyl) phosphine (TCEP).[92] TCEP is a mild one-electron reductant unable to reductively quench the $[Ru(bpy)_3]^{2+}$ excited state, but able to reduce dehydroascorbic acid to ascorbic acid. In the experimental setup, this would imply that excited $[Ru(bpy)_3]^{2+}$ is first quenched by ascorbate and the oxidized ascorbate is then subsequently reduced by TCEP. Therefore, TCEP·HCl (0.2 M) was additionally added to the catalytic mixture.

Excitation of the $[Ru(bpy)_3]^{2+}$ photosensitizer occurred at 455 nm and NMR spectra were measured after 1, 5 and 24 h of irradiation time. Unfortunately, the addition of TCEP did not assist catalysis. For Ru-NDI-Ru / [RhBpyCp*Cl]Cl and Ru-NDI-Rh, no indication for BNAH formation could be found after sample irradiation for 24 hours. The $[Ru(bpy)_3]^{2+}$ / [RhBpyCp*Cl]Cl sample, however, decomposed within the first hour of the experiment and the Ru-Rh-NDI triad decomposed within 24 hours. In all four samples, no BNA^+ reduction could be observed.

Summary

The concept underlying the Ru-NDI-Rh and Ru-Rh-NDI triads was to increase the BNAH formation rate by covalent linkage of the different catalytic moieties to reduce the number of molecular encounters necessary that lead to product formation. In the experiments performed, however, the BNAH formation rate was just slightly increased (Ru-NDI-Rh) or even lowered (Ru-Rh-NDI) compared to the intermolecular approach. Attempts to highlight the advantages of the designed triads when using a purely one-electron donor were not successful.

4.3 General Summary

In Chapter 3, two electrons could be accumulated on NDI. In Chapter 4, the concept was to use those two electrons to perform two-electron catalysis. Therefore, the reduction of BNA^+ to BNAH was chosen, as the reduction requires two electrons and a proton to proceed. For successful 1,4-reduction of BNA^+, the co-catalyst [RhBpyCp*Cl]Cl was added. In these intermolecular experiments, BNA^+ reduction could be obtained, but the photosensitizer $[Ru(bpy)_3]^{2+}$ yielded better product formation rates than the Ru-NDI-Ru triad. With these findings, it was concluded that the product formation process most likely does not take place via a preceding charge-accumulation but mainly via a disproportionation process of two Rh^{II} species. This overall process was found to be rather slow, most likely due to the multitude of molecular encounters necessary for successful product formation.

To enhance the BNAH formation rate, covalent linkage of photosensitizer, Rh co-catalyst and intermediate electron acceptor was considered, which led to the synthesis of the Ru-NDI-Rh and Ru-Rh-NDI triads. Upon examination of these triads, however, no significant increase in the BNAH formation rate could be found for the Ru-NDI-Rh triad, while the Ru-Rh-NDI triad even lowered the BNAH formation rate compared to the intermolecular approach.

The rather surprising conclusion of these studies is that the reduction of BNA^+ to BNAH does not necessarily require prior charge-accumulation and proceeds faster if no electron acceptor is attached to the $[Ru(bpy)_3]^{2+}$ photosensitizer. Proceeding from reductively quenched Ru^I, several electron-transfer pathways are possible leading to the potential main products BNAH and $(BNA)_2$. However, the reduction of Rh^{III} by Ru^I seems to be favored over the direct reduction of BNA^+ by Ru^I. Therefore, the desired BNAH was assigned as the main product in the catalytic experiment.

Covalent linkage of the different molecular moieties in the conducted experiments did not accelerate the BNAH formation process. It is therefore doubtable that the underlying concept of the triads was functioning as hypothesized. The use of a multi-component system relying on intermolecular encounters for BNAH generation proved to be at par or even outperformed the specifically designed molecular systems. This shows that multi-component systems can be advantageous over covalently-connected systems.

5 Studies of Charge-Accumulation: a Two-Electron Donor, Two-Electron Acceptor Pentad

In Chapter 3, two electrons could be successfully accumulated on the NDI acceptor in a molecular triad with the help of a sacrificial electron donor. In a related pentad with reversible triarylamine (TAA) electron donors, however, only a singly charge-separated state was observed.

During the examination of the triad it was found that charge-accumulation on NDI is most likely ascribed to a disproportionation process taking place in solution: as soon as most of the NDI moieties are reduced to NDI^{-}, two NDI^{-} triads can encounter and undergo a disproportionation process forming NDI^{0} and NDI^{2-}. As soon as NDI^{0} is formed, it is immediately photochemically re-reduced to NDI^{-}. While only a small fraction of the molecules undergo disproportionation, the constant re-formation of NDI^{-} and removal of NDI^{0} leads to an accumulation of NDI^{2-} over time.

In the case of the pentad, the lifetime of the charge-separated state is not long enough to allow for this rather slow bimolecular disproportionation pathway to take place. Therefore, charge-accumulation would need to follow the regular route: excitation of the photosensitizer, followed by electron transfer from TAA to NDI would generate NDI^{-}; second excitation of the photosensitizer followed by a second electron transfer from the second TAA to NDI^{-} would then lead to the NDI^{2-} state. As mentioned previously, the second electron transfer, however, is not observed in the pentad. Two main reasons are assigned for this: lack of driving force and alternate excited state quenching.

Having a look at the reduction potentials of NDI, the first reduction takes place at $E_{red,1}$ = -0.51 V vs. SCE and the second reduction at $E_{red,2}$ = -0.96 V vs. SCE.[82] This difference of 0.45 V amounts to a strong decrease in the driving force for the second reduction process. In fact, excited $[Ru(bpy)_3]^{2+}$ is not energetically able to reduce NDI^{-} to NDI^{2-} (ΔG_{ET} = +0.15 eV), it requires reductive quenching of the $[Ru(bpy)_3]^{2+}$ excited state by the second TAA moiety to form the reduced $[Ru(bpy)_3]^{+}$, which is then able to transfer the second electron to NDI^{-} (ΔG_{ET} = -0.37 eV). Unfortunately, there is little to

no driving force (ΔG_{ET} = -0.01 eV) for the reductive quenching process of $^{*}[Ru(bpy)_3]^{2+}$ with TAA.[1]

Here a second issue arises, namely the alternate excited state quenching. NDI^0 is a good electron acceptor, therefore the first electron transfer is rather easy to achieve. As soon as NDI^- is present, the situation changes to some point: NDI^- is a worse acceptor than NDI^0 (the difference of first and second reduction potential amounts to 0.45 V), while NDI^- at the same time is a good electron donor to the excited $[Ru(bpy)_3]^{2+}$ photosensitizer. The driving force of NDI^- reductively quenching excited $[Ru(bpy)_3]^{2+}$ amounts to ΔG_{ET} = - 1.28 eV and therefore outperforms the reductive quenching with TAA and its driving force of ΔG_{ET} = -0.01 eV nearly quantitatively.

This finding does not necessarily mean that the charge-accumulating electron-transfer step does not take place at all. A recent publication from our group shows charge-accumulation on a TAA-Ru-AQ-Ru-TAA pentad despite having a higher driving force of ΔG_{ET} = -1.60 eV for the back-electron transfer from the singly reduced acceptor.[28] The increased driving-force in fact might even be the reason why charge-accumulation could be observed in the TAA-Ru-AQ-Ru-TAA pentad and not in the TAA-Ru-NDI-Ru-TAA pentad. According to Marcus theory, increasing the driving force for an electron-transfer process will first lead to an increase in the rate constant (normal regime) and will then at some point reach a maximum. Upon further increase of the driving force, the maximum of the rate constant will be surpassed and the rate constant for an electron-transfer process decreases (inverted regime).[93, 94] While the driving force of -1.60 eV most probably lies in the inverted regime of the Marcus parabola, the driving force of -1.28 eV for the TAA-Ru-NDI-Ru-TAA pentad could be close to the maximum of the Marcus parabola, implying that back-electron transfer in the TAA-Ru-NDI-Ru-TAA pentad is preferred relative to the TAA-Ru-AQ-Ru-TAA pentad.

The observations made for the TAA-Ru-NDI-Ru-TAA pentad, however, imply that photoexcited $[Ru(bpy)_3]^{2+}$ is most likely quenched by NDI^- and the electron on the photosensitizer subsequently gets transferred back onto NDI^0 due to a driving force of ΔG_{ET} = -0.82 eV. This shortcut effectively prevents the accumulation of two electrons on the pentad.

When wanting to achieve efficient charge-accumulation, those two main drawbacks need to be overcome. In a recently published paper in our group,[31] an electron acceptor with potential inversion was used. Potential inversion describes the phenomenon that the second electron acceptance or removal is easier to achieve than the first one.[95–97] This behavior is relatively seldom and normally associated with a structural change following oxidation or reduction.[98–100] If potential inversion is present in an electron donor or acceptor, it is

[1] The corresponding calculations are presented in the appendix.

of huge benefit for the overall charge-accumulation process: with the driving force for the transfer of the second electron being even higher than for the first electron, the formation of a doubly oxidized or reduced state should be fostered significantly. It therefore is ideal if both acceptor and donor possess inverted reduction or oxidation potentials.

The second, more important, point is the suppression of excited state quenching by the singly reduced acceptor or oxidized donor. As seen in the NDI pentad, these unwanted quenching processes can totally prevent charge-accumulation. Therefore, some sort of barrier needs to be present in the molecule that can actively suppress back-electron transfer from the reduced acceptor or towards the oxidized donor. At this point, the concept of an intermediate donor or acceptor comes into play. For depicting the general principle, the way such an intermediate electron acceptor or donor works will be explained focusing on the acceptor part. The general principle is also applicable to the donor part.

As mentioned above, the intermediate electron acceptor acts as a barrier in the charge-accumulation process. It is located between the photosensitizer and the terminal electron acceptor moiety and needs to fulfill two requirements. First, its reduction potential must be appropriate for oxidative quenching of the excited photosensitizer. Second, there must be enough driving force for the electron not to stay on the intermediate acceptor but to transfer to the terminal acceptor. As soon as the electron is stored on the terminal acceptor, the intermediate acceptor is returned to its neutral state. It can therefore oxidatively quench the newly excited photosensitizer and then transfer a second electron to the terminal acceptor (with increased driving force for the transfer of the second electron due to potential inversion). At the same time, the distance between the electron on the terminal acceptor and the photosensitizer is significantly enlarged due to the incorporated electron relay. This results in retardation of the unwanted charge-recombination process. Oxidative quenching of the re-excited photosensitizer by the intermediate acceptor in close proximity, however, is energetically downhill and consequently should dominate.

With these two modifications being incorporated to overcome the difficulties encountered in the NDI pentad, a new pentad for charge-accumulation can be outlined as: terminal electron donor (ED) – intermediate electron donor (iED) – photosensitizer (PS) – intermediate electron acceptor (iEA) – terminal electron acceptor (EA). A scheme showcasing the pentad layout and the associated electron-transfer processes is depicted in Figure 5.1.

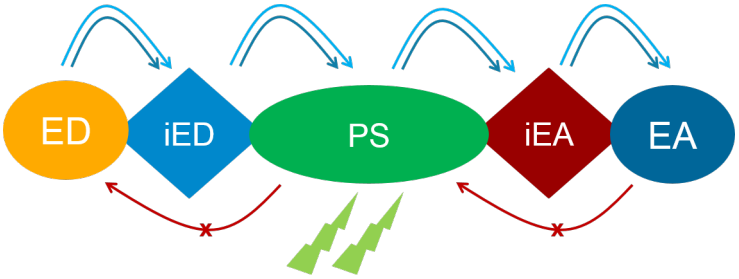

Figure 5.1: Schematic depiction of a pentad designed to facilitate charge-accumulation. Blue arrows indicate productive electron-transfer pathways whereas red arrows show unproductive pathways that should be suppressed by the pentad design.

Examples of donor and acceptor moieties with potential inversion are rare compared to the number of 'regular' electron donors and acceptors found in the literature. Some examples exhibiting potential inversion are given in the references.[22, 101–116]

To follow the formation of the singly and doubly oxidized or reduced species on our laser systems, each species needs to have a characteristic spectroscopic signature in the visible range (300-800 nm). This requirement further limits the number of potential donors and acceptors utilizable in the designed pentad.

A suitable electron donor was identified as a π-extended tetrathiafulvalene, namely 9,10-di(1,3-dithiol-2-ylidene)-9,10-dihydroanthracene (exTTF).[117–119] exTTF is a two-electron donor with inverted oxidation potentials.[120, 121] A potential of $E_{1/2}$ = 0.44 V vs. SCE for a two-electron oxidation process has been reported.[122–125] Ground state, singly oxidized and doubly oxidized states can be distinguished by their absorption signatures (ground state: absorption band at 428 nm; singly oxidized state: absorption band at 660 nm; doubly oxidized state: absorption band at 470 nm).[23, 126, 127]

For the acceptor, 11,11,12,12-tetracyano-9,10-anthraquinodimethane (TCAQ) was identified.[128, 129] The acceptor is derived from 9,10-anthraquinone where the two carbonyl groups have been substituted by malononitrile groups. TCAQ also exhibits inverted potentials with the reduction at a potential of $E_{1/2}$ = -0.43 V vs. SCE involving two electrons.[129–132] Ground state absorption (bands at 343 nm and 303 nm), singly reduced absorption (band at 600 nm) and doubly reduced absorption (band at 540 nm) spectra are sufficiently differentiable from one another.[21–23, 133] Additionally, they also differ from the spectral changes induced by the oxidation of exTTF. Therefore, exTTF and TCAQ were chosen as the terminal electron donor and acceptor, respectively.

Photoexcited $[Ru(bpy)_3]^{2+}$ is reduced at a potential of $E^{*II/I}$ = 0.77 V vs. SCE[77] while exTTF is oxidized at a potential of $E_{exTTF^{+/0}}$ = 0.44 V vs. SCE.[122] For the intermediate electron donor to work as described above, its potential needs to be located between the exTTF oxidation potential and the excited $[Ru(bpy)_3]^{2+}$ reduction potential. In this

rather narrow range, the intermediate electron donor should optimally be in the middle between those two values to have sufficient driving force for both electron-transfer steps. 10-(4-Methoxyphenyl) phenothiazine (PTZ) was chosen due to its oxidation potential being $E_{PTZ^{+/0}}$ = 0.68 V vs. SCE.[134, 135] Upon oxidation, PTZ features characteristic spectral changes with the maxima of the absorption bands being centered around 450, 480 and 710 nm.[136] While the spectral characteristics of PTZ^+ are rather pronounced, they do not interfere with the exTTF and TCAQ spectral signatures and are basically not even expected to appear in a transient spectrum due to the hypothesized short lifespan of the intermediate species.

The same principle that was applied to the intermediate donor is also applicable on the acceptor side. Photoexcited $[Ru(bpy)_3]^{2+}$ is oxidized at a potential of $E^{III/*II}$ = -0.81 V vs. SCE,[77] TCAQ is reduced at $E_{TCAQ^{0/-}}$ = -0.43 V vs SCE.[129] To fulfill the ascribed features, the intermediate electron acceptor must have a reduction potential lying between these values. To allow for sufficient driving force for both electron-transfer processes, the intermediate acceptor's potential is optimally located around -0.62 V vs. SCE. This requirement led to the electron acceptor fluoren-9-ylidene malononitrile (FMN) which has a reduction potential of $E_{FMN^{0/-}}$ = -0.63 V vs. SCE.[137, 138] As shown in the following sections (especially Figure 5.39), the reduced intermediate acceptor does not exhibit any significant absorption changes between 400 and 800 nm and therefore does not interfere with the terminal acceptor's and donor's spectral changes.

Putting together the different donor and acceptor parts yields the pentad shown in Figure 5.2.

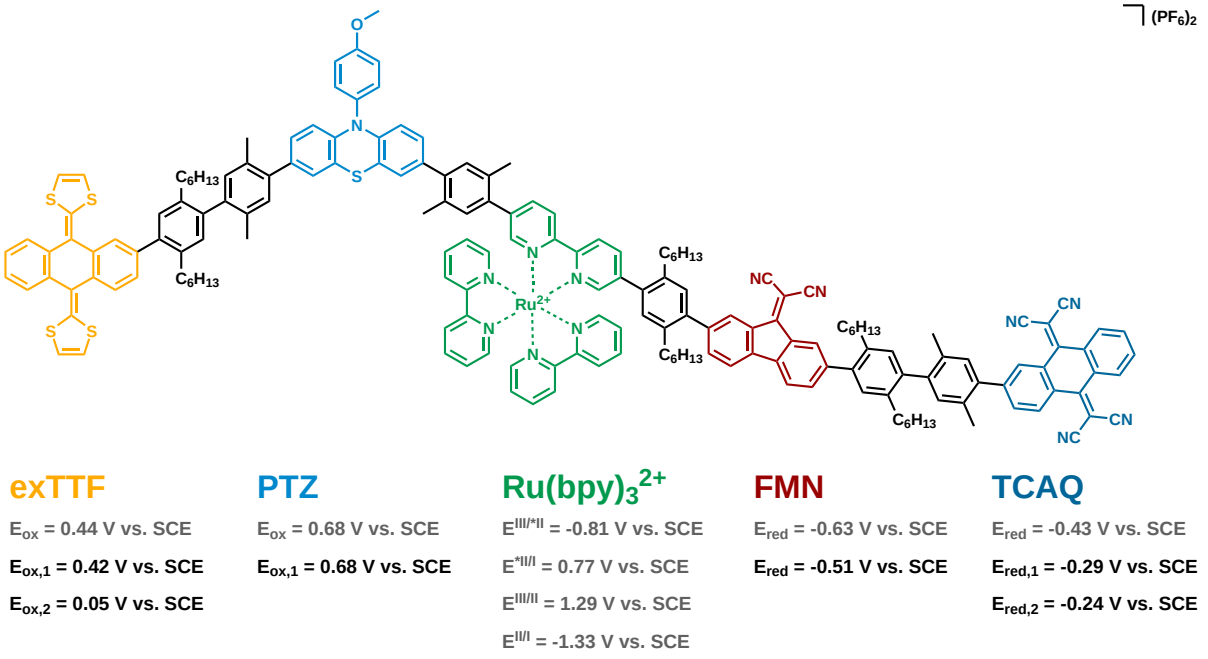

Figure 5.2: Designed pentad for facilitated charge-accumulation. Reduction/oxidation potentials in gray are taken from the literature and (if necessary) converted to vs. SCE with the conversion constants published by Pavlishchuk and Addison.[139] Black reduction/oxidation potentials originate from cyclovoltammetric measurements shown in the following sections (exTTF and PTZ from donor triad, TCAQ and FMN from their corresponding reference molecules) and are given in V vs. SCE.

In the pentad, the donor and acceptor moieties, as well as the photosensitizer, are spatially separated via *p*-xylene- (xy) or *p*-(di-*n*-hexyl)phenyl (hxy) spacers to reduce electronic coupling and to increase solubility. Between the intermediate acceptor/donor and the terminal acceptor/donor, a second phenyl-spacer was integrated to further retard back-electron transfer from/to the singly reduced/oxidized terminal acceptor/donor moieties.

Scheme 5.1 shows an energy estimation for the formation of the primary charge-separated state following the $[Ru(bpy)_3]^{2+}$ excitation as well as the electron-transfer paths leading to the final charge-accumulated state after the second excitation of the photosensitizer. For clarity reasons, unproductive electron-transfer pathways are omitted. Notable in the energy scheme is the stored energy of the charge-accumulated state. With 1.00 eV it is just 40% higher than the 0.71 eV stored in the singly charge-separated state. This is due to the inverted potentials of exTTF and TCAQ. While the driving force for the second electron-transfer step is higher, the additional energy stored in this second electron-transfer step is smaller.

In the literature, numerous examples of molecular systems exhibiting charge-separated states upon excitation can be found, while there are only a handful of molecular systems showing charge-accumulation without sacrificial reagents. To the best of our knowledge,

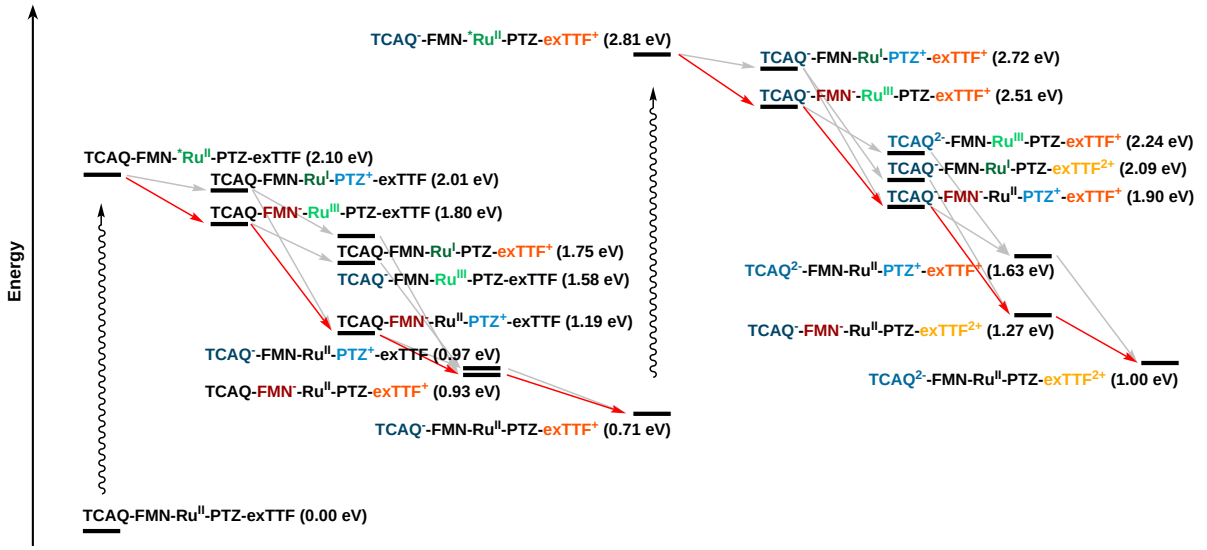

Scheme 5.1: Energy scheme for the formation of the charge-separated states in the proposed pentad following excitation. Energy levels are based on the redox potentials of the donor triad, Ref-TCAQ and Ref-FMN (determined experimentally, see subsequent sections); $[Ru(bpy)_3]^{2+}$ values taken from the literature.[77] The energy of the ground state was set as zero. Red arrows indicate the energetically most favorable electron-transfer pathway, gray arrows show additional (energetically possible) electron-transfer paths. The calculation of the individual energy levels is presented in the appendix.

up to now no purely molecular system is known that – upon excitation – leads to a charge-accumulated state with two electrons being on one acceptor and two holes being on one donor. The concept of having intermediate electron donors and acceptors forming a redox gradient for increased spatial separation of positive and negative charges in combination with the use of electron donors and acceptors with potential inversion to ease charge-accumulation resembles the general principle used in natural photosynthesis. In a molecular system, this concept has not yet been implemented and therefore is the first of its kind.

For examining the concept sketched above, variants of the pentad shown in Figure 5.2 were planned: a donor triad to investigate the donor part of the pentad, an acceptor triad to examine the acceptor part, the above shown pentad itself and a variation of the pentad where donor and acceptor parts are placed on different ligands. The examination of those variants is presented in the individual subsections of this chapter.

5.1 The Donor Triad: exTTF-PTZ-Ru

The electron donor moiety of the donor triad consists of the two-electron donor 9,10-di(1,3-dithiol-2-ylidene)-9,10-dihydroanthracene (exTTF) and the intermediate electron donor 10-(4-methoxyphenyl)phenothiazine (PTZ). PTZ is able to quench the excited state of the $[Ru(bpy)_3]^{2+}$ photosensitizer, but its oxidation potential is higher in energy compared to the exTTF electron donor and therefore the oxidized PTZ will be reduced back to its ground state by the exTTF moiety in a secondary step. Upon addition of an external electron acceptor (see Section 5.1.2, *Experiments with MV^{2+} as Temporary Electron Acceptor*), oxidation of $[Ru(bpy)_3]^{+}$ recovers the $[Ru(bpy)_3]^{2+}$ photosensitizer ground-state. When the photosensitizer is excited for a second time, the positive charge located on exTTF is unlikely to oxidatively quench the excited $[Ru(bpy)_3]^{2+}$ photosensitizer due to the fact that the PTZ intermediate donor back in its ground state acts as a good electron donor to the excited photosensitizer. At the same time, the distance between photoexcited $[Ru(bpy)_3]^{2+}$ and oxidized exTTF moiety should retard unwanted back-electron transfer.

The synthetic route pursued to obtain the donor triad is shown in Scheme 5.2. Experimental details are given in the experimental section 7.5.

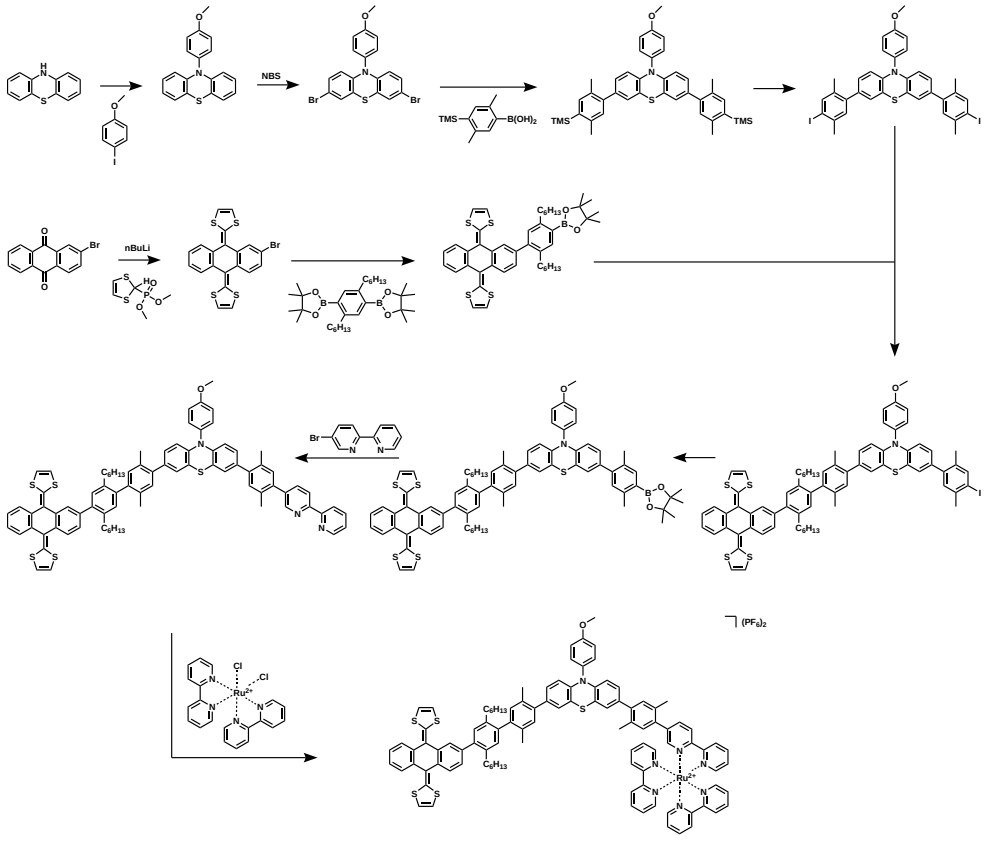

Scheme 5.2: Synthetic route pursued to obtain the donor triad.

5.1.1 exTTF, PTZ and exTTF-PTZ-exTTF Reference Molecules

For analyzing the different donor moieties in isolated and covalently connected forms, three reference molecules were utilized: exTTF-hxy-TMS, I-xy-PTZ-xy-I and exTTF-hxy-xy-PTZ-xy-hxy-exTTF. In the following sections, they are referenced as Ref-exTTF, Ref-PTZ and Ref-exTTF-PTZ. While Ref-exTTF and Ref-PTZ show the characteristics of the single moieties, Ref-exTTF-PTZ can show potential changes in absorbance or in oxidation potential arising from the covalent linkage of the donor moieties.

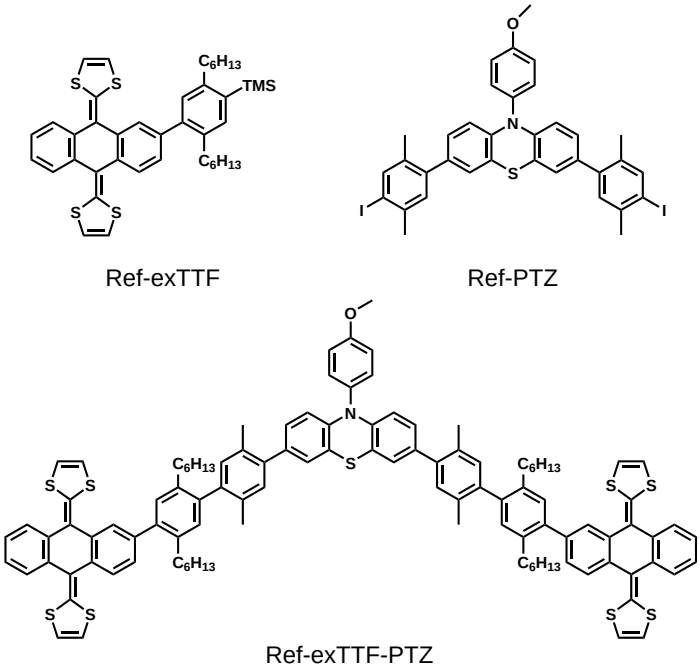

Figure 5.3: Schematic representation of the reference molecules used for analyzing the electron donor moieties.

Optical Absorption Spectroscopy

For spectroscopic characterization, UV-Vis absorption spectra of the three reference molecules were measured.

Ref-exTTF

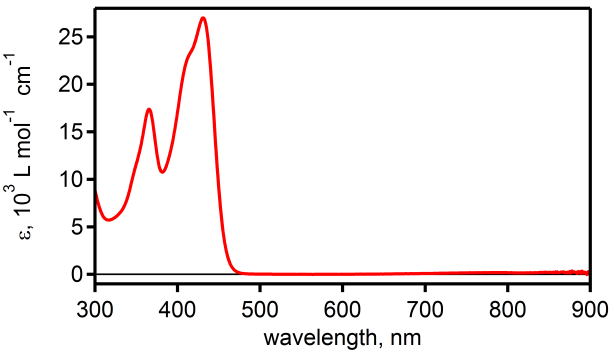

Figure 5.4: UV-Vis absorption spectrum of Ref-exTTF in dry, de-oxygenated CH_2Cl_2.

The UV-Vis absorption spectrum of Ref-exTTF in Figure 5.4 shows two absorption bands at 430 nm (ε = 26'700 L mol^{-1} cm^{-1}) and 365 nm (ε = 17'100 L mol^{-1} cm^{-1}). These two bands are characteristic for the exTTF moiety and can be found in similar exTTF-containing compounds.[23, 124, 140] Above 470 nm and up to 900 nm, no absorption bands can be detected.

Ref-PTZ

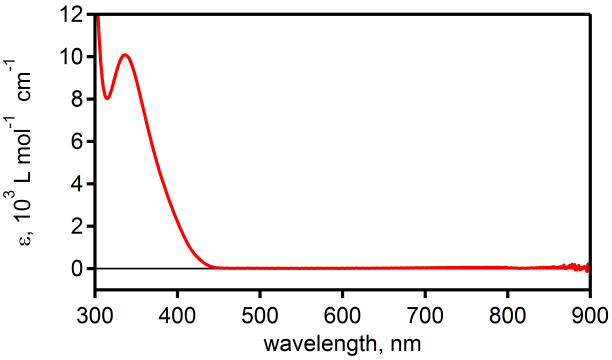

Figure 5.5: UV-Vis absorption spectrum of Ref-PTZ in dry, de-oxygenated CH_2Cl_2.

The UV-Vis absorption spectrum of Ref-PTZ in Figure 5.5 shows a single absorption band with a maximum at 335 nm (ε = 10'050 L mol^{-1} cm^{-1}).[134] Its tail absorption ends at 445 nm and no other absorption bands can be detected up to 900 nm.

Ref-exTTF-PTZ

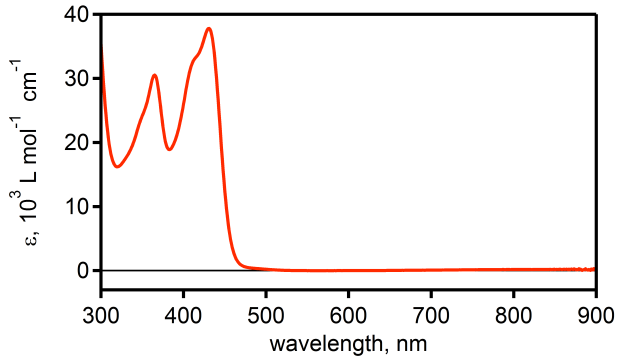

Figure 5.6: UV-Vis absorption spectrum of Ref-exTTF-PTZ in dry, de-oxygenated CH_2Cl_2.

The UV-Vis absorption spectrum of Ref-exTTF-PTZ in Figure 5.6 resembles the one of Ref-exTTF. At 430 nm ($\varepsilon = 37'550$ L mol^{-1} cm^{-1}) and 365 nm ($\varepsilon = 30'300$ L mol^{-1} cm^{-1}), the characteristic bands for the exTTF moiety show up. The increased extinction coefficients in Ref-exTTF-PTZ compared to the ones in Ref-exTTF are due to two exTTF moieties being present in the molecule. The absorption band for the PTZ moiety at 335 nm is not visible due to the high general absorption at this wavelength (ε = 18'400 L mol^{-1} cm^{-1}), presumably hiding the comparatively weak absorption band of PTZ (ε = 10'050 L mol^{-1} cm^{-1}) at 335 nm. From 480 nm towards the red, no additional absorption bands can be detected.

Electrochemistry

Cyclic voltammetric measurements were performed to verify the oxidation potentials of the different electron donors. Additional studies were carried out to investigate potential inversion in the exTTF moiety. All measurements were performed in dry, Ar-purged solvents with 0.1 M tetra-n-butylammonium hexafluorophosphate ($TBAPF_6$) as supporting electrolyte. For all measurements, a saturated calomel electrode (SCE) was used as the reference electrode and a glassy carbon electrode (GCE) as the working electrode.

Ref-exTTF

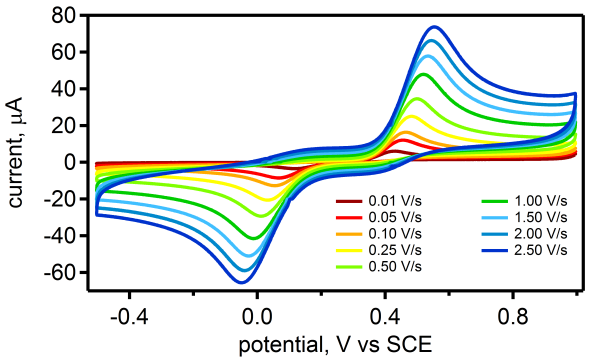

Figure 5.7: Cyclic voltammogram of Ref-exTTF (1 mM) in dry, Ar-purged DMF. Different scan rates as given in the inset, supporting electrolyte 0.1 M $TBAPF_6$.

Cyclic voltammograms (CV) of Ref-exTTF can be seen in Figure 5.7. There is just one peak for the two-electron oxidation as well as for the re-reduction to its neutral form. Measuring at different scan rates show the peak potentials on anodic and subsequent cathodic scans to vary significantly. With increasing scan rate, the oxidation potential as well as the current become more positive. Upon re-reduction, both the peak potential and the current get more negative. This behavior is known for other moieties exhibiting potential inversion, e.g. 3,8-diiodo-dibenzo[1,2]dithiin,[141] dibenzo[1,2]dithiin[31] or 4,4'-bipyridiyl-3,3'-disulfide.[142]

In addition, a linear correlation of the peak current with the square root of the scan rate (Figure 5.8) can be observed. This is in conformity with findings in the above-mentioned moieties exhibiting potential inversion and shows that the electrode reaction is diffusion controlled, the analyte remains homogeneous during the experiment and that the investigated system is electrochemically reversible.[143, 144]

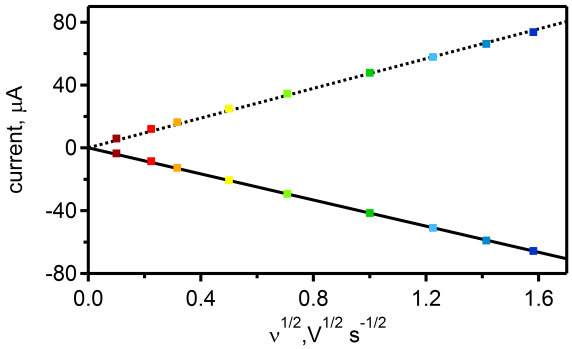

Figure 5.8: Linear correlation of the peak current with the square root of the different scan rates applied. Colors match the scan rates given in Figure 5.7. Dotted line for oxidative sweep, solid line for reductive sweep.

The potential inversion in exTTF can be attributed to structural changes associated with the oxidation process: in the neutral state, the central anthracene core has a butterfly-like geometry with the two dithiol rings bending slightly below the anthracene plane. Upon oxidation, the anthracene core becomes planar and the dithiol rings rotate out of plane.[117, 121] In the doubly oxidized state, both dithiol rings then bear one positive charge each, isolated by the anthracene core in between and therefore minimizing electrostatic repulsion.[119] If this conformational change is hindered by suitable modification of the side-chains, no potential inversion can be observed anymore and two one-electron oxidation waves result.[145]

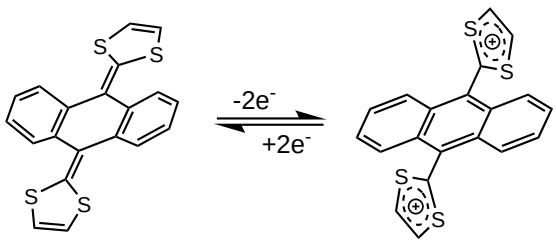

Figure 5.9: Structural change accompanying the two-electron oxidation process in exTTF. The central anthracene unit switches from a butterfly-like structure to planar. Exterior dithiol rings rotate out of plane.

Due to the CV only showing one oxidation wave for a two-electron oxidation process it is not simple to give the potentials for the first and second oxidation step. Clearly, the measured oxidation potential can be assigned to the first oxidation step. Given the fact that - due to potential inversion - the second oxidation is easier than the first one, it can be assumed that the second oxidation potential is given by the potential of the re-reduction wave. With the peak potentials shifting with the scan rate, average potentials for oxidation and re-reduction are constructed. For each of the nine scan rate maxima,

the FWHM potentials are determined, added up and subsequently divided by 9 to give the average oxidation potential. The same procedure applies for the minima of the re-reduction waves. Therefore, the first and second oxidation potentials are proposed to be $E_{ox,1} = 0.43$ V and $E_{ox,2} = 0.10$ V vs. SCE in the following sections.

Ref-PTZ

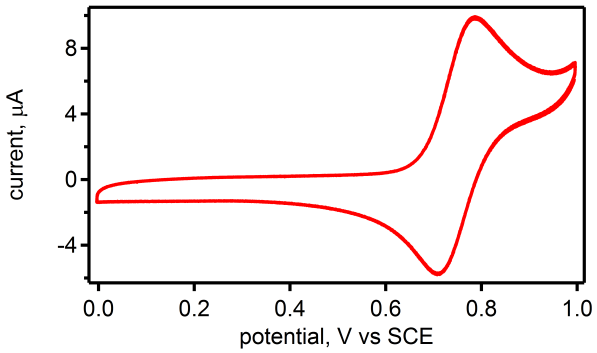

Figure 5.10: Cyclic voltammogram of Ref-PTZ (1 mM) in dry, Ar-purged DMF. Scan rate 0.1 V/s, supporting electrolyte 0.1 M $TBAPF_6$.

The cyclic voltammogram of Ref-PTZ in Figure 5.10 shows the oxidation of the PTZ moiety and its subsequent re-reduction at $E_{1/2} = 0.75$ V vs. SCE. The value determined here is slightly higher than the potential reported in the literature.[134] Upon several oxidation and reduction cycles, the molecule is chemically stable and the oxidation process is fully reversible.

Ref-exTTF-PTZ

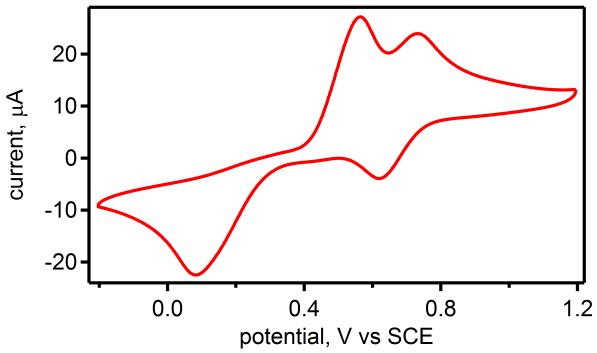

Figure 5.11: Cyclic voltammogram of Ref-exTTF-PTZ (1 mM) in dry, Ar-purged DMF. Scan rate 0.1 V/s, supporting electrolyte 0.1 M $TBAPF_6$.

The cyclic voltammogram of Ref-exTTF-PTZ is represented in Figure 5.11. On the anodic scan, two distinct waves can be seen which can clearly be attributed to the two different electron donor moieties present in the molecule. In analogy to the isolated Ref-exTTF moiety, the oxidation potentials for the exTTF-part can be given with $E_{ox,1}$ = 0.48 V and $E_{ox,2}$ = 0.20 V vs. SCE. For the PTZ-part, the oxidation potential is 0.68 V vs. SCE, perfectly matching the oxidation potential reported in the the literature[134]. Comparing the values obtained for Ref-exTTF, Ref-PTZ and Ref-exTTF-PTZ, it can be observed that the electron donor moieties being covalently connected still exhibit similar oxidation potentials as in their isolated states.

Chemical Oxidation

For investigating the optical changes in the absorption spectrum upon oxidation of the donor moieties, chemical oxidation with $SbCl_5$ in dry CH_2Cl_2 was conducted. The ground state UV-Vis spectrum was measured, then the chemical oxidant was added, the solution mixed for 2 minutes and the absorbance measured again. This procedure was repeated several times so that the oxidation of the different species could be monitored.

Ref-exTTF

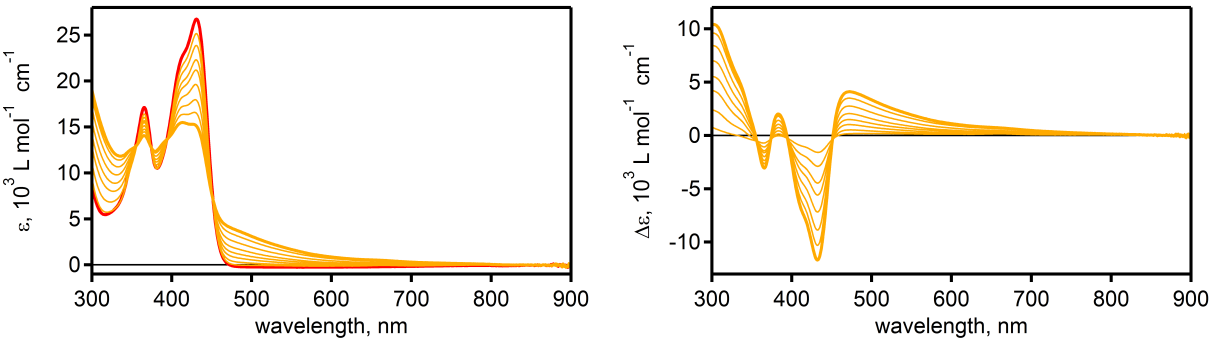

Figure 5.12: Chemical oxidation of Ref-exTTF ($2 \cdot 10^{-5}$M) in dry CH_2Cl_2 with the oxidant $SbCl_5$. The oxidant was added in portions of 0.25 equivalents, the thick yellow spectrum corresponds to the addition of 2 equivalents of oxidant. ***Left:*** Spectrum shows the ground state absorption before oxidation (red) and the subsequent spectra measured after each portion of $SbCl_5$ added (yellow). Thick yellow line gives the final state after oxidation. ***Right:*** Difference spectra generated from the spectra of the oxidized states shown in yellow by subtracting the ground state absorption spectrum (red).

The UV-Vis spectroscopic changes associated with the chemical oxidation of Ref-exTTF can be seen in Figure 5.12. Due to potential inversion and the second electron being abstracted easier than the first electron, only the doubly oxidized species can be observed

with this method. The doubly oxidized state is characterized by a broad absorption band ranging from 450 to 800 nm with a maximum at 472 nm. The ground state absorption band at 430 nm decreases and therefore forms a bleach in the difference spectrum. Below 400 nm, a minor band at 383 nm and a bleach at 365 nm are also formed. The observations here are in accordance with literature reports.[123, 126, 127] For the spectral signature of the one-electron oxidized Ref-exTTF, transient absorption spectroscopy needs to be performed. This measurement can be found in the transient absorption spectroscopy section.

Ref-PTZ

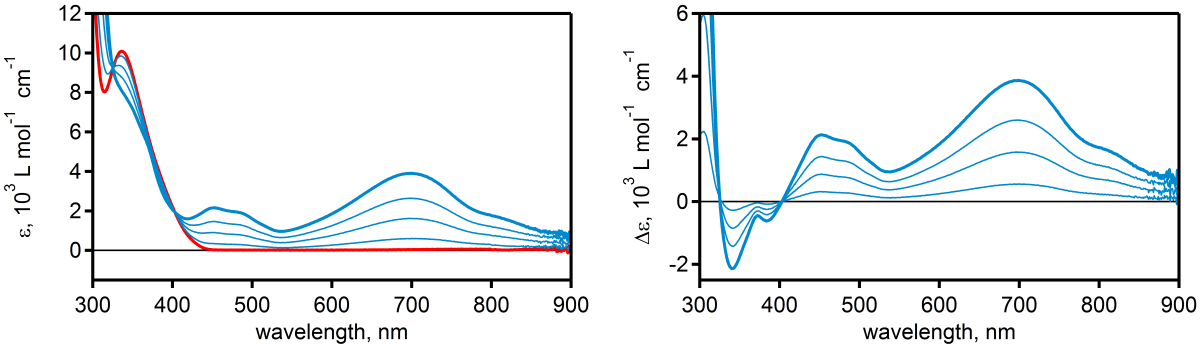

Figure 5.13: Chemical oxidation of Ref-PTZ ($2 \cdot 10^{-5}$M) in dry CH_2Cl_2 with the oxidant $SbCl_5$. The oxidant was added in portions of 0.25 equivalents, the thick blue spectrum corresponds to the addition of 1 equivalent of oxidant. ***Left:*** Spectrum shows the ground state absorption before oxidation (red) and the subsequent spectra measured after each portion of $SbCl_5$ added (blue). Thick blue line gives the final state after oxidation. ***Right:*** Difference spectra generated from the spectra of the oxidized states shown in blue by subtracting the ground state absorption spectrum (red).

Figure 5.13 shows the spectral changes arising from the oxidation of PTZ. A broad absorption band is formed between 400 and 900 nm with two maxima being located at 452 and 700 nm. Below 400 nm, two minima are located at 340 and 385 nm. These findings match with the spectrum reported in the literature.[136]

Ref-exTTF-PTZ

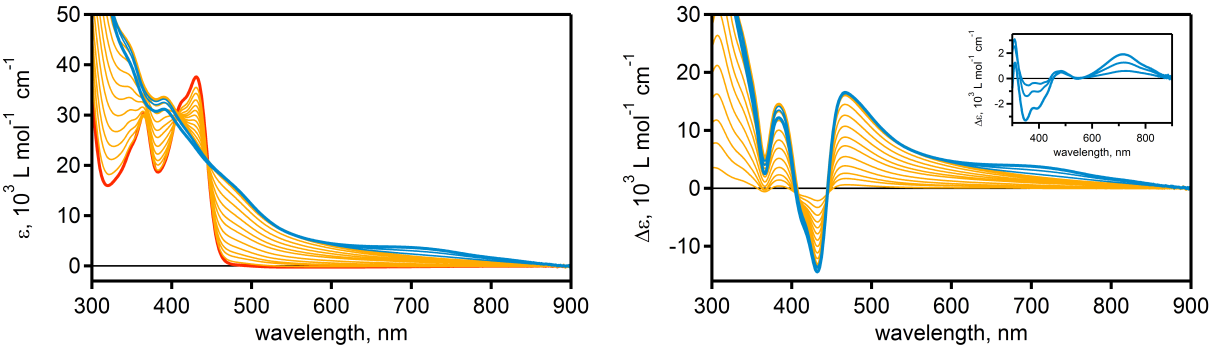

Figure 5.14: Chemical oxidation of Ref-exTTF-PTZ ($2 \cdot 10^{-5}$M) in dry CH_2Cl_2 with the oxidant $SbCl_5$. The oxidant was added in portions of 0.33 equivalents, the thick yellow spectrum corresponds to the addition of 4 equivalents of oxidant, the thick blue spectrum correlates to 5 equivalents of oxidant. ***Left:*** Spectrum shows the ground state absorption before oxidation (red) and the subsequent spectra measured after each portion of $SbCl_5$ added. Yellow spectra indicate the oxidation of exTTF, blue spectra indicate the oxidation of the PTZ moiety. Thick lines give the final oxidation states for each electron donor. ***Right:*** Difference spectra generated from the spectra of the oxidized states shown in yellow and blue by subtracting the ground state absorption spectrum. Inset shows the spectral characteristics of PTZ^+ obtained by subtracting the oxidized exTTF spectrum (thick yellow line) from the spectra measured afterwards (blue spectra).

The UV-Vis spectroscopic changes associated with the chemical oxidation of Ref-exTTF-PTZ are presented in Figure 5.14. After consecutive addition of the oxidant, first the oxidation of the exTTF moieties can be seen (yellow) followed by the oxidation of the PTZ moiety (blue). For the observations of the chemical oxidation experiment here one needs to consider that Ref-exTTF-PTZ contains two exTTF moieties but only one PTZ moiety. Therefore the intensity of the PTZ signal is underrepresented in comparison with the exTTF signal.

The oxidized exTTF moiety shows the same spectral characteristics as in the isolated state with a broad absorption band ranging from 445 to 850 nm and its maximum at 467 nm. At 432 nm, the bleach from the ground state absorption is found. Interestingly, the bleach at 432 nm is not as pronounced as in Ref-exTTF. Also below 400 nm, the spectrum differs slightly from the one of the isolated exTTF-moiety. While the band formed at 383 nm is stronger in intensity, the bleach at 365 nm found in Ref-exTTF is not a bleach here but rather an absorption minimum. Nevertheless, the general spectral characteristic of the exTTF dication is the same. As soon as the oxidation of the exTTF moieties is completed, the oxidation of the PTZ moiety can be seen (blue). Again, the characteristics are similar to the ones of the isolated PTZ moiety. The broad absorption band in Ref-PTZ between 400 and 900 nm splits into two independent maxima being

formed at 477 and 718 nm here. The bleaches below 445 nm are more pronounced than in Ref-PTZ and have their minima at 352 and 392 nm. Again, the overall characteristics of PTZ^+ remain the same.

Transient Absorption Spectroscopy

Transient absorption spectroscopy is a convenient method to detect the spectral features of short-lived species. Therefore, a ground state spectrum of the sample solution is recorded, then the sample is excited with a short laser pulse and another spectrum is recorded over a specific timeframe. By subtracting the spectrum before the laser pulse from the spectrum after the laser pulse, a difference spectrum is created that shows the spectral changes induced by the laser excitation. With this, species that have a lifetime of ns, µs or ms can be detected with our setup.

Ref-exTTF

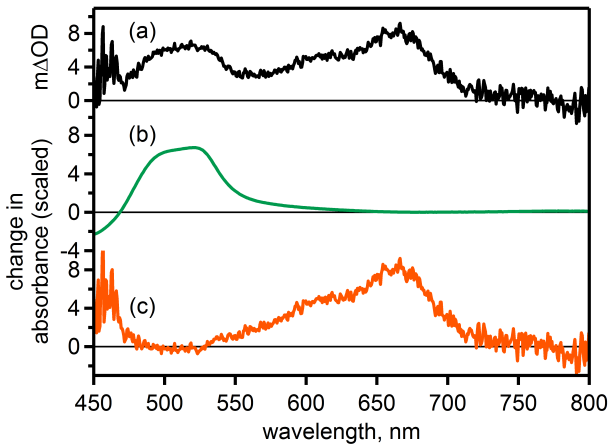

Figure 5.15: (a) Transient absorption spectrum of Ref-exTTF (2 mM) with $[Ru(bpy)_3](PF_6)_2$ ($3{\cdot}10^{-5}$ M) as photosensitizer in dry, de-oxygenated DMF. Spectrum was recorded 2000 ns after excitation at 532 nm to exclude emission interference. Laser pulse duration 10 ns, integration time 200 ns. (b) Difference spectrum of $[Ru(bpy)_3]^+$ in dry, Ar-purged DMF obtained via spectro-electrochemistry (see Figure 5.20). (c) Difference spectrum obtained by subtracting the scaled $[Ru(bpy)_3]^+$ difference spectrum (b) from the transient absorption spectrum (a).

The transient absorption spectrum of Ref-exTTF with $[Ru(bpy)_3](PF_6)_2$ as photosensitizer can be seen in Figure 5.15a. Under the experimental conditions, not all excited photosensitizer was quenched by Ref-exTTF, therefore, a delay of 2000 ns was applied to ensure that all emissive states had decayed. The long lifetime of the observed signal here is an effect of the bimolecular experiment and the resulting slow recombination processes

of the involved species. In addition, only the segment 450 to 800 nm could be recorded due to the high concentration of Ref-exTTF giving rise to a large absorption below 450 nm which rendered signal detection in this part of the spectrum impossible.

In the transient absorption experiment, $[Ru(bpy)_3]^{2+}$ in its excited state is a good electron donor as well as a good electron acceptor. With Ref-exTTF being a good electron donor, Ref-exTTF is expected to transfer one electron to photoexcited $[Ru(bpy)_3]^{2+}$ yielding the photoproducts Ref-exTTF$^+$ and $[Ru(bpy)_3]^+$. Therefore, the spectral features of exTTF$^+$ and $[Ru(bpy)_3]^+$ are expected to show up in the transient spectrum.

Doubly oxidized exTTF in contrast is unlikely to occur in the spectrum due to photoexcited $[Ru(bpy)_3]^{2+}$ being a one electron acceptor and the low probability of exTTF$^+$ encountering a second photoexcited $[Ru(bpy)_3]^{2+}$ molecule leading to charge-accumulation instead of charge-recombination in the short timeframe of the measurement. Another potential pathway leading to exTTF^{2+} is the disproportionation of two exTTF$^+$ cations. While the timeframe between laser pulse and detection start (2000 ns) can allow for disproportionation reactions to take place, the amount of exTTF$^+$ formed with the laser pulse is rather small and the encounter probability of two exTTF$^+$ cations thus rather low. Therefore, at best, only a minor amount of exTTF^{2+} is expected to be seen in the transient spectrum.

The transient spectrum obtained in this setup exhibits two main bands with absorption maxima at 513 and 666 nm. While a band rising at 660 nm is expected for exTTF$^+$ from literature reports, the band forming at 513 nm is assigned to $[Ru(bpy)_3]^+$. This is verified by spectro-electrochemical reduction experiments of $[Ru(bpy)_3]^{2+}$. The difference spectrum for $[Ru(bpy)_3]^+$ is shown in Figure 5.15b. To subtract the difference spectrum of $[Ru(bpy)_3]^+$ from the transient spectrum (a), spectrum (b) was scaled to the value of spectrum (a) at 523 nm. At this wavelength, the absorption band of $[Ru(bpy)_3]^+$ is at its maximum value while the absorption of exTTF^{2+}has its maximum at 470 nm and at 523 nm just shows around 60% of the maximum absorption intensity. The subtraction of the scaled spectrum (b) should therefore remove the $[Ru(bpy)_3]^+$ spectral features from the transient spectrum while at the same time only partially removing the exTTF^{2+} spectral features. This should allow detection of exTTF^{2+} in the spectrum, if present.

By subtracting the scaled difference spectrum of $[Ru(bpy)_3]^+$ from the transient spectrum (a), spectrum 5.15c is obtained. Here, one absorption band at 666 nm is present that gradually decreases until it reaches the baseline at 530 nm. This absorption band represents the spectral features of singly oxidized exTTF, being consistent with the spectra reported in the literature obtained by radiolytic oxidation[23, 126, 127] or in charge-separation dyads.[146–149] In addition, the literature spectrum for exTTF$^+$ shows a bleach at 440 nm for the exTTF$^+$ cation absorption[126] which could not be seen in the experimental setup

used here due to the restricted wavelength window.

Having a closer look at the spectrum between 450 and 530 nm, a slight absorption increase from 500 towards 470 nm can be seen in spectrum (c). This could indicate the formation of some $exTTF^{2+}$ via the above addressed disproportionation mechanism. The signal intensity however is weak and the noise caused by the large Ref-exTTF absorption starts to affect the spectrum below 500 nm such that this observation could be an artefact of the measurement. Therefore, no clear answer of the origin of this absorption increase can be given.

Summary

In the previous sections, the two-electron donor exTTF and the intermediate electron donor PTZ were studied. The electron donors in their isolated state show the same behavior as in the covalently linked state. The oxidation potentials of exTTF and PTZ are sufficiently separated to allow the postulated electron transfer to excited $[Ru(bpy)_3]^{2+}$ from exTTF via the PTZ intermediate donor. Both exTTF and PTZ proved to be stable upon reversible electron release and subsequent uptake. The inverted potential behavior of exTTF was confirmed and should facilitate the second electron transfer. In addition, the spectral signatures of the oxidized electron donors allow to clearly distinguish oxidized PTZ from singly- and from doubly oxidized exTTF.

5.1.2 exTTF-PTZ-Ru Triad

In the following sections, the exTTF-PTZ-Ru triad shown in Figure 5.16 will be referenced as donor triad. The donor triad was obtained as pure substance and is fully characterized as can be seen in the experimental section.

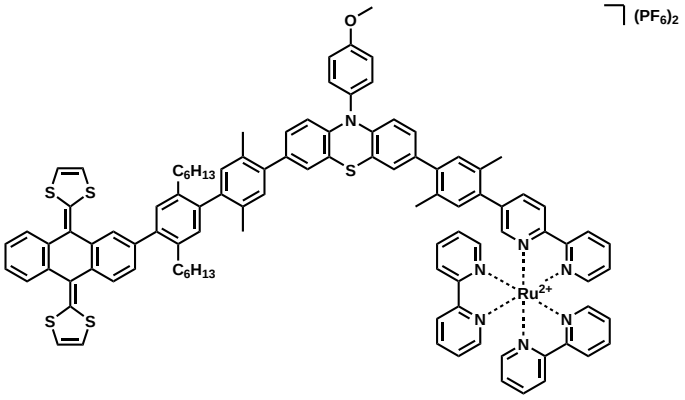

Figure 5.16: Schematic representation of the exTTF-PTZ-Ru donor triad.

Optical Absorption Spectroscopy

For spectroscopic characterization, the ground state UV-Vis absorption spectrum of the donor triad was recorded.

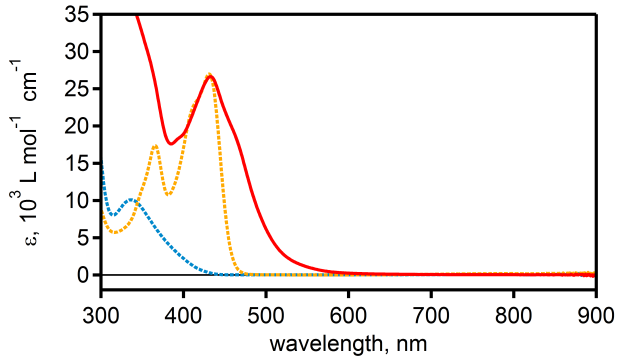

Figure 5.17: UV-Vis absorption spectrum of the donor triad (red), Ref-exTTF (dashed yellow) and Ref-PTZ (dashed blue) in dry, de-oxygenated CH_2Cl_2.

The UV-Vis absorption spectrum of the donor triad, as seen in Figure 5.17, exhibits a broad absorption band between 380 and 600 nm that consists of an overlap of the exTTF absorption at 430 nm ($\varepsilon = 26'500$ L mol^{-1} cm^{-1} at peak maximum) and the MLCT absorption of $[Ru(bpy)_3]^{2+}$ at 450 nm,[150] which appears as a shoulder in the UV-Vis spectrum shown. Below 380 nm, the absorption of the donor triad increases strongly showing the overlap of the exTTF absorption band at 365 nm and the PTZ absorption

band at 335 nm. In contrast to Ref-exTTF and Ref-PTZ, the donor triad possesses a significant absorption feature between 480 and 600 nm. This feature can be attributed to the $[Ru(bpy)_3]^{2+}$ moiety solely and therefore this region is suitable for specific excitation of the $[Ru(bpy)_3]^{2+}$ photosensitizer.

Electrochemistry

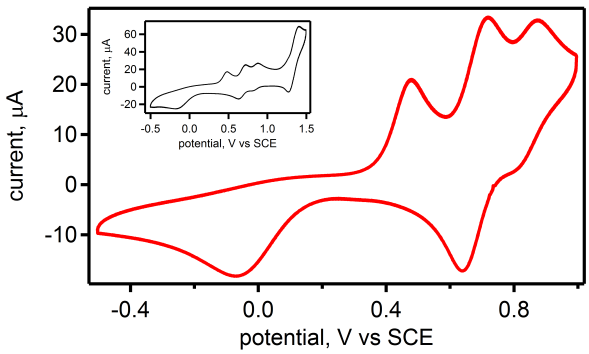

Figure 5.18: Cyclic voltammogram of the donor triad (1 mM) in dry, Ar-purged MeCN. Scan rate 0.5 V/s, supporting electrolyte 0.1 M $TBAPF_6$. Inset shows an extended potential window additionally showing the oxidation of the $[Ru(bpy)_3]^{2+}$ photosensitizer. Complex stability decreased upon each $[Ru(bpy)_3]^{2+}$ oxidation cycle.

The cyclic voltammogram of the donor triad in Figure 5.18 displays the oxidation of the three triad segments. The exTTF moiety is oxidized first with potentials of $E_{ox,1}$ = 0.42 V and $E_{ox,2}$ = 0.05 V vs. SCE. In analogy to the exTTF reference molecules, the FWHM potential of the exTTF oxidation wave is considered as the first electron oxidation potential while the second electron oxidation potential is assumed to be given by the FWHM potential of the re-reduction wave. Upon increasing the applied potential, the first oxidation of PTZ appears at $E_{ox,1}$ = 0.68 V vs. SCE, followed by the second PTZ oxidation at $E_{ox,2}$ = 0.84 V vs. SCE. Further increasing the applied potential then leads to the oxidation of the $[Ru(bpy)_3]^{2+}$ moiety at E_{ox} = 1.34 V vs. SCE as shown in the inset. While the oxidation of the $[Ru(bpy)_3]^{2+}$ photosensitizer is reversible upon several cycles, the exTTF moiety seems to degenerate with each cycle at a potential necessary to oxidize $[Ru(bpy)_3]^{2+}$. Therefore, the $[Ru(bpy)_3]^{2+}$ oxidation potential was determined in a separate measurement to retain the accuracy of the electron donor potentials. The hereby obtained potentials of the donor triad coincide with the potentials measured in the reference molecules and the literature value for $[Ru(bpy)_3]^{2+}$.[77] Table 5.1 gives an overview of the oxidation potentials of the donor triad and the corresponding potentials of the reference molecules.

	Ref-exTTF	Ref-PTZ	Ref-exTTF-PTZ	Donor Triad	$[Ru(bpy)_3]^{2+}$
$E(exTTF^{+/0})$	0.43		0.48	0.42	
$E(exTTF^{2+/+})$	0.10		0.20	0.05	
$E(PTZ^{+/0})$		0.75	0.68	0.68	
$E(Ru^{II/I})$					-1.33
$E(Ru^{*II/I})$					0.77
$E(Ru^{III/II})$				1.34	1.29
$E(Ru^{III/*II})$					-0.81

Table 5.1: Redox potentials (V vs SCE) for the donor triad and reference molecules, measured in MeCN (donor triad) or DMF (reference molecules). Values for $[Ru(bpy)_3]^{2+}$ in MeCN obtained from the literature.[77]

Chemical Oxidation

As with the reference molecules, the donor triad was oxidized chemically to investigate spectral changes upon oxidation. $SbCl_5$ in dry CH_2Cl_2 was used as an oxidant. The ground state UV-Vis spectrum was measured, then the chemical oxidant was added, the solution mixed for 2 minutes and the absorption spectrum measured again. This procedure was repeated several times so that the oxidation of the different species could be monitored.

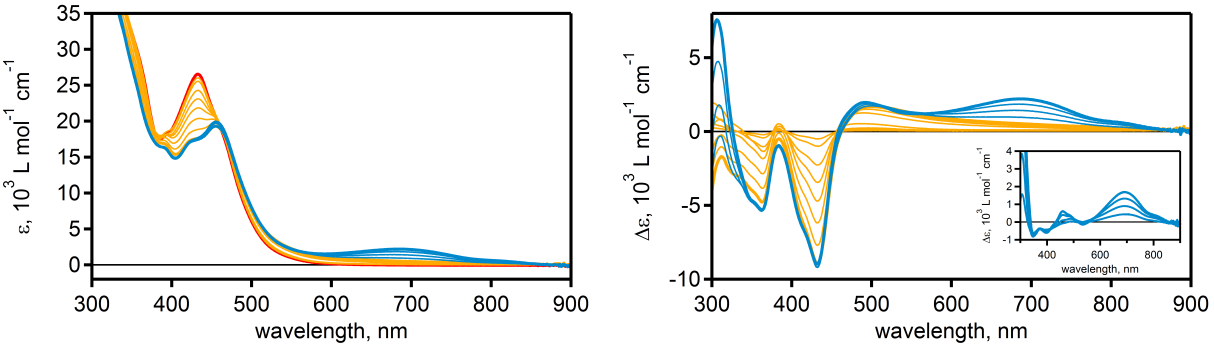

Figure 5.19: Chemical oxidation of the donor triad ($2 \cdot 10^{-5}$M) in dry CH_2Cl_2 with the oxidant $SbCl_5$. The oxidant was added in portions of 0.25 equivalents, the thick yellow spectrum corresponds to the addition of 2 equivalents of oxidant, the thick blue spectrum corresponds to 3 equivalents of oxidant. ***Left:*** Spectrum shows the ground state absorption before oxidation (red) and the subsequent spectra measured after each portion of $SbCl_5$ added. Yellow spectra show the oxidation of exTTF, blue spectra the oxidation of the PTZ moiety. Thick lines give the final oxidation states for each electron donor. ***Right:*** Difference spectra generated from the spectra of the oxidized states shown in yellow and blue by subtracting the ground state absorption spectrum (red). Inset shows the spectral characteristics of PTZ^+ obtained by subtracting the oxidized exTTF spectrum (thick yellow line) from the spectra measured afterwards (blue spectra).

The UV-Vis spectroscopic changes associated with the chemical oxidation of the donor triad are presented in Figure 5.19. As with Ref-exTTF-PTZ, first the oxidation of the exTTF moiety can be seen (yellow) followed by the oxidation of the PTZ moiety (blue). The oxidized exTTF moiety exhibits the characteristic features of the doubly oxidized donor as seen in the experiments with Ref-exTTF (Figure 5.12) and Ref-exTTF-PTZ (Figure 5.14). A broad absorption band ranges from 460 to 850 nm with a maximum at 495 nm. At 432 nm the bleach from the ground state absorption is found. In the donor triad, the bleach at 432 nm is much more pronounced than the band at 495 nm, this being in consensus with the oxidation of Ref-exTTF (and unlike in Ref-exTTF-PTZ). Below 400 nm, a bleach with its minimum at 365 nm is found matching the spectral properties of Ref-exTTF. In analogy with the observations during the oxidation of the reference molecules, the singly oxidized exTTF moiety is not detectable under the experimental setup used here.

Once the oxidation of the exTTF moiety is completed, the oxidation of the PTZ moiety can be monitored. Two bands at 465 and 692 nm form, again in line with the characteristics observed in Ref-PTZ (Figure 5.13) and Ref-exTTF-PTZ (Figure 5.14). Below 430 nm, a bleach with minima at 350 and 397 nm can be observed.

Spectro-Electrochemistry

Spectro-electrochemistry is a convenient method to monitor the spectral changes following reduction or oxidation processes in solution. The ground state UV-Vis spectrum is measured as the baseline, then a certain potential is applied, and the absorption is measured again. When reduction or oxidation potentials are sufficiently separated, the spectral features of different reduction or oxidation states can be detected.

$[Ru(bpy)_3]^{2+}$

To allow for an easier interpretation of the transient absorption spectroscopy in the following sections, the spectroscopic signature of one-electron reduced $[Ru(bpy)_3]^{2+}$ was measured.

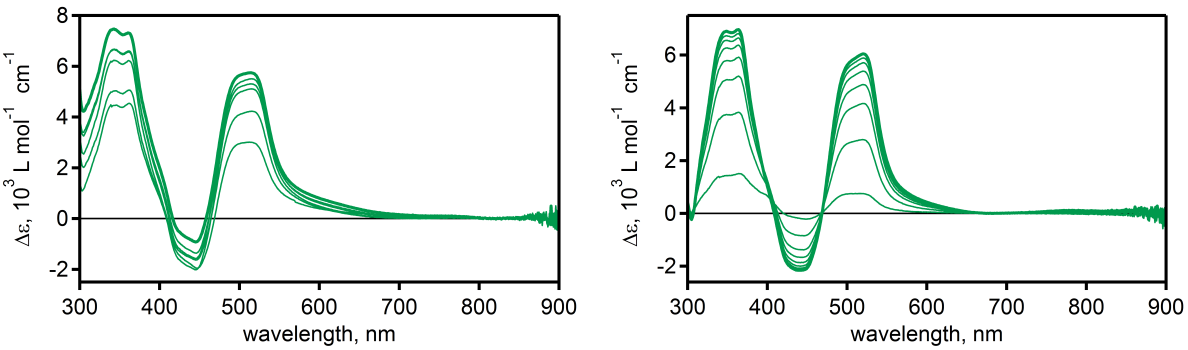

Figure 5.20: Difference spectrum of $[Ru(bpy)_3](PF_6)_2$ ($2 \cdot 10^{-4}$ M) with 0.1 M $TBAPF_6$ as supporting electrolyte in dry, de-oxygenated MeCN (left) and in dry, de-oxygenated DMF (right). Reduction was performed at -1.4 V vs. SCE.

Upon reduction of $[Ru(bpy)_3]^{2+}$, two absorption bands and one bleach occur. Regarding the solvent, there is just a slight shift in the absorption band maxima between MeCN and DMF, but the general spectral characteristic is the same. Two broad absorption bands around 355 and 515 nm can be seen originating from the formation of reduced bipyridine ligand while the bleach around 450 nm is formed by depletion of the MLCT ground state absorption.[151–153]

$MV(PF_6)_2$

Methyl viologen (MV^{2+}) was used as an electron acceptor in transient absorption experiments. Therefore, in addition to the spectrum of reduced $[Ru(bpy)_3]^{2+}$, the spectroscopic signature of one-electron reduced methyl viologen was measured as well.

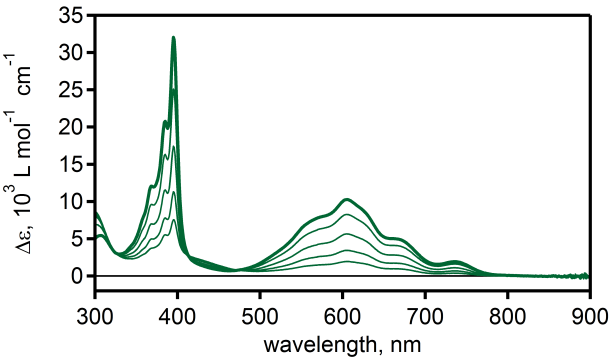

Figure 5.21: Difference spectrum of $MV(PF_6)_2$ ($2 \cdot 10^{-4}$ M) with 0.1 M $TBAPF_6$ as supporting electrolyte in dry, de-oxygenated MeCN. Reduction was performed at -0.55 V vs. SCE.

The spectroscopic signature of MV^+ is rather specific with a broad absorption band between 480 and 800 nm and a more intense, finger-like absorption between 330 and

410 nm with the maximum being at 395 nm. It is therefore easy to identify in the transient spectrum as soon as it is formed. The difference spectrum generated via spectroelectrochemistry shown in Figure 5.21 is in conformance with literature reports.[134, 151, 154]

Transient Absorption Spectroscopy

Single-Pulse Experiments

Upon excitation of the triad, the excited $[Ru(bpy)_3]^{2+}$ photosensitizer is expected to be reductively quenched by the primary electron donor PTZ, leading to the intermediate state exTTF-PTZ$^+$-Ru$^+$. The positive charge (denoted as 'hole') on PTZ would then move on to the secondary electron donor exTTF due to exTTF being the better electron donor in comparison to PTZ. This would lead to the final charge-separated state exTTF$^+$-PTZ-Ru$^+$. Charge-recombination processes would then return the triad to its ground state. The primary electron donor PTZ should help retard charge-recombination kinetics and therefore increase the lifetime of the charge-separated state. Energy estimations for the different states of the triad involved during charge-separation confirm the probability of the above-mentioned electron and hole transfer processes to take place. The corresponding energy scheme is presented in Scheme 5.3.

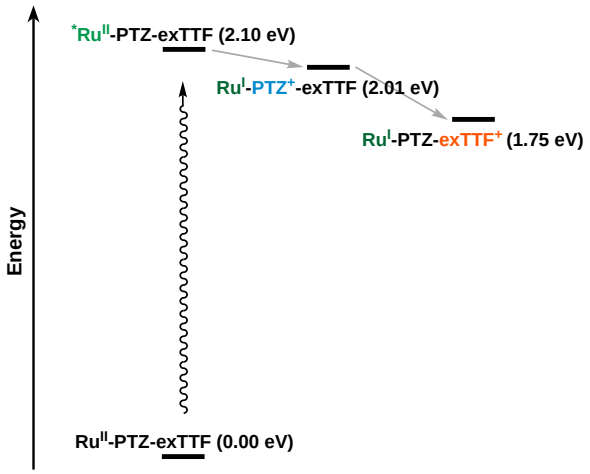

Scheme 5.3: Energy scheme for the formation of the charge-separated states in the donor triad following excitation. Energy levels are based on the redox potentials in Table 5.1, their calculation is presented in the appendix.

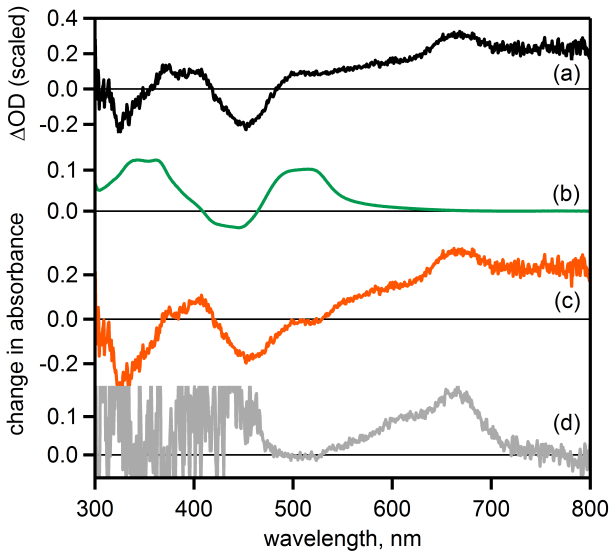

Figure 5.22: (a) Transient absorption spectrum of the donor triad ($2.5 \cdot 10^{-5}$ M) in dry, de-oxygenated MeCN, measured 60 ns after excitation at 532 nm with 10 ns laser pulses, pulse power 45 mJ; (b) difference spectrum of $[Ru(bpy)_3]^{2+}$ in dry, de-oxygenated MeCN reduced at a potential of -1.4 V vs. SCE; (c) difference spectrum of (a) minus (b) to remove the spectral features of $[Ru(bpy)_3]^{+}$ from the transient absorption spectrum of the donor triad; (d) difference spectrum of $exTTF^{+}$ (from Figure 5.15) for comparison.

To track the processes following excitation of the donor triad, the transient absorption spectrum of the donor triad in dry, de-oxygenated MeCN was measured. The sample was excited at 532 nm with a laser pulse duration of 10 ns. The spectrum was measured with a time delay of 60 ns and an integration time of 200 ns and is presented in Figure 5.22a. Expecting the charge-separated state $exTTF^{+}$-PTZ-Ru^{+}, spectrum (a) should involve the spectral characteristics of $[Ru(bpy)_3]^{+}$ and $exTTF^{+}$. To deconvolute the spectrum, the difference spectrum of $[Ru(bpy)_3]^{+}$ obtained via spectro-electrochemistry (b) and the transient spectrum (a) were scaled to the same value at 370 nm. At this wavelength, neither $exTTF^{+}$, $exTTF^{2+}$ nor PTZ^{+} show any significant absorption bands or bleaches. Subtracting the scaled difference spectrum of $[Ru(bpy)_3]^{+}$ (b) from the transient absorption spectrum (a) then gives difference spectrum (c). The obtained spectrum features a bleach between 420 and 500 nm and a broad absorption band ranging from 530 up to 800 nm with a maximum at 666 nm. These spectral characteristics can be clearly assigned to the $exTTF^{+}$ monocation with the spectral changes being consistent with the spectral changes seen for Ref-exTTF (Figure 5.22d) and in literature reports.[126, 148]

The single-pulse experiment with the donor triad shows that the proposed electron-transfer cascade from exTTF via PTZ to photoexcited $[Ru(bpy)_3]^{2+}$ functions. No spectral features of PTZ^{+} can seen in the difference spectrum (c). This implies that, as soon as the excited $[Ru(bpy)_3]^{2+}$ photosensitizer is reductively quenched, the positive charge on PTZ

is quenched by subsequent electron transfer from exTTF. This process seems to be highly efficient, probably due to a reaction free energy of ΔG_{ET} = -0.26 eV for the secondary electron-transfer process. Due to this secondary electron transfer, the transient spectrum of the intermediate charge-separated state cannot be observed in the experimental setup used here.

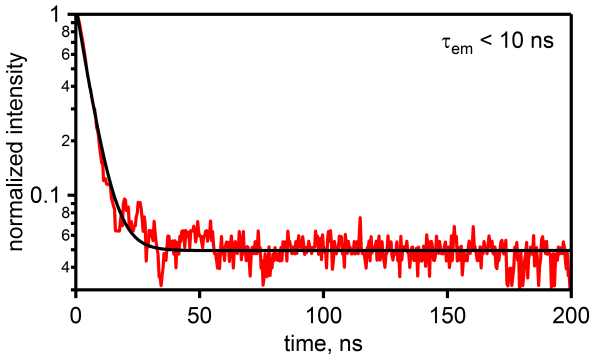

Figure 5.23: Normalized emission decay at 610 nm after excitation at 532 nm for the donor triad in MeCN (red) and corresponding exponential fit (black). The emission lifetime of 10 ns is instrumentally limited.

In Figure 5.23, the emission decay of the excited donor triad is shown. Without a quencher, the emission lifetime of $^{*}[Ru(bpy)_3]^{2+}$ is around 1100 ns in MeCN.[77] The exponential fit gives a lifetime of less then 10 ns for the triad's excited state. This short lifetime of the $[Ru(bpy)_3]^{2+}$ excited state corresponds to fast excited-state quenching by the PTZ donor moiety leading to the primary charge-separated state exTTF-PTZ^{+}-Ru^{+}.

An unexpected sidenote of the emission measurement is the fact that the emission at 610 nm does not decay back to the original baseline but forms a stable plateau at approx. 5% of the original signal. This might be due to partial decomposition or luminescence originating from an energy transfer from photoexcited $[Ru(bpy)_3]^{2+}$ to the exTTF moiety. In measurements reported by Guldi *et al.*, however, the exTTF triplet energy was determined to be around 2.5 eV.[23] This would preclude energy transfer from photoexcited $[Ru(bpy)_3]^{2+}$ to the exTTF moiety. Experiments to directly excite the exTTF triplet were not successful.

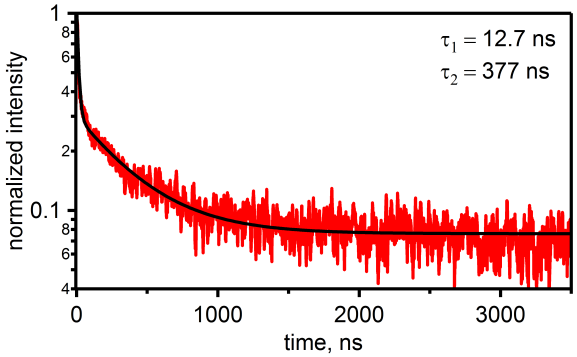

Figure 5.24: Normalized transient absorption decay at 665 nm following excitation (at 532 nm) of the donor triad in MeCN (red) and corresponding biexponential fit (black).

Having a look at the kinetics of the charge-recombination process at 665 nm (see Figure 5.24), two lifetimes result of the biexponential fitting process: 12.7 ns and 377 ns. Considering that the $[Ru(bpy)_3]^{2+}$ excited state is quenched within 10 ns and that the PTZ^+ cation shows a broad absorption band around 700 nm, the short-lived species can be attributed to the exTTF-PTZ^+-Ru^+ state which rapidly transforms into the final charge-separated exTTF$^+$-PTZ-Ru^+ state. The lifetime of 377 ns then belongs to the exTTF$^+$-PTZ-Ru^+ state seen in the transient absorption spectrum shown above. This interpretation is supported by the transient absorption spectrum measured at a 60 ns delay which does not show any spectral signature of the PTZ^+ cation. At the time the transient spectrum is recorded, the short-lived PTZ^+ species is already fully decayed.

Similar to the emission decay experiment, the signal of the absorption decay at 665 nm does not decay back to the original baseline but forms a stable plateau at approx. 8% of the original signal. As luminescence originating from energy transfer to exTTF is excluded, partial decomposition of the donor triad is probable. Additionally, disproportionation of $exTTF^+$ yielding the more stable $exTTF^{2+}$ and $exTTF^0$ moieties could also contribute to this finding.

Single-Pulse Experiments with MV^{2+} as Temporary Electron Acceptor

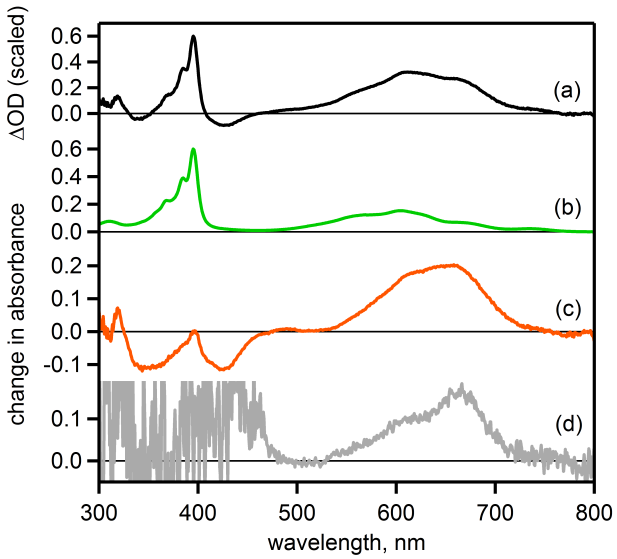

Figure 5.25: (a) Transient absorption spectrum of the donor triad ($2.5 \cdot 10^{-5}$ M) with $MV(PF_6)_2$ (50 mM) in dry, de-oxygenated MeCN. The sample was excited at 532 nm and the spectrum recorded with a delay of 500 ns to allow for complete electron transfer from photoexcited $[Ru(bpy)_3]^{2+}$ onto MV^{2+}. Laser pulse duration 10 ns, integration time 200 ns. (b) Spectral characteristics of MV^+ in MeCN, generated spectroelectrochemically from MV^{2+} (see Figure 5.21). (c) Difference spectrum generated by subtraction of the MV^+ difference spectrum (b) from the measured transient absorption spectrum (a). (d) Difference spectrum of $exTTF^+$ (from Figure 5.15) for comparison.

In contrast to the single-pulse experiment with the donor triad in the previous section, the temporary electron acceptor MV^{2+} was added in the measurement shown in Figure 5.25. Following excitation, the charge-separated state $exTTF^+$-PTZ-Ru^+ is formed within 12.7 ns. Subsequently, the electron on the reduced photosensitizer is transferred onto MV^{2+}, yielding the final charge-separated state $exTTF^+$-PTZ-Ru^{2+} // MV^+. With the electron and the hole being located on two different molecules, the lifetime of the charge-separated state increases dramatically (up to several minutes in this experiment) and allows for further reactions on the donor triad to take place.

In the transient spectrum measured (a), the specific spectral characteristics of MV^+ (shown in (b)) can be seen. A difference that meets the eye is the more intense absorption between 500 and 700 nm compared to the finger-like absorption structure below 400 nm. Additionally, the transient spectrum (a) shows a small bleach at 428 nm that is not visible in the difference spectrum of MV^+. In the same approach as for the donor triad in the absence of a quencher, the transient spectrum of MV^+ (b) and the transient spectrum (a) were scaled to the same value at 395 nm. The wavelength of 395 nm was chosen due to the strong intensity of this MV^+ absorption band and no significant absorption bands or

bleaches of $exTTF^{+}$, $exTTF^{2+}$ and PTZ^{+} being located at this wavelength. The hereby obtained difference spectrum (c) is characterized by an absorption band between 530 and 730 nm with a maximum located at 660 nm and two bleaches at 355 and 425 nm. This spectrum perfectly matches the spectral characteristics of $exTTF^{+}$ as shown in (d) and Figure 5.22c. Therefore, the experiment shows the expected photoproducts to be formed, namely $exTTF^{+}$ and MV^{+}.

Having a closer look at spectrum (c), an additional, very small absorption band is located at 490 nm. This absorption band (together with the bleach at 425 nm) would correspond to the spectral changes expected for $exTTF^{2+}$ (see Figures 5.12 and 5.19). The partial formation of $exTTF^{2+}$ could either be explained by a disproportionation reaction of $exTTF^{+}$ or alternatively by a small fraction of the excited molecules undergoing double excitation during the laser pulse duration and therefore forming the doubly oxidized species.

To further pursue the potential formation of doubly oxidized exTTF, a two-pulse experiment was designed that would allow for the first oxidation to take place after the first pulse and then a second pulse would excite the already oxidized triad to form the doubly oxidized state. This experiment is presented in the next section.

Two-Pulse Experiments with MV^{2+} as Temporary Electron Acceptor

In the single-pulse experiment shown in the previous section, an indication for the partial formation of the doubly oxidized donor triad could be found following excitation with MV^{2+} as temporary electron acceptor. Therefore, a two-pulse experiment was designed with a first pulse exciting the triad at 532 nm. Due to the long lifetime of the charge-separated state $exTTF^{+}$-PTZ-Ru^{2+} // MV^{+}, a delay of 500 ns was integrated to allow for maximum charge-separation (see Figure 5.26) before a second pulse was applied to re-excite the singly oxidized donor triad leading to the possible formation of the doubly oxidized triad. The wavelength for the second excitation was chosen to be 460 nm as neither $exTTF^{+}$ nor $exTTF^{2+}$ show any significant absorption at this wavelength.

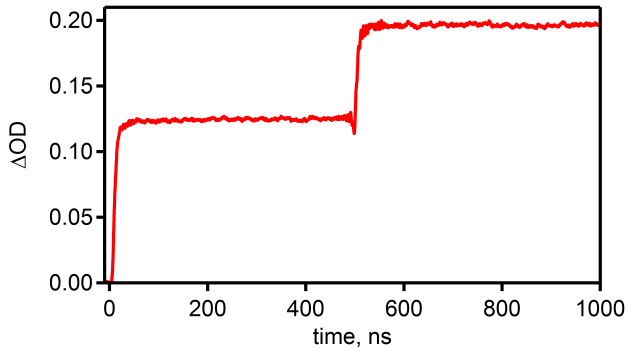

Figure 5.26: Formation of the absorption signal at 610 nm over time. The first rise of the signal (at 0 ns) originates from the first laser pulse at 532 nm while the second rise (at 500 ns) follows the second excitation at 460 nm. The absorption at 610 nm represents MV^+, being formed by electron transfer from the excited donor triad ($2.5 \cdot 10^{-5}$ M) to $MV(PF_6)_2$ (50 mM) in dry, de-oxygenated MeCN. Due to the signal representing MV^+ formation still slightly increasing up to 400 ns after the first laser pulse, a delay of 500 ns was integrated before the second laser pulse was applied.

An energy estimation for the pathway leading to the doubly oxidized donor triad is shown in Scheme 5.4. For clarity reasons, unproductive electron transfer pathways are omitted. The calculations indicate oxidative quenching by MV^{2+} to be energetically more favorable than reductive quenching of the excited state by PTZ. However, as the overall excited state quenching is strongly dependent on kinetics and therefore on the MV^{2+} concentration, both oxidative and reductive excited state quenching is expected to contribute to the charge-separation and accumulation process.

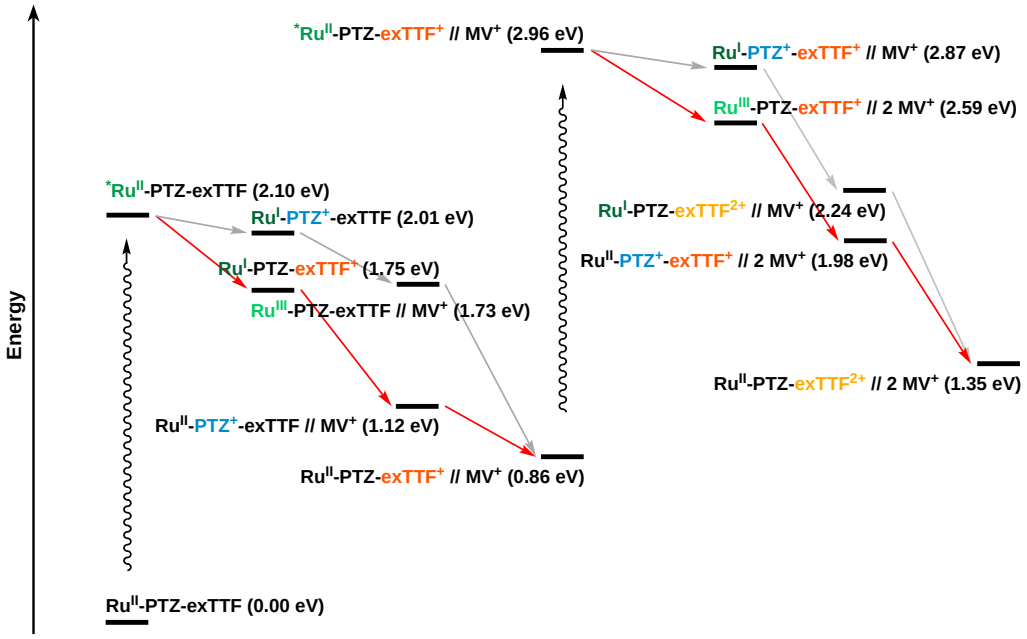

Scheme 5.4: Energy scheme for the formation of the charge-separated states in the donor triad following excitation. Methyl viologen was added as temporary electron acceptor. Energy levels are based on the redox potentials in Table 5.1, methyl viologen reduction potentials are taken from the literature.[151] Red arrows indicate the energetically favorable pathway while gray arrows show other energetically possible pathways leading to the same final state. Underlying calculations are presented in the appendix.

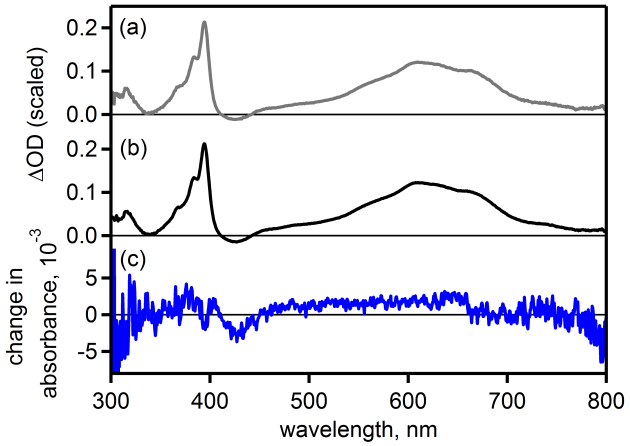

Figure 5.27: (a) Transient absorption spectrum of the donor triad ($2.5 \cdot 10^{-5}$ M) with $MV(PF_6)_2$ (50 mM) in dry, de-oxygenated MeCN. Spectrum recorded after the first laser pulse (excitation at 532 nm, duration 10 ns) with a delay of 200 ns and an integration time of 200 ns. (b) Transient absorption spectrum of the donor triad ($2.5 \cdot 10^{-5}$ M) with $MV(PF_6)_2$ (50 mM) in dry, de-oxygenated MeCN. Spectrum recorded after the second laser pulse (second excitation at 460 nm, delay of second laser 500 ns, pulse duration 10 ns) with a delay of 100 ns after the second laser pulse and an integration time of 200 ns. Spectrum was scaled at 395 nm to match the intensity of the spectrum after the first pulse. (c) Difference spectrum generated by subtracting the transient spectrum after the first pulse (a) from the transient spectrum after the second pulse (b).

In the two-pulse experiment presented in Figure 5.27, the transient absorption spectra recorded after the first pulse (a) and after the second pulse (b) can be seen. Both spectra are scaled to the same intensity at 395 nm in analogy to the single-pulse experiment. The original absorption at 395 nm in spectrum (b) was approx. 1.5 times higher than in spectrum (a). Both spectra before and after the second laser pulse exhibit the same spectral features and look nearly identical. Subtraction of the spectrum after the first pulse (a) from the spectrum after the second pulse (b) results in spectrum (c). Spectrum (c) is very low in intensity and essentially shows a noisy baseline. A weak absorption band between 500 and 650 nm as well as a weak bleach at 430 nm can still be detected, both being characteristic features of $exTTF^{+}$.

Around 490 nm however, no absorption band of $exTTF^{2+}$ is visible, indicating that the two-pulse experiment did not lead to the formation of the $exTTF^{2+}$ dication. Instead, the second laser pulse led to increased formation of the singly charge-separated state $exTTF^{+}$-PTZ-Ru^{2+} // MV^{+} as revealed by the much stronger absorption intensity measured after the second laser pulse. It therefore seems that the energy of the first laser pulse was not sufficient to excite all the triad molecules in the detection window. The second laser pulse then excited mostly the donor triad in its ground state leading to more photoproduct of the singly charge-separated state instead of the doubly oxidized exTTF moiety. Thus, the two-pulse experiment does not show any difference in formed photoproducts compared to the single-pulse experiment.

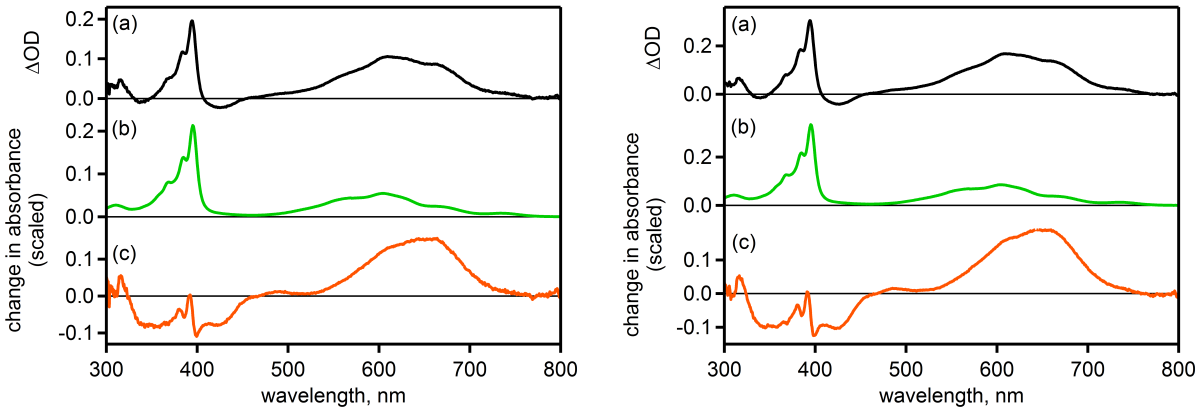

Figure 5.28: ***Left:*** (a) Transient absorption spectrum of the donor triad ($2.5 \cdot 10^{-5}$ M) with $MV(PF_6)_2$ (50 mM) in dry, de-oxygenated MeCN. Spectrum recorded after the first laser pulse (excitation at 532 nm, duration 10 ns) with a delay of 200 ns and an integration time of 200 ns. (b) Difference spectrum of MV^+ obtained via spectro-electrochemistry (from Figure 5.21) and scaled at 395 nm to match the signal intensity of the transient spectrum. (c) Difference spectrum generated by subtracting the MV^+ difference spectrum (b) from the transient absorption spectrum (a). ***Right:*** (a) Transient absorption spectrum of the donor triad ($2.5 \cdot 10^{-5}$ M) with $MV(PF_6)_2$ (50 mM) in dry, de-oxygenated MeCN. Spectrum recorded after the second laser pulse (first excitation at 532 nm, second excitation at 460 nm, delay of second laser pulse 500 ns) with a delay of 100 ns after the second laser pulse and an integration time of 200 ns. (b) Difference spectrum of MV^+ obtained via spectro-electrochemistry (from Figure 5.21) and scaled at 395 nm to match the signal intensity of the transient spectrum. (c) Difference spectrum generated by subtracting the MV^+ difference spectrum (b) from the transient absorption spectrum (a).

Going back to the transient absorption spectra measured after the first (Figure 5.28a left) and after the second pulse (Figure 5.28a right) and subtracting the MV^+ spectral features, both spectra feature the spectral characteristics of $exTTF^+$: a broad absorption band at 660 nm and a less pronounced bleach at 425 nm. The finger-like absorption band between 370 and 395 nm seems to be caused by the subtraction process and therefore is considered an artefact. However, in both spectra, a small band at 490 nm is present, this being in accordance with the observations made in the single-pulse experiment. The intensity at 490 nm hereby correlates with the intensity of the general absorption signal and is identical if both spectra are scaled to the same MV^+ intensity. It therefore remains unclear if the band observed at 490 nm indeed originates from doubly oxidized exTTF or if this rather small band is an artefact of the oxidized MV^+ species that could not be captured by the MV^+ difference spectrum generated via spectro-electrochemical methods.

Further experiments

Due to the uncertainties in regard to the absorption band at 490 nm observed in the experiments with methyl viologen, another electron acceptor was considered. Bis(tetrabutylammonium) peroxydisulfate ($(TBA)_2S_2O_8$) was chosen because of it being a sacrificial electron acceptor that upon reduction does not induce spectral changes in the visible range.[155–157] As a result of the tetrabutylammonium counterion, $(TBA)_2S_2O_8$ is soluble in neat MeCN and no solvent mixtures needed to be used. However, peroxydisulfate thermally reacted with the donor triad nearly instantly even without photoexcitation. In the UV-Vis spectrum, a strong decrease in the ground-state absorption could be monitored, yet no indication of a doubly oxidized exTTF could be observed. With peroxydisulfate decomposing the donor triad, no further measurements based on the acceptor $(TBA)_2S_2O_8$ were conducted.

Another, steady-state-like excitation experiment was performed with the donor triad and methyl viologen. A cw-laser at 447 nm with a power of 1 W was used to excite the photosensitizer, and UV-Vis absorption spectra were measured after defined time intervals (seconds to minutes). Surprisingly, the characteristic spectrum of the long-lived MV^+ radical was not observable. Instead, weak spectral changes were forming that could neither be attributed to an oxidized moiety ($exTTF^{2+/+}$, PTZ^+, $[Ru(bpy)_3]^{3+}$) nor to reduced methyl viologen ($MV^{+/0}$). It might be possible that the exTTF ground state absorption band is sufficiently excited at 447 nm and consequent decomposition of the donor triad occurs.

Summary

In the previous sections, the donor triad was examined. Oxidation potentials and spectral changes upon chemical oxidation do not differ from the reference molecules examined in the previous subchapter. Upon excitation, the donor triad forms a charge-separated state comprised of oxidized PTZ and reduced $[Ru(bpy)_3]^{2+}$ within 10 ns. This primary charge-separated state has a very short lifetime of 12.7 ns and transforms rapidly into the secondary charge-separated state $exTTF^+$-PTZ-Ru^+. Its lifetime (377 ns) is much longer and its spectrum can be recorded via transient absorption spectroscopy. Addition of the external electron acceptor methyl viologen led to a spectrum of the $exTTF^+$ monocation with hints of the $exTTF^{2+}$ dication being formed in minor amounts. Two-pulse experiments however did not lead to an increased formation of $exTTF^{2+}$.

Even as there is no solid evidence for the $exTTF^{2+}$ dication to form in the experiments performed, it must be noted that the general concept of the intermediate electron donor quenching the $[Ru(bpy)_3]^{2+}$ excited state and the subsequent hole transfer from PTZ

to exTTF functions as presumed. The addition of such a redox-relay herein is a very promising concept as it allows for very efficient electron transfer over long distances. The long distance hereby has the advantage of retarding charge-recombination, therefore enabling longer lifetimes of the charge-separated or -accumulated states, in analogy to nature's photosystem II.

5.2 The Acceptor Triad: TCAQ-FMN-Ru

For the acceptor triad, the same basic principle as in the donor triad applies. The two-electron acceptor 11,11,12,12-tetracyano-9,10-anthraquinodimethane (TCAQ) was chosen due to its inverted reduction potentials. The intermediate electron acceptor, fluoren-9-ylidene malononitrile (FMN) was selected due to its ability to oxidatively quench the excited state of the $[Ru(bpy)_3]^{2+}$ photosensitizer. At the same time, its reduction potential is more negative than that of TCAQ, allowing the electron to move on to the TCAQ moiety, re-oxidizing FMN to its neutral state. The negative charge generated on TCAQ is then quite unlikely to reductively quench the re-excited $[Ru(bpy)_3]^{2+}$ photosensitizer due to the fact that the FMN intermediate acceptor back in its ground state acts as a good electron acceptor while the long distance between TCAQ and photosensitizer additionally retards back-electron transfer.

The synthetic route pursued to obtain the acceptor triad is shown in Scheme 5.5. Experimental details are given in the experimental section 7.6.

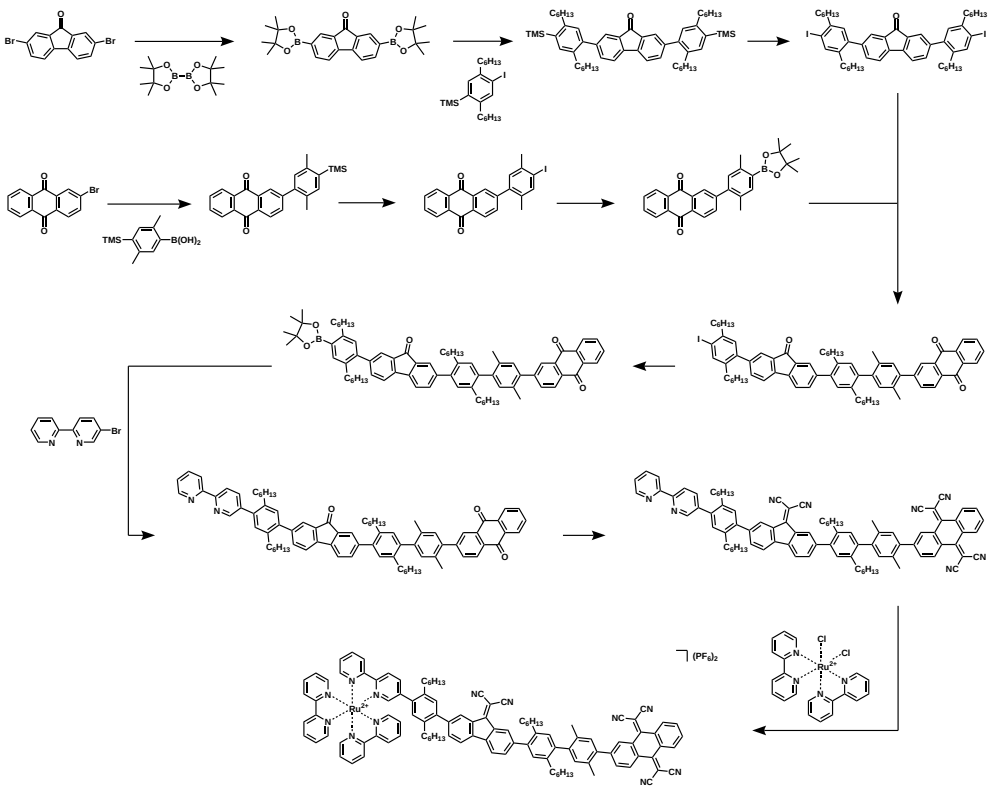

Scheme 5.5: Synthetic route pursued to obtain the acceptor triad.

5.2.1 TCAQ, FMN and TCAQ-FMN-TCAQ Reference Molecules

To analyze the acceptor moieties in their isolated and covalently linked forms, three reference molecules were used: TCAQ (referenced as Ref-TCAQ to differentiate it from a TCAQ moiety in a molecular system), I-hxy-FMN-hxy-I (Ref-FMN) and TCAQ-xy-hxy-FMN-hxy-xy-TCAQ (Ref-TCAQ-FMN). While Ref-TCAQ and Ref-FMN show the characteristics of the single moieties, Ref-TCAQ-FMN can show potential changes in absorbance or in reduction potential arising from the covalent linkage of the acceptor moieties.

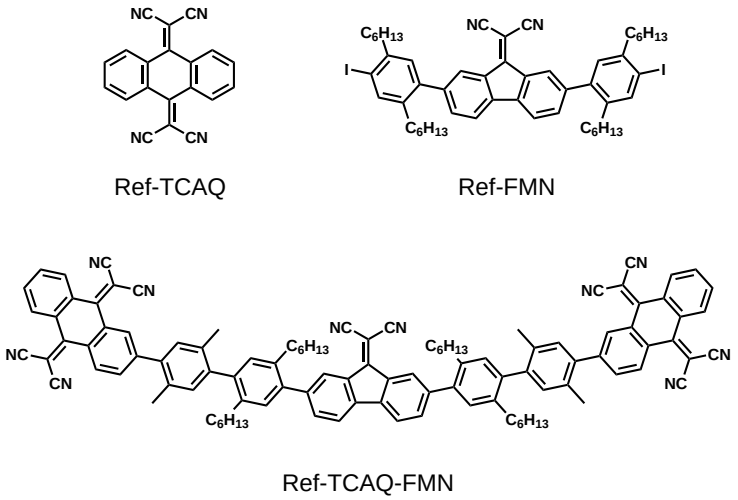

Figure 5.29: Schematic representation of the reference molecules used for analyzing the electron acceptor moieties.

Optical Absorption Spectroscopy

UV-Vis absorption spectra of the three reference molecules were measured to examine their ground state absorption.

Ref-TCAQ

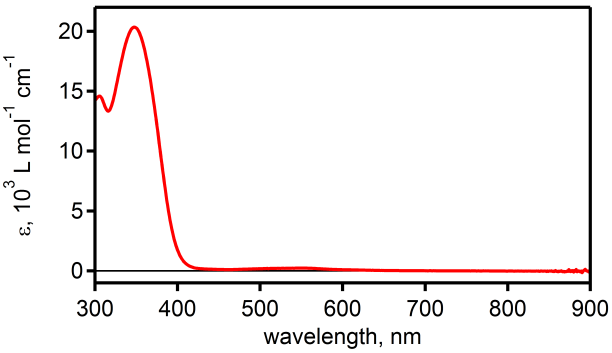

Figure 5.30: UV-Vis absorption spectrum of Ref-TCAQ in dry, de-oxygenated DMF.

The UV-Vis absorption spectrum of Ref-TCAQ in Figure 5.30 exhibits an intense absorption band at 348 nm (ε = 20'300 L mol^{-1} cm^{-1}) and a second, less intense absorption band at 305 nm (ε = 14'600 L mol^{-1} cm^{-1}), both in accordance with literature reports.[22, 129, 158]

Ref-FMN

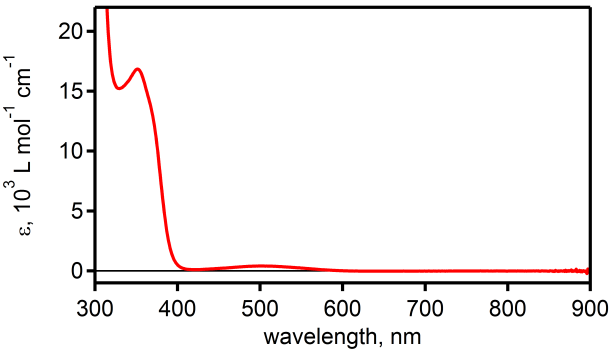

Figure 5.31: UV-Vis absorption spectrum of Ref-FMN in dry, de-oxygenated DMF.

Figure 5.31 shows the UV-Vis absorption spectrum of Ref-FMN. It features an absorption band at 352 nm (ε = 16'800 L mol^{-1} cm^{-1}) and a weak broad absorption centered at 500 nm (ε = 400 L mol^{-1} cm^{-1}). The absorption spectrum resembles the ones reported in the literature.[138, 159, 160]

Ref-TCAQ-FMN

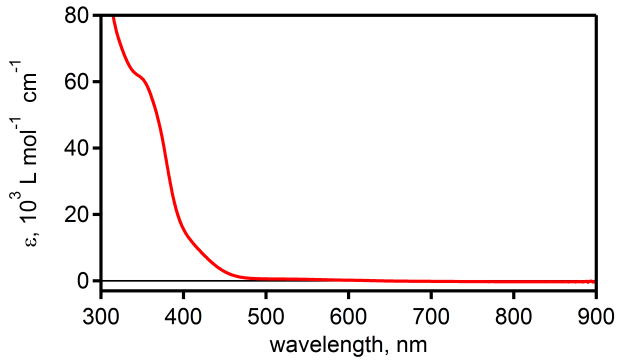

Figure 5.32: UV-Vis absorption spectrum of Ref-TCAQ-FMN in dry, de-oxygenated DMF.

The UV-Vis absorption spectrum of Ref-TCAQ-FMN in Figure 5.32 does not show any distinct absorption bands. Instead, absorption starts at 500 nm and increases towards shorter wavelengths. At 350 nm, a shoulder is present caused by an overlap of the absorption bands of TCAQ at 348 nm and FMN at 352 nm. Below 340 nm, the absorption increases strongly. Overall, the spectrum of Ref-TCAQ-FMN can be considered as a result of the superimposition of TCAQ and FMN spectral features.

Electrochemistry

Cyclic voltammetric measurements were performed to confirm the reduction potentials for TCAQ and FMN found in the literature. For TCAQ, additional experiments were executed to investigate the potential inversion behavior of the two-electron acceptor. All measurements were performed in dry, Ar-purged DMF with 0.1 M tetra-n-butylammonium hexafluorophosphate ($TBAPF_6$) as supporting electrolyte. For all measurements, a saturated calomel electrode (SCE) was used as the reference electrode and a glassy carbon electrode (GCE) as the working electrode.

Ref-TCAQ

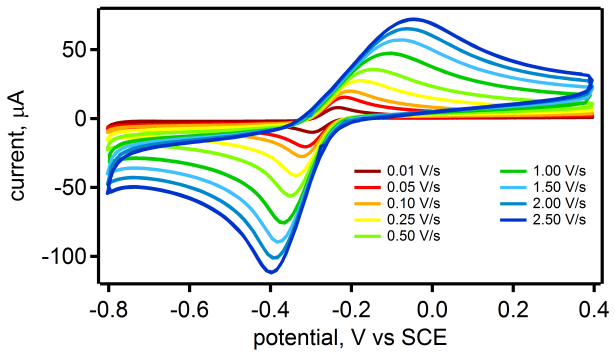

Figure 5.33: Cyclic voltammograms of Ref-TCAQ (1 mM) in dry, Ar-purged DMF. Different scan rates as given in the inset, supporting electrolyte 0.1 M $TBAPF_6$.

The cyclic voltammogram of Ref-TCAQ can be seen in Figure 5.33. Even though TCAQ is a two-electron acceptor, just one wave for the reduction and for the corresponding re-oxidation to the neutral species is observed. This is due to the potential inversion behavior of TCAQ, where the first reduction is energetically more difficult than the second reduction. As a result, the second electron reduction directly follows the first electron reduction and a single reduction wave comprised of two electrons results.

Measuring the CV at different scan rates show the peak potentials of cathodic and subsequent anodic scans to vary. Increasing the scan rate, the separation between reduction and re-oxidation potential gets larger. Upon reduction, peak potential and peak current become more negative, upon re-oxidation, peak potential and peak current become more positive with increasing scan rate. It is the same behavior as seen for the exTTF moiety in Figure 5.7. As with exTTF, a linear correlation of the peak current with the square root of the scan rate can be observed which shows that the electrode reaction is diffusion controlled, the analyte remains homogeneous during the experiment and that the investigated system is electrochemically reversible.[143, 144]

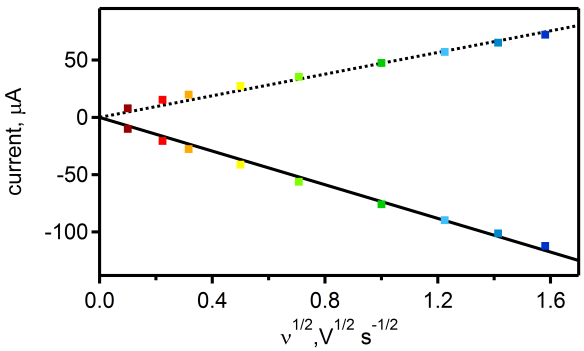

Figure 5.34: Linear correlation of the peak current with the square root of the different scan rates applied. Colors match the scan rates given in Figure 5.33. Dotted line for oxidative sweep, solid line for reductive sweep.

The potential inversion in TCAQ can be attributed to an effect very similar to the exTTF donor in the previous section: TCAQ in its neutral state has a boat-like structure in the anthracene moiety. Upon reduction, the first electron is located on one of the malononitrile moieties whereas the anthracene moiety keeps the boat-like structure. When the second electron is added, TCAQ undergoes a structural change. The anthracene moiety becomes planar and the malononitrile groups rotate out of plane. The second electron is then located on the second malononitrile group, which makes the two electrons spatially separated from each other and explains why the first and second reduction occur at the same potential.[128, 131, 161, 162]

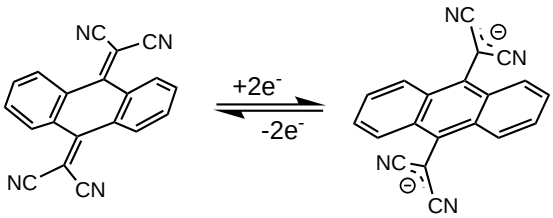

Figure 5.35: Structural change accompanying the two-electron reduction process in TCAQ. The central anthracene unit switches from a boat-like structure to planar. Exterior malononitrile groups rotate out of plane.

Due to the geometrical change, the re-oxidation potential of $TCAQ^{2-}$ is shifted considerably compared to its reduction potential. As in the case of exTTF, the measured reduction potential is assigned to the first electron reduction in the molecule whereas the potential for the second reduction is given by the re-oxidation potential. With the peak potentials shifting with the scan rate, average potentials for reduction and re-oxidation are constructed. For each of the nine scan rate minima, the FWHM potentials are determined, added up and subsequently divided by 9 to give the average reduction potential. The same

procedure applies for the maxima of the re-oxidation waves.Therefore, the first and second reduction potentials are proposed to be $E_{red,1}$ = -0.29 V and $E_{red,2}$ = -0.24 V vs. SCE in the following sections. Remarkable here is that the first and second reduction potential differ by only 0.05 V whereas the gap between the first and second oxidation potential of exTTF amounts for 0.33 V. The potential inversion behavior of TCAQ therefore seems to be less pronounced than for exTTF.

Ref-FMN

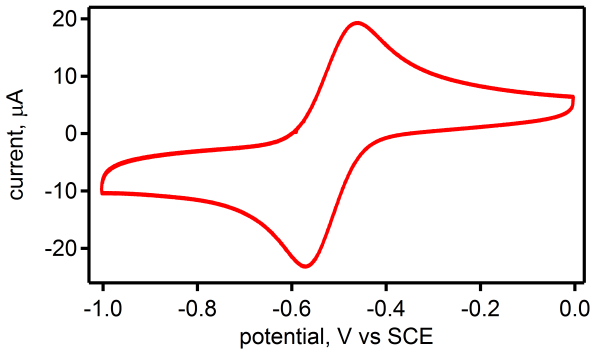

Figure 5.36: Cyclic voltammogram of Ref-FMN (1 mM) in dry, Ar-purged DMF. Scan rate 0.5 V/s, supporting electrolyte 0.1 M $TBAPF_6$.

The cyclic voltammogram of Ref-FMN in Figure 5.36 shows the reduction of the FMN moiety and the subsequent re-oxidation at a potential of $E_{1/2}$ = -0.51 V vs. SCE. The value only slightly differs from the potential reported in the literature.[137, 138, 160] As with TCAQ, FMN is stable upon several reduction and re-oxidation cycles making FMN a reversible electron acceptor. With the oxidation potential of excited $[Ru(bpy)_3]^{2+}$ being $E^{III/*II}$ = -0.81 V vs. SCE,[77] there is enough driving force for the first and the second electron to move from photoexcited $[Ru(bpy)_3]^{2+}$ via FMN to the terminal TCAQ acceptor moiety.

Ref-TCAQ-FMN

In the acceptor triad, the two acceptor moieties and the photosensitizer are connected via *p*-xylene (xy) or 1,4-dihexylbenzene (hxy) linkers. Due to the possible conjugation in the molecule, the reduction potentials of the acceptors might shift. Therefore, a byproduct from the ligand synthesis was used for further investigation.

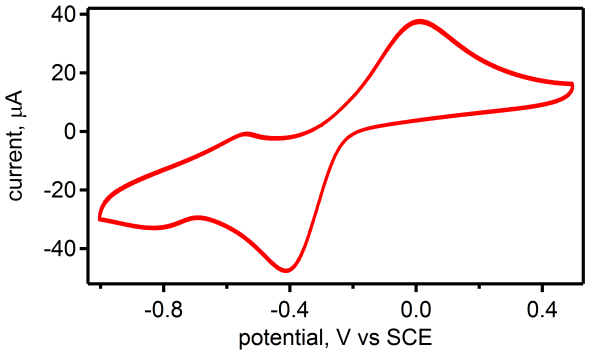

Figure 5.37: Cyclic voltammogram of Ref-TCAQ-FMN (1 mM) in dry, Ar-purged DMF. Scan rate 0.5 V/s, supporting electrolyte 0.1 M $TBAPF_6$.

In the cyclic voltammogram of Ref-TCAQ-FMN shown in Figure 5.37, the reduction of TCAQ can be seen followed by the reduction of FMN. Again, the reduction wave of TCAQ and its re-oxidation wave vary significantly. Under the same measurement conditions as with the individual moieties, the reduction potentials of TCAQ are given with $E_{red,1}$ = -0.31 V vs. SCE and $E_{red,2}$ = -0.15 V vs. SCE at a scan rate of 0.5 V/s. For FMN, the reduction potential E_{red} = -0.68 V vs. SCE is nearly 0.2 V more negative than in the isolated FMN component. This might be partly due to the electron-withdrawing iodine substituents in the FMN reference molecule, but at the same time, the difference between reduction wave minimum and re-oxidation wave maximum is $\Delta E = 0.28$ V in this case versus $\Delta E = 0.11$ V in Ref-FMN at the same scan rate. Therefore, the linkage of the different moieties seems to affect the reduction potential of FMN more than expected. However, the FWHM potential of the FMN reduction wave E_{red} = -0.76 V vs. SCE still lies between the oxidation potential of excited $[Ru(bpy)_3]^{2+}$ at $E^{III/*II}$ = -0.81 V vs. SCE[77] and the reduction potential of Ref-TCAQ at $E_{red,1}$ = -0.29 V and $E_{red,2}$ = -0.24 V vs. SCE which allows the postulated electron transfer cascade from $^*[Ru(bpy)_3]^{2+}$ via FMN to TCAQ to take place.

Spectro-Electrochemistry

Ref-TCAQ

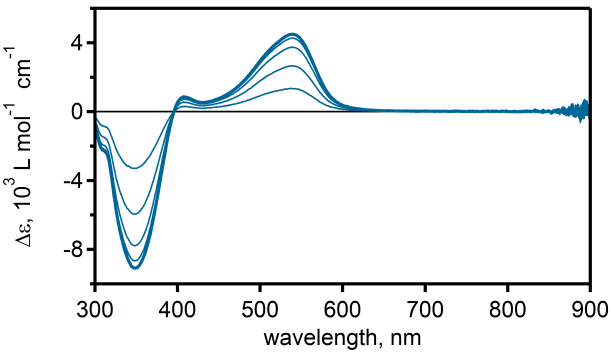

Figure 5.38: Difference spectrum of Ref-TCAQ ($1 \cdot 10^{-4}$ M) with 0.1 M $TBAPF_6$ as supporting electrolyte in dry, de-oxygenated DMF. Reduction was performed at -0.5 V vs. SCE.

Upon spectro-electrochemical reduction of Ref-TCAQ, a band centered at 540 nm is formed, accompanied by a minor band at 408 nm. During reduction, the ground state absorption at 348 nm bleaches in the difference spectrum. Due to potential inversion and the second electron being more easily accepted by the TCAQ moiety than the first, only the doubly reduced species can be detected. Therefore, the spectral changes observed here are in good accordance with literature reports for the doubly reduced TCAQ moiety.[22, 133]

To measure the spectral signature of one-electron reduced TCAQ, transient absorption spectroscopy was performed. The conducted measurements are presented in Figure 5.41.

Ref-FMN

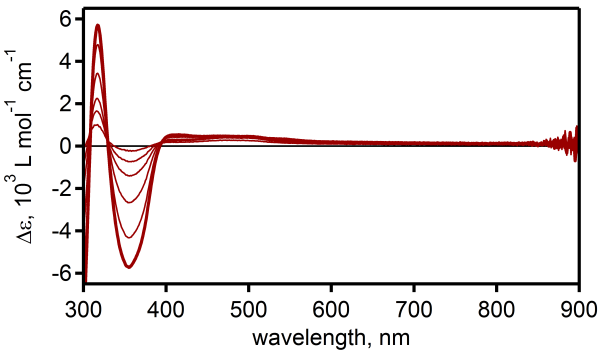

Figure 5.39: Difference spectrum of Ref-FMN ($1 \cdot 10^{-4}$ M) with 0.1 M $TBAPF_6$ as supporting electrolyte in dry, de-oxygenated DMF. Reduction was performed at -0.7 V vs. SCE.

During the spectro-electrochemical reduction of Ref-FMN, a broad weak absorption band between 400 and 550 nm forms. At 355 nm, the ground state absorption bleaches. Therefore, the formation of FMN^{-} can only be properly detected by the bleach at 355 nm. With FMN only being the intermediate electron acceptor, however, no overlay is expected with the spectral changes occurring due to the oxidation or reduction of the other moieties present in the triad.

Ref-TCAQ-FMN

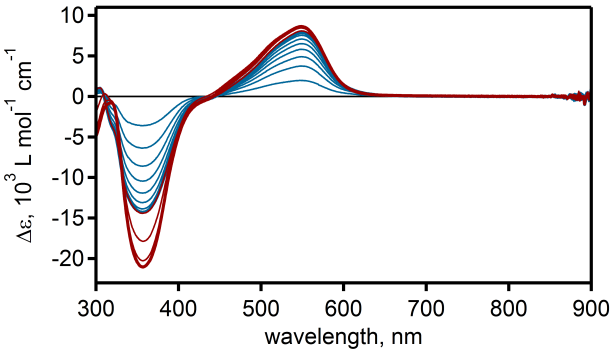

Figure 5.40: Difference spectrum of Ref-TCAQ-FMN ($1 \cdot 10^{-4}$ M) with 0.1 M $TBAPF_6$ as supporting electrolyte in dry, de-oxygenated DMF. Reduction was performed at -0.5 V vs. SCE (blue traces) followed by -0.8 V vs. SCE (red traces).

Upon spectro-electrochemical reduction of Ref-TCAQ-FMN, the TCAQ moiety is reduced first. This leads to the formation of an absorption band at 550 nm and a bleach at 357 nm, both spectral features being in line with the formation of $TCAQ^{2-}$ as shown in the spectro-electrochemical experiments for Ref-TCAQ. As with Ref-TCAQ, the formation of $TCAQ^{-}$ cannot be detected by the experimental setup used here. When changing the applied potential to -0.8 V vs. SCE, the FMN moiety is reduced as well. This can be seen in a weak broad band forming between 400 and 550 nm and in an intensified bleach at 357 nm. Both spectral changes are in accordance with the behavior of the isolated FMN reference explored in the previous section.

Transient Absorption Spectroscopy

Ref-TCAQ and $[Ru(bpy)_3]^{2+}$

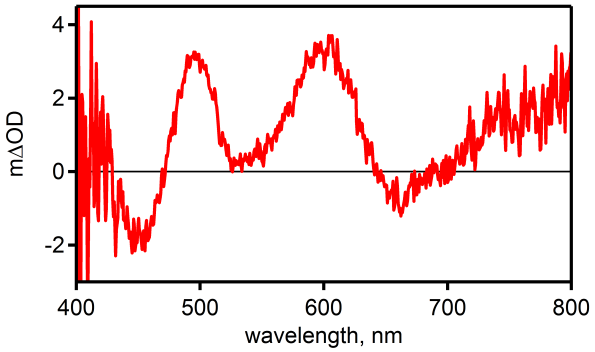

Figure 5.41: Transient absorption spectrum of Ref-TCAQ (10 mM) with $[Ru(bpy)_3](PF_6)_2$ ($1 \cdot 10^{-5}$ M) as photosensitizer in dry, de-oxygenated DMSO. Spectrum was recorded with a delay of 20 ns after excitation at 532 nm and an integration time of 200 ns. Laser pulse duration 10 ns.

The transient absorption spectrum of Ref-TCAQ with $[Ru(bpy)_3]^{2+}$ as photosensitizer is shown in Figure 5.41. Due to the high concentration of Ref-TCAQ and the hence increased absorption, spectral changes could just be observed in the spectral window ranging from 400 to 800 nm.

When excited, $[Ru(bpy)_3]^{2+}$ is a good electron donor and a good electron acceptor.[150, 163] In the experimental setup here, photoexcited $[Ru(bpy)_3]^{2+}$ can donate an electron to the acceptor Ref-TCAQ yielding the photoproducts $[Ru(bpy)_3]^{3+}$ and Ref-TCAQ^{-}. The transient absorption spectrum therefore should exhibit the spectral features of $[Ru(bpy)_3]^{3+}$ and TCAQ^{-}.

The transient spectrum in Figure 5.41 exhibits two absorption bands with their maxima located at 495 and 600 nm. According to the literature, the 600 nm band is characteristic for the singly reduced TCAQ moiety.[23] Oxidized $[Ru(bpy)_3]^{2+}$ however does not exhibit any intense absorption bands in the observed spectral range but shows a bleach of the ground state absorption at 450 nm.[151] ^{3}MLCT absorption of $[Ru(bpy)_3]^{2+}$ should not be present any more due to the delay of 20 ns before the spectrum was recorded, however, the $[Ru(bpy)_3]^{2+}$ ^{3}MLCT state does not exhibit an absorption band around 500 nm, either.[164] The observed absorption band at 495 nm therefore probably results from an excited triplet state of TCAQ formed by energy transfer from photoexcited $[Ru(bpy)_3]^{2+}$. Unfortunately, no reports of the energy or the spectral features of the TCAQ excited triplet state could be found in the literature.

In addition, two bleaches can be observed at 450 and 660 nm. While the first bleach is

caused by the decreasing MLCT absorption band of $[Ru(bpy)_3]^{2+}$ following the oxidation of the photosensitizer, the latter originates from luminescence of excited $[Ru(bpy)_3]^{2+}$ not being quenched by TCAQ.[77]

Ref-TCAQ and $[Os(bpy)_3]^{2+}$

To verify the hypothesis of energy transfer from photoexcited $[Ru(bpy)_3]^{2+}$ to TCAQ, a second transient absorption experiment was designed with $[Os(bpy)_3]^{2+}$ replacing the $[Ru(bpy)_3]^{2+}$ photosensitizer in the experiment above. $[Os(bpy)_3]^{2+}$ in its excited state is a slightly better reductant than $[Ru(bpy)_3]^{2+}$,[165] but its triplet energy of 1.7 eV is notably lower than the triplet energy of $[Ru(bpy)_3]^{2+}$ (2.1 eV).[165–167]

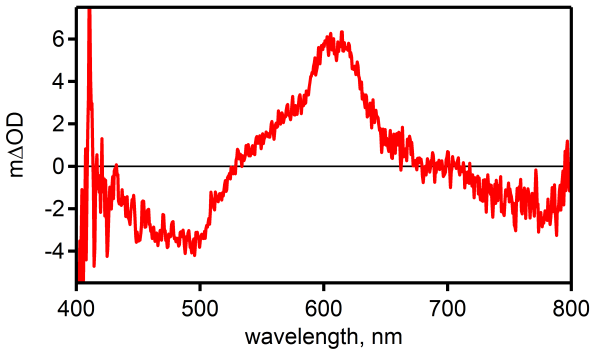

Figure 5.42: Transient absorption spectrum of Ref-TCAQ (10 mM) with $[Os(bpy)_3](PF_6)_2$ ($1{\cdot}10^{-5}$ M) as photosensitizer in dry, de-oxygenated DMSO. Spectrum was recorded with a delay of 20 ns after excitation at 532 nm and an integration time of 200 ns. Laser pulse duration 10 ns.

The transient absorption spectrum of Ref-TCAQ with $[Os(bpy)_3]^{2+}$ is shown in Figure 5.42. In analogy to the experiment with $[Ru(bpy)_3]^{2+}$, the transient spectrum of this experiment should exhibit the spectral features of $[Os(bpy)_3]^{3+}$ and $TCAQ^{-}$.

In the transient spectrum obtained, a single absorption band around 610 nm can be observed which can be assigned to the $TCAQ^{-}$ anion.[23] Additionally, two bleaches can be observed that can be attributed to the bleach of the $[Os(bpy)_3]^{2+}$ ground state absorption (480 nm) and a bleach caused by partial luminescence of unquenched $^{*}[Os(bpy)_3]^{2+}$ (around 750 nm).[166, 168]

In contrast to the experiment with $[Ru(bpy)_3]^{2+}$, however, no absorption band around 495 nm is visible in the spectrum. This indicates that the absorption band at 495 nm indeed originates from an energy transfer of photoexcited $[Ru(bpy)_3]^{2+}$ to TCAQ, implying that the energy of the TCAQ triplet state must be between 1.7 and 2.1 eV.

Summary

As shown with the previous experiments it is feasible to differentiate the reduced states of TCAQ in the visible spectral range. Due to TCAQ being a two-electron acceptor with potential inversion, the second electron-transfer step is energetically more favorable than the first. This should facilitate electron-accumulation on the acceptor moiety. During the above shown studies, TCAQ proved to be stable under the measurement conditions applied. For the intermediate acceptor, FMN proved to be a suitable choice. Even with the reduction potential differing between Ref-FMN and Ref-TCAQ-FMN, the intermediate acceptor is still able to fulfill its purpose as a primary electron acceptor and subsequently can transfer the accepted electron to the terminal acceptor TCAQ. As with the donor triad, the increased distance between photosensitizer and terminal electron acceptor potentially retards back-electron transfer and therefore increases the lifetime of the charge-separated or -accumulated state. A potential problem on the acceptor part could be the low-lying triplet state of TCAQ which could cause significant parts of the excitation energy to be 'wasted' in unproductive energy-transfer instead of productive electron-transfer reactions.

5.2.2 TCAQ-FMN-Ru Triad

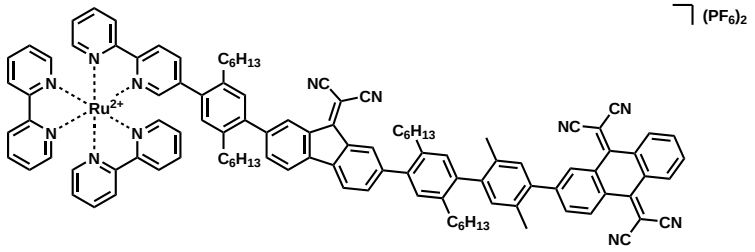

Figure 5.43: Schematic representation of the TCAQ-FMN-Ru acceptor triad.

The synthesis of the acceptor triad TCAQ-FMN-Ru shown in Figure 5.43 proved to be more complicated than expected. While the formation of the acceptor moieties TCAQ and FMN from their precursors 9,10-anthraquinone (AQ) and 9-fluorenone (FO) was conducted following the literature procedure with Lehnert's reagent[169, 170] without major difficulties, the lability of the acceptor moieties under C-C-coupling conditions did cause some trouble. Unfortunately, the malononitrile groups at the final acceptors are prone to substitution and therefore tend to be substituted by oxygen (and yielding back the original AQ or FO reactants) or easily undergo single or multiple cross couplings located at the cyano groups. Therefore, a mixture of products was obtained from e.g. Suzuki couplings that could not be used for further reactions. Consequently, the malononitrile groups needed to be attached to the acceptor moiety in the last step after all the C-C-couplings were done. This approach succeeded, and the designed ligand was obtained.

The next complications arose from the complexation procedure. Unlike the other complexes synthesized in this work, complexation in a mixture of $CHCl_3$ and EtOH (1:3) heated at reflux did not give the final product but led to degradation of the ligand. Upon pre-treatment of the $[Ru(bpy)_2Cl_2]$ precursor with excess AgOTf in dry DMF under exclusion of light and under stirring at room temperature for two days, some of the ligand could be complexed to the desired product, but most of the ligand still degradated. This did not just complicate the complex purification process, it also resulted in a yield of only 10%. NMR and ESI-HRMS measurements indicate that the complex was indeed obtained, but the total amount of acceptor triad obtained by this procedure was not enough to perform the planned measurements. Additionally, NMR data suggests that further purification of the obtained complex is still necessary. Therefore, no studies on the acceptor triad can be presented herein.

Summary and Outlook

The electron acceptors TCAQ and FMN show the features underlying the triad and pentad concept outlined at the beginning of this chapter. In the experiments with the reference molecules it could be shown that the different reduced states of the acceptors are clearly distinguishable in their UV-Vis spectra and that the reduction potentials correspond to their estimations. A potential pitfall in the designed system hereby might be the low-lying triplet state of the TCAQ moiety.

Unfortunately, the acceptor triad could not be successfully synthesized within the time-frame of the project. The ligand could be obtained but was not stable under complexation conditions. It therefore is essential to either further optimize the complexation conditions or to find another reaction path leading to the acceptor triad in satisfying yields. One approach could be to complex the pre-ligand and then attach the malononitrile groups in a last step to form the final acceptor moieties on the complex. If the complex will tolerate the conditions required to attach the malononitrile groups, this would represent a practical way to synthesize the acceptor triad.

Another option lies in replacing the electron acceptors TCAQ and FMN with other electron acceptors bearing the same potential inversion behavior as TCAQ and the same intermediate acceptor quality as FMN. If suitable acceptors are found where the different reduced states are clearly differentiable in the UV-Vis spectral range and there is no energetically low-lying triplet state, then a total redesign of the acceptor triad is recommended.

5.3 The Donor-Acceptor Pentad: exTTF-PTZ-Ru-FMN-TCAQ (One-Ligand Approach)

While the electron donor part of the molecule is reasonably stable under the reaction conditions, the electron acceptor part proved to be more challenging than expected. As mentioned in the previous section, the malononitrile groups of FMN and TCAQ turned out to be labile under C-C-coupling conditions. This resulted either in the malononitrile groups being hydrolyzed and restoring the original carbonyl groups or random coupling to the cyano groups yielding a multitude of coupling products that were neither separable nor identifiable. Therefore, the transformation from anthraquinone or fluorenone to the final acceptors needed to take place after the C-C-couplings were conducted.

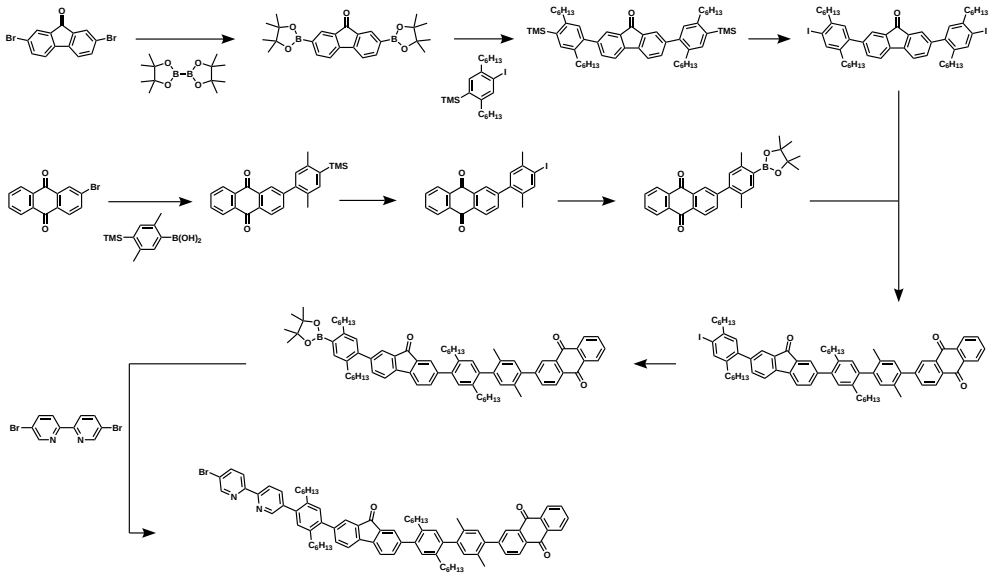

Scheme 5.6: Reaction scheme for synthesizing the pentad, part I. Scheme continued in Scheme 5.7.

The reactions were performed as shown in Schemes 5.6 and 5.7. The pre-ligand (without the malononitrile groups on the acceptors) was successfully obtained, but the conditions required to attach the malononitrile groups (malononitrile, $TiCl_4$, pyridine, heat) were not compatible with one of the donor moieties. At the end of this reaction step, a substance was obtained that was unidentifiable via NMR or ESI-MS and did not show any indication for the product or the reactant to still be present. With this finding it became clear that there is no easy way to have the donor and the acceptor moieties on the same ligand. Therefore, a two-ligand approach was addressed with the donor moieties being on one ligand and the acceptor moieties being on a second ligand. This approach is covered in the next section.

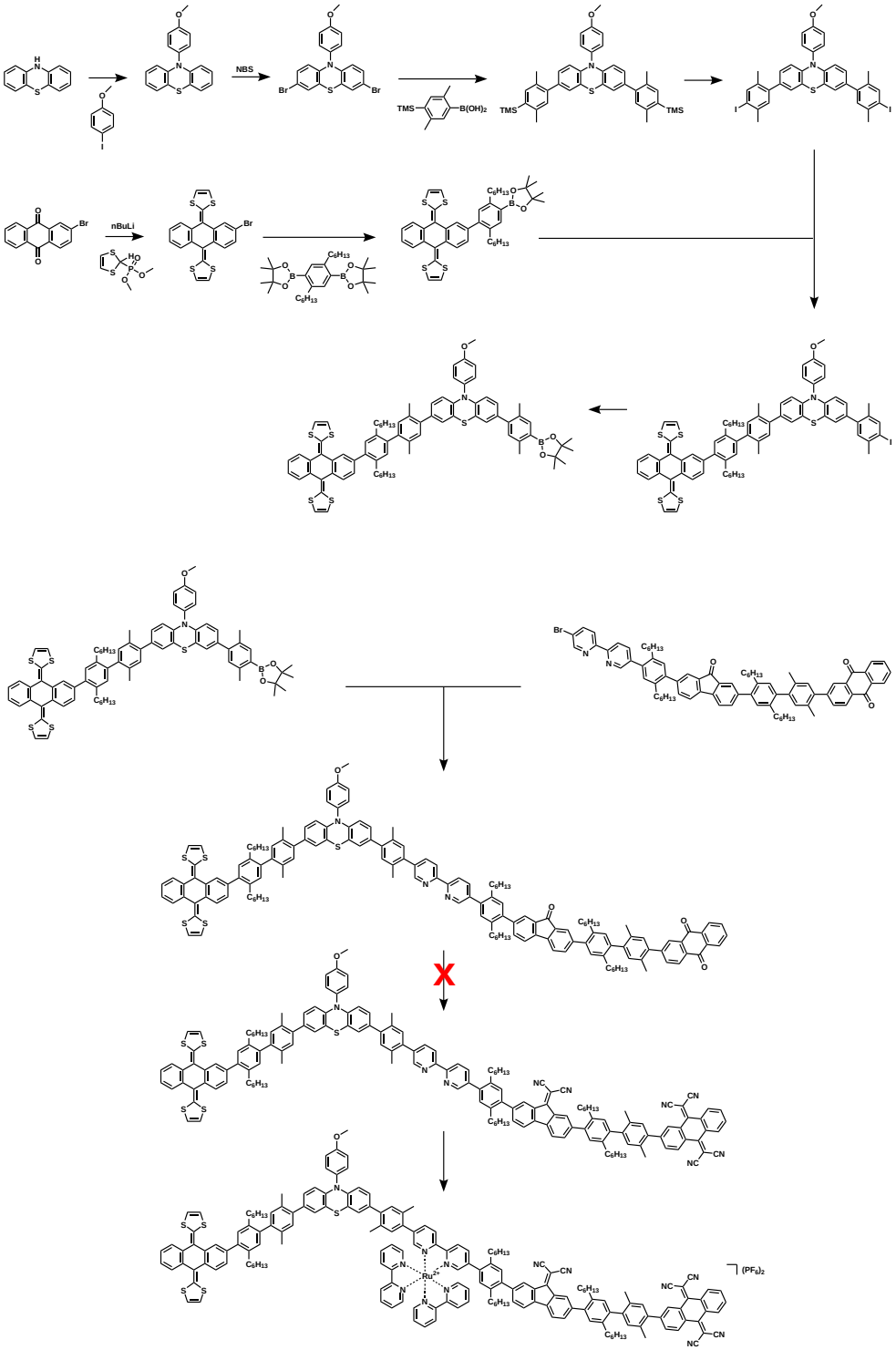

Scheme 5.7: Reaction scheme for synthesizing the pentad, part II. Red X at reaction step that did not succeed.

5.4 The Donor-Acceptor Pentad: exTTF-PTZ-Ru-FMN-TCAQ (Two-Ligand Approach)

As described in the previous subchapter, an approach where the donor moieties are located on one ligand and the acceptor moieties on a second was considered due to synthetic problems in attaching both donor and acceptor moieties on the same ligand.

Unfortunately, the two-ligand approach exhibits another problem that needs to be considered: being located on one ligand, the donor and acceptor moieties are separated by a defined distance and a defined angle from one another as a result of the covalent linkage. Having donor and acceptor parts separated on different ligands, the system in general gets more flexible and donor and acceptor arms can approach one another. Therefore, a Molecular Mechanics Force Field (MMFF) calculation was performed to estimate the energetically lowest structure of the two-ligand pentad. The resulting structure can be seen in Figure 5.44.

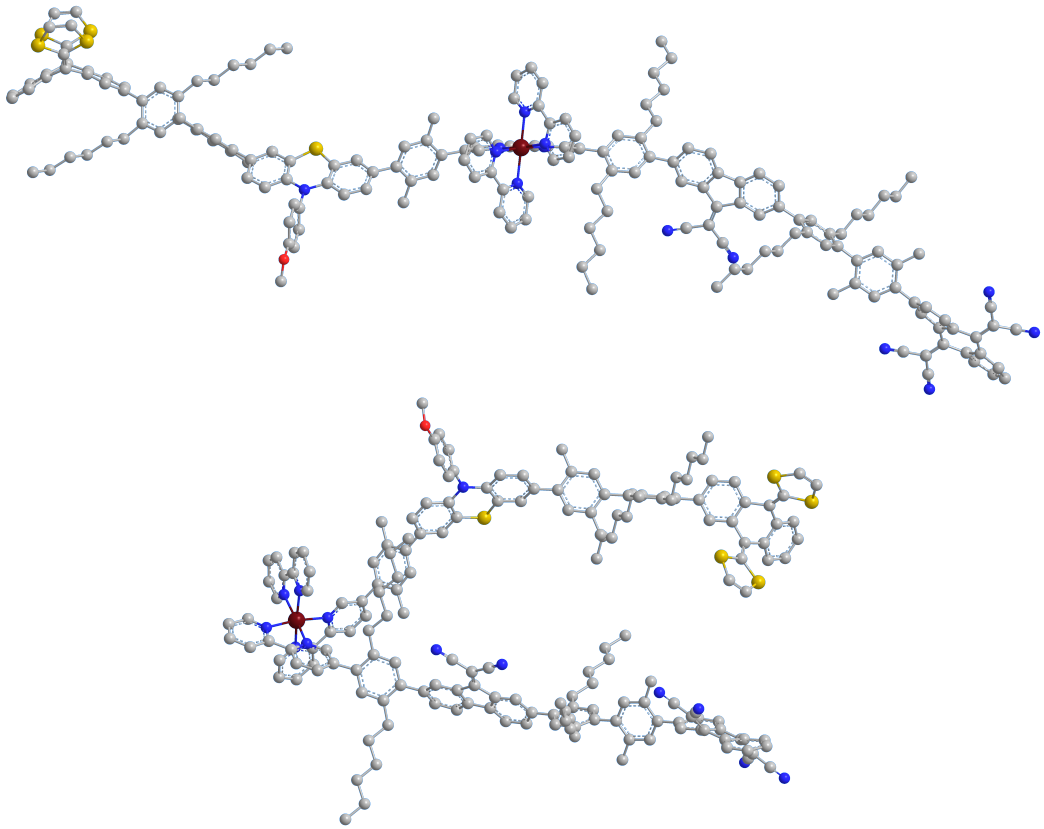

Figure 5.44: Estimated ground-state structures of the one-ligand (above) and two-ligand (below) pentads. Whereas there is a long distance between donor and acceptor in the one-ligand complex, donor and acceptor arms come quite close in the two-ligand approach.

As it can be seen in Figure 5.44, donor and acceptor moieties can come quite close in the two-ligand approach. Nevertheless, there still is, at least in the neutral state, a sufficiently large distance between the TCAQ and the exTTF moieties. Upon electron transfer, this distance might decrease due to coulombic attraction of the charged species. This attraction might be tunable depending on the polarity of the solvents used in the experimental setup.

As a consequence of the acceptable spatial separation predicted for the donor and acceptor moieties, the two-ligand approach for the pentad was pursued. To synthesize the two-ligand complex, the same ligands were used as in the donor triad and in the acceptor triad. Scheme 5.8 shows the synthetic route following a literature procedure[171] leading to the pentad with acceptor and donor moieties being located on different ligands.

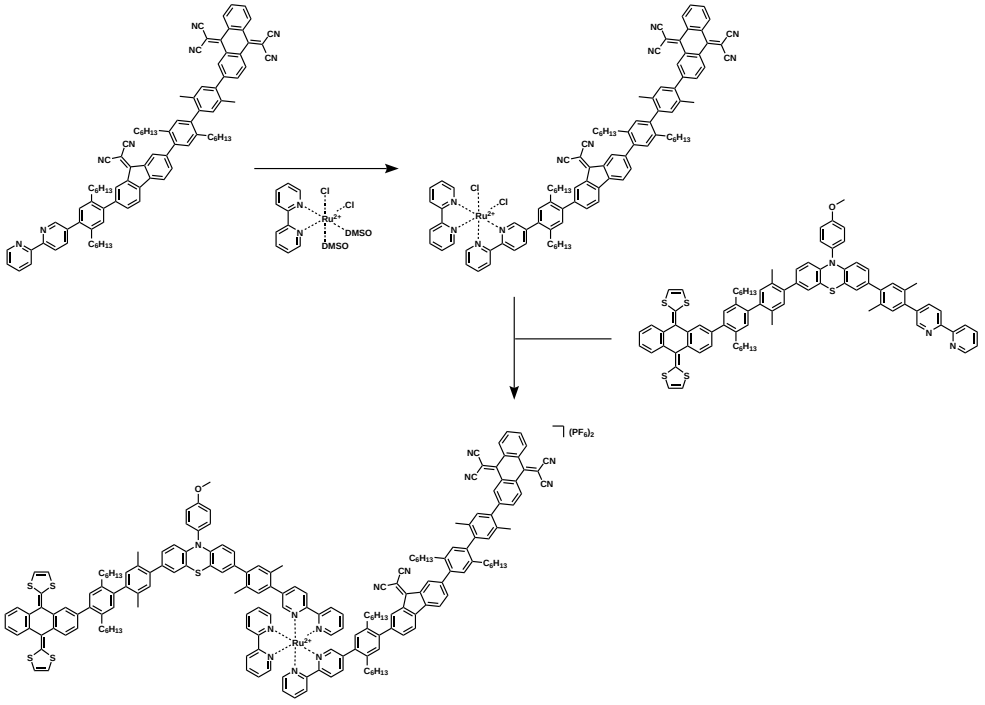

Scheme 5.8: Reaction scheme for the stepwise assembly of the ligands to form the final two-ligand pentad.

The synthetic route started with a ruthenium precursor where one equivalent of 2,2'-bipyridine was complexed. Then, one equivalent of acceptor ligand was complexed at room temperature in dry DMF. The resulting pre-complex could be isolated and characterized. In the last step, the donor ligand was attached under the standard complexation conditions (EtOH:$CHCl_3$ = 3:1, heating to 80 °C). This reaction did not work as expected: at first, no complexation of the donor ligand was observed, then, upon addition of AgOTf, complexation took place, but the resulting product was not identifiable. The complex had a typical red color, but neither NMR, (HR)ESI-MS, elemental analysis nor spectroscopic

examinations could indicate the structure of the formed compound. The problematic step here probably lies in the complexation process. As seen in the acceptor triad, the acceptor ligand is not stable under standard complexation conditions (EtOH:$CHCl_3$ = 3:1, heating to 80 °C). However, the complexation of the acceptor ligand in dry DMF under exclusion of light and upon prior treatment of the ruthenium precursor with AgOTf is possible, but yields are limited to 10% in the experiments performed. Therefore, suitable complexation conditions need to be found that tolerate both the donor and the acceptor arm and allow for efficient complexation. If no satisfying method is found for this, the acceptor part needs to be redesigned.

5.5 General Summary and Outlook

In this chapter, a concept for a two-electron donor, two-electron acceptor pentad was presented which should facilitate the formation of a two-electron, two-hole charge-accumulated state upon photoexcitation. The strategy here lies in the usage of electron donor and acceptor moieties exhibiting potential inversion. Additionally, intermediate electron donor and acceptor moieties were incorporated to prohibit excited-state quenching from the singly oxidized donor or the singly reduced acceptor. Suitable donor and acceptor moieties were determined and their oxidation/reduction potentials as well as their spectral changes upon oxidation/reduction examined. For the terminal electron donor exTTF and electron acceptor TCAQ, potential inversion behavior was confirmed. Additionally, hints of a low-lying triplet state (1.7 - 2.1 eV) were found for TCAQ which could allow for energy transfer from the excited $[Ru(bpy)_3]^{2+}$ photosensitizer to the TCAQ moiety. This process would adversely affect the charge-accumulation in the pentad and therefore the energy of the TCAQ triplet state should be thoroughly analyzed.

The donor triad was successfully prepared and examined. Photoexcitation at 532 nm led to the formation of $exTTF^+$ in the transient spectrum, showcasing functional hole transfer from the initially generated PTZ^+ to exTTF. Measuring the electron transfer kinetics showed the $[Ru(bpy)_3]^{2+}$ excited-state to be quenched within 10 ns, yielding the primary exTTF-PTZ^+-Ru^+ state. Measurements of the absorption decay at 665 nm then showed the following electron-transfer steps: a fast one (12.7 ns) that was attributed to the decay of the primary exTTF-PTZ^+-Ru^+ state to yield the final charge-separated $exTTF^+$-PTZ-Ru^+ state, and a slow one (377 ns) which was attributed to the final charge-recombination leading back to the exTTF-PTZ-Ru^{2+} ground state. Addition of an external electron acceptor led to $exTTF^+$ monocation formation with a hint that the $exTTF^{2+}$ dication was formed in minor amounts as well. The subsequent two-pulse experiment however did not display enhanced formation of the $exTTF^{2+}$ dication. With the experimental setup available, the formation of the doubly oxidized $exTTF^{2+}$ moiety could not be evidenced with certainty. However, this result does not indicate the general concept to be wrong. The facile formation of $exTTF^{2+}$ could be shown in chemical oxidation experiments and with a suitable two-electron acceptor readily being present in the pentad, the second electron oxidation of exTTF should be facilitated in the pentad compared to the bimolecular approach pursued with the donor triad in the experiments presented herein.

For the acceptor triad, the final ligand was obtained, but the complexation step did not work as expected. Therefore, measurements were limited to the acceptor reference molecules. Cyclic voltammetric measurements showed the potential inversion on TCAQ; the different spectral features of $TCAQ^-$, $TCAQ^{2-}$ and FMN^- could be identified

via spectro-electrochemical and transient absorption measurements. As soon as a satisfiable method is found to complex the acceptor ligand, measurements similar to the ones performed with the donor triad can take place. As external electron donors, the sacrificial donor triethylamine and the reversible donor ascorbate could be used just like in the experiments with the NDI triad.

During the synthesis of the pentad, several problems occurred. Therefore, two possible pentads were considered, either with acceptor and donor moieties being on the same ligand (one-ligand approach) or with donor and acceptor moieties being located on different ligands (two-ligand approach). Unfortunately, neither of the pentads could be successfully obtained. Problems lie in the lability of the acceptor moieties under C-C-coupling and complexation conditions and the incompatibility of the donor moieties with Lehnert's reagent. Another way to connect the individual moieties needs to be found that preserves the acceptor (and to a lesser part donor) moieties upon linkage. Possible ways of connecting the acceptor could involve the Staudinger reaction,[172] esterification,[133] an approach like the one used by Guldi *et al.*[23] or a click-type reaction.[173, 174] How the different connections affect the overall electron-transfer process then needs to be determined.

With parts of the pentad concept being proven to work in the case of the donor triad, the synthesis of the final pentad is still pending. The general concept of the pentad however continues to be very promising. Using donor and acceptor moieties with potential inversion results in higher driving-forces for the second, charge-accumulating electron-transfer step. As seen in the donor triad, the use of intermediate electron donor and acceptor moieties facilitates electron transfer in the intended direction while the spatial separation of the terminal donor and acceptor moieties from the photosensitizer results in reduced back-electron transfer and therefore longer lifetimes of the charge-separated or -accumulated states. The successful implementation of this concept into future molecular systems could be the next step forward in light-induced charge-accumulation.

6 Overall Summary

In this thesis, molecular systems for light-induced charge-accumulation were investigated. These systems containing (multi-)electron donor and acceptor moieties were examined for their electron-transfer pathways following excitation of the $[Ru(bpy)_3]^{2+}$ photosensitizer, as well as for the reaction pathways leading to or preventing charge-accumulation.

In the first project (Chapter 3), the two-electron acceptor NDI provided the basis for charge-accumulation studies. A molecular triad (Ru-NDI-Ru) was synthesized where the central acceptor moiety is flanked by two $[Ru(bpy)_3]^{2+}$ photosensitizers. Upon addition of a sacrificial electron donor and under steady-state irradiation, first the formation of a singly reduced NDI could be monitored followed then by the formation of doubly reduced NDI. Following these results, a molecular pentad (TAA-Ru-NDI-Ru-TAA) was prepared wherein internal TAA electron donor moieties were added to replace the sacrificial electron donor. In this pentad, however, only the singly reduced NDI moiety could be observed and no charge-accumulation on NDI took place. This finding was explained by low driving forces for the second, electron-accumulating transfer step, as well as with substantial excited state quenching by singly reduced NDI. For electron-accumulation on the Ru-NDI-Ru triad, a disproportionation reaction from NDI^- to NDI^0 and NDI^{2-} and subsequent re-reduction of the formed NDI^0 was determined as the main process leading to charge-accumulation.

In the second project (Chapter 4), a light-induced two-electron reduction was investigated; namely the reduction of $BNA^+$to BNAH. Following two-electron accumulation on the Ru-NDI-Ru triad, these two electrons were used to reduce the [RhBpyCp*Cl]Cl co-catalyst from Rh^{III} to Rh^{I}. Upon protonation, the formed Rh^{I} species is then able to reduce BNA^+ to BNAH. In the primary intermolecular approach with the Ru-NDI-Ru triad, the formation of NDI^- could be observed upon excitation, followed by the formation of BNAH. In a control experiment with $[Ru(bpy)_3]^{2+}$ and without the NDI electron acceptor, however, the formation of BNAH could be monitored as well and even at a superior rate. It was concluded that the formation of BNAH mainly relies on a disproportionation process of two Rh^{II} species, which, in this intermolecular approach, renders preceding charge-accumulation of no benefit for the overall BNAH formation process. Based on this, two molecular triads (Ru-NDI-Rh and Ru-Rh-NDI) were designed to accelerate the BNAH

formation by making the Rh^{II} disproportionation redundant: upon excitation of these triads, the first electron is stored on NDI. Upon second excitation, the second electron, in combination with the first electron stored on NDI, can perform a two-electron reduction of the co-catalyst and reduces Rh^{III} to Rh^{I} in a single step. Despite this promising concept, the performed measurements did not reveal a significant increase in the overall BNAH formation rate. It therefore could be concluded that molecular systems are not necessarily superior to their multi-component counterparts.

In the third project (Chapter 5), the throwbacks observed for the charge-accumulation process on the TAA-Ru-NDI-Ru-TAA pentad were addressed and a new pentad design was developed. Two tricks were employed to increase the probability for charge-accumulation: first, electron donors and acceptors with potential inversion were employed to ensure that the driving force for the transfer of the second electron is at least the same or even higher than for the first electron transfer. Secondly, intermediate electron donors and acceptors were used to accelerate electron transfer in the favored direction while retarding undesired back-electron transfer. While the successful synthesis of the pentad is still pending due to synthetic difficulties, the donor and acceptor moieties were examined and their applicability for the pentad verified. A donor triad was synthesized that, upon excitation, exhibited rapid excited-state quenching from the intermediate electron donor followed by rapid electron transfer from the terminal electron donor to the oxidized intermediate donor. The lifetime of the singly charge-separated state of 377 ns is rather long and, in combination with the electron movements observed, demonstrates the concept of an intermediate electron donor to be successful. The underlying concept of the pentad therefore is very promising and could be the next step forward in successful light-induced charge-accumulation in molecular systems.

7 Experimental Part

7.1 General Remarks

Commercially available reagents were purchased from commercial sources and used as received. Dry solvents were purchased from Sigma-Aldrich or dried through a solvent purification system from Innovative Technology. Deuterated solvents were purchased from Sigma-Aldrich or Cambridge Isotope Laboratories. Column chromatography was performed on silica gel (Silicycle, 40-63 µm, 60 Å). Silica plates for thin layer chromatography were obtained from Merck (60 F254).

^{1}H-NMR spectra were recorded on a Bruker Avance III NMR spectrometer with an operation frequency of 250 or 400 MHz at 298 K. The chemical shifts (δ) reported in this thesis are given in ppm and were referenced on residual solvent peaks.[175] Coupling constants are given in Hz. ESI mass spectra were measured on a Bruker Esquire 3000plus Ion-trap ESI-MS. High resolution ESI mass spectra were recorded on a Bruker maXis 4G QTOF ESI spectrometer. MALDI spectra were measured on a Bruker Microflex. Elemental analysis was performed on a Vario Micro Cube from Elementar.

UV-Vis absorption spectra were measured on a Varian Cary-5000 UV-Vis-NIR spectrometer. Cyclic voltammograms were recorded with a Versastat3-200 potentiostat from Princeton Applied Research. A three-electrode setup containing a glassy carbon working electrode, a silver wire counter electrode and an SCE reference electrode was used to measure the cyclic voltammograms. For spectro-electrochemical measurements, the Cary-5000 UV-Vis-NIR spectrometer and the Versastat3-200 potentiostat were used in combination. Here, a platinum-net was used as working electrode, a platinum wire as counter electrode and a SCE as reference electrode.

Transient absorption spectra were recorded with an LP920-KS spectrometer from Edinburgh Instruments equipped with an Andor iCCD camera. For single-wavelength kinetics, a R928 photomultiplier tube was used. A frequency-doubled Quantel Brilliant b laser served as light source for sample excitation, the duration of the laser pulse lasted approx. 10 ns with the pulse energy in the transient absorption measurements ranging from 10 mJ up to 60 mJ depending on the performed measurement. All measurements

were performed under inert conditions; solutions were degassed prior to measurements by four freeze-pump-thaw cycles.

Molecular mechanics energy minimization calculations were performed at the Molecular Mechanics Force Field (MMFF) level of theory using Spartan '08 Version 1.2.0.

Photoredox catalysis was performed in regular NMR tubes sealed with septa under inert atmosphere. Reaction solutions were degassed by four freeze-pump-thaw cycles before irradiation. The sample solutions were irradiated at 410 nm with a Fluorolog-322 from Horiba Jobin-Yvon or at 455 nm with an M455L2 LED (1020 mW) from Thorlabs at room temperature.

7.2 Synthesis of the Ru-NDI-Ru Triad and the TAA-Ru-NDI-Ru-TAA Pentad

For the Ru-NDI-Ru triad as well as the TAA-Ru-NDI-Ru-TAA pentad, the experimental data can be found in the supporting information of the published paper presented on the following pages.

Supporting Information to:

Electron Accumulation on Naphthalene Diimide Photosensitized by [Ru(2,2'-Bipyridine)$_3$]$^{2+}$

Michael Skaisgirski, Xingwei Guo, and Oliver S. Wenger*

Department of Chemistry, University of Basel, St. Johanns-Ring 19, CH-4056 Basel, Switzerland
E-mail: oliver.wenger@unibas.ch

Table of contents

Syntheses and product characterization data for triad **I**

The syntheses and characterization data of compounds **2**,[1] **5**,[2] and **9** [3] have been reported previously. For the syntheses of compounds **3** and **4**, we followed procedures reported earlier for structurally similar compounds.[4, 5] Compounds **1** and **6** are commercially available.

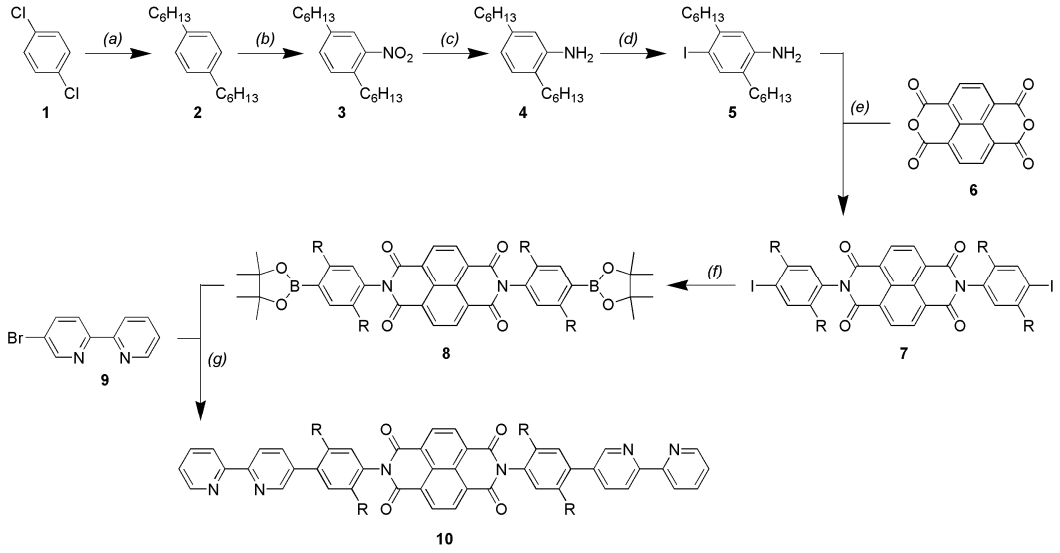

Scheme S1. (a) Mg, 1-bromohexane, Ni(dppp)Cl_2, Et_2O, reflux; (b) H_2SO_4, CH_3COOH, HNO_3, -10 °C; (c) HCl, Fe, EtOH, reflux; (d) *N*-iodosuccinimide, DMSO, r. t.; (e) DMF, 100 °C; (f) bis(pinacolato)diboron, KOAc, Pd$(PPh_3)_2Cl_2$, DMF, 100 °C; (g) Pd$(PPh_3)_4$, Na_2CO_3, THF, H_2O, reflux. R = C_6H_{13}.

1,4-Di-*n*-hexylbenzene (**2**). This procedure followed a previously published protocol.[1] Dry diethyl ether (50 ml) was added to magnesium (4.861 g, 200 mmol) under inert atmosphere. A portion of 1-bromohexane (~3 ml) was added rapidly to initiate the reaction. The remaining 1-bromohexane (33.014 g in total, 200 mmol) was added dropwise while keeping the reaction mixture gently at reflux. Heating was continued for 5 hours after all 1-bromohexane had been added. After cooling to room temperature, the desired Grignard reagent was added dropwise to a solution of 1,4-dichlorobenzene (**1**) (11.76 g, 80 mmol) and Ni(dppp)Cl_2 (81.3 mg, 0.15 mmol) in dry diethyl ether (30 ml) under N_2 at 0 °C. After complete addition of Grignard reagent, the reaction mixture was heated to reflux under N_2 for 24 hours. Water (40 ml) and 1 M aqueous HCl (120 ml) were then added carefully while cooling in an ice bath. The phases were separated, and the aqueous phase was extracted with diethyl ether (3×50 ml). The combined organic phases were washed with water (50 ml) and brine (50 ml) prior to drying over anhydrous Na_2SO_4. After solvent evaporation, the crude product was purified by chromatography on silica gel using pentane as the eluent. This afforded the pure product as a colorless liquid (19.62 g, 79.6 mmol, 99%). ^{1}H NMR (400 MHz, $CDCl_3$): δ [ppm] = 7.09 (s, 4 H), 2.62-2.53 (m, 4 H), 1.66-1.54 (m, 4 H), 1.41-1.23 (m, 12 H), 0.94-0.84 (m, 6 H).

2,5-Di-*n*-hexyl-1-nitrobenzene (**3**). This procedure followed a previously published method.[4] A mixture of concentrated sulfuric acid (95%, 15 ml) and glacial acetic acid (10 ml) were cooled to temperatures between -5 and -10 °C by addition of dry ice while stirring. 1,4-Di-*n*-hexylbenzene (4.93 g, 20 mmol) was added dropwise while keeping the temperature of the reaction mixture below 0 °C with dry ice. In a separate flask, a mixture of concentrated sulfuric acid (95%, 10 ml) and concentrated nitric acid (65%, 1.5 ml, ~21.5 mmol) was cooled to temperatures between -5 and -10 °C by adding dry ice. The nitrating acid mixture was then added dropwise to the solution containing 1,4-di-*n*-hexylbenzene while continuing to cool with dry ice. After complete addition, stirring of the reaction mixture at -10 °C was continued for 10 minutes, and then it was poured onto an ice / water mixture (100 ml). After extraction with diethyl ether (4×30 ml) the combined organic phases were washed with brine (3×50 ml) and dried over anhydrous Na_2SO_4. Following solvent evaporation, the crude product was purified by chromatography on silica gel with pentane. The desired product was obtained as a yellow oily liquid (3.73 g, 12.8 mmol, 64%). ^{1}H NMR (400 MHz, $CDCl_3$): δ [ppm] 7.67 (d, J = 1.8 Hz, 1 H), 7.30 (dd, J = 7.8, 1.8 Hz, 1 H), 7.22 (d, J = 7.8 Hz, 1 H), 2.88-2.78 (m, 2 H), 2.68-2.59 (m, 2 H), 1.68-1.54 (m, 4 H), 1.43-1.23 (m, 12 H), 0.95-0.84 (m, 6 H).

1-Amino-2,5-di-*n*-hexylbenzene (**4**). Following previously published protocols,[5] 2,5-di-*n*-hexyl-1-nitrobenzene (**3**) (1.46 g, 5.0 mmol) and iron powder (1.68 g, 30 mmol) were suspended in 50% aqueous ethanol (50 ml) and concentrated HCl (~0.36 g, ~10 mmol). The reaction mixture was heated to reflux for 19 hours, and then aqueous KOH (0.56 g, 10 mmol) was added. The mixture was filtered over a pluck of SiO_2 and rinsed with ethanol (4×30 ml). The filtrate was collected and the solvent was removed. The solid residue was taken up in CH_2Cl_2 (100 ml), dried over anhydrous Na_2SO_4, and then the solvent was evaporated. The crude product was chromatographed on silica gel with a 20:1 (v:v) mixture of pentane and ethyl acetate. This afforded the pure product as a light brown oil (1.06 g, 4.05 mmol, 81%). ^{1}H NMR (400 MHz, $CDCl_3$): δ [ppm] = 6.94 (d, J = 7.6 Hz, 1 H), 6.56 (dd, J = 7.6, 1.8 Hz, 1 H), 6.51 (d, J = 1.8 Hz, 1 H), 3.56 (s, 2 H), 2.53-2.39 (m, 4 H), 1.66-1.50 (m, 4 H), 1.46-1.21 (m, 12 H), 0.95-0.84 (m, 6 H).

1-Amino-2,5-di-*n*-hexyl-4-iodobenzene (**5**). The synthesis of this compound was reported earlier,[2] but we developed the following method. *N*-iodosuccinimide (0.45 g, 2.0 mmol) was added to a stirred solution of 1-amino-2,5-di-*n*-hexylbenzene (**4**) (0.52 g, 2.0 mmol) in DMSO (10 ml), and the mixture was reacted at room temperature for 26 hours. Water (20 ml) and diethyl ether (20 ml) were added. After phase separation, the aqueous phase was extracted with diethyl ether (3×20 ml). The combined organic phases were dried over anhydrous Na_2SO_4 before evaporating the solvent under reduced pressure. Chromatography of the crude product on silica gel using a 20:1 (v:v) mixture of pentane and ethyl acetate yielded the desired product as a pale brown oil (0.64 g, 1.65 mmol, 83%). ^{1}H NMR (400 MHz, $CDCl_3$): δ [ppm] = 7.41 (s, 1 H), 6.57 (s, 1 H), 3.79 (s, 2 H), 2.60-2.51 (m, 2 H), 2.44-2.35 (m, 2 H), 1.63-1.48 (m, 4 H), 1.42-1.24 (m, 12 H), 0.94-0.82 (m, 6 H).

Compound **7**. The following procedure was adapted from literature.[6] 1,4,5,8-Naphthalenetetracarboxylic dianhydride (**6**) (0.67 g, 2.5 mmol) and 1-amino-2,5-di-*n*-hexyl-4-iodobenzene (**5**) (2.13 g, 5.5 mmol) were stirred in vacuo for 2 hours. Then, dry DMF (10 ml) was added and the solution was heated to 100 °C for 72 hours. After cooling to room temperature, water (20 ml) and CH_2Cl_2 (15 ml) were added. The organic phase was separated, and the aqueous phase

was extracted with CH_2Cl_2 (3×15 ml). The combined organic phases were washed with water (25 ml) and brine (25 ml). The solvents were removed under reduced pressure after drying over anhydrous Na_2SO_4. The crude product was purified by chromatography on silica gel with a 2:1 (v:v) mixture of pentane and CH_2Cl_2. The desired product was obtained as a yellow solid (2.23 g, 2.2 mmol, 88%). ^{1}H NMR (400 MHz, $CDCl_3$): δ [ppm] = 8.86 (s, 4 H), (7.90 (s, 2 H), 7.02 (s, 2 H), 2.75-2.66 (m, 4 H), 2.41-2.31 (m, 4 H), 1.68-1.47 (m, 8 H), 1.45-1.09 (m, 24 H), 0.92-0.84 (m, 6 H), 0.77-0.67 (m, 6 H).

Compound **8**. Compound **7** (1.007 g, 1.0 mmol), bis(pinacolato)diboron (0.762 g, 3.0 mmol), KOAc (0.883 g, 9.0 mmol), and $PdCl_2(PPh_3)_2$ (70.2 mg, 0.1 mmol) were placed into a reaction flask and put under inert atmosphere prior to adding dry DMF (15 ml). The reaction mixture was de-aerated thoroughly before heating to 100 °C under N_2 for 72 hours. After cooling to room temperature, saturated aqueous NH_4Cl solution (30 ml) and CH_2Cl_2 (10 ml) were added. After phase separation, the aqueous phase was extracted with CH_2Cl_2 (3×50 ml). The combined organic phases were dried over Na_2SO_4 before removing the solvents on a rotary evaporator. Residual DMF had to be removed by heating under a Schlenk line vacuum. Chromatography on silica gel column with 6:1 (v:v) pentane / diethyl ether afforded the pure product as a yellow solid (0.90 g, 0.89 mmol, 89%). ^{1}H NMR (400 MHz, $CDCl_3$): δ [ppm] = 8.85 (s, 4 H), 7.85 (s, 2 H), 7.01 (s, 2 H), 2.95-2.84 (m, 4 H), 2.46-2.36 (m, 4 H), 1.63-1.50 (m, 8 H), 1.42-1.09 (m, 48 H), 0.93-0.84 (m, 6 H), 0.75-0.65 (m, 6 H).

Ligand **10**. Compound **8** (403 mg, 0.4 mmol), 5-bromo-2,2'-bipyridine (**9**)[3] (282 mg, 1.2 mmol) and Na_2CO_3 (254 mg, 2.4 mmol) in THF (15 ml) and H_2O (5 ml) were de-aerated prior to adding $Pd(PPh_3)_4$ (46.2 mg, 0.04 mmol). The reaction mixture was heated to reflux under N_2 for 1.5 days. After cooling to room temperature, water (50 ml) and CH_2Cl_2 (30 ml) were added. After phase separation, the aqueous phase was extracted with CH_2Cl_2 (3×40 ml). The combined organic phases were dried over anhydrous Na_2SO_4 and then evaporated. The crude product was purified by chromatography on silica gel column using the following sequence of eluents: (i) 6:1 (v:v) pentane / Et_2O; (ii) 2:1 (v:v) pentane / Et_2O; (iii) 1:1 (v:v) pentane / Et_2O; (iv) CH_2Cl_2; (v) acetone. Part of the desired product eluted with CH_2Cl_2, the remainder eluted with acetone. The product was obtained as a yellow solid (0.10 g, 0.094 mmol, 24% from CH_2Cl_2; 0.27 g, 0.25 mmol, 63% from acetone). ^{1}H NMR (400 MHz, $CDCl_3$): δ [ppm] = 8.94-8.86 (m, 4 H), 8.79-8.71 (m, 4 H), 8.54-8.45 (m, 4 H), 7.94-7.83 (m, 4 H), 7.40-7.31 (m, 4 H), 7.23-7.16 (m, 2 H), 2.68-2.60 (m, 4 H), 2.53-2.43 (m, 4 H), 1.64-1.56 (m, 8 H), 1.28-1.12 (m, 24 H), 0.82-0.76 (m, 6 H), 0.76-0.66 (m, 6 H). ESI-HRMS (m/z): calcd. for $C_{70}H_{74}N_6O_4+H^+$: 1063.5844; found: 1063.5842 ($M+H^+$).

Triad **I**. Ligand **10** (213 mg, 0.2 mmol) and $Ru(bpy)_2Cl_2 \cdot 2H_2O$ (208 mg, 0.4 mmol) in CH_2Cl_2 (5 ml) and ethanol (15 ml) were reacted at 72 °C for 48 hours. Then the solvents were evaporated. The red solid was purified by chromatography on silica gel using the following sequence of eluents: (i) acetone; (ii) 10:1 (v:v) acetone / H_2O; (iii) 85:15 (v:v) acetone / saturated aqueous KNO_3. Acetone was evaporated from the desired chromatography fractions, and then saturated aqueous KPF_6 solution was added. The resulting orange precipitate was collected, washed with water and diethyl ether. Drying in vacuum afforded an orange solid (280 mg, 0.11 mmol; 55%). ^{1}H NMR (400 MHz, CD_3CN): δ [ppm] = 8.80-8.70 (m, 4 H), 8.64-8.56 (m, 4 H), 8.55-8.47 (m, 8 H), 8.19-7.99 (m, 12 H), 7.93-7.86 (m, 2

H), 7.82-7.68 (m, 10 H), 7.49-7.35 (m, 10 H), 7.27-7.19 (m, 4 H), 2.46-2.29 (m, 6 H), 2.28-2.15 (m, 2 H), 1.50-1.35 (m, 4 H), 1.31-0.90 (m, 28 H), 0.83-0.75 (m, 6 H), 0.73-0.61 (m, 6 H). ESI-HRMS (*m/z*): calcd. for $C_{110}H_{106}N_{14}O_4Ru_2^{4+}$: 472.6657; found: 472.6665 (M^{4+}). Anal. Calcd. for $C_{110}H_{106}N_{14}O_4F_{24}P_4Ru_2 \cdot 4H_2O$: C, 51.97; H, 4.52; N, 7.71; found: C, 52.07; H, 4.67; N, 7.78.

Syntheses and product characterization data for pentad **II**

The syntheses and characterization data of compounds **13**,[7] **14**,[7a, 8] and **15** [9] have been reported previously. Compounds **12** and **16** were commercially available.

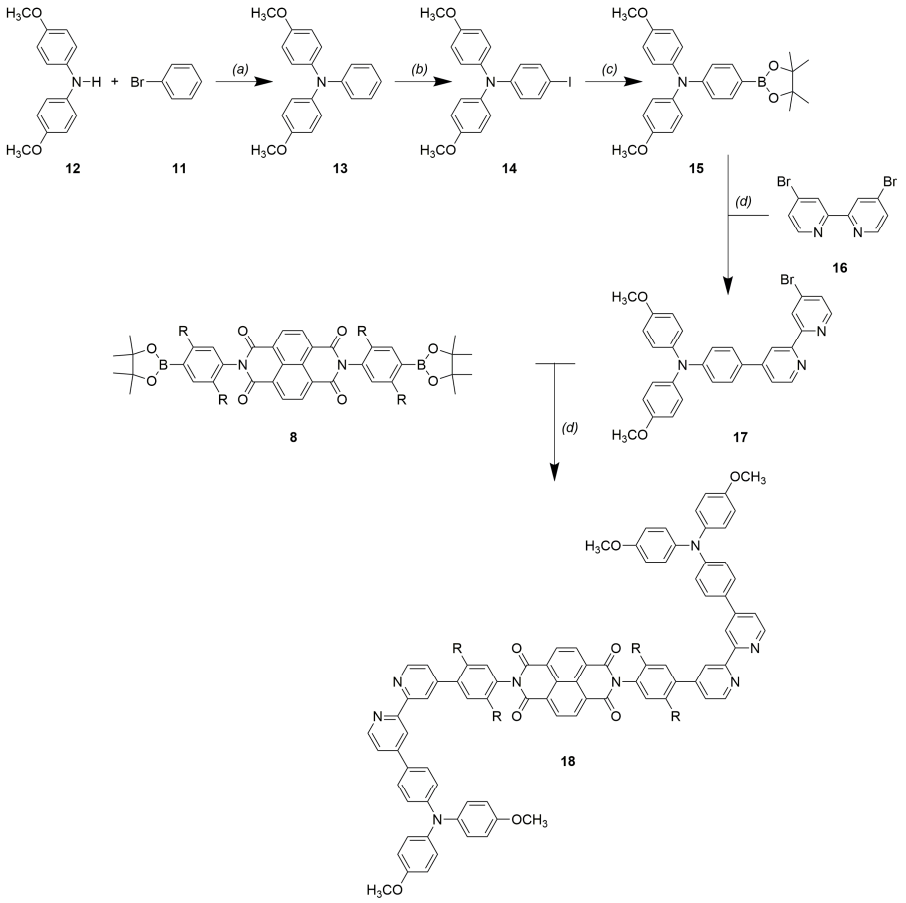

Scheme S2. (a) ^{t}BuOK, Pd(dba)$_2$, P^{t}Bu$_3$, toluene, 100 °C; (b) $C_6H_5I(CF_3COO)_2$, I_2, CH_2Cl_2, r. t.; (c) bis(pinacolato)diboron, KOAc, $Pd(PPh_3)_2Cl_2$, DMF, 100 °C; (d) $Pd(PPh_3)_4$, Na_2CO_3, THF/H_2O, 80 °C. R = C_6H_{13}.

Compound **13**.[7] 4,4'-Dimethoxydiphenylamine (**12**) (0.92 g, 4.01 mmol), bromobenzene (**11**) (0.75 g, 0.50 ml, 4.78 mmol) and ^{t}BuOK (1.35 g, 12.03 mmol) were put under N_2 atmosphere in a two-neck reaction flask. Dry toluene (15 ml) was added, followed by $Pd(dba)_2$ (0.11 g, 0.19 mmol) and P^{t}Bu$_3$ (41 mg, 0.06 ml, 0.20 mmol). After bubbling N_2 through the reaction mixture for 20 minutes, it was heated to 100 °C for 24 hours. After cooling to room temperature, water (20 ml) and CH_2Cl_2 (10 ml) were added, and the phases were separated. The aqueous phase was extracted with CH_2Cl_2 (3×20 ml), and the combined organic phases were dried over anhydrous Na_2SO_4. The solvents were evaporated under reduced pressure, and the crude product was purified by chromatography on silica gel column using 10:1 (v:v) pentane / diethyl ether as an eluent. This afforded the pure product as a white solid (1.12 g, 3.67 mmol, 92%). ^{1}H NMR (400 MHz, $CDCl_3$): δ [ppm] 7.20-7.14 (m, 2 H), 7.07-7.02 (m, 4 H), 6.95-6.91 (m, 2 H), 6.88-6.79 (m, 5 H), 3.79 (s, 6 H).

Compound **14**.[7a, 8] Iodine (2.30 g, 9.06 mmol) and bis(trifluoroacetoxy)iodobenzene (3.87 g, 9.0 mmol) were placed under N_2 atmosphere, and dry CH_2Cl_2 (30 ml) was added. The solution was stirred at room temperature for 1 hour, and then compound **13** (2.75 g, 9.0 mmol) was added. The reaction mixture was refluxed under N_2 for 1 hour. Meanwhile, a second solution of iodine (1.15 g, 4.53 mmol) and bis(trifluoroacetoxy)iodobenzene (2.04 g, 4.74 mmol) in dry CH_2Cl_2 (15 ml) was stirred at room temperature. This solution was then added to the reaction mixture, and the latter was continued refluxing under N_2 for another hour. After cooling to room temperature, saturated aqueous $Na_2S_2O_3$ solution (40 ml) was added. After stirring at room temperature for 2 hours, CH_2Cl_2 (20 ml) was added, the phases were separated, and the aqueous phase was extracted with CH_2Cl_2 (2×30 ml). The combined organic phases were dried over anhydrous Na_2SO_4, and the solvents were removed on a rotary evaporator. The crude product was dissolved in some CH_2Cl_2 to deposit it on silica gel. Column chromatography on silica gel using 5:3 (v:v) pentane / CH_2Cl_2 as the eluent gave the pure product as a colorless oil (1.71 g, 3.97 mmol, 44%). ^{1}H NMR (400 MHz, $CDCl_3$): δ [ppm] 7.43-7.38 (m, 2 H), 7.06-7.00 (m, 4 H), 6.85-6.79 (m, 4 H), 6.70-6.65 (m, 2 H), 3.79 (s, 6 H).

Compound **15**.[9] Bis(pinacolato)diboron (0.49 g, 1.93 mmol), KOAc (0.53 g, 5.40 mmol), and $Pd(PPh_3)_2Cl_2$ (0.09 g, 0.13 mmol) were placed into a two-neck reaction flask and put under N_2 atmosphere. Compound **14** (0.54 g, 1.25 mmol) was dissolved in dry DMF (15 ml) and the resulting solution was added to the two-neck reaction flask. N_2 was bubbled through the reaction mixture for 40 minutes prior to heating to 100 °C under N_2 for 66 hours. After cooling to room temperature, saturated aqueous NH_4Cl (30 ml) and CH_2Cl_2 (30 ml) were added. After phase separation, the aqueous phase was extracted with CH_2Cl_2 (3×30 ml), and the combined organic phases were dried over anhydrous Na_2SO_4. Following solvent removal on a rotary evaporator and at the Schlenk line (DMF), the crude product was purified on silica gel column using a 7:1 (v:v) mixture of pentane and diethyl ether as the eluent. This afforded the product as a white solid (0.31 g, 0.72 mmol, 58%). ^{1}H NMR (400 MHz, $CDCl_3$): δ [ppm] 7.60 (d, J = 8.0 Hz, 2 H), 7.06 (d, J = 5.9 Hz, 4 H), 6.92-6.77 (m, 6 H), 3.80 (s, 6 H), 1.32 (s, 12 H).

Compound **17**.[3] Compound **15** (0.65 g, 1.51 mmol), commercial 4,4'-dibromo-2,2'-bipyridine (**16**) (0.58 g, 1.85 mmol), Na_2CO_3 (0.72 g, 6.79 mmol), and $Pd(PPh_3)_4$ (0.10 g, 0.09 mmol) were dissolved in a mixture of THF (20 ml) and H_2O (5 ml). After de-oxygenating by bubbling N_2 gas for 30 minutes, the reaction mixture was heated to 80 °C for

69 hours. H_2O (25 ml) and CH_2Cl_2 (25 ml) were added after cooling to room temperature, and the organic and aqueous phases were separated. The latter was extracted with CH_2Cl_2 (3×30 ml), and the combined organic phases were dried over anhydrous Na_2SO_4 prior to removing the solvents on a rotary evaporator. Column chromatography on silica gel with CH_2Cl_2 containing 2% CH_3OH as the eluent afforded the pure product as a yellow solid (0.42 g, 0.78 mmol, 52%). ^{1}H NMR (400 MHz, $CDCl_3$): δ [ppm] 8.71 (s, 1 H), 8.66 (d, *J* = 5.3 Hz, 1 H), 8.62 (s, 1 H), 8.50 (d, *J* = 5.2 Hz, 1 H), 7.63-7.47 (m, 4 H), 7.11 (d, *J* = 8.3 Hz, 4 H), 6.99 (d, *J* = 8.7 Hz, 2 H), 6.87 (d, *J* = 9.0 Hz, 4 H), 3.82 (s, 6 H).

Ligand **18**. Compound **17** (358 mg, 0.665 mmol), compound **8** (227 mg, 0.225 mmol), Na_2CO_3 (210 mg, 0.020 mmol), and $Pd(PPh_3)_4$ (23 mg, 0.020 mmol) were dissolved in a mixture of THF (20 ml) and H_2O (5 ml). N_2 was bubbled through the reaction mixture during 30 minutes before heating it to 80 °C under N_2 for 91 hours. After cooling to room temperature, H_2O (20 ml) and CH_2Cl_2 (25 ml) were added, and the two phases were separated. The aqueous phase was extracted with CH_2Cl_2 (3×30 ml). Then the combined organic phases were dried over anhydrous Na_2SO_4. The solvents were removed on a rotary evaporator. Purification occurred on a silica gel column using first a 5:1 (v:v) mixture of pentane and ethyl acetate as the eluent, and later pure ethyl acetate. The product was obtained as a dark green solid (320 mg, 0.192 mmol, 84%). ^{1}H NMR (400 MHz, $CDCl_3$): δ [ppm] 8.93-8.87 (m, 4 H), 8.81 (d, *J* = 5.0 Hz, 2 H), 8.77-8.69 (m, 4 H), 8.59 (s, 2 H), 7.70-7.64 (m, 4 H), 7.61-7.54 (m, 2 H), 7.49-7.42 (m, 2 H), 7.39 (s, 2 H), 7.20 (s, 1 H), 7.17 (s, 1 H), 7.15-7.11 (m, 8 H), 7.01 (d, *J* = 8.9 Hz, 4 H), 6.91-6.86 (m, 8 H), 3.83 (s, 12 H), 2.68-2.58 (m, 4 H), 2.52-2.42 (m, 4 H), 1.66-1.47 (m, 8 H), 1.31-1.08 (m, 24 H), 0.80-0.67 (m, 12 H). ESI-HRMS (*m/z*): calcd. for $C_{110}H_{108}N_8O_8+2H^+$: 835.9234; found: 835.9233 ($M+2H^+$). Anal. Calcd. for $C_{110}H_{108}N_8O_8 \cdot 1.5H_2O$: C, 77.85; H, 6.59; N, 6.60; found: C, 77.91; H, 6.42; N, 6.63.

Pentad **II**. Ligand **18** (150 mg, 0.090 mmol) and $Ru(bpy)_2Cl_2 \cdot 2H_2O$ (94.3 mg, 0.181 mmol) were dissolved in $CHCl_3$ (5 ml) and EtOH (15 ml). The purple solution was heated to 80 °C for 137 hours, and then the solvents were evaporated. The red solid was dissolved in some CH_2Cl_2 and was then loaded onto a silica gel column. Three different eluents were used one after the other: (i) neat acetone, (ii) a 10:1 (v:v) mixture of acetone and H_2O, (iii) a 85%:15% (v:v) mixture of acetone and saturated aqueous KNO_3 solution. After evaporation of acetone from the desired chromatography fractions, saturated aqueous KPF_6 solution was added. The resulting orange precipitate was filtered, washed with H_2O and diethyl ether prior to drying under vacuum. This afforded the pure product as an orange solid (137 mg, 0.044 mmol, 49%). ^{1}H NMR (400 MHz, CD_3CN): δ [ppm] 8.84-8.72 (m, 8 H), 8.60 (m, 8 H), 8.15-8.06 (m, 8 H), 7.93-7.88 (m, 4 H), 7.84-7.73 (m, 10 H), 7.67-7.58 (m, 4 H), 7.52-7.38 (m, 14 H), 7.16 (d, *J* = 8.9 Hz, 8 H), 6.97 (d, *J* = 8.9 Hz, 8 H), 6.88 (d, *J* = 8.9 Hz, 4 H), 3.81 (s, 12 H), 2.68 (t, *J* = 7.9 Hz, 4 H), 2.52 (q, *J* = 8.0 Hz, 4 H), 1.60-1.41 (m, 8 H), 1.40-1.03 (m, 24 H), 0.78-0.62 (m, 12 H). ESI-HRMS (*m/z*): calcd. for $C_{150}H_{140}N_{16}O_8Ru_2^{4+}$: 624.2289; found: 624.2304. Anal. Calcd. for $C_{150}H_{140}N_{16}O_8F_{24}P_4Ru_2 \cdot 8H_2O$: C, 55.93; H, 4.88; N, 6.96; found: C, 55.86; H, 4.78; N, 7.37.

Syntheses and product characterization data for NDI reference compound

1,4,5,8-Naphthalenetetracarboxylic dianhydride (**6**) (0.244 g, 0.91 mmol) and 1-amino-2,5-di-*n*-hexylbenzene (**4**) (0.536 g, 2.05 mmol) were stirred in vacuo for 2 hours. Then, dry DMF (2 mL) was added and the solution heated to 140 °C for 96 h. The solvent was removed under reduced pressure and purified by chromatography on silica gel with a 20:1 (v:v) mixture of pentane and ethyl acetate. The desired product was obtained as a light brown solid (0.50 g, 0.66 mmol, 73%).

^{1}H NMR (400 MHz, $CDCl_3$): δ [ppm] = 8.86 (s, 4H), 7.37 (d, *J* = 7.9 Hz, 2H), 7.29 (dd, *J* = 7.9, 1.8 Hz, 2H), 7.01 (d, *J* = 1.7 Hz, 2H), 2.65 (t, 4H), 2.42 (t, 4H), 1.70 – 1.61 (m, 4H), 1.59 – 1.50 (m, 4H), 1.43 – 1.08 (m, 24H), 0.88 (t, 6H), 0.72 (t, 6H). ESI-HRMS (m/z): calcd. for $C_{50}H_{62}N_2O_4$+H^+: 755.4782; found: 755.4772 ($M+H^+$). Anal. Calcd. for $C_{50}H_{62}N_2O_4$: C, 79.54; H, 8.28; N, 3.71; found: C, 79.28; H, 7.99; N, 3.76.

Equipment and methods

NMR spectra were measured on a Bruker Avance III instrument. Mass spectrometry was performed using Bruker esquire 3000 plus and Bruker maxis 4G QTOF EDI instruments. Ms. Sylvie Mittelheisser conducted elemental analysis on a Vario Micro Cube instrument in the Department of Chemistry at University of Basel. Cyclic voltammetry was measured using a Versastat3-200 potentiostat from Princeton Applied Research. The working electrode was a platinum disk. In the case of triad **I**, two silver wires served as counter electrode and quasi-reference electrode, respectively. The potential was calibrated by adding a small amount of ferrocene to the sample. In the case of pentad **II**, an SCE reference electrode was employed. The electrolyte was 0.1 M tetra-*n*-butylammonium hexafluorophosphate ($TBAPF_6$), the potential scan rate was 0.1 V/s. Potentials measured against SCE were then converted to potentials vs. Fc^+/Fc by subtracting -0.38 V.[10] Optical absorption spectra were measured on a Cary 5000 instrument from Varian. Chemical reduction of naphthalene diimide to its mono- and dianionic forms in the triad was achieved by using benzophenone radical anion as a chemical reductant. In the case of the pentad, NDI^- and NDI^{2-} were generated using sodium as a chemical reductant. The latter was prepared directly in gas-tight cuvettes from sodium and benzophenone in dry THF. Photoirradiation occurred on a Fluorolog3-22 instrument from Horiba Jobin-Yvon using light of 410 nm wavelength. The flux was $(3.22\pm0.14)\cdot10^{16}$ photons/s as determined by ferrioxalate actinometry.[11] Samples were thoroughly de-oxygenated by three consecutive freeze-pump-thaw cycles in gas-tight cuvettes.

Nanosecond transient absorption and time-resolved luminescence experiments were measured on an LP920-KS spectrometer from Edinburgh Instruments, equipped with a Quantel Brilliant b laser as an excitation source. In the two-color pump-pump probe experiment, the secondary excitation occurred with a Quantel Brilliant laser equipped with an OPO from Opotek. Synchronization of the two lasers and the detection system occurred with a 9520 digital delay pulse generator from Quantum Composers.

Picosecond transient absorption studies were performed on a TRASS instrument from Hamamatsu, using a mode-locked picosecond Nd:YVO_4/YAG laser (model PL2251B-20-SH/TH/FH with PRETRIG option) as an excitation source.

Cyclic voltammetry of triad **I** and pentad **II**

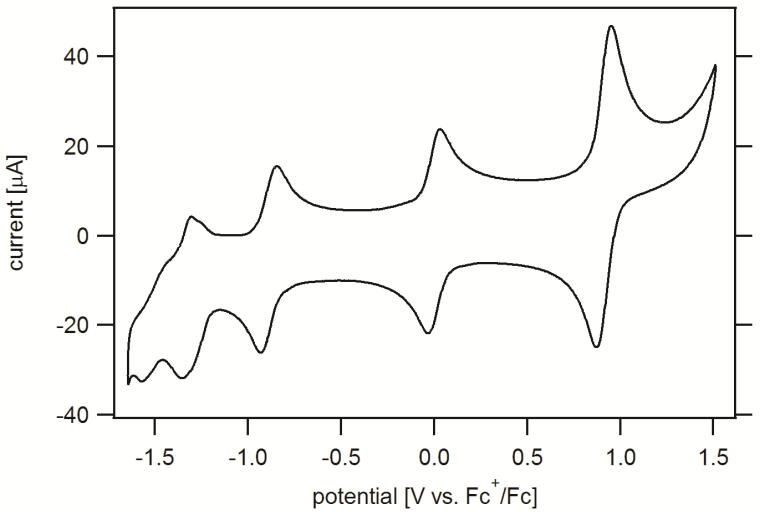

Figure S1. Cyclic voltammogram for triad **I** in CH_3CN with 0.1 M $TBAPF_6$. The wave at 0.0 V is due to a small quantity of ferrocene, which was added for potential calibration. The potential sweep rate was 0.1 V/s.

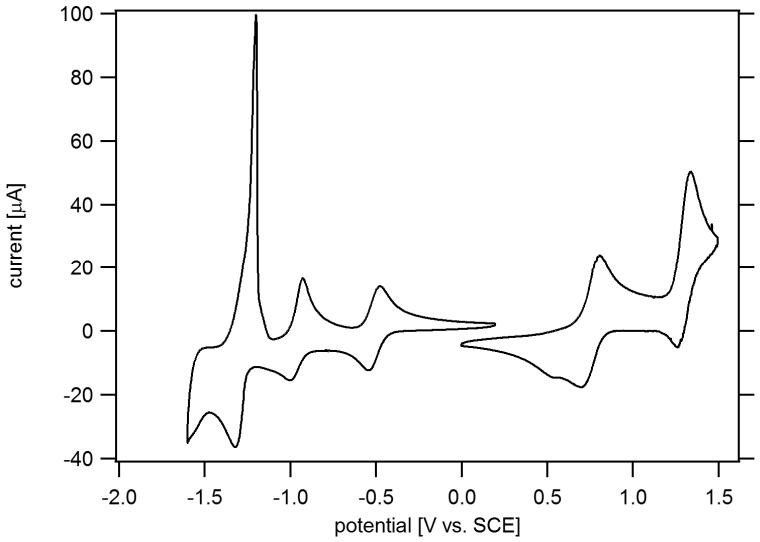

Figure S2. Cyclic voltammograms for pentad **II** in CH_3CN with 0.1 M $TBAPF_6$. Oxidative and reductive sweeps were conducted separately because this gave higher quality results. The potential sweep rate was 0.1 V/s.

UV-Vis spectra of triad **I** and pentad **II**

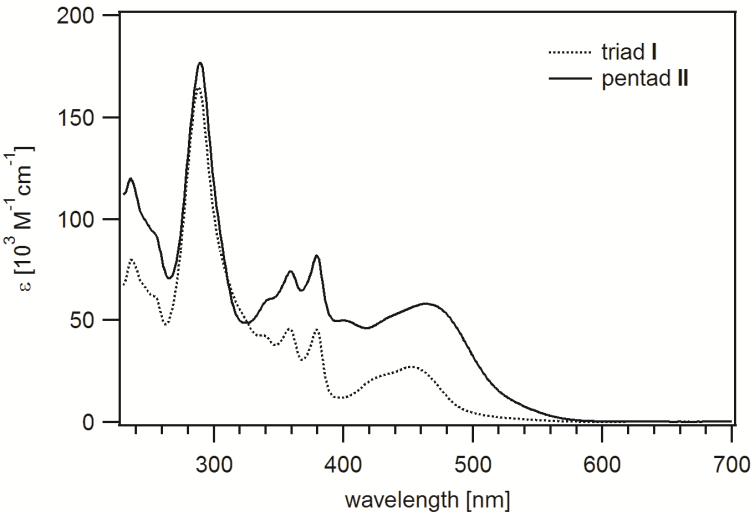

Figure S3. UV-Vis spectra of triad **I** and pentad **II** in CH_3CN at 25 °C.

Photoirradiation of triad **I** in presence of Et_3N

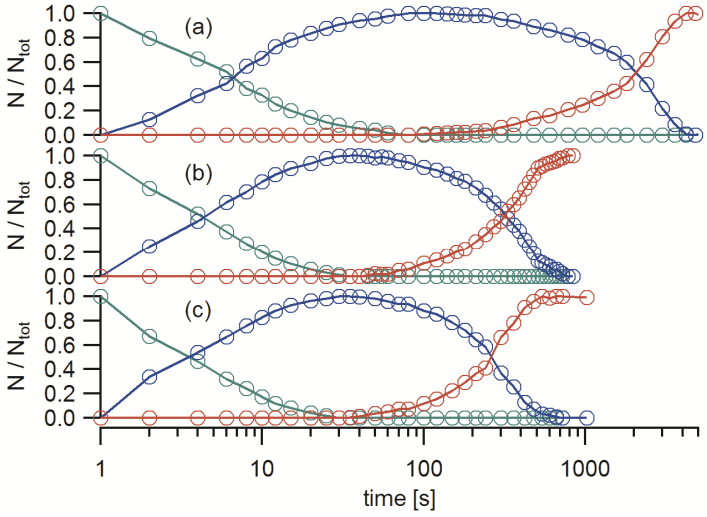

Figure S4. Relative proportions (molar fractions) of NDI (green), NDI^- (blue), and NDI^{2-} (red) forms of triad **I** after different irradiation times in presence of (a) 0.1 M, (b) 0.25 M, and (c) 0.5 M Et_3N in de-aerated CH_3CN at 25 °C. The samples contained $3.4 \cdot 10^{-8}$ mol of triad **I**, the photon flux used for excitation at 410 nm was $(3.22 \pm 0.14) \cdot 10^{16}$ photons / s. This corresponds to roughly 2 photons per triad molecule per second. The data in Figure S4 were determined based on the UV-Vis difference spectra in Figure S5 and the UV-Vis difference spectra obtained after chemical reduction of triad **I** in Figure 1b and Figure 1d of the main paper. (The spectra in Figure S5 are essentially linear combinations of the NDI, NDI^-, and NDI^{2-} forms of triad **I**).

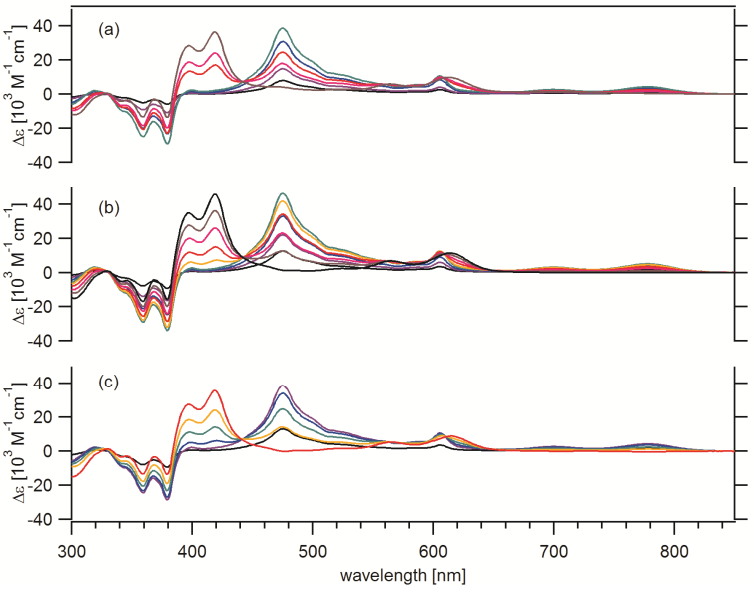

Figure S5. UV-Vis difference spectra obtained in the course of irradiating a $1.7 \cdot 10^{-5}$ M solution of triad **I** at 410 nm in presence of (a) 0.1 M, (b) 0.25 M, and (c) 0.5 M Et_3N in de-aerated CH_3CN. The photon flux was $(3.22 \pm 0.14) \cdot 10^{16}$ photons / s. Irradiation times were as follows: (a) 2 s, 4 s, 15 s, 120 s, 360 s, 1800 s, 2400 s, 5400 s; (b) 2 s, 4 s, 8 s, 40 s, 100 s, 210 s, 330 s, 450 s, 780 s; (c) 2 s, 30 s, 100 s, 210 s, 300 s, 720 s.

Transient absorption studies of triad **I**

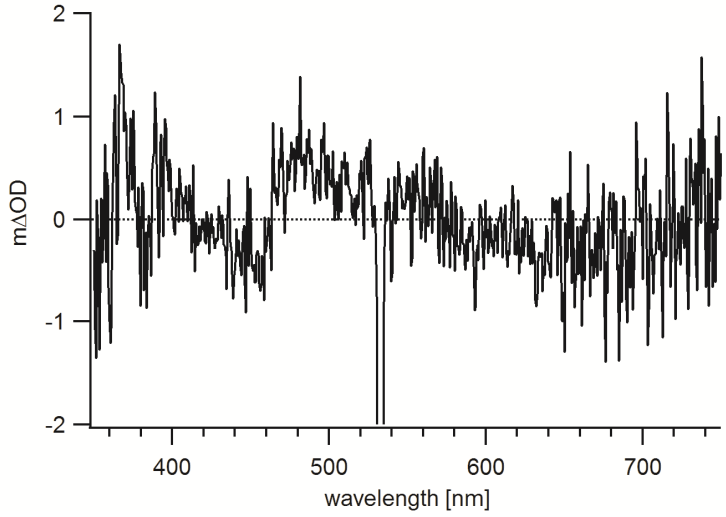

Figure S6. Transient difference spectrum obtained from a $3 \cdot 10^{-5}$ M solution of triad **I** in de-aerated CH_3CN at 25 °C. Excitation occurred at 532 nm with laser pulses of ~10 ns duration. The signal was time-integrated over 200 ns immediately after excitation. Due to the short lifetime of the photoproduct (Figure S7b), the NDI^- signal at ~480 nm and the $[Ru(bpy)_3]^{2+}$-associated bleach at ~450 nm are very weak.

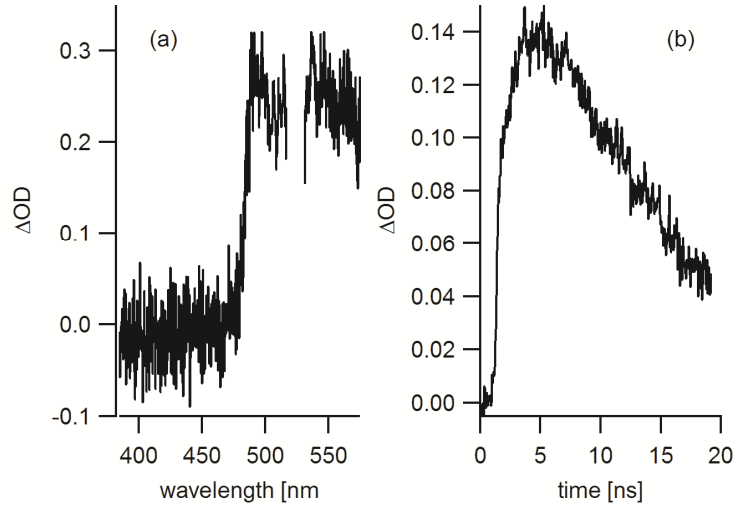

Figure S7. Transient absorption data obtained from a $3 \cdot 10^{-5}$ M solution of triad **I** in de-aerated CH_3CN at 25 °C. Excitation occurred at 532 nm with laser pulses of ~30 ps duration: (a) Transient difference spectrum indicating the formation of the NDI^- absorption band; (b) Temporal evolution of the transient signal in the spectral range between 470 and 520 nm. The time window is limited to 20 ns in this experiment due to technical restrictions.

Photoirradiation reference experiments for triad **I**

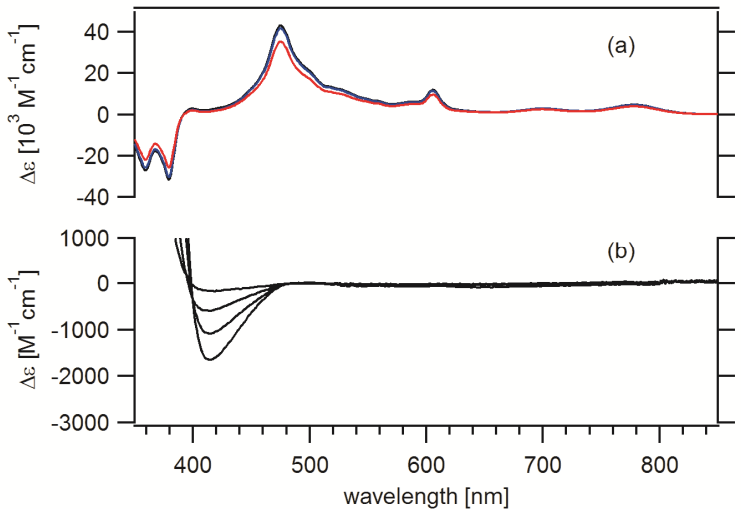

Figure S8. (a) UV-Vis difference spectra obtained from a solution of $1.7 \cdot 10^{-5}$ M triad **I** in de-aerated CH_3CN with 0.5 M Et_3N. The sample was irradiated at 410 nm with a flux of $(3.22 \pm 0.14) \cdot 10^{16}$ photons / s leading to the nearly quantitative formation of the NDI^- form of triad **I** (black trace). Then, the sealed sample was left standing in the dark and the spectrum was re-measured after 30 minutes (blue trace) and after 90 minutes (red trace). (b) UV-Vis difference spectra obtained from a solution of $1.7 \cdot 10^{-5}$ M triad **I** in de-aerated CH_3OH with 0.1 M 5,6 tetra-*n*-butylammonium isopropylidene ascorbate. Irradiation occurred at 410 nm with the same photon flux as noted above. The spectra were measured after 1, 5, 15, and 30 minutes. Even after these long irradiation times (compare to Figure 2 of the main paper and Figures S4 and S5 in the Supporting Information) the typical spectral features for NDI^- and NDI^{2-} remain undetectable.

^{3}MLCT excited state quenching by 5,6-isopropylidene ascorbate

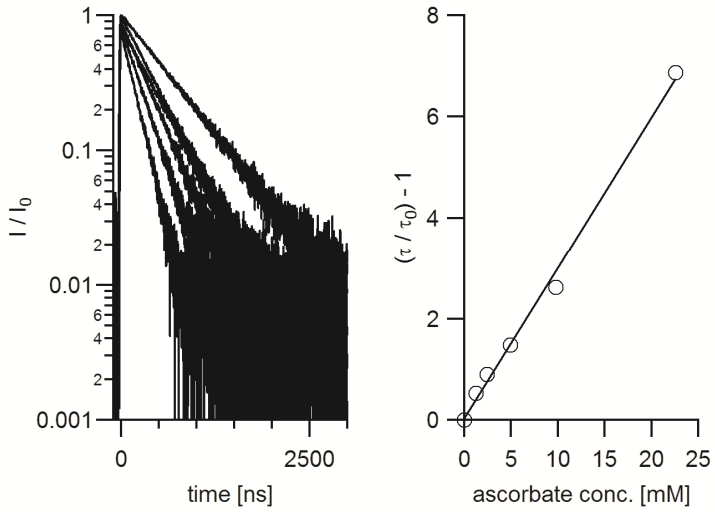

Figure S9. (a) Luminescence decays of $[Ru(bpy)_3]^{2+}$ in CH_3OH at 25 °C in absence and in presence of different concentrations of tetra-*n*-butylammonium 5,6-isopropylidene ascorbate. Excitation occurred at 532 nm with laser pulses of ~10 ns duration, detection was at 610 nm. (b) Stern-Volmer plot based on the luminescence lifetime data from panel (a). The solid line is a linear regression fit yielding a rate constant of $4.8 \cdot 10^8$ M^{-1} s^{-1} for ^{3}MLCT excited-state quenching of $[Ru(bpy)_3]^{2+}$ by 5,6-isopropylidene ascorbate in CH_3OH at 25 °C.

S16

Transient absorption of triad **I** in presence of ascorbate

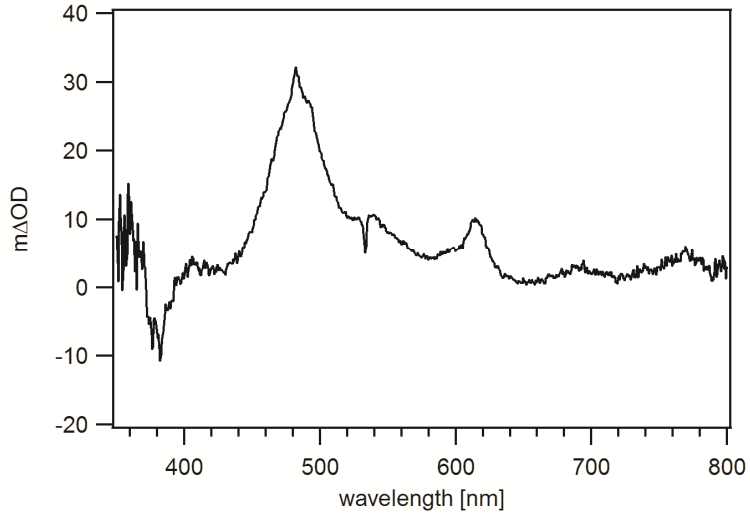

Figure S10. Transient difference spectrum recorded from a $1.7 \cdot 10^{-5}$ M solution of triad **I** in de-aerated CH_3OH at 25 °C with 0.1 M 5,6-isopropylidene ascorbate. Excitation occurred at 532 nm with laser pulses of ~10 ns duration. The signal was time-integrated over 200 ns immediately after excitation.

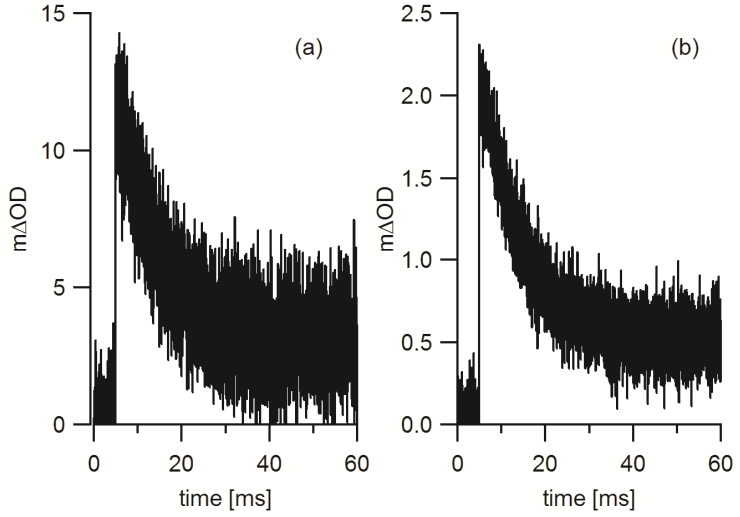

Figure S11. Decays of the transient absorption signals at (a) 484 nm and (b) 615 nm obtained from the solution in Figure S10 following excitation at 532 nm with laser pulses of ~10 ns duration.

Chemical reduction of pentad **II**

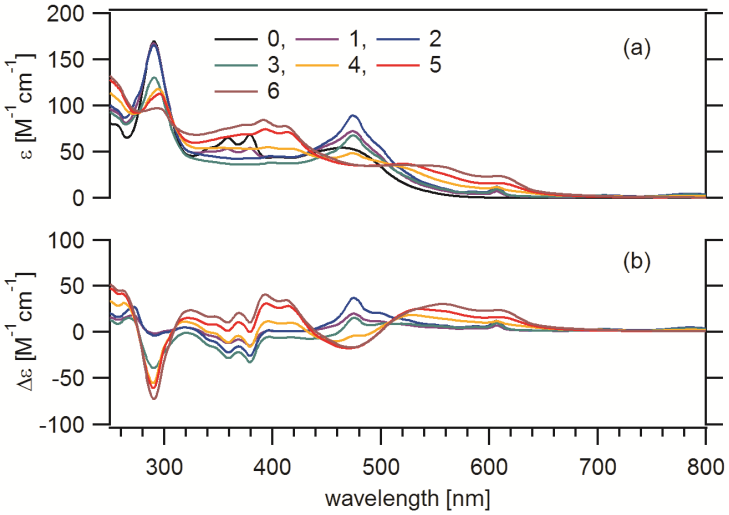

Figure S12. (a) UV-Vis absorption spectra obtained from a solution of pentad **II** in dry THF at 25 °C in absence (black trace) and in presence (colored trace) of increasing exposure time to Na(s) reductant. (b) UV-Vis difference spectra resulting from subtraction of the black trace from (a) from the colored traces from (a). In the course of this chemical reduction experiment, initially NDI is converted to NDI^{-}, manifesting in the absorption band at ~475 nm. After addition of increasing amounts of chemical reductant, bands at 395 and 415 nm appear, compatible with the formation of NDI^{2-}. However, the bleach at ~290 nm increases concomitantly, suggesting that reduction of the $[Ru(bpy)_3]^{2+}$ photosensitizer units does also occur.

Chemical oxidation of pentad **II**

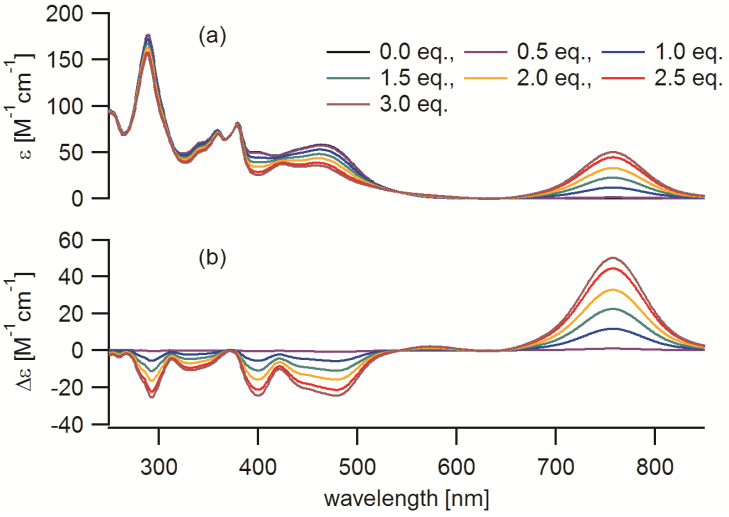

Figure S13. (a) UV-Vis absorption spectra obtained from a solution of pentad **II** in CH_3CN at 25 °C in absence (black trace) and in presence (colored trace) of increasing amounts of $Cu(ClO_4)_2$. (b) UV-Vis difference spectra resulting from subtraction of the black trace from (a) from the colored traces of (a).

Transient absorption data for pentad **II**

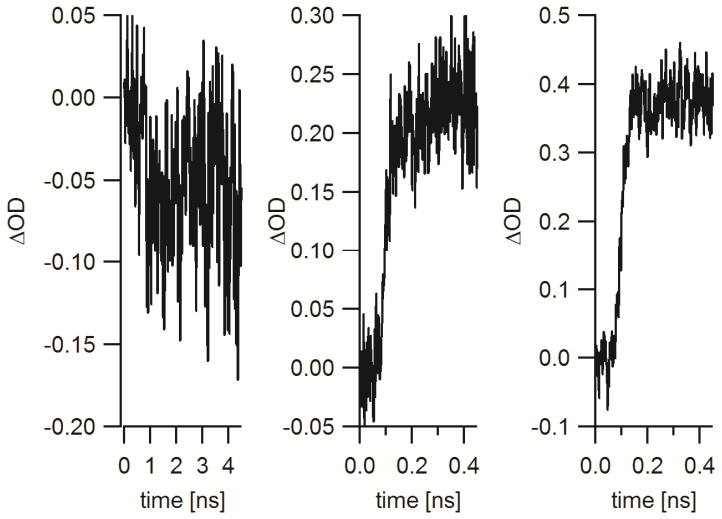

Figure S14. Temporal evolution of the transient absorption signals at (a) 370 nm, (b) 480 nm, and (c) 730 nm after pulsed excitation of pentad **II** in CH_3CN at 25 °C. The excitation wavelength was 532 nm, the pulse width was ~30 ps. The individual wavelengths monitor (a) disappearance of charge-neutral NDI, (b) the formation of NDI^-, and (c) the formation of TAA^+. The sample concentration was $5.8 \cdot 10^{-5}$ M.

S20

Two-color pump-pump probe experiment with pentad **II**

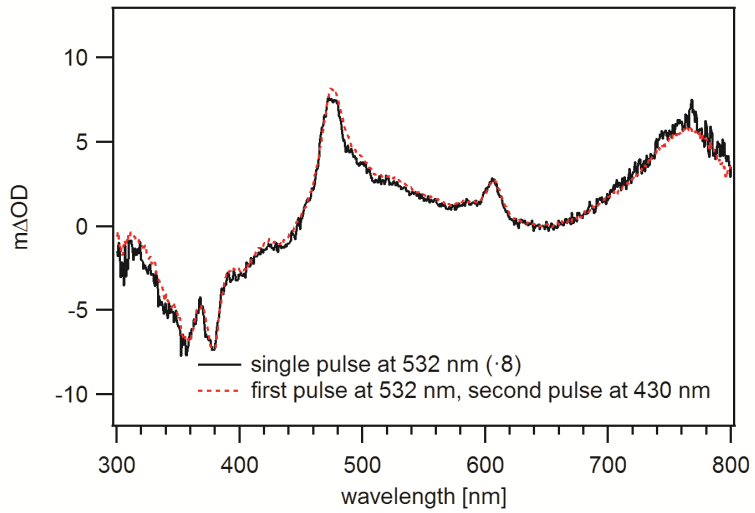

Figure S15. Transient difference spectra recorded from a $1.5 \cdot 10^{-5}$ M solution of pentad **II** in de-aerated CH_3CN at 25 °C. Solid black line: Following excitation at 532 nm with 30 mJ. Dashed red line: After primary excitation at 532 nm with 30 mJ, followed by secondary excitation at 430 nm with 21 mJ. The duration of the laser pulses was ~10 ns, the delay between the 532 and 430 nm laser pulses was 50 ns. Detection occurred by time-integration of the signal over 50 ns immediately after the last pulse. The black trace was multiplied by a factor of 8 to match the intensity of the signal in the red trace.

Photoirradiation of $[Ru(bpy)_3]^{2+}$ in presence of NDI reference compound and Et_3N

A de-aerated solution containing $3.9 \cdot 10^{-5}$ M $[Ru(bpy)_3]^{2+}$, $1.7 \cdot 10^{-5}$ M NDI reference compound (page S8), and 0.5 M triethylamine was photo-irradiated under the same conditions as triad **I**. In this experiment, the photosensitizer and NDI concentrations were comparable to those in the triad experiment, but this three-component system now entirely relies on inter-molecular electron transfer reactions (rather than a combination of intra- and inter-molecular reactions). In the course of photoirradiation, the UV-Vis spectral changes shown in Figure S16 were observable.

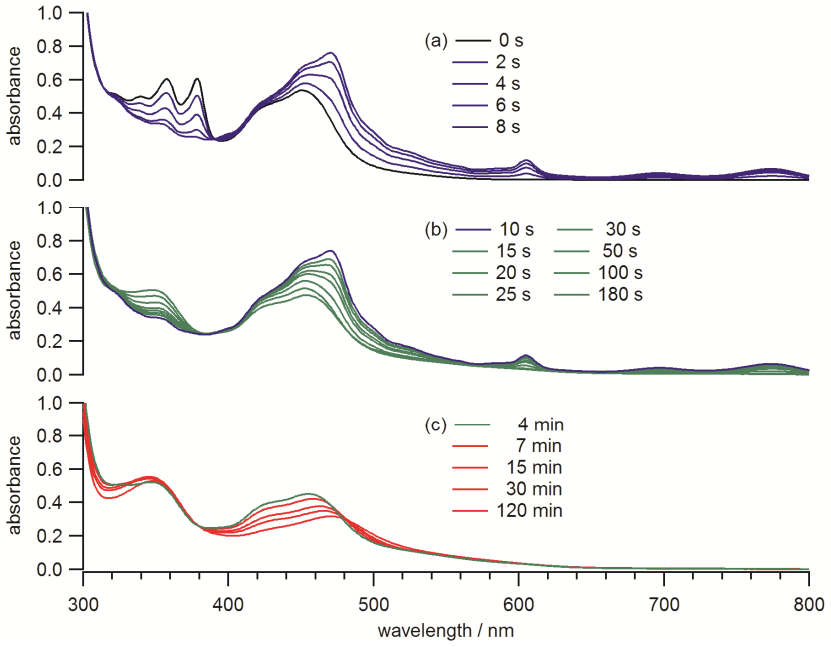

Figure S16. UV-Vis spectral changes observed after irradiating a solution of $3.9 \cdot 10^{-5}$ M $[Ru(bpy)_3]^{2+}$, $1.7 \cdot 10^{-5}$ M NDI reference compound (page S8), and 0.5 M Et_3N in de-aerated CH_3CN (20 °C) at 410 nm with a flux of $(4.42 \pm 0.06) \cdot 10^{16}$ photons / s. Irradiation times are given in the insets.

Initially (Figure S16a), one detects rapid disappearance of the NDI^0 related absorptions at 357 and 378 nm, combined with simultaneous growth of the NDI^- related absorptions at 470 and 605 nm. With continued irradiation (Figure S16b), these NDI^- absorptions disappear again, but without concomitant formation of NDI^{2-} which would manifest by absorptions at 397 and 420 nm (Figure 1 of the main paper). When irradiation is continued even further (Figure S16c), then the MLCT absorption band of $[Ru(bpy)_3]^{2+}$ red-shifts and becomes weaker, and there is new absorption between 480 and 540 nm, suggesting that decomposition of the photosensitizer takes place.

We speculate that NDI^{2-} is only formed transitorily in the form of a tight-ion pair together with the cationic photosensitizer, and as such it is not readily identifiable as a two-electron reduced species, because the spectral

signature of this ion-pair photo-product is different from that of isolated NDI^{2-} as a result of electron delocalization. On longer irradiation timescales, photo-decomposition occurs.
Ion-pairing is expected to be particularly prominent in the case of NDI^{2-} in the reference compound. In the case of triad **I** or pentad **II**, there are adjacent cationic charges due to the covalently attached photosensitizers, and there is more steric congestion around the central NDI unit.

The NDI reference compound exhibits similar electrochemical properties as NDI in triad **I** and pentad **II**. A cyclic voltammogram is shown in Figure S17.

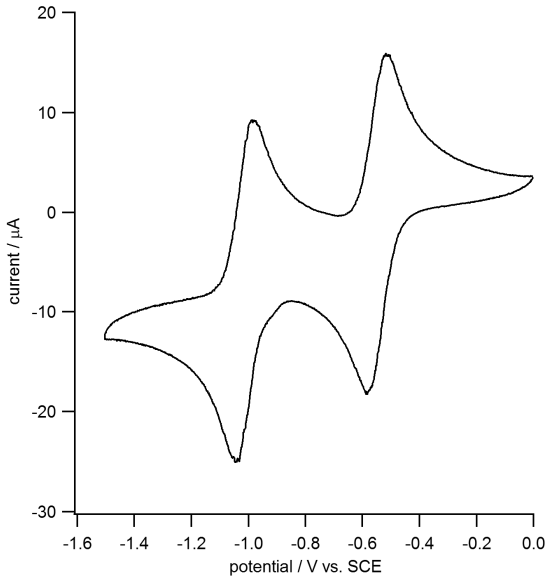

Figure S17. Cyclic voltammogram of NDI reference compound (page S8) in de-aerated CH_3CN with 0.1 M $TBAPF_6$. The potential sweep rate was 0.1 V/s.

References

(1) Mössinger, D.; Jester, S. S.; Sigmund, E.; Müller, U.; Höger, S., *Macromolecules* **2009,** *42*, 7974.

(2) Shen, H.; Vollhardt, K. P. C., *Synlett* **2012**, 208.

(3) Kuss-Petermann, M.; Wenger, O. S., *J. Phys. Chem. A* **2013,** *117*, 5726.

(4) Kobe, K. A.; Doumani, T. F., *Org. Synth.* **1941,** *21*, 96.

(5) (a) Curran, D. P.; Geib, S.; DeMello, N., *Tetrahedron* **1999,** *55*, 5681. (b) Mahood, S. A.; Schaffner, P. V. L., *Org. Synth.* **1931,** *11*, 32.

(6) (a) Guha, S.; Goodson, F. S.; Roy, S.; Corson, L. J.; Gravenmier, C. A.; Saha, S., *J. Am. Chem. Soc.* **2011,** *133*, 15256. (b) Dinolfo, P. H.; Williams, M. E.; Stern, C. L.; Hupp, J. T., *J. Am. Chem. Soc.* **2004,** *126*, 12989.

(7) (a) Heinz, L. G.; Yushchenko, O.; Neuburger, M.; Vauthey, E.; Wenger, O. S., *J. Phys. Chem. A* **2015,** *119*, 5676. (b) Costa, R. D.; Orti, E.; Bolink, H. J.; Monti, F.; Accorsi, G.; Armaroli, N., *Angew. Chem. Int. Ed.* **2012,** *51*, 8178.

(8) Keefe, M. H.; Benkstein, K. D.; Hupp, J. T., *Coord. Chem. Rev.* **2000,** *205*, 201.

(9) Bonn, A. G.; Yushchenko, O.; Vauthey, E.; Wenger, O. S., *Inorg. Chem.* **2016,** *55*, 2894.

(10) Pavlishchuk, V. V.; Addison, A. W., *Inorg. Chim. Acta* **2000,** *298*, 97.

(11) (a) Hatchard, C. G.; Parker, C. A., *Proc. R. Soc. Math. Phys. Eng. Sci* **1956,** *235*, 518. (b) Pozdnyakov, I. P.; Kel, O. V.; Plyusnin, V. F.; Grivin, V. P.; Bazhin, N. M., *J. Phys. Chem. A* **2008,** *112*, 8316. (c) Vitz, E. W., *J. Chem. Educ.* **1981,** *58*, 655.

7.3 Synthesis of the Ru-NDI-Rh Triad

[(bpy)$_2$Ru(bpy)-hxy-NDI-hxy-bpy] (NO$_3$)$_2$

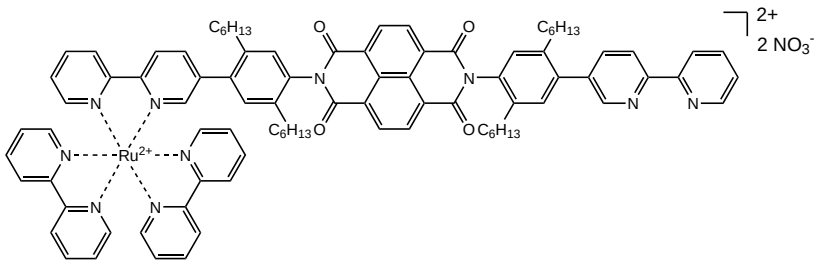

Under a flow of N_2, bpy-hxy-NDI-hxy-bpy (0.107 g, 0.100 mmol, 1.0 eq) and $[Ru(bpy)_2Cl_2]\cdot 2H_2O$ (0.052 g, 0.100 mmol, 1.0 eq) were dissolved in a mixture of $CHCl_3$ (3 mL) and EtOH (9 mL) and heated to reflux at 85 °C for 45 h. The solution was cooled to RT and the solvent removed at reduced pressure. The red solid was dissolved in DCM and preloaded onto SiO_2. The product was purified via column chromatography (SiO_2, i) acetone, ii) acetone:H_2O = 10:1, iii) acetone: H_2O = 85:15 sat. w. KNO_3). From the red solution eluted with iii) the organic solvent was removed and the red precipitate formed isolated via filtration. Washing with water and pentane and drying in vacuo yielded the product (0.090 g, 0.056 mmol, 56%) as a red solid.

^{1}H NMR (400 MHz, Chloroform-*d*) δ 8.96 – 8.82 (m, 6H), 8.82 – 8.70 (m, 4H), 8.65 (dd, J = 8.7, 3.5 Hz, 2H), 8.51 – 8.42 (m, 2H), 8.15 – 8.00 (m, 6H), 7.93 – 7.77 (m, 6H), 7.77 – 7.72 (m, 2H), 7.59 (t, J = 6.9 Hz, 1H), 7.53 – 7.41 (m, 4H), 7.37 – 7.30 (m, 2H), 7.28 (d, J = 2.3 Hz, 1H), 7.17 (d, J = 14.3 Hz, 1H), 7.08 (d, J = 14.8 Hz, 1H), 2.61 (t, J = 8.1 Hz, 2H), 2.49 – 2.09 (m, 10H), 1.60 – 1.42 (m, 4H), 1.29 – 0.92 (m, 24H), 0.81 – 0.73 (m, 6H), 0.72 – 0.63 (m, 6H) ppm.

[(bpy)$_2$Ru(bpy)-hxy-NDI-hxy-(bpy)Rh(Cp*)Cl] (NO$_3$)$_2$ Cl

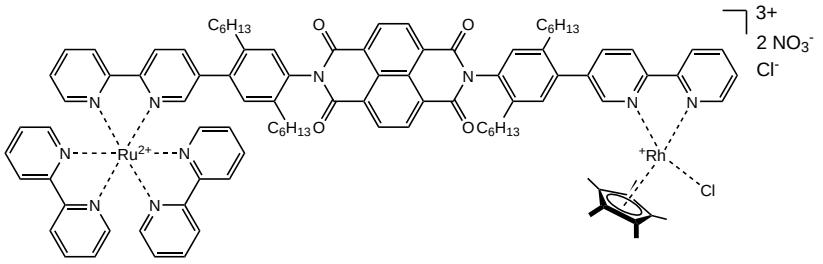

Under a flow of N_2, $[Rh(Cp^*)Cl_2]_2$ (18 mg, 29 μmol, 0.5 eq) was suspended in dry MeOH (2 mL). [(Bpy)$_2$Ru(bpy)-hxy-NDI-hxy-bpy] (NO$_3$)$_2$ (90 mg, 56 μmol, 1.0 eq) was dissolved in dry MeOH (6 mL), added to the suspension and stirred at RT for 4.5 h. The solvent volume was reduced by 75%, then Et_2O (40 mL) was added. The orange precipitate

formed was isolated via filtration, washed with Et_2O and dried in vacuo to give the product (77 mg, 40 µmol, 71%) as an orange solid.

^{1}H NMR (400 MHz, Acetonitrile-d_3) δ 8.94 (dd, J = 5.6, 1.5 Hz, 1H), 8.87 – 8.67 (m, 7H), 8.66 – 8.51 (m, 6H), 8.35 – 8.23 (m, 2H), 8.20 – 8.01 (m, 6H), 7.92 (dd, J = 5.6, 1.4 Hz, 1H), 7.88 – 7.69 (m, 6H), 7.51 – 7.35 (m, 7H), 7.25 (dd, J = 10.0, 2.0 Hz, 2H), 2.76 – 2.59 (m, 2H), 2.59 – 2.48 (m, 2H), 2.47 – 2.30 (m, 4H), 1.70 (s, 15H), 1.60 – 1.39 (m, 8H), 1.30 – 0.92 (m, 24H), 0.83 – 0.75 (m, 6H), 0.73 – 0.63 (m, 6H) ppm.

ESI-HRMS (m/z): calcd. for $C_{100}H_{105}N_{10}O_4ClRhRu^{3+}$: 583.2042; found: 583.2031.

Elemental analysis calcd. for $C_{100}H_{105}N_{12}O_{10}Cl_2RhRu{\cdot}8H_2O$ (%): C, 58.48; H, 5.94; N, 8.18. Found: C, 58.06; H, 5.60; N, 8.11.

7.4 Synthesis of the Ru-Rh-NDI Triad

hxy-NDI

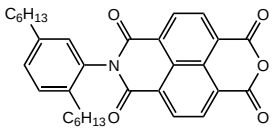

Under a flow of N_2, 1,4,5,8-naphthalenetetracarboxylic dianhydride (1.61 g, 6.00 mmol, 2.0 eq) was suspended in dry DMF (15 mL) and heated to 150 °C. A solution of 2,5-(di-*n*-hexyl)aniline (0.78 g, 2.98 mmol, 1.0 eq) in dry DMF (10 mL) was added dropwise over a period of 20 minutes. The reaction mixture was stirred at 150 °C for 5 days and cooled to 5 °C. Cold DCM (50 mL) and H_2O (50 mL) were added and the mixture placed in the fridge overnight. The black precipitate formed was filtered off and the filtrate extracted with DCM (4 × 50 mL). The combined organic layers were dried over Na_2SO_4 and the solvents removed at reduced pressure. Purification via column chromatography (SiO_2, i) DCM, ii) DCM + 5% MeOH, iii) acetone) gave the product (0.80 g, 1.56 mmol, 52%) as a black solid.

^{1}H NMR (400 MHz, Acetone-d_6) δ 9.48 – 7.67 (m, 4H), 7.42 – 6.95 (m, 3H), 2.97 – 2.11 (m, 4H), 1.65 – 0.61 (m, 22H) ppm.

ESI (m/z): calcd. for $[C_{32}H_{35}NO_6+H]^+$: 530.25; found: 530.16.

hxy-NDI-hxy-I

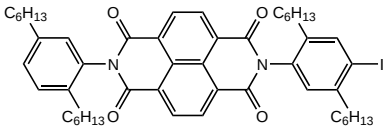

Under a flow of N_2, hxy-NDI (0.29 g, 0.54 mmol, 1.0 eq) and I-hxy-NH_2 (0.28 g, 0.71 mmol, 1.3 eq) were dissolved in acetic acid (5 mL) and heated to 120 °C for 45 h. The solution was cooled to RT, the solvent removed, the brown solid redissolved in DCM and preloaded onto SiO_2. Purification via column chromatography (SiO_2, pentane:Et_2O = 6:1) gave the product (0.21 g, 0.24 mmol, 44%) as a brown solid.

^{1}H NMR (400 MHz, Chloroform-d) δ 8.87 (s, 4H), 7.91 (s, 1H), 7.38 (d, J = 7.9 Hz, 1H), 7.30 (dd, J = 7.9, 1.8 Hz, 1H), 7.04 – 7.00 (m, 2H), 2.75 – 2.62 (m, 4H), 2.46 – 2.34 (m, 4H), 1.70 – 1.60 (m, 4H), 1.60 – 1.50 (m, 4H), 1.44 – 1.11 (m, 24H), 0.91 – 0.86 (m, 6H), 0.77 – 0.70 (m, 6H) ppm.

hxy-NDI-hxy-Bpin

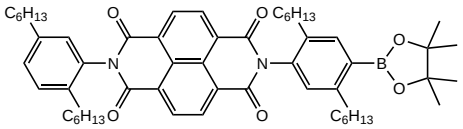

Under a flow of N_2, hxy-NDI-hxy-I (0.21 g, 0.24 mmol, 1.0 eq), $(Bpin)_2$ (0.11 g, 0.43 mmol, 2.0 eq), KOAc (0.11 g, 1.11 mmol, 4.6 eq) and $Pd(PPh_3)_2Cl_2$ (14 mg, 20 µmol, 0.083 eq) were dissolved in dry DMF (8 mL), the mixture degassed for 30 min and heated to 100 °C for 18 h. The solution was cooled to RT, the solvent removed, the brown solid redissolved in DCM and preloaded onto SiO_2. Purification via column chromatography (SiO_2, pentane:Et_2O = 6:1) gave the product (0.14 g, 0.16 mmol, 67%) as a yellow oil.

^{1}H NMR (400 MHz, Chloroform-*d*) δ 8.86 (d, J = 2.3 Hz, 4H), 7.86 (d, J = 1.5 Hz, 1H), 7.39 – 7.35 (m, 1H), 7.31 – 7.27 (m, 1H), 7.05 – 6.98 (m, 2H), 2.94 – 2.85 (m, 2H), 2.69 – 2.61 (m, 2H), 2.47 – 2.36 (m, 4H), 1.71 – 1.48 (m, 8H), 1.38 (s, 12H), 1.43 – 1.07 (m, 24H), 0.92 – 0.83 (m, 6H), 0.76 – 0.66 (m, 6H) ppm.

[(bpy)$_2$Ru(bpy)-xy-B(OH)$_2$] (PF$_6$)$_2$

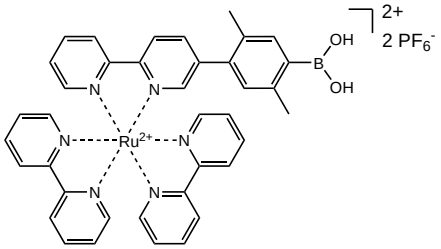

Under a flow of N_2, bpy-xy-Bpin (0.31 g, 0.81 mmol, 1.0 eq) and $[Ru(bpy)_2Cl_2]\cdot 2H_2O$ (0.53 g, 1.01 mmol, 1.2 eq) were dissolved in a mixture of $CHCl_3$ (3 mL) and EtOH (9 mL) and heated to reflux at 80 °C for 24 h. The solution was cooled to RT, the solvent removed, the red solid redissolved in DCM and preloaded onto SiO_2. The product was purified via column chromatography (SiO_2, i) acetone, ii) acetone:H_2O = 10:1, iii) acetone:H_2O = 10:1 sat. w. KNO_3). From the orange solution eluted with iii), the organic solvent was removed, a solution of aq. KPF_6 added and the orange precipitate formed isolated via filtration. Washing with water and Et_2O and drying in vacuo yielded the product (0.71 g, 0.70 mmol, 86%) as an orange solid.

^{1}H NMR (400 MHz, Acetone-d_6) δ 8.90 – 8.80 (m, 6H), 8.25 – 8.15 (m, 7H), 8.14 – 8.04 (m, 4H), 7.93 – 7.86 (m, 1H), 7.64 – 7.52 (m, 5H), 7.49 – 7.45 (m, 2H), 2.42 (s, 3H), 1.94 (s, 3H) ppm.

$[(bpy)_2Ru(bpy)\text{-}xy\text{-}bpy\text{-}Br]\ (PF_6)_2$

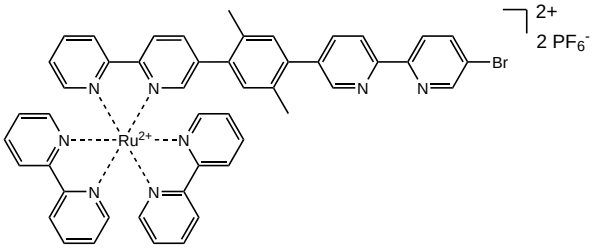

Under a flow of N_2, $[(bpy)_2Ru(bpy)\text{-}xy\text{-}B(OH)_2](PF_6)_2$ (0.20 g, 0.20 mmol, 1.0 eq), Br-bpy-Br (0.096 g, 0.30 mmol, 1.5 eq) and Na_2CO_3 (0.089 g, 0.84 mmol, 4.2 eq) were dissolved in a mixture of DMSO (4 mL) and H_2O (0.2 mL). The solution was degassed by three freeze-pump-thaw cycles, then $Pd(PPh_3)_4$ (0.014 g, 0.012 mmol, 0.06 eq) was added and the solution heated to 80 °C for 40 h. A flask with ice-cold sat. aq. KPF_6 (25 mL) was prepared and the reaction mixture transferred into the KPF_6 solution. The orange precipitate was isolated via filtration, washed with water and Et_2O and dried in vacuo. The product was purified via column chromatography (SiO_2, acetone:H_2O = 5:1, sat. w. KNO_3 + 2% NEt_3). From the orange solution eluted, the organic solvent was removed, a solution of aq. KPF_6 added and the orange precipitate formed isolated via filtration. Washing with water and Et_2O and drying in vacuo yielded the product (0.16 g, 0.13 mmol, 65%) as an orange solid.

^{1}H NMR (400 MHz, Acetonitrile-d_3) δ 8.77 (s, 1H), 8.63 (s, 1H), 8.59 – 8.43 (m, 7H), 8.38 (d, J = 8.5 Hz, 1H), 8.14 – 7.99 (m, 7H), 7.89 – 7.82 (m, 2H), 7.80 – 7.71 (m, 4H), 7.66 (d, J = 1.8 Hz, 1H), 7.46 – 7.33 (m, 5H), 7.22 (s, 1H), 7.12 (s, 1H), 2.27 (s, 3H), 2.00 (s, 3H) ppm.

[(bpy)$_2$Ru(bpy)-xy-bpy-hxy-NDI-hxy] (PF$_6$)$_2$

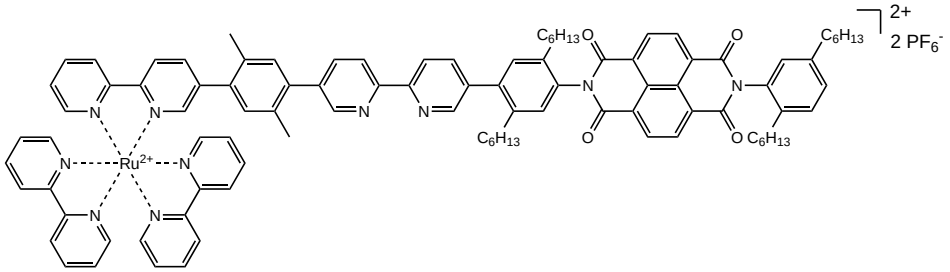

Under a flow of N_2, Na_2CO_3 (39.5 mg, 0.373 mmol, 8.9 eq) was dissolved in 10 drops of H_2O. Hxy-NDI-hxy-Bpin (62.4 mg, 70.2 µmol, 1.7 eq) and [(bpy)$_2$Ru(bpy)-xy-bpy-Br](PF$_6$)$_2$ (50.2 mg, 41.9 µmol, 1.0 eq) were added followed by DMSO (2 mL) and the mixture degassed by four freeze-pump-thaw cycles. $Pd(PPh_3)_4$ (9.7 mg, 8.4 µmol, 0.2 eq) was added and the reaction heated to 100 °C for 40 h. The reaction mixture was cooled to RT and transferred into an ice-cold sat. aq. KPF_6-solution. The brown precipitate was isolated via filtration, washed with H_2O and Et_2O and dried in vacuo. The product was purified via column chromatography (SiO_2, i) acetone, ii) acetone:H_2O = 10:1, iii) acetone:H_2O = 10:1 sat. w. KNO_3, iv) acetone:H_2O = 5:1 sat. w. KNO_3). From the product-containing orange solution eluted with iii) and iv), the organic solvent was removed, a solution of aq. KPF_6 added and the orange precipitate formed isolated via filtration. Washing with water and Et_2O and drying in vacuo yielded the product (30.1 mg, 16.1 µmol, 38%) as an orange solid.

^{1}H NMR (400 MHz, Chloroform-*d*) δ 9.08 – 8.94 (m, 3H), 8.89 (s, 4H), 8.74 – 8.40 (m, 6H), 8.37 – 8.22 (m, 2H), 8.14 – 7.90 (m, 6H), 7.90 – 7.70 (m, 5H), 7.64 – 7.39 (m, 6H), 7.39 – 7.32 (m, 2H), 7.32 – 7.18 (m, 4H), 7.12 (s, 1H), 7.05 – 6.98 (m, 1H), 2.68 – 2.55 (m, 4H), 2.51 – 2.37 (m, 4H), 2.26 (s, 3H), 1.93 (s, 3H), 1.71 – 1.43 (m, 8H), 1.41 – 0.95 (m, 24H), 0.90 – 0.63 (m, 12H) ppm.

ESI (m/z): calcd. for $C_{98}H_{98}N_{10}O_4Ru^{2+}$: 790.34; found: 790.54.

$[(bpy)_2Ru(bpy)\text{-}xy\text{-}(bpy)Rh(Cp^*)Cl\text{-}hxy\text{-}NDI\text{-}hxy]\ (PF_6)_3$

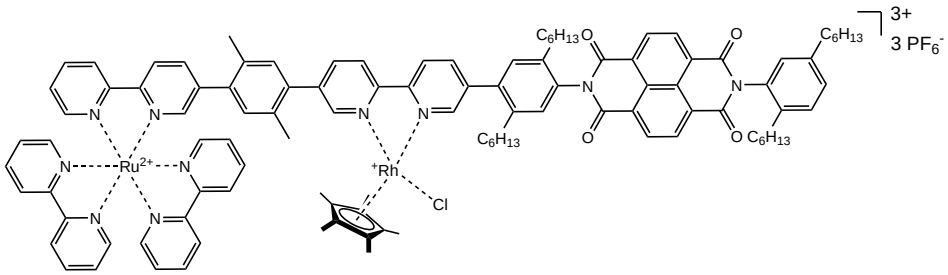

Under a flow of N_2, $[(bpy)_2Ru(bpy)\text{-}xy\text{-}bpy\text{-}hxy\text{-}NDI\text{-}hxy](PF_6)_2$ (30.1 mg, 16.1 µmol, 1.0 eq) and $[RhCp^*Cl_2]_2$ (5.0 mg, 8.1 µmol, 0.5 eq) were dissolved in dry MeOH (2 mL) and stirred at RT for 2 h. The solvent was removed, the crude dissolved in a mixture of sat. aq. KPF_6(2 mL) and acetone (5 mL) and stirred at RT for 30 minutes. The reaction mixture was extracted with DCM (3 × 10 mL), the combined organic phases dried over Na_2SO_4 and the solvent removed at reduced pressure. The orange solid was dissolved in few DCM and transferred in an excess of pentane. The orange precipitate was isolated via filtration, washed with pentane and dried in vacuo to give the product (25.6 mg, 11.2 µmol, 70%) as an orange solid.

^{1}H NMR (400 MHz, Acetonitrile-d_3) δ 8.87 (s, 1H), 8.83 – 8.73 (m, 5H), 8.67 – 8.50 (m, 8H), 8.34 (d, J = 7.8 Hz, 1H), 8.24 (d, J = 7.8 Hz, 1H), 8.17 – 8.01 (m, 6H), 7.90 (d, J = 5.3 Hz, 1H), 7.83 – 7.73 (m, 4H), 7.68 (s, 1H), 7.48 – 7.36 (m, 8H), 7.33 – 7.27 (m, 2H), 7.23 (s, 1H), 7.16 (s, 1H), 2.74 – 2.61 (m, 4H), 2.58 – 2.50 (m, 2H), 2.46 – 2.37 (m, 2H), 2.33 (s, 3H), 2.05 (s, 3H), 1.69 (s, 15H), 1.74 – 1.43 (m, 8H), 1.41 – 1.06 (m, 24H), 0.92 – 0.82 (m, 6H), 0.74 – 0.64 (m, 6H) ppm.

ESI-HRMS (m/z): calcd. for $C_{108}H_{113}N_{10}O_4ClRhRu^{3+}$: 617.8914; found: 617.8917.

Elemental analysis calcd. for $C_{108}H_{113}N_{10}O_4F_{18}P_3ClRhRu{\cdot}4H_2O$ (%): C, 54.93; H, 5.16; N, 5.93. Found: C, 54.94; H, 5.53; N, 5.71.

7.5 Synthesis of the exTTF-PTZ-Ru Triad

Suzuki couplings and Miyaura borylations were performed following the general procedure published for the NDI triad and pentad shown in section 7.2. TMS-group deprotection was performed with ICl following a well-established procedure.[176]

I-hxy-I

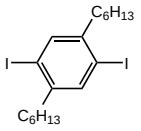

The title compound was synthesized after the procedure published in the literature.[177]

TMS-hxy-I

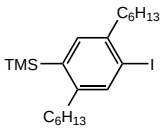

Under a flow of N_2, I-hxy-I (5.00 g, 10.0 mmol, 1.0 eq) was dissolved in dry Et_2O (50 mL) and cooled to 0 °C. nBuLi (4.80 mL, 2.5 M in hexanes, 12.0 mmol, 1.2 eq) was slowly added and the reaction stirred at 0 °C for 30 min. TMSCl (1.37 g, 1.60 mL, 12.6 mmol, 1.3 eq) was added at 0 °C and then left to warm to RT over night while stirring. H_2O (50 mL) was added and the mixture stirred at RT for 10 min. The organic layer was separated and the aqueous layer extracted with DCM (3 × 50 mL). Combined organic layers were washed with sat. aq. $Na_2S_2O_3$-solution (30 mL), dried over Na_2SO_4 and the solvent removed at reduced pressure. The light brown oil obtained (quant.) was used in the next step without further purification.

Bpin-hxy-Bpin

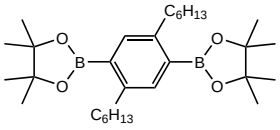

Under a flow of N_2, I-hxy-I (7.47 g, 15.0 mmol, 1.0 eq), $(Bpin)_2$ (11.4 g, 45.0 mmol, 3.0 eq), KOAc (11.8 g, 120 mmol, 8.0 eq) and $Pd(PPh_3)_2Cl_2$ (0.52 g, 0.74 mmol, 0.05 eq) were dissolved in dry DMSO (50 mL), degassed for 30 min and heated to 90 °C for 16 h. The solution was cooled to RT, sat. aq. NH_4Cl was added and the mixture extracted with DCM (3 × 30 mL). Combined organic layers were dried over Na_2SO_4. The solvent was

removed under reduced pressure, the crude product redissolved in DCM and preloaded onto SiO_2. Purification via column chromatography (SiO_2, pentane:DCM = 4:1) gave the product (5.87 g, 11.8 mmol, 79%) as a white solid.

^{1}H NMR (250 MHz, Chloroform-*d*) δ 7.52 (s, 2H), 2.87 – 2.73 (m, 4H), 1.61 – 1.44 (m, 4H), 1.34 (s, 24H), 1.40 – 1.22 (m, 12H), 0.94 – 0.82 (m, 6H) ppm.

exTTF-Br

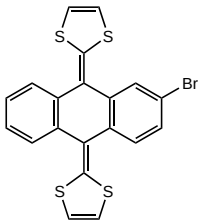

The synthesis of the title compound was based on a procedure described in the literature.[113, 124]

Under a flow of N_2, dimethyl 2-(1,3-dithiole)phosphonate (2.57 g, 12.1 mmol, 4.1 eq) was dissolved in dry THF (120 mL) and cooled to -78 °C. nBuLi (5.30 mL, 2.5 M in hexanes, 13.3 mmol, 4.5 eq) was added and the suspension stirred at -78 °C for 40 min. 2-Bromoanthraquinone (0.85 g, 2.96 mmol, 1.0 eq) was dissolved in dry THF (140 mL) and added to the reaction mixture over 20 min. The solution was stirred at -78 °C for 90 min, heated to RT and stirred at RT for another 18 h. The solvent was removed at reduced pressure, water (120 mL) and DCM (120 mL) were added to dissolve all solid and the organic solvent was removed at reduced pressure. The yellow precipitate was isolated via filtration and washed thoroughly with pentane:DCM = 9:1 and with pure pentane. After drying in air, the product (1.06 g, 2.31 mmol, 78%) was obtained as a yellow solid.

^{1}H NMR (400 MHz, Methylene Chloride-d_2) δ 7.80 (d, J = 2.1 Hz, 1H), 7.69 (t, J = 4.5 Hz, 2H), 7.57 (d, J = 8.2 Hz, 1H), 7.41 (dd, J = 8.3, 2.1 Hz, 1H), 7.36 – 7.26 (m, 2H), 6.35 (d, J = 5.8 Hz, 4H) ppm.

exTTF-Bpin

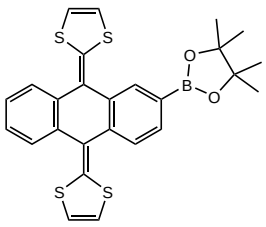

Under a flow of N_2, exTTF-Br (0.69 g, 1.50 mmol, 1.0 eq), $(Bpin)_2$ (0.59 g, 2.32 mmol, 1.5 eq) and KOAc (0.62 g, 6.32 mmol, 4.2 eq) were dissolved in dry DMF (20 mL) and

the solution degassed for 20 min. $Pd(PPh_3)_2Cl_2$ (61 mg, 87 µmol, 0.06 eq) was added and the solution heated to 100 °C for 38 h. The solution was cooled to RT and the solvent removed at reduced pressure. The solid was redissolved in DCM and preloaded onto SiO_2. Purification via column chromatography (SiO_2, i) pentane:DCM = 3:1, ii) pentane:DCM = 1:1, iii) neat DCM) gave the product (0.74 g, 1.46 mmol, 97%) as a yellow solid.

^{1}H NMR (400 MHz, Chloroform-*d*) δ 7.70 (dd, J = 5.7, 3.3 Hz, 4H), 7.29 (dd, J = 5.8, 3.3 Hz, 3H), 6.34 – 6.25 (m, 4H), 1.25 (s, 12H) ppm.

exTTF-hxy-TMS

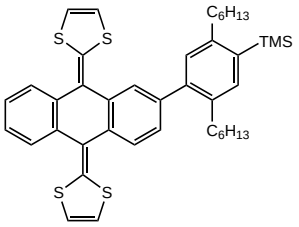

Under a flow of N_2, exTTF-Bpin (0.78 g, 1.54 mmol, 1.0 eq), I-hxy-TMS (1.03 g, 2.32 mmol, 1.5 eq) and Na_2CO_3 (0.65 g, 6.13 mmol, 4.0 eq) were dissolved in a mixture of THF (80 mL) and H_2O (20 mL). The solution was degassed for 25 min, $Pd(PPh_3)_4$ (82 mg, 71 µmol, 0.05 eq) added and the solution heated to reflux at 85 °C for 18 h. The solution was cooled to RT, H_2O (50 mL) and DCM (50 mL) added, the organic layer separated and the aqueous layer extracted with DCM (3 × 50 mL). Combined organic layers were dried over Na_2SO_4 and the solvent removed at reduced pressure. Purification via column chromatography (SiO_2, pentane:EtOAc = 15:1) gave the product (1.02 g, 1.46 mmol, 95%) as a yellow solid.

^{1}H NMR (400 MHz, Chloroform-*d*) δ 7.74 – 7.66 (m, 3H), 7.65 – 7.60 (m, 1H), 7.38 (s, 1H), 7.33 – 7.29 (m, 2H), 7.29 – 7.27 (m, 1H), 7.10 (s, 1H), 6.26 – 6.17 (m, 4H), 2.74 – 2.63 (m, 4H), 1.67 – 1.46 (m, 4H), 1.36 – 1.15 (m, 12H), 0.90 – 0.84 (m, 3H), 0.82 – 0.76 (m, 3H), 0.36 (s, 9H) ppm.

exTTF-hxy-I

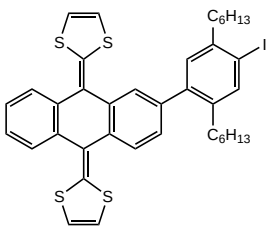

Under a flow of N_2, exTTF-hxy-TMS (1.02 g, 1.46 mmol, 1.0 eq) was dissolved in dry

DCM (100 mL). The solution was cooled to 0 °C and a solution of ICl (0.53 g, 3.26 mmol, 2.2 eq) in dry DCM (10 mL) was added while stirring. The reaction mixture was stirred at 0 °C for 1 h. Sat. aq. $Na_2S_2O_3$ (50 mL) was added to quench the reaction, then DCM (50 mL) was added. The organic layer was separated, the aqueous layer extracted with DCM (3 × 50 mL), combined organic layers dried over Na_2SO_4 and the solvent removed at reduced pressure. The crude product was redissolved in DCM and preloaded on celite. Purification via column chromatography (SiO_2, pentane:EtOAc = 15:1) gave the product (0.60 g, 0.80 mmol, 55%) as a yellow oil.

^{1}H NMR (400 MHz, Chloroform-*d*) δ 7.75 – 7.71 (m, 3H), 7.59 (d, J = 1.7 Hz, 1H), 7.34 – 7.28 (m, 3H), 7.20 (dd, J = 7.9, 1.8 Hz, 1H), 7.07 (s, 1H), 6.34 – 6.21 (m, 4H), 2.74 – 2.56 (m, 4H), 1.67 – 1.37 (m, 4H), 1.37 – 1.14 (m, 12H), 0.92 – 0.87 (m, 3H), 0.84 – 0.77 (m, 3H) ppm.

exTTF-hxy-Bpin (Method 1)

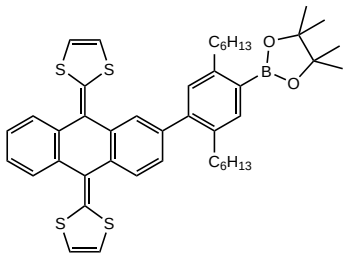

Under a flow of N_2, exTTF-hxy -I (0.60 g, 0.80 mmol, 1.0 eq), $(Bpin)_2$ (0.43 g, 1.69 mmol, 2.1 eq) and KOAc (0.40 g, 4.08 mmol, 5.1 eq) were dissolved in dry DMF (30 mL) and the solution degassed for 20 min. $Pd(PPh_3)_2Cl_2$ (26 mg, 37 µmol, 0.05 eq) was added and the solution heated to 100 °C for 96 h. The solution was cooled to RT and the solvent removed at reduced pressure. The solid was redissolved in DCM and preloaded onto SiO_2. Purification via column chromatography (SiO_2, i) pentane:DCM = 5:1, ii) pentane:DCM = 1:1) gave the product (0.23 g, 0.30 mmol, 38%) as a yellow solid.

^{1}H NMR (400 MHz, Chloroform-*d*) δ 7.75 – 7.70 (m, 4H), 7.62 (d, J = 1.7 Hz, 1H), 7.32 – 7.29 (m, 2H), 7.23 (dd, J = 7.9, 1.7 Hz, 1H), 7.08 (s, 1H), 6.32 – 6.25 (m, 4H), 2.91 – 2.83 (m, 2H), 2.74 – 2.61 (m, 2H), 1.67 – 1.44 (m, 4H), 1.37 (s, 12H), 1.34 – 1.15 (m, 12H), 0.91 – 0.85 (m, 3H), 0.81 – 0.76 (m, 3H) ppm.

exTTF-hxy-Bpin (Method 2)

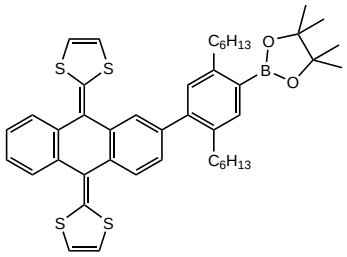

Under a flow of N_2, exTTF-Br (0.751 g, 1.63 mmol, 1.0 eq), Bpin-hxy-Bpin (1.59 g, 3.19 mmol, 2.0 eq), Na_2CO_3 (0.56 g, 5.28 mmol, 3.2 eq) and $Pd(PPh_3)_4$ (0.11 g, 95 µmol, 0.06 eq) were dissolved in a mixture of THF (400 mL) and H_2O (100 mL). The solution was degassed for 40 min and heated to reflux at 75 °C for 96 h. The solution was cooled to RT, H_2O (100 mL) and DCM (200 mL) added and the organic layer separated. The aqueous layer was extracted with DCM (5 × 70 mL) and the combined organic layers were dried over Na_2SO_4. The solvent was removed at reduced pressure, the resulting oil redissolved in DCM and preloaded onto SiO_2. Purification via column chromatography (SiO_2, pentane:EtOAc = 5:1) gave the product (0.590 g, 0.786 mmol, 48%) as a yellow solid.

^{1}H NMR (400 MHz, Chloroform-*d*) δ 7.78 – 7.71 (m, 4H), 7.65 (d, J = 1.7 Hz, 1H), 7.35 – 7.28 (m, 2H), 7.26 (dd, J = 7.9, 1.8 Hz, 1H), 7.11 (s, 1H), 6.27 (d, J = 10.8 Hz, 4H), 2.97 – 2.83 (m, 2H), 2.77 – 2.63 (m, 2H), 1.68 – 1.48 (m, 4H), 1.40 (s, 12H), 1.36 – 1.17 (m, 12H), 0.94 – 0.89 (m, 3H), 0.85 – 0.78 (m, 3H) ppm.

PTZ

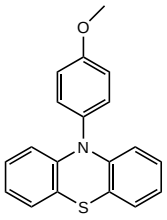

The title compound was obtained via a modified literature procedure.[178, 179]

Under a flow of N_2, 10*H*-phenothiazine (1.99 g, 9.99 mmol, 1.0 eq), 1-iodo-4-methoxybenzene (2.81 g, 12.01 mmol, 1.2 eq), $Pd(dba)_2$ (0.29 g, 0.50 mmol, 0.05 eq) and $(HP^tBu_3)BF_4$ (0.15 g, 0.52 mmol, 0.05 eq) were dissolved in toluene (30 mL). The solution was degassed for 30 min, KO^tBu (3.37 g, 30.0 mmol, 3.0 eq) was added and the reaction heated to 120 °C for 3.5 h. The solution was cooled to RT, H_2O (50 mL) and DCM (50 mL) added and the organic layer separated. The aqueous phase was extracted with DCM (3 × 50 mL) and the combined organic layers were dried over Na_2SO_4. The solvent was removed at reduced

pressure, the crude product redissolved in DCM and preloaded onto SiO_2. Purification via column chromatography (SiO_2, pentane:DCM = 5:1) gave the product (2.89 g, 9.47 mmol, 95%) as a white solid.

^{1}H NMR (250 MHz, Acetone-d_6) δ 7.39 – 7.30 (m, 2H), 7.26 – 7.19 (m, 2H), 7.04 – 6.98 (m, 2H), 6.94 – 6.78 (m, 4H), 6.24 – 6.18 (m, 2H), 3.92 (s, 3H) ppm.

Br-PTZ-Br

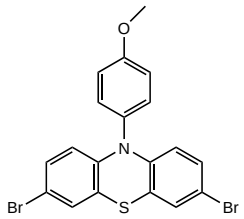

The title compound was synthesized following a literature procedure.[178]

Under a flow of N_2, PTZ (2.89 g, 9.46 mmol, 1.0 eq) and NBS (3.89 g, 22.0 mmol, 2.3 eq) were dissolved in dry DCM (80 mL) and the reaction mixture was stirred at RT for 2.5 h under the exclusion of light. The reaction was quenched with aq. sat. $Na_2S_2O_3$ (50 mL), the organic layer separated, the aqueous phase extracted with DCM (3 × 50 mL) and the combined organic layers dried over Na_2SO_4. The solvent was removed at reduced pressure, the crude product redissolved in DCM and preloaded onto SiO_2. Purification via column chromatography (SiO_2, pentane:DCM = 2:1) gave the product (4.11 g, 8.87 mmol, 94%) as a light yellow solid.

^{1}H NMR (400 MHz, Acetone-d_6) δ 7.39 – 7.32 (m, 2H), 7.26 – 7.20 (m, 2H), 7.18 (d, J = 2.3 Hz, 2H), 7.06 (dd, J = 8.8, 2.3 Hz, 2H), 6.11 (d, J = 8.8 Hz, 2H), 3.92 (s, 3H) ppm.

TMS-xy-B(OH)$_2$

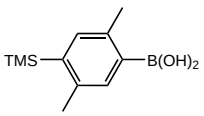

The title compound was synthesized in two steps from 2,5-dibromo-*p*-xylene after the procedure published in the literature.[180]

TMS-xy-PTZ-xy-TMS

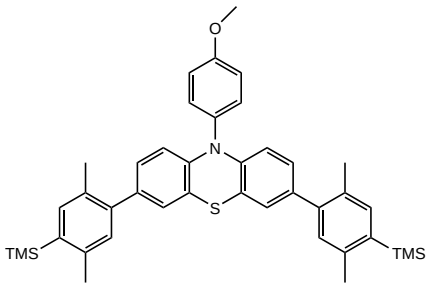

Under a flow of N_2, Br-PTZ-Br (1.85 g, 3.99 mmol, 1.0 eq), $(HO)_2$B-xy-TMS (2.13 g, 9.59 mmol, 2.4 eq) and Na_2CO_3 (2.54 g, 24.0 mmol, 6.0 eq) were dissolved in a mixture of THF (32 mL) and H_2O (8 mL). The solution was degassed for 20 min, $Pd(PPh_3)_4$ (0.46 g, 0.40 mmol, 0.1 eq) added and the solution heated to reflux at 85 °C for 16 h. The solution was cooled to RT, H_2O (50 mL) and DCM (50 mL) added, the organic layer separated and the aqueous layer extracted with DCM (3 × 50 mL). Combined organic layers were dried over Na_2SO_4 and the solvent removed at reduced pressure. The crude product was redissolved in DCM and preloaded onto SiO_2. Purification via column chromatography (SiO_2, pentane:DCM = 5:1) gave the product (2.58 g, 3.92 mmol, 98%) as a yellow solid. ^{1}H NMR (250 MHz, Acetone-d_6) δ 7.48 – 7.42 (m, 2H), 7.32 (s, 2H), 7.30 – 7.25 (m, 2H), 7.01 (d, J = 2.0 Hz, 2H), 6.98 (s, 2H), 6.90 (dd, J = 8.5, 2.1 Hz, 2H), 6.28 (d, J = 8.5 Hz, 2H), 3.94 (s, 3H), 2.42 (s, 6H), 2.23 (s, 6H), 0.33 (s, 18H) ppm.

I-xy-PTZ-xy-I

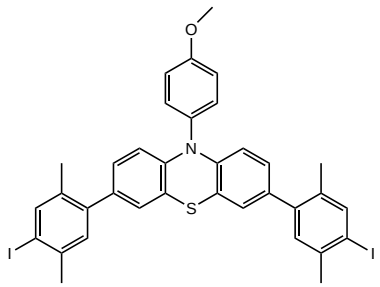

Under a flow of N_2, TMS-xy-PTZ-xy-TMS (2.58 g, 3.92 mmol, 1.0 eq) was dissolved in dry DCM (50 mL). The solution was cooled to -78 °C and a solution of ICl (2.66 g, 16.4 mmol, 4.2 eq) in dry DCM (3 mL) was added while stirring. The reaction mixture was stirred at -78 °C for 1 h. Sat. aq. $Na_2S_2O_3$ (80 mL) was added to quench the reaction, then DCM (50 mL) was added. The organic layer was separated, the aqueous layer extracted with DCM (3 × 50 mL), combined organic layers dried over Na_2SO_4 and the solvent removed at reduced pressure. The crude product was redissolved in DCM and preloaded onto SiO_2. Purification via column chromatography (SiO_2, pentane:DCM = 3:1) gave the product

(2.91 g, 3.80 mmol, 97%) as a yellow solid.

^{1}H NMR (400 MHz, Acetone-d_6) δ 7.72 (s, 2H), 7.46 – 7.41 (m, 2H), 7.30 – 7.25 (m, 2H), 7.12 (s, 2H), 7.01 (d, J = 2.1 Hz, 2H), 6.90 (dd, J = 8.5, 2.1 Hz, 2H), 6.28 (d, J = 8.5 Hz, 2H), 3.93 (s, 3H), 2.38 (s, 6H), 2.20 (s, 6H) ppm.

exTTF-hxy-xy-PTZ-xy-I

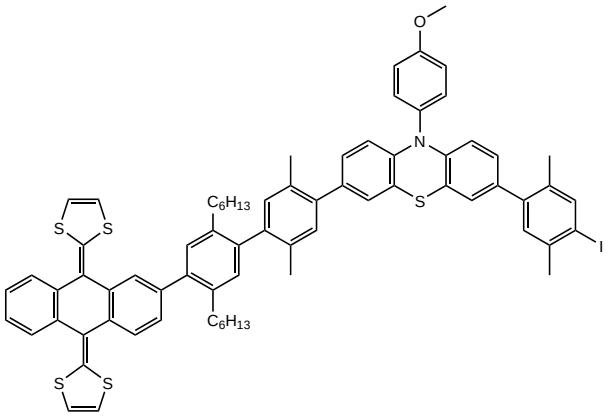

Under a flow of N_2, exTTF-hxy-Bpin (0.590 g, 0.786 mmol, 1.0 eq), I-xy-PTZ-xy-I (1.00 g, 1.31 mmol, 1.7 eq), Na_2CO_3 (0.402 g, 3.79 mmol, 4.8 eq) and $Pd(PPh_3)_4$ (80 mg, 69 µmol, 0.09 eq) were dissolved in a mixture of THF (100 mL) and H_2O (25 mL). The solution was degassed for 30 min and heated to reflux at 75 °C for 65 h. The solution was cooled to RT, H_2O (20 mL) and DCM (50 mL) added and the solution stirred at RT for 10 min. The organic layer was separated and the aqueous layer extracted with DCM (3 × 50 mL). Organic layers were dried over Na_2SO_4 and the solvent removed at reduced pressure. The resulting oil was redissolved in DCM and preloaded onto SiO_2. Purification via column chromatography (SiO_2, pentane:EtOAc = 5:1) gave the product (0.571 g, 0.452 mmol, 58%) as a yellow solid.

^{1}H NMR (400 MHz, Chloroform-d) δ 7.79 – 7.68 (m, 5H), 7.45 – 7.38 (m, 2H), 7.36 – 7.28 (m, 3H), 7.21 – 7.15 (m, 3H), 7.12 – 7.02 (m, 5H), 6.99 – 6.96 (m, 1H), 6.92 (dd, J = 8.4, 2.1 Hz, 1H), 6.78 (dd, J = 8.4, 2.1 Hz, 1H), 6.35 – 6.22 (m, 6H), 3.93 (s, 3H), 2.76 – 2.64 (m, 2H), 2.53 – 2.32 (m, 2H), 2.41 (s, 3H), 2.30 (s, 3H), 2.21 (s, 3H), 2.12 (s, 3H), 1.60 – 1.42 (m, 4H), 1.35 – 1.12 (m, 12H), 0.82 (q, J = 7.0 Hz, 6H) ppm.

exTTF-hxy-xy-PTZ-xy-hxy-exTTF

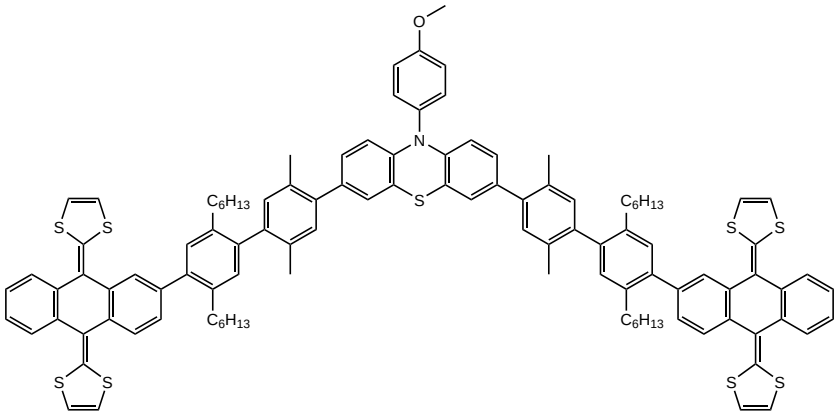

The product was obtained as a side-product from the synthesis of exTTF-hxy-xy-PTZ-xy-I.

^{1}H NMR (400 MHz, Chloroform-*d*) δ 7.77 – 7.69 (m, 8H), 7.46 – 7.42 (m, 2H), 7.33 – 7.29 (m, 6H), 7.20 – 7.16 (m, 4H), 7.10 – 7.04 (m, 8H), 6.91 (dd, J = 8.4, 2.1 Hz, 2H), 6.34 – 6.26 (m, 10H), 3.94 (s, 3H), 2.74 – 2.65 (m, 4H), 2.48 – 2.42 (m, 2H), 2.40 – 2.36 (m, 2H), 2.29 (s, 6H), 2.11 (s, 6H), 1.75 – 1.07 (m, 32H), 0.80 (dt, J = 8.7, 6.7 Hz, 12H) ppm.

exTTF-hxy-xy-PTZ-xy-Bpin

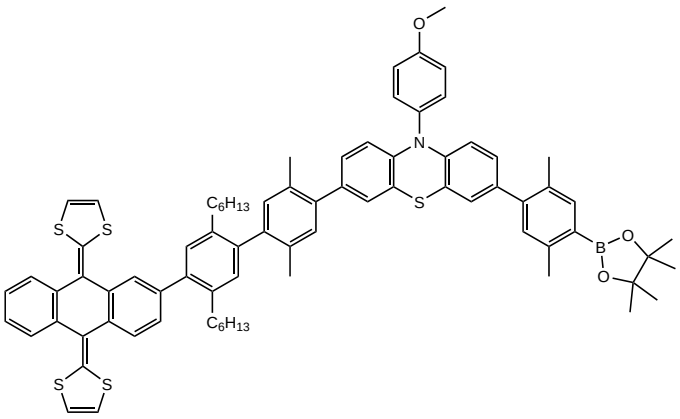

Under a flow of N_2, exTTF-hxy-xy-PTZ-xy-I (0.334 g, 0.265 mmol, 1.0 eq), $(Bpin)_2$ (0.145 g, 0.571 mmol, 2.2 eq), KOAc (0.166 g, 1.69 mmol, 6.4 eq) and $Pd(PPh_3)_2Cl_2$ (19 mg, 27 µmol, 0.1 eq) were dissolved in dry DMF (20 mL) and the solution degassed for 30 min. After heating to 100 °C for 60 h, the solution was cooled to RT and the solvent removed at reduced pressure. The solid was redissolved in DCM and preloaded onto SiO_2. Purification via column chromatography (SiO_2, pentane:EtOAc = 4:1) gave the product (0.199 g, 0.158 mmol, 60%) as a light brown oil.

^{1}H NMR (400 MHz, Chloroform-*d*) δ 7.80 – 7.68 (m, 4H), 7.65 (s, 1H), 7.44 – 7.38 (m, 2H), 7.34 – 7.27 (m, 3H), 7.20 – 7.13 (m, 3H), 7.11 – 7.04 (m, 4H), 7.02 – 6.99 (m, 2H),

6.90 (dd, J = 8.4, 2.1 Hz, 1H), 6.82 (dd, J = 8.5, 2.1 Hz, 1H), 6.36 – 6.18 (m, 6H), 3.92 (s, 3H), 2.74 – 2.64 (m, 2H), 2.52 (s, 3H), 2.48 – 2.33 (m, 2H), 2.29 (s, 3H), 2.26 (s, 3H), 2.11 (s, 3H), 1.80 – 1.62 (m, 2H), 1.57 – 1.42 (m, 2H), 1.36 (s, 12H), 1.33 – 1.08 (m, 12H), 0.84 – 0.77 (m, 6H) ppm.

exTTF-hxy-xy-PTZ-xy-bpy (L^D)

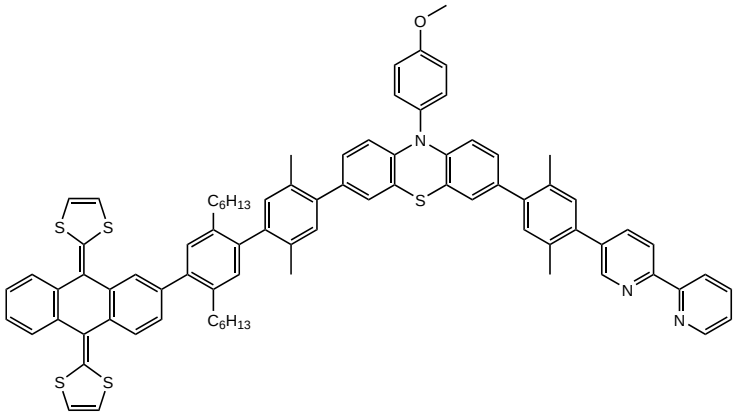

Under a flow of N_2, exTTF-hxy-xy-PTZ-xy-Bpin (113 mg, 90 µmol, 1.0 eq), 5-bromo-2,2'-bipyridine (33 mg, 141 µmol, 1.6 eq) and Na_2CO_3 (44 mg, 417 µmol, 4.6 eq) were dissolved in a mixture of THF (20 mL) and H_2O (5 mL). The solution was degassed for 20 min, $Pd(PPh_3)_4$ (12 mg, 11 µmol, 0.12 eq) added and the solution heated to reflux at 75 °C for 43 h. The solution was cooled to RT, H_2O (50 mL) and DCM (30 mL) added and the solution stirred at RT for 10 min. The organic layer was separated and the aqueous layer extracted with DCM (3 × 30 mL). Organic layers were dried over Na_2SO_4 and the solvent removed at reduced pressure. The yellow oil was redissolved in DCM and preloaded onto SiO_2. Purification via column chromatography (SiO_2, pentane:EtOAc = 1:1) gave the product (75 mg, 58 µmol, 65%) as a yellow solid.

^{1}H NMR (400 MHz, Chloroform-d) δ 8.83 – 8.62 (m, 2H), 8.48 (t, J = 8.2 Hz, 2H), 8.41 – 8.30 (m, 1H), 8.03 – 7.90 (m, 1H), 7.90 – 7.79 (m, 2H), 7.79 – 7.65 (m, 3H), 7.43 (d, J = 8.7 Hz, 2H), 7.39 – 7.27 (m, 4H), 7.18 (t, J = 7.3 Hz, 5H), 7.13 – 7.04 (m, 5H), 6.96 – 6.85 (m, 2H), 6.30 (d, J = 10.4 Hz, 5H), 3.93 (s, 3H), 2.41 – 2.24 (m, 9H), 2.12 (s, 3H), 1.62 – 1.43 (m, 4H), 1.38 – 1.07 (m, 16H), 0.95 – 0.72 (m, 6H) ppm.

$[Ru(L^D)(bpy)_2]\ (PF_6)_2$

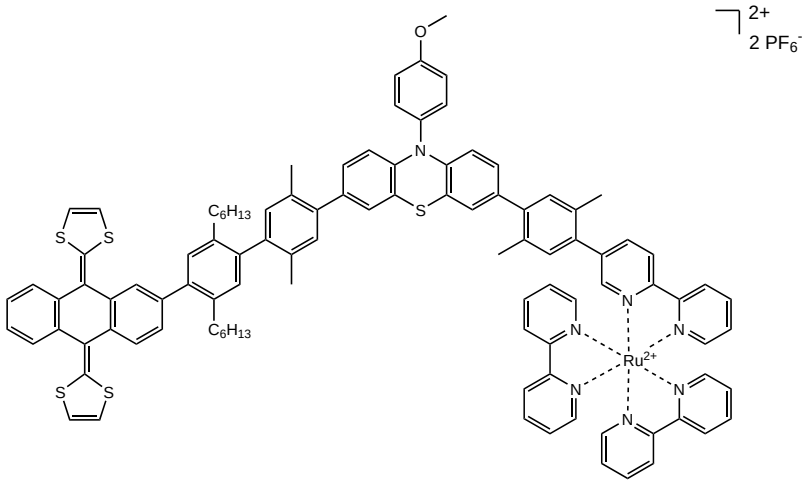

Under a flow of N_2, exTTF-hxy-xy-PTZ-xy-bpy (25.2 mg, 19.5 μmol, 1.0 eq) and $[Ru(bpy)_2Cl_2]\cdot 2H_2O$ (12.5 mg, 24.0 μmol, 1.2 eq) were dissolved in a mixture of EtOH (3 mL) and $CHCl_3$ (1 mL). The mixture was refluxed at 80 °C for 20 h, cooled to RT and the solvents removed at reduced pressure. The solid was redissolved in DCM and preloaded onto TiO_2. The product was purified via column chromatography (TiO_2, i) neat acetone, ii) acetone:H_2O = 10:1, iii) acetone:H_2O = 5:1, iv) acetone:H_2O = 5:1 sat. w. KNO_3). From the red fractions eluted with iv) the organic solvent was removed and a saturated solution of aq. KPF_6 added. The red solid formed was dissolved in DCM, the aqueous phase extracted with DCM (3 × 30 mL), the combined organic layers dried over Na_2SO_4 and the solvent removed at reduced pressure afterwards. The solid was dissolved in a minimum of DCM and transferred into an excess of Et_2O. The solid formed was isolated via filtration, washed with several portions of Et_2O and dried in air to give the product (14.0 mg, 7.02 μmol, 36%) as an orange solid.

^{1}H NMR (400 MHz, Methylene Chloride-d_2) δ 8.57 – 8.39 (m, 7H), 8.29 – 8.21 (m, 1H), 8.15 – 7.97 (m, 8H), 7.83 – 7.64 (m, 10H), 7.54 – 7.37 (m, 9H), 7.22 – 7.15 (m, 3H), 7.11 – 7.01 (m, 6H), 6.98 – 6.87 (m, 2H), 6.82 – 6.76 (m, 1H), 6.58 – 6.49 (m, 1H), 6.28 (t, J = 8.5 Hz, 2H), 3.91 (s, 3H), 2.74 – 2.56 (m, 2H), 2.53 – 2.30 (m, 2H), 2.27 (d, J = 2.5 Hz, 3H), 2.24 (s, 3H), 2.10 (d, J = 3.5 Hz, 3H), 1.93 (s, 3H), 1.51 – 1.40 (m, 4H), 1.33 – 1.08 (m, 12H), 0.84 – 0.72 (m, 6H) ppm.

^{1}H NMR (400 MHz, Acetonitrile-d_3) δ 8.57 – 8.45 (m, 8H), 8.11 – 8.04 (m, 7H), 7.80 – 7.70 (m, 8H), 7.63 – 7.60 (m, 1H), 7.45 – 7.33 (m, 10H), 7.25 – 7.19 (m, 3H), 7.13 – 7.10 (m, 1H), 7.07 – 6.98 (m, 7H), 6.93 – 6.88 (m, 1H), 6.86 – 6.81 (m, 1H), 6.46 (s, 1H), 6.28 – 6.23 (m, 2H), 3.89 (d, J = 0.8 Hz, 3H), 2.70 – 2.64 (m, 1H), 2.63 – 2.55 (m, 1H), 2.54 – 2.43 (m, 1H), 2.38 – 2.27 (m, 1H), 2.24 (d, J = 2.0 Hz, 3H), 2.20 (s, 3H), 2.13 (s, 3H), 2.06 – 2.03 (m, 3H), 1.49 – 1.36 (m, 4H), 1.31 – 1.23 (m, 2H), 1.21 – 1.04 (m, 10H), 0.81

– 0.66 (m, 6H) ppm.

ESI-HRMS (m/z): calcd. for $C_{103}H_{91}N_7OS_5Ru^{2+}$: 852.2477; found: 852.2477.

Elemental analysis calcd. for $C_{103}H_{91}N_8O_4F_6PS_5Ru{\cdot}3CH_2Cl_2$: C, 58.78; H, 4.51; N, 5.17; found: C, 58.86; H, 4.66; N, 5.26.

7.6 Synthesis of the TCAQ-FMN-Ru Triad

Suzuki couplings and Miyaura borylations were performed following the general procedure published for the NDI triad and pentad shown in section 7.2. TMS-group deprotection was performed with ICl following a well-established procedure.[176]

AQ-xy-Bpin

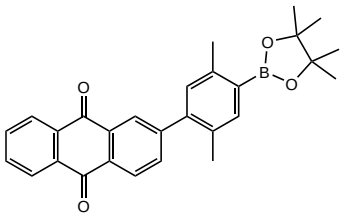

The title compound was obtained through an established three-step procedure.[176]

Bpin-FO-Bpin

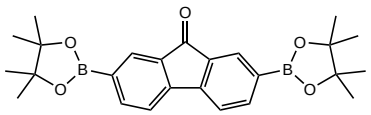

Under a flow of N_2, Br-FO-Br (1.41 g, 4.17 mmol, 1.0 eq), $(Bpin)_2$ (3.25 g, 12.8 mmol, 3.1 eq), KOAc (3.92 g, 39.9 mmol, 9.6 eq) and $Pd(PPh_3)_2Cl_2$ (0.154 g, 0.219 mmol, 0.05 eq) were dissolved in dry DMF (40 mL) and the solution degassed for 15 min. After heating to 100 °C for 17 h, the solution was cooled to RT and the solvent removed at reduced pressure. The solid was redissolved in DCM and preloaded onto SiO_2. Purification via column chromatography (SiO_2, pentane:EtOAc = 5:1) gave the product (1.54 g, 3.56 mmol, 85%) as a yellow solid.

^{1}H NMR (400 MHz, Chloroform-*d*) δ 8.13 (s, 2H), 7.95 (d, J = 7.3 Hz, 2H), 7.55 (d, J = 7.3 Hz, 2H), 1.35 (s, 24H) ppm.

TMS-hxy-FO-hxy-TMS

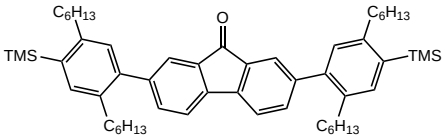

Under a flow of N_2, Bpin-FO-Bpin (0.85 g, 1.97 mmol, 1.0 eq), I-hxy-TMS (2.87 g, 6.46 mmol, 3.3 eq), Na_2CO_3 (1.42 g, 13.4 mmol, 6.8 eq) and $Pd(PPh_3)_4$ (148 mg, 128 µmol, 0.065 eq) were dissolved in a mixture of THF (60 mL) and H_2O (15 mL). The solution

was degassed for 25 min and heated to reflux at 75 °C for 39 h. The solution was cooled to RT, H_2O (50 mL) and DCM (50 mL) added and the solution stirred at RT for 10 min. The organic layer was separated and the aqueous layer extracted with DCM (3 × 50 mL). Organic layers were dried over Na_2SO_4 and the solvent removed at reduced pressure. The crude product was redissolved in DCM and preloaded onto SiO_2. Purification via column chromatography (SiO_2, i) pentane, ii) pentane:EtOAc = 20:1) gave the product (1.38 g, 1.70 mmol, 86%) as a yellow oil.

^{1}H NMR (400 MHz, Chloroform-*d*) δ 7.69 – 7.64 (m, 2H), 7.59 (d, J = 7.7 Hz, 2H), 7.47 (dd, J = 7.5, 1.6 Hz, 2H), 7.39 (s, 2H), 7.08 (s, 2H), 2.77 – 2.68 (m, 4H), 2.64 – 2.55 (m, 4H), 1.69 – 1.60 (m, 4H), 1.53 – 1.40 (m, 4H), 1.38 – 1.17 (m, 24H), 0.98 – 0.71 (m, 12H), 0.38 (s, 18H) ppm.

I-hxy-FO-hxy-I

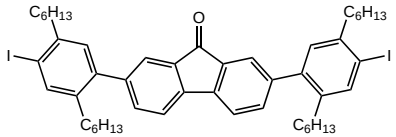

Under a flow of N_2, TMS-hxy-FO-hxy-TMS (1.38 g, 1.70 mmol, 1.0 eq) was dissolved in dry DCM (100 mL) and cooled to 0 °C. A solution of ICl (1.13 g, 6.96 mmol, 4.1 eq) in dry DCM (20 mL) was added carefully, the reaction mixture stirred at 0 °C for 1 h and then left to warm to RT over night while stirring. Sat. aq. $Na_2S_2O_3$-solution (50 mL) was added and the reaction mixture stirred vigorously for 10 min. The organic layer was separated and the aqueous layer extracted with DCM (3 × 50 mL). Organic layers were dried over Na_2SO_4 and the solvent removed at reduced pressure. The yellow oil was redissolved in DCM and preloaded onto celite. Purification via column chromatography (SiO_2, pentane:DCM = 4:1) gave the product (1.37 g, 1.49 mmol, 88%) as a yellow oil.

^{1}H NMR (400 MHz, Chloroform-*d*) δ 7.77 (s, 2H), 7.65 – 7.58 (m, 4H), 7.43 (dd, J = 7.6, 1.7 Hz, 2H), 7.07 (s, 2H), 2.76 – 2.67 (m, 4H), 2.58 – 2.50 (m, 4H), 1.68 – 1.60 (m, 4H), 1.54 – 1.39 (m, 8H), 1.39 – 1.28 (m, 8H), 1.27 – 1.17 (m, 12H), 0.95 – 0.90 (m, 6H), 0.86 – 0.81 (m, 6H) ppm.

AQ-xy-hxy-FO-hxy-I

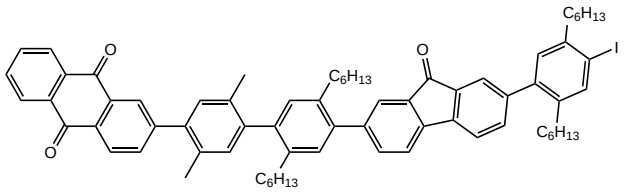

Under a flow of N_2, I-hxy-FO-hxy-I (1.13 g, 1.23 mmol, 1.0 eq), AQ-xy-Bpin (0.52 g, 1.19 mmol, 1.0 eq), Na_2CO_3 (0.39 g, 3.68 mmol, 3.1 eq) and $Pd(PPh_3)_4$ (66 mg, 57 µmol, 0.05 eq) were dissolved in a mixture of THF (60 mL) and H_2O (15 mL). The solution was degassed for 20 min and heated to reflux at 75 °C for 64 h. The solution was cooled to RT, H_2O (50 mL) and DCM (50 mL) added and the solution stirred at RT for 10 min. The organic layer was separated and the aqueous layer extracted with DCM (3 × 50 mL). Organic layers were dried over Na_2SO_4 and the solvent removed at reduced pressure. The yellow oil was redissolved in DCM and preloaded onto celite. Purification via column chromatography (SiO_2, pentane:DCM = 1:1) gave the product (0.53 g, 0.48 mmol, 40%) as a yellow oil.

^{1}H NMR (400 MHz, Chloroform-*d*) δ 8.44 – 8.32 (m, 4H), 7.90 – 7.78 (m, 3H), 7.77 – 7.70 (m, 2H), 7.66 – 7.58 (m, 3H), 7.55 (dd, J = 7.6, 1.6 Hz, 1H), 7.42 (dd, J = 7.6, 1.6 Hz, 1H), 7.23 (s, 1H), 7.16 (d, J = 2.9 Hz, 2H), 7.06 (d, J = 15.0 Hz, 2H), 2.73 – 2.66 (m, 2H), 2.65 – 2.57 (m, 2H), 2.55 – 2.36 (m, 4H), 2.34 (s, 3H), 2.15 (s, 3H), 1.65 – 1.55 (m, 2H), 1.55 – 1.38 (m, 8H), 1.37 – 1.30 (m, 4H), 1.27 – 1.13 (m, 18H), 0.94 – 0.75 (m, 12H) ppm.

AQ-xy-hxy-FO-hxy-xy-AQ

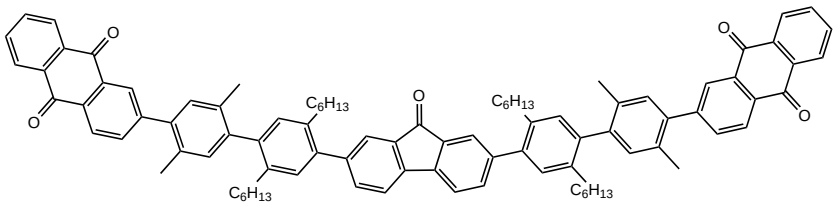

The product was obtained as a side-product from the synthesis of AQ-xy-hxy-FO-hxy-I.

^{1}H NMR (400 MHz, Chloroform-*d*) δ 8.40 – 8.32 (m, 4H), 8.32 – 8.24 (m, 4H), 7.83 (dd, J = 7.9, 1.8 Hz, 2H), 7.79 – 7.70 (m, 6H), 7.61 (d, J = 7.6 Hz, 2H), 7.53 (dd, J = 7.3, 1.6 Hz, 2H), 7.23 (s, 2H), 7.17 (d, J = 8.7 Hz, 4H), 7.08 (s, 2H), 2.69 – 2.56 (m, 4H), 2.55 – 2.46 (m, 2H), 2.43 – 2.35 (m, 2H), 2.33 (s, 6H), 2.15 (s, 6H), 1.55 – 1.44 (m, 8H), 1.24 – 1.15 (m, 24H), 0.80 (dt, J = 9.8, 6.6 Hz, 12H) ppm.

AQ-xy-hxy-FO-hxy-Bpin

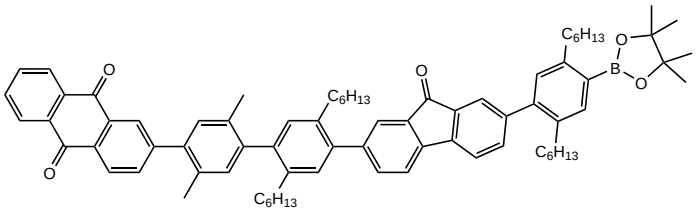

Under a flow of N_2, AQ-xy-hxy-FO-hxy-I (0.53 g, 0.48 mmol, 1.0 eq), $(Bpin)_2$ (0.24 g, 0.95 mmol, 2.0 eq), KOAc (0.25 g, 2.55 mmol, 5.3 eq) and $Pd(PPh_3)_2Cl_2$ (32 mg, 46 µmol, 0.1 eq) were dissolved in dry DMF (22 mL) and the solution degassed for 25 min. After heating to 100 °C for 14 h, the solution was cooled to RT and the solvent removed at reduced pressure. The solid was redissolved in DCM and preloaded onto celite. Purification via column chromatography (SiO_2, pentane:DCM = 1:1) gave the product (0.45 g, 0.41 mmol, 85%) as a yellow oil.

^{1}H NMR (400 MHz, Chloroform-*d*) δ 8.44 – 8.32 (m, 4H), 7.91 – 7.78 (m, 3H), 7.76 – 7.69 (m, 2H), 7.67 – 7.58 (m, 3H), 7.55 (dd, J = 7.6, 1.7 Hz, 1H), 7.46 (dd, J = 7.5, 1.7 Hz, 1H), 7.24 (s, 1H), 7.17 (d, J = 3.5 Hz, 2H), 7.07 (d, J = 15.1 Hz, 2H), 2.93 – 2.84 (m, 2H), 2.68 – 2.55 (m, 4H), 2.56 – 2.46 (m, 1H), 2.43 – 2.36 (m, 1H), 2.35 (s, 3H), 2.16 (s, 3H), 1.66 – 1.45 (m, 8H), 1.38 (s, 12H), 1.35 – 1.13 (m, 24H), 0.94 – 0.76 (m, 12H) ppm.

AQ-xy-hxy-FO-hxy-bpy

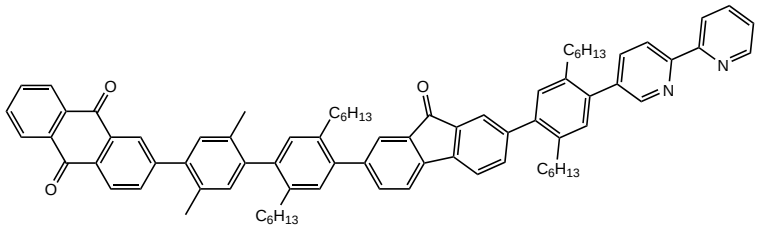

Under a flow of N_2, AQ-xy-hxy-FO-hxy-Bpin (0.55 g, 0.50 mmol, 1.0 eq), 5-bromo-2,2'-bipyridine (0.31 g, 1.32 mmol, 2.7 eq) and Na_2CO_3 (0.26 g, 2.45 mmol, 4.9 eq) were dissolved in a mixture of THF (60 mL) and H_2O (15 mL). The solution was degassed for 20 min, $Pd(PPh_3)_4$ (28 mg, 24 µmol, 0.09 eq) added and the solution heated to reflux at 75 °C for 44 h. The solution was cooled to RT, H_2O (50 mL) and DCM (50 mL) added and the solution stirred at RT for 10 min. The organic layer was separated and the aqueous layer extracted with DCM (3 × 50 mL). Combined organic layers were dried over Na_2SO_4 and the solvent removed at reduced pressure. The yellow oil was redissolved in DCM and preloaded onto SiO_2. Purification via column chromatography (SiO_2, pentane:EtOAc = 10:1 + 1% NEt_3) gave the product (0.45 g, 0.40 mmol, 80%) as a yellow oil.

^{1}H NMR (400 MHz, Chloroform-*d*) δ 8.78 – 8.66 (m, 2H), 8.48 (t, J = 8.7 Hz, 2H), 8.42

– 8.30 (m, 4H), 7.90 – 7.76 (m, 5H), 7.73 (dd, J = 11.3, 1.5 Hz, 2H), 7.65 (d, J = 7.6 Hz, 2H), 7.60 – 7.48 (m, 2H), 7.38 – 7.30 (m, 1H), 7.27 – 7.12 (m, 5H), 7.09 (s, 1H), 2.69 – 2.59 (m, 6H), 2.58 – 2.45 (m, 1H), 2.46 – 2.35 (m, 1H), 2.35 (s, 3H), 2.16 (s, 3H), 1.56 – 1.46 (m, 8H), 1.25 – 1.18 (m, 24H), 0.86 – 0.78 (m, 12H) ppm.

TCAQ-xy-hxy-FMN-hxy-bpy (L^A)

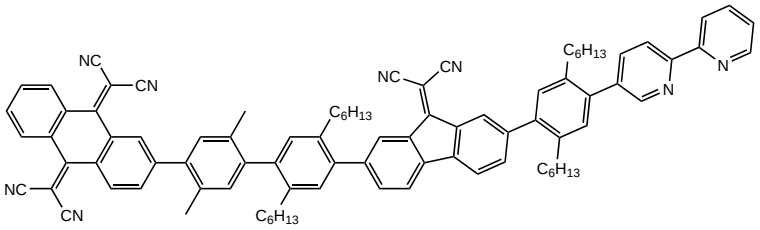

The conversion of AQ and FO to TCAQ and FMN followed a literature procedure[129, 133, 181] with Lehnert's reagent.[169, 170]

Under a flow of N_2, AQ-xy-hxy-FO-hxy-bpy (0.13 g, 0.11 mmol, 1.0 eq) and malononitrile (0.09 g, 1.30 mmol, 11 eq) were dissolved in dry DCM (60 mL). $TiCl_4$ (0.20 mL, 0.35 g, 1.82 mmol, 16 eq) was added followed by pyridine (0.30 mL, 0.30 g, 3.73 mmol, 32 eq). The solution was heated to reflux at 55 °C, and after 4 and 8 h respectively, equal amounts of malononitrile (11 eq), $TiCl_4$(16 eq) and pyridine (32 eq) were added. After 24 h total reflux time, the solution was cooled to RT, H_2O (50 mL) added and the solution stirred at RT for 1 h. The organic layer was separated and the aqueous layer extracted with DCM (3 × 30 mL). Organic layers were dried over Na_2SO_4 and the solvent removed at reduced pressure. The red solid was purified via column chromatography (SiO_2, i) neat DCM, ii) DCM:EtOAc = 20:1) to give the product (0.13 g, 0.10 mmol, 88%) as a red solid.

^{1}H NMR (400 MHz, Chloroform-d) δ 8.78 – 8.70 (m, 2H), 8.54 – 8.41 (m, 4H), 8.38 – 8.25 (m, 4H), 7.91 – 7.83 (m, 2H), 7.83 – 7.74 (m, 3H), 7.68 (d, J = 7.7 Hz, 2H), 7.59 – 7.51 (m, 2H), 7.38 – 7.31 (m, 1H), 7.24 – 7.13 (m, 5H), 7.08 (s, 1H), 2.72 – 2.57 (m, 6H), 2.55 – 2.45 (m, 1H), 2.44 – 2.33 (m, 4H), 2.16 (s, 3H), 1.60 – 1.46 (m, 8H), 1.28 – 1.18 (m, 24H), 0.87 – 0.79 (m, 12H) ppm.

$[Ru(L^A)(bpy)_2]\ (PF_6)_2$

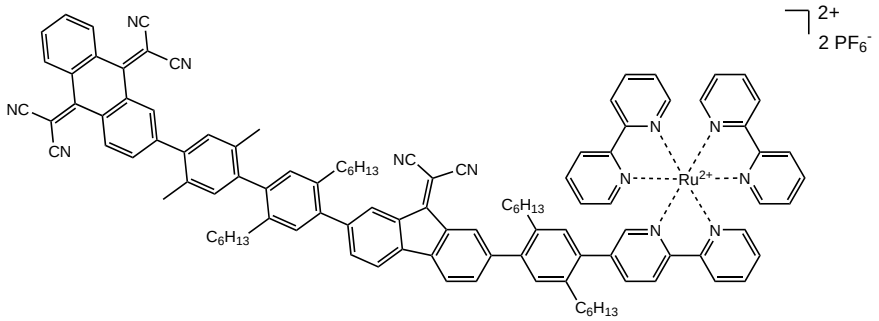

Under a flow of N_2, $[Ru(bpy)_2Cl_2]\cdot 2H_2O$ (19.6 mg, 37.7 µmol, 1.2 eq) and AgOTf (20.8 mg, 81.0 µmol, 2.6 eq) were dissolved in dry DMF (5 mL) under exclusion of light. The reaction mixture was stirred at RT for 1.5 h, then TCAQ-xy-hxy-FMN-hxy-bpy (40.0 mg, 31.3 µmol, 1.0 eq) dissolved in dry DMF (3 mL) was added. The solution was stirred in the dark at RT for 64 h, then the solvent was removed at reduced pressure. The crude was dissolved in DCM and preloaded onto SiO_2. The product was purified via column chromatography (SiO_2, i) neat acetone, ii) acetone:H_2O = 10:1, iii) acetone:H_2O = 10:1 sat. w. KNO_3). From the orange fractions eluted with iii) the organic solvent was removed and a saturated solution of aq. KPF_6 was added. The precipitate formed was isolated via filtration, washed with water and Et_2O and dried in air to give the product (7.1 mg, 3.6 µmol, 11%) as a brown solid.

^{1}H NMR (400 MHz, Methylene Chloride-d_2) δ 8.58 – 8.37 (m, 7H), 8.37 – 8.21 (m, 5H), 8.14 – 8.05 (m, 5H), 8.02 (td, J = 8.0, 1.5 Hz, 1H), 7.87 – 7.76 (m, 5H), 7.75 – 7.67 (m, 6H), 7.58 – 7.40 (m, 7H), 7.26 – 7.05 (m, 6H), 2.67 – 2.54 (m, 4H), 2.53 – 2.45 (m, 1H), 2.43 – 2.25 (m, 5H), 2.22 – 2.07 (m, 4H), 1.57 – 1.39 (m, 8H), 1.32 – 1.08 (m, 24H), 0.88 – 0.72 (m, 12H) ppm.

^{1}H NMR (400 MHz, Acetonitrile-d_3) δ 8.62 – 8.45 (m, 6H), 8.37 – 8.22 (m, 5H), 8.22 – 8.19 (m, 1H), 8.13 – 8.03 (m, 5H), 8.00 (td, J = 7.9, 1.4 Hz, 1H), 7.92 – 7.86 (m, 2H), 7.86 – 7.78 (m, 5H), 7.77 – 7.73 (m, 3H), 7.65 (d, J = 1.9 Hz, 1H), 7.60 (d, J = 7.6 Hz, 1H), 7.50 (dd, J = 7.7, 1.4 Hz, 1H), 7.47 – 7.38 (m, 4H), 7.38 – 7.33 (m, 1H), 7.30 – 7.22 (m, 2H), 7.16 (d, J = 4.8 Hz, 2H), 7.11 – 7.06 (m, 2H), 2.68 – 2.61 (m, 2H), 2.61 – 2.55 (m, 2H), 2.42 – 2.29 (m, 5H), 2.27 – 2.20 (m, 2H), 2.14 – 2.06 (m, 3H), 1.57 – 1.35 (m, 8H), 1.31 – 1.12 (m, 20H), 1.02 – 0.94 (m, 4H), 0.83 – 0.71 (m, 12H) ppm.

ESI (m/z): calcd. for $C_{110}H_{100}N_{12}Ru^{2+}$: 845; found: 845 and fragments without one or two of the malononitrile groups.

TCAQ

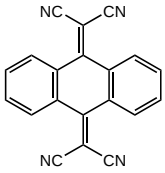

The synthesis of the title compound followed a literature procedure[129, 133] with Lehnert's reagent.[169, 170]

Under a flow of N_2, *p*-anthraquinone (0.55 g, 2.64 mmol, 1.0 eq) and malononitrile (0.51 g, 7.70 mmol, 2.9 eq) were suspended in dry $CHCl_3$ (20 mL). $TiCl_4$ (0.82 mL, 1.42 g, 7.5 mmol, 2.8 eq) was added followed by pyridine (1.20 mL, 1.18 g, 14.9 mmol, 5.6 eq) and the mixture heated to reflux. After 24 h, the same amounts of malononitrile (2.9 eq), $TiCl_4$(2.8 eq) and pyridine (5.6 eq) were added. After a total reflux time of 48 h, the reaction mixture was cooled to RT and transferred into an ice/water mixture. The solid was filtered off and washed with several portions of DCM. The organic layer was separated, the aqueous phase extracted with DCM (3 × 30 mL), the combined organic layers dried over Na_2SO_4 and the solvent removed at reduced pressure. The residue was washed with Et_2O to remove the excess malononitrile, then the crude was dissolved in DCM and filtered over a plug of SiO_2. After solvent removal, the product (90 mg, 296 µmol, 11%) was obtained as a yellow solid.

^{1}H NMR (400 MHz, Chloroform-*d*) δ 8.25 (dd, J = 5.8, 3.3 Hz, 4H), 7.74 (dd, J = 5.8, 3.2 Hz, 4H) ppm.

TCAQ-xy-hxy-FMN-hxy-xy-TCAQ

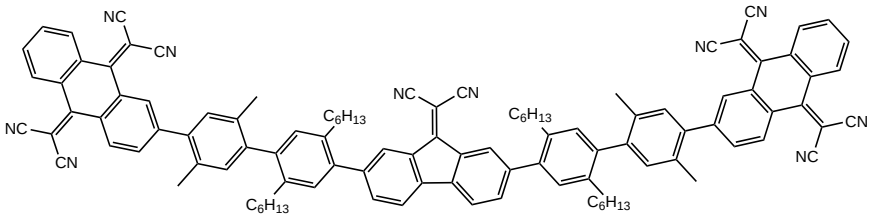

The conversion of AQ and FO to TCAQ and FMN followed a literature procedure[129, 133, 181] with Lehnert's reagent.[169, 170]

Under a flow of N_2, AQ-xy-hxy-FO-hxy-xy-AQ (0.25 g, 0.19 mmol, 1.0 eq) and malononitrile (0.26 g, 3.94 mmol, 20 eq) were dissolved in dry DCM (40 mL). $TiCl_4$ (0.45 mL, 0.78 g, 4.11 mmol, 21 eq) was added followed by pyridine (0.65 mL, 0.64 g, 8.09 mmol, 42 eq). The solution was heated to reflux at 55 °C, and after 2 h equal amounts of malononitrile (20 eq), $TiCl_4$ (21 eq) and pyridine (42 eq) were added. After 21 h total reflux time, the solution was cooled to RT, H_2O (30 mL) was added and the solution stirred

at RT for 30 min. The organic layer was separated and the aqueous layer extracted with DCM (3 × 50 mL). The combined organic layers were dried over Na_2SO_4 and the solvent removed at reduced pressure. The red solid was purified via column chromatography (SiO_2, pentane:EtOAc = 3:1) to give the product (0.23 g, 0.15 mmol, 77%) as a red solid.

^{1}H NMR (400 MHz, Chloroform-*d*) δ 8.41 (dd, J = 1.3, 0.6 Hz, 2H), 8.34 – 8.23 (m, 8H), 7.81 – 7.75 (m, 6H), 7.67 (d, J = 7.7 Hz, 2H), 7.54 (dd, J = 7.6, 1.5 Hz, 2H), 7.18 – 7.12 (m, 6H), 7.06 (s, 2H), 2.65 – 2.57 (m, 4H), 2.53 – 2.44 (m, 2H), 2.41 – 2.32 (m, 2H), 2.35 (s, 6H), 2.14 (s, 6H), 1.56 – 1.45 (m, 8H), 1.28 – 1.11 (m, 24H), 0.84 – 0.79 (m, 12H) ppm.

I-hxy-FMN-hxy-I

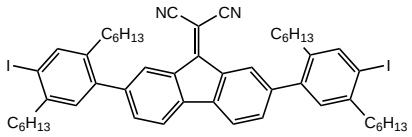

The conversion of FO to FMN followed an established literature procedure[181] with Lehnert's reagent.[169, 170]

Under a flow of N_2, I-hxy-FO-hxy-I (0.20 g, 0.22 mmol, 1.0 eq) and malononitrile (0.12 g, 1.82 mmol, 8.4 eq) were dissolved in dry DCM (60 mL). $TiCl_4$ (0.2 mL, 0.35 g, 1.82 mmol, 8.4 eq) was added followed by pyridine (0.3 mL, 0.30 g, 3.73 mmol, 17 eq). The solution was heated to reflux at 55 °C for 17 h, then the reaction mixture was cooled to RT, H_2O (50 mL) was added and the solution stirred at RT for 20 min. The organic layer was separated and the aqueous layer extracted with DCM (3 × 30 mL). The combined organic layers were dried over Na_2SO_4 and the solvent removed at reduced pressure. The red solid was purified via column chromatography (SiO_2, pentane:DCM = 4:1) to give the product (0.17 g, 0.18 mmol, 82%) as a red solid.

^{1}H NMR (400 MHz, Chloroform-*d*) δ 8.34 (d, J = 1.3 Hz, 2H), 7.77 (s, 2H), 7.64 (d, J = 7.7 Hz, 2H), 7.44 (dd, J = 7.7, 1.5 Hz, 2H), 7.05 (s, 2H), 2.75 – 2.66 (m, 4H), 2.58 – 2.48 (m, 4H), 1.67 – 1.58 (m, 4H), 1.54 – 1.46 (m, 4H), 1.45 – 1.38 (m, 4H), 1.38 – 1.31 (m, 8H), 1.27 – 1.18 (m, 12H), 0.94 – 0.87 (m, 6H), 0.86 – 0.80 (m, 6H) ppm.

7.7 Synthesis of the exTTF-PTZ-Ru-FMN-TCAQ Pentad - One-Ligand Approach

Suzuki couplings were performed following the general procedure published for the NDI triad and pentad shown in section 7.2.

AQ-xy-hxy-FO-hxy-bpy-Br

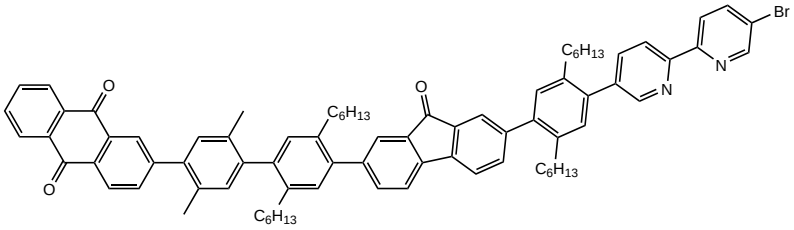

Under a flow of N_2, AQ-xy-hxy-FO-hxy-Bpin (0.30 g, 0.27 mmol, 1.0 eq), 5,5'-dibromo-2,2'-bipyridine (0.42 g, 1.34 mmol, 4.9 eq), Na_2CO_3 (0.13 g, 1.23 mmol, 4.5 eq) and $Pd(PPh_3)_4$ (28 mg, 24 µmol, 0.09 eq) were dissolved in a mixture of THF (60 mL) and H_2O (15 mL). The solution was degassed for 20 min and heated to reflux at 75 °C for 15 h. The solution was cooled to RT, H_2O (50 mL) and DCM (50 mL) were added and the solution stirred at RT for 10 min. The organic layer was separated and the aqueous layer extracted with DCM (3 × 50 mL). Combined organic layers were dried over Na_2SO_4 and the solvent removed at reduced pressure. The yellow oil was redissolved in DCM and preloaded onto celite. Purification via column chromatography (SiO_2, pentane:EtOAc = 20:1 + 1% NEt_3) gave the product (0.25 g, 0.21 mmol, 78%) as a yellow oil.

^{1}H NMR (400 MHz, Chloroform-*d*) δ 8.73 (dd, J = 21.2, 2.3 Hz, 2H), 8.50 – 8.29 (m, 6H), 7.97 (dd, J = 8.5, 2.4 Hz, 1H), 7.92 – 7.78 (m, 4H), 7.73 (dd, J = 12.7, 1.6 Hz, 2H), 7.64 (d, J = 7.6 Hz, 2H), 7.59 – 7.48 (m, 2H), 7.26 – 7.14 (m, 5H), 7.09 (s, 1H), 2.68 – 2.55 (m, 8H), 2.34 (s, 3H), 2.16 (s, 3H), 1.57 – 1.44 (m, 8H), 1.28 – 1.13 (m, 24H), 0.88 – 0.76 (m, 12H) ppm.

exTTF-hxy-xy-PTZ-xy-bpy-hxy-FO-hxy-xy-AQ

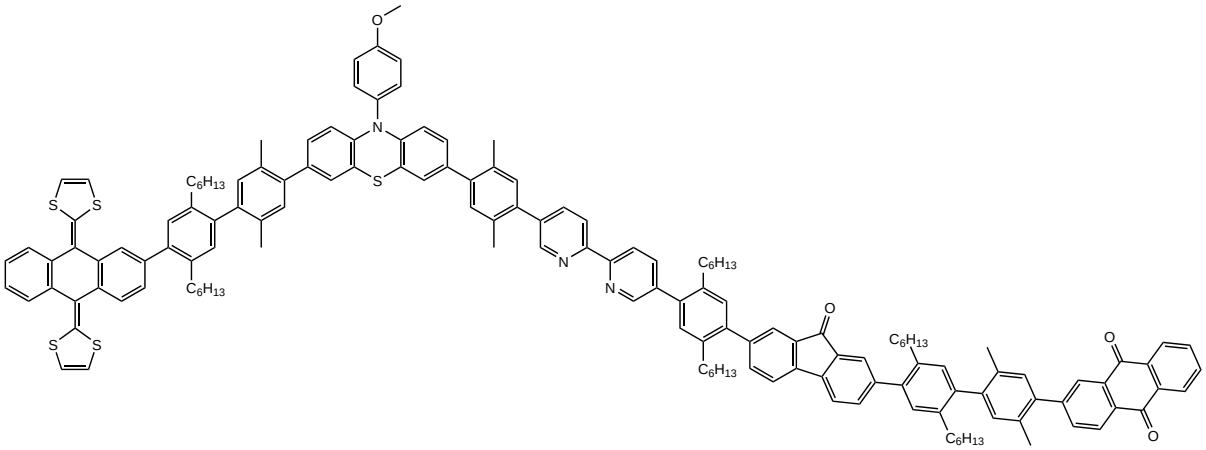

Under a flow of N_2, exTTF-hxy-xy-PTZ-xy-Bpin (97 mg, 77 µmol, 1.0 eq), AQ-xy-hxy-FO-hxy-bpy-Br (120 mg, 99 µmol, 1.3 eq), Na_2CO_3 (76 mg, 717 µmol, 9.3 eq) and $Pd(PPh_3)_4$ (6 mg, 5 µmol, 0.07 eq) were dissolved in a mixture of THF (60 mL) and H_2O (15 mL). The solution was degassed for 35 min and heated to reflux at 75 °C for 68 h. The solution was cooled to RT, H_2O (50 mL) and DCM (50 mL) were added and the solution stirred at RT for 10 min. The organic layer was separated and the aqueous layer extracted with DCM (3 × 50 mL). The combined organic layers were dried over Na_2SO_4 and the solvent removed at reduced pressure. The yellow oil was redissolved in DCM and preloaded onto celite. Purification via column chromatography (SiO_2, i) pentane:EtOAc = 7:2 + 1% NEt_3, ii) pentane:EtOAc = 5:2 + 1% NEt_3, iii) pentane:EtOAc = 2:1 + 1% NEt_3) gave the product (140 mg, 61.7 µmol, 80%) as a yellow oil.

^{1}H NMR (400 MHz, Chloroform-*d*) δ 8.70 (s, 2H), 8.49 (d, J = 8.2 Hz, 2H), 8.38 – 8.27 (m, 4H), 7.86 – 7.75 (m, 5H), 7.73 – 7.54 (m, 8H), 7.53 – 7.35 (m, 5H), 7.29 – 7.22 (m, 2H), 7.21 – 7.08 (m, 11H), 7.07 – 6.96 (m, 6H), 6.85 (t, J = 9.0 Hz, 2H), 6.33 – 6.13 (m, 5H), 3.88 (s, 3H), 2.68 – 2.50 (m, 8H), 2.51 – 2.32 (m, 4H), 2.33 – 2.21 (m, 12H), 2.10 (s, 3H), 2.05 (s, 3H), 1.55 – 1.38 (m, 12H), 1.28 – 1.04 (m, 36H), 0.85 – 0.69 (m, 18H) ppm.

MALDI-MS (m/z): calcd. for $C_{154}H_{151}N_3O_4S_5$: 2267; found: 2267.

exTTF-hxy-xy-PTZ-xy-bpy-hxy-FMN-hxy-xy-TCAQ

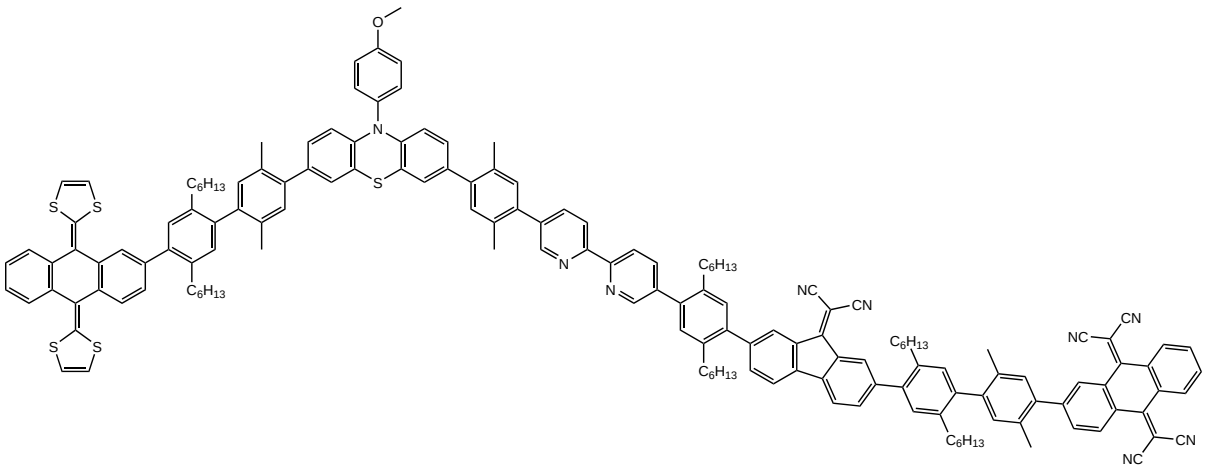

The conversion of AQ and FO to TCAQ and FMN followed a literature procedure[129, 133, 181] with Lehnert's reagent.[169, 170]

Under a flow of N_2, AQ-xy-hxy-FO-hxy-bpy-xy-PTZ-xy-hxy-exTTF (140 mg, 61.6 mmol, 1.0 eq) and malononitrile (0.104 g, 1.57 mmol, 25 eq) were dissolved in dry DCM (100 mL). $TiCl_4$ (0.160 mL, 0.276 g, 1.46 mmol, 24 eq) was added followed by pyridine (0.240 mL, 0.236 g, 2.98 mmol, 48 eq). The solution was heated to reflux at 55 °C, and after each 12 h, equal amounts of malononitrile (25 eq), $TiCl_4$ (24 eq) and pyridine (48 eq) were added (four times in total). After 110 h total reflux time, the solution was cooled to RT, H_2O (50 mL) was added and the solution stirred at RT for 2 h. The reaction mixture was filtered over celite, then the organic layer was separated and the aqueous layer extracted with DCM (3 × 50 mL). The combined organic layers were dried over Na_2SO_4 and the solvent was removed at reduced pressure. The crude product was redissolved in DCM and preloaded onto celite. The red solid was purified via column chromatography (SiO_2, several solvent mixtures used: i) pentane:EtOAc = 2:1, ii) pentane:EtOAc = 1:1, iii) pentane:EtOAc = 1:2, iv) neat acetone, v) neat DCM). Several spots were isolated, but none of them proved to be the wanted product. One of the donor moieties does not seem to be stable under the reaction conditions performed.

7.8 Synthesis of the exTTF-PTZ-Ru-FMN-TCAQ Pentad - Two-Ligand Approach

$[Ru(DMSO)_4Cl_2]$

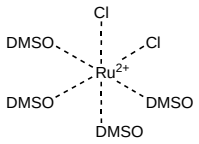

The title compound was obtained by modification of a published procedure.[182]

Under a flow of N_2, dry DMSO (10 mL) was degassed for 30 min. $RuCl_3 \cdot H_2O$ (1.90 g, 8.43 mmol, 1.0 eq.) was added and the mixture was stirred at RT until the solid was completely dissolved. 2-Propanol (30 mL) was added to the red solution and the mixture was heated to reflux for 48 h. The yellow-orange suspension was cooled to room temperature and the precipitate was filtered off. The solid was washed with several portions of acetone and toluene and dried in vacuo to give the product (3.81 g, 7.86 mmol, 93%) as a yellow powder.

Selected FT-IR absorptions (cm^{-1}): ν(DMSO-S-Ru) 1081 (s), ν(DMSO-O-Ru) 923 (s).

$[Ru(bpy)(DMSO)_2Cl_2]$

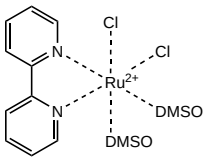

The attachment of the first ligand on the Ru-precursor follows a literature procedure.[183]

Under a flow of N_2, $[Ru(DMSO)_4Cl_2]$ (0.97 g, 2.00 mmol, 1.0 eq) and 2,2'-bipyridine (0.32 g, 2.05 mmol, 1.0 eq) were dissolved in a mixture of EtOH (18 mL) and DMSO (2 mL). The mixture was heated to reflux at 85 °C for 3 h, then cooled to 0 °C and the orange precipitate was isolated. The solid was washed with cold EtOH and pentane and dried in vacuo to yield the product (0.76 g, 1.57 mmol, 79%) as an orange solid.

^{1}H NMR (400 MHz, DMSO-d_6) δ 9.61 (dd, J = 41.4, 5.7 Hz, 2H), 8.64 (dd, J = 20.4, 8.1 Hz, 2H), 8.16 (dt, J = 47.9, 7.8 Hz, 2H), 7.69 (dt, J = 63.7, 6.6 Hz, 2H), 3.40 (s, 3H), 3.36 (s, 3H), 2.98 (s, 3H), 2.28 (s, 3H) ppm.

[Ru(bpy)(L^A)Cl_2]

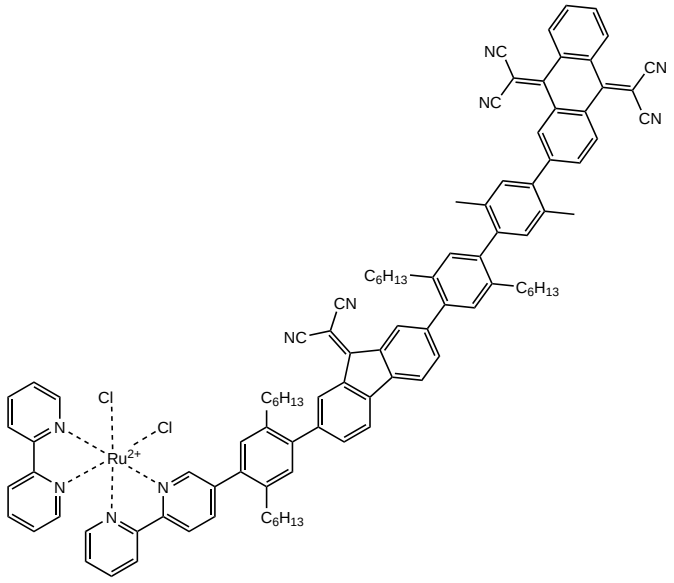

The stepwise assembly of the different ligands follows a published procedure.[171]

Under a flow of N_2, TCAQ-xy-hxy-FMN-hxy-bpy (81 mg, 63 µmol, 1.0 eq) and [Ru(bpy)-$(DMSO)_2Cl_2$] (66 mg, 136 µmol, 2.2 eq) were dissolved in dry DMF (10 mL) and heated to 130 °C for 15 h under the exclusion of light. After solvent removal, the crude product was redissolved in DCM and preloaded onto celite. Purification via column chromatography (SiO_2, acetone:pentane = 5:1) gave the product (45.8 mg, 28.5 µmol, 45%) as a dark violet solid.

MALDI-MS (m/z): calcd. for $C_{100}H_{92}N_{10}Cl_2Ru$: 1605; found: 1605.

$[Ru(bpy)(L^A)(L^D)]\ (PF_6)_2$

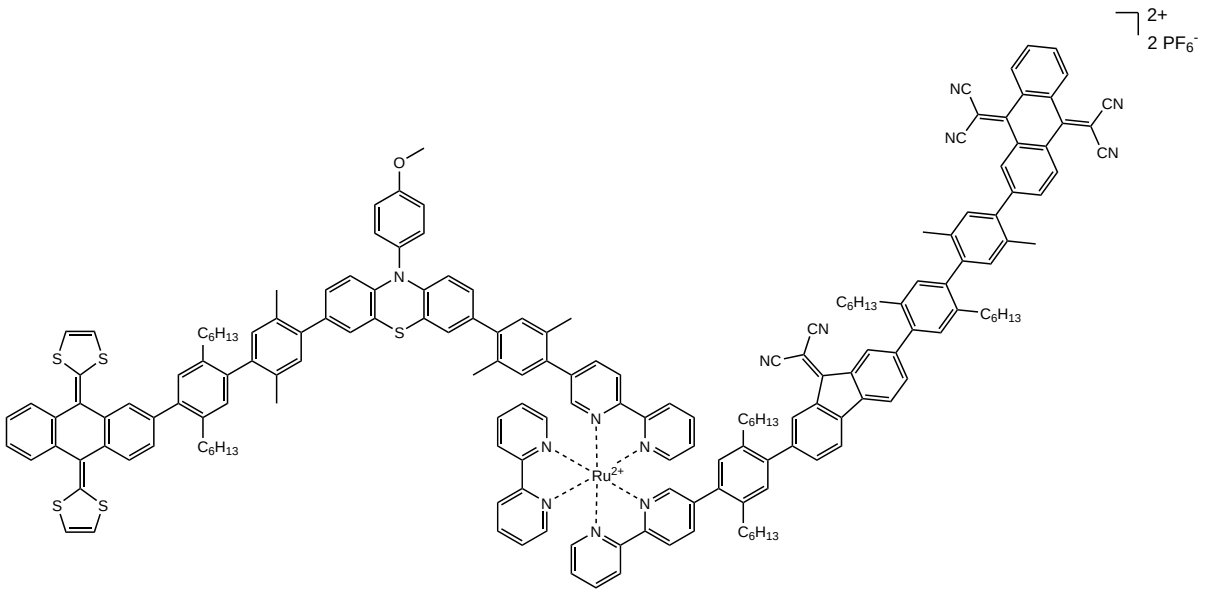

The stepwise assembly of the different ligands follows a published procedure.[171]

Under a flow of N_2, exTTF-hxy-xy-PTZ-xy-bpy (37 mg, 29 µmol, 1.0 eq), [Ru(bpy)-(L^A)Cl_2] (46 mg, 29 µmol, 1.0 eq) and $AgNO_3$ (80 mg, 470 µmol, 16 eq) were dissolved in a mixture of EtOH (15 mL) and $CHCl_3$ (5 mL). The mixture was refluxed at 80 °C for 22 h, cooled to RT and the solvents removed at reduced pressure. The crude product was stirred in a 1:1-mixture of acetone and EtOH saturated with KPF_6 for 10 minutes followed by solvent removal. The solid was dissolved in acetone and filtered over a short silica gel column. The solvent was removed and the crude product dissolved in DCM to remove excess KPF_6. The product was purified via column chromatography (SiO_2, i) neat acetone, ii) acetone:H_2O = 10:1, iii) acetone:H_2O = 5:1 sat. w. KNO_3). The red solution eluted with iii) was mixed with sat. aq. KPF_6, the organic solvent was removed and the aqueous phase extracted with DCM (3 × 30 mL). The combined organic phases were dried over Na_2SO_4 and the solvent was removed at reduced pressure to give a red solid (35.6 mg).

Although a complex was obtained, the analytical data (NMR, MALDI-MS, ESI-HRMS) is not conclusive. It is safe to assume the title compound was not obtained, but it remains unclear what complex was formed during the synthetic procedure.

8 Appendix

Energy Estimations of the Different Species Involved in the BNA$^+$ Reduction Experiments in Chapter 4

For the energy estimations of the molecular species involved in the BNA$^+$ reduction process, the excited state energy of $[Ru(bpy)_3]^{2+}$ was taken from the literature.[77, 163] The driving forces for each electron-transfer step (ΔG_{ET}) were estimated with the equation

$$\Delta G_{ET} = -e\,(E_{red} - E_{ox})$$

where E_{red}/E_{ox} represents the reduction/oxidation potential for the respective electron-transfer step. Reduction and oxidation potentials were taken from Table 4.1.

The ground-state prior to excitation of the $[Ru(bpy)_3]^{2+}$ photosensitizer was set to **0.00 eV**. The energy of the $[Ru(bpy)_3]^{2+}$ excited state corresponds to the lowest ^{3}MLCT state of $[Ru(bpy)_3]^{2+}$ with an energy of **2.10 eV**.[163] The energies of the NDI$^-$ and NDI^{2-} states in the Ru-NDI-Ru triad were calculated to be **1.14 eV** and **2.78 eV**, respectively.

- Electron transfer from $^*\mathbf{Ru^{2+}}$ to $\mathbf{BNA^+}$:
  $\Delta G_{ET} = -e\,(-1.08\,V + 0.81\,V) = +0.27\,eV$
- Electron transfer from $^*\mathbf{Ru^{2+}}$ to $\mathbf{Rh^{III}}$:
  $\Delta G_{ET} = -e\,(-0.74\,V + 0.81\,V) = -0.07\,eV$
- Electron transfer from **TEOA** to $\mathbf{Ru^{3+}}$:
  $\Delta G_{ET} = -e\,(1.29\,V - 0.69\,V) = -0.60\,eV$
- Electron transfer from **TEOA** to $^*\mathbf{Ru^{2+}}$:
  $\Delta G_{ET} = -e\,(0.77\,V - 0.69\,V) = -0.08\,eV$
- Electron transfer from $\mathbf{Ru^+}$ to $\mathbf{BNA^+}$:
  $\Delta G_{ET} = -e\,(-1.08\,V + 1.33\,V) = -0.25\,eV$
- Electron transfer from $\mathbf{Ru^+}$ to $\mathbf{Rh^{III}}$:
  $\Delta G_{ET} = -e\,(-0.74\,V + 1.33\,V) = -0.59\,eV$

- Electron transfer from $\mathbf{Rh^{II}}$ to $\mathbf{BNA^{+}}$**:**
  $\Delta G_{ET} = -e\,(-1.08\,V + 0.74\,V) = +0.34\,eV$
- Electron transfer from $\mathbf{{}^{*}Ru^{2+}}$ to $\mathbf{NDI^{0}}$**:**
  $\Delta G_{ET} = -e\,(-0.45\,V + 0.81\,V) = -0.36\,eV$
- Electron transfer from $\mathbf{{}^{*}Ru^{2+}}$ to $\mathbf{NDI^{-}}$**:**
  $\Delta G_{ET} = -e\,(-0.95\,V + 0.81\,V) = +0.14\,eV$
- Electron transfer from $\mathbf{Ru^{+}}$ to $\mathbf{NDI^{0}}$**:**
  $\Delta G_{ET} = -e\,(-0.45\,V + 1.33\,V) = -0.88\,eV$
- Electron transfer from $\mathbf{Ru^{+}}$ to $\mathbf{NDI^{-}}$**:**
  $\Delta G_{ET} = -e\,(-0.95\,V + 1.33\,V) = -0.38\,eV$
- Electron transfer from $\mathbf{NDI^{-}}$ to $\mathbf{Rh^{III}}$**:**
  $\Delta G_{ET} = -e\,(-0.74\,V + 0.45\,V) = +0.29\,eV$
- Electron transfer from $\mathbf{NDI^{2-}}$ to $\mathbf{Rh^{III}}$**:**
  $\Delta G_{ET} = -e\,(-0.74\,V + 0.95\,V) = -0.21\,eV$
- Electron transfer from $\mathbf{NDI^{-}}$ to $\mathbf{BNA^{+}}$**:**
  $\Delta G_{ET} = -e\,(-1.08\,V + 0.45\,V) = +0.63\,eV$
- Electron transfer from $\mathbf{NDI^{2-}}$ to $\mathbf{BNA^{+}}$**:**
  $\Delta G_{ET} = -e\,(-1.08\,V + 0.95\,V) = +0.13\,eV$

Energy Estimations of the Different Species Involved During Charge-Accumulation in the Pentad Shown in Chapter 5

Energy Estimations of the Different Species Involved in the NDI Pentad

The driving forces for each electron-transfer step (ΔG_{ET}) presented in the beginning of Chapter 5 were estimated with the equation

$$\Delta G_{ET} = -e\,(E_{red} - E_{ox})$$

where E_{red}/E_{ox} represents the reduction/oxidation potential for the respective electron-transfer step. Reduction and oxidation potentials were taken from the cyclovoltammetric measurements of the NDI pentad listed in the publication in Chapter 3. Reduction and oxidation potentials of $[Ru(bpy)_3]^{2+}$ were taken from the literature.[77]

- Electron transfer from $\mathbf{TAA^0}$ to $\mathbf{^*Ru^{2+}}$:
  $\Delta G_{ET} = -e\,(0.77\,V - 0.76\,V) = -0.01\,eV$
- Electron transfer from $\mathbf{^*Ru^{2+}}$ to $\mathbf{NDI^0}$:
  $\Delta G_{ET} = -e\,(-0.51\,V + 0.81\,V) = -0.30\,eV$
- Electron transfer from $\mathbf{^*Ru^{2+}}$ to $\mathbf{NDI^-}$:
  $\Delta G_{ET} = -e\,(-0.96\,V + 0.81\,V) = +0.15\,eV$
- Electron transfer from $\mathbf{Ru^+}$ to $\mathbf{NDI^0}$:
  $\Delta G_{ET} = -e\,(-0.51\,V + 1.33\,V) = -0.82\,eV$
- Electron transfer from $\mathbf{Ru^+}$ to $\mathbf{NDI^-}$:
  $\Delta G_{ET} = -e\,(-0.96\,V + 1.33\,V) = -0.37\,eV$
- Electron transfer from $\mathbf{^*Ru^{2+}}$ to $\mathbf{TAA^+}$:
  $\Delta G_{ET} = -e\,(0.76\,V + 0.81\,V) = -1.57\,eV$
- Electron transfer from $\mathbf{NDI^-}$ to $\mathbf{^*Ru^{2+}}$:
  $\Delta G_{ET} = -e\,(0.77\,V + 0.51\,V) = -1.28\,eV$

Energy Estimations of the Different Species Involved in the Pentad

For the energy estimations of the molecular species involved in the electron-transfer processes, the excited state energy of $[Ru(bpy)_3]^{2+}$ was taken from the literature.[77, 163] The driving forces for each electron-transfer step (ΔG_{ET}) were estimated with the equation

$$\Delta G_{ET} = -e\,(E_{red} - E_{ox})$$

where E_{red}/E_{ox} represents the reduction/oxidation potential for the respective electron-transfer step. Reduction and oxidation potentials were taken from the cyclovoltammetric measurements of the donor triad, Ref-TCAQ and Ref-FMN. Reduction and oxidation potentials of $[Ru(bpy)_3]^{2+}$ were taken from the literature.[77]

- exTTF-PTZ-Ru^{2+}-FMN-TCAQ
  This state is the ground state and its energy is set to **0.00 eV**.
- exTTF-PTZ-$^{*}Ru^{2+}$-FMN-TCAQ
  This state corresponds to the lowest ^{3}MLCT state of $[Ru(bpy)_3]^{2+}$ with an energy of **2.10 eV**.[163] The second excitation of the photosensitizer adds another **2.10 eV** of energy.
- Electron transfer from $\mathbf{PTZ^0}$ to $\mathbf{^{*}Ru^{2+}}$:
  $\Delta G_{ET} = -e\,(0.77\,V - 0.68\,V) = -0.09\,eV$
- Electron transfer from $\mathbf{^{*}Ru^{2+}}$ to $\mathbf{FMN^0}$:
  $\Delta G_{ET} = -e\,(-0.51\,V + 0.81\,V) = -0.30\,eV$
- Electron transfer from $\mathbf{exTTF^0}$ to $\mathbf{PTZ^+}$:
  $\Delta G_{ET} = -e\,(0.68\,V - 0.42\,V) = -0.26\,eV$
- Electron transfer from $\mathbf{FMN^-}$ to $\mathbf{TCAQ^0}$:
  $\Delta G_{ET} = -e\,(-0.29\,V + 0.51\,V) = -0.22\,eV$
- Electron transfer from $\mathbf{PTZ^0}$ to $\mathbf{Ru^{3+}}$:
  $\Delta G_{ET} = -e\,(1.29\,V - 0.68\,V) = -0.61\,eV$
- Electron transfer from $\mathbf{Ru^+}$ to $\mathbf{FMN^0}$:
  $\Delta G_{ET} = -e\,(-0.51\,V + 1.33\,V) = -0.82\,eV$
- Electron transfer from $\mathbf{exTTF^+}$ to $\mathbf{PTZ^+}$:
  $\Delta G_{ET} = -e\,(0.68\,V - 0.05\,V) = -0.63\,eV$
- Electron transfer from $\mathbf{FMN^-}$ to $\mathbf{TCAQ^-}$:
  $\Delta G_{ET} = -e\,(-0.24\,V + 0.51\,V) = -0.27\,eV$

For each electron-transfer step, the respective driving force ΔG_{ET} is added to the previous energy level the electron-transfer step started from. This results in the various energy lev-

els of the charge-separated states shown in Scheme 5.1. For the final, charge-accumulated state, the energy amounts to (following the red arrows in Scheme 5.1):

- $E_{CA\text{-}state}$ = 2.10 eV - 0.30 eV - 0.61 eV - 0.26 eV - 0.22 eV + 2.10 eV - 0.30 eV - 0.61 eV - 0.63 eV - 0.27 eV = **1.00 eV**

Energy Estimations of the Different Species Involved in the Donor Triad

For the energy estimations of the molecular species involved in the electron-transfer processes, the excited state energy of $[Ru(bpy)_3]^{2+}$ was taken from the literature.[77, 163] The driving forces for each electron-transfer step (ΔG_{ET}) were estimated with the equation

$$\Delta G_{ET} = -e\,(E_{red} - E_{ox})$$

where E_{red}/E_{ox} represents the reduction/oxidation potential for the respective electron-transfer step. Reduction and oxidation potentials were taken from the cyclovoltammetric measurements of the donor triad as shown in Table 5.1. Reduction and oxidation potentials of $[Ru(bpy)_3]^{2+}$ as well as the reduction potentials of MV^{2+} were taken from the literature.[77, 151]

In the Absence of an External Electron Acceptor

- exTTF-PTZ-Ru^{2+}
  This state is the ground state and its energy is set to **0.00 eV**.
- exTTF-PTZ-$^{*}Ru^{2+}$
  This state corresponds to the lowest ^{3}MLCT state of $[Ru(bpy)_3]^{2+}$ with an energy of **2.10 eV**.[163] The second excitation of the photosensitizer adds another **2.10 eV** of energy.
- Electron transfer from $\mathbf{PTZ^0}$ to $\mathbf{^{*}Ru^{2+}}$:
  $\Delta G_{ET} = -e\,(0.77\,V - 0.68\,V) = -0.09\,eV$
- Electron transfer from $\mathbf{exTTF^0}$ to $\mathbf{PTZ^{+}}$:
  $\Delta G_{ET} = -e\,(0.68\,V - 0.42\,V) = -0.26\,eV$
- The energy of the final charge-separated state therefore amounts to
  $E_{CS\text{-}state}$ = 2.10 eV - 0.09 eV - 0.26 eV = **1.75 eV**.

In the Presence of the External Electron Acceptor MV^{2+}

- exTTF-PTZ-Ru^{2+}
  This state is the ground state and its energy is set to **0.00 eV**.
- exTTF-PTZ-$^{*}Ru^{2+}$
  This state corresponds to the lowest ^{3}MLCT state of $[Ru(bpy)_3]^{2+}$ with an energy of **2.10 eV**.[163]
- Electron transfer from $\mathbf{PTZ^0}$ to $\mathbf{^{*}Ru^{2+}}$:
  $\Delta G_{ET} = -e\,(0.77\,V - 0.68\,V) = -0.09\,eV$
- Electron transfer from $\mathbf{^{*}Ru^{2+}}$to $\mathbf{MV^{2+}}$:
  $\Delta G_{ET} = -e\,(-0.44\,V + 0.81\,V) = -0.37\,eV$
- Electron transfer from $\mathbf{^{*}Ru^{2+}}$to $\mathbf{MV^{+}}$:
  $\Delta G_{ET} = -e\,(-0.83\,V + 0.81\,V) = +0.02\,eV$
- Electron transfer from $\mathbf{exTTF^0}$ to $\mathbf{PTZ^{+}}$:
  $\Delta G_{ET} = -e\,(0.68\,V - 0.42\,V) = -0.26\,eV$
- Electron transfer from $\mathbf{PTZ^0}$ to $\mathbf{Ru^{3+}}$:
  $\Delta G_{ET} = -e\,(1.29\,V - 0.68\,V) = -0.61\,eV$
- Electron transfer from $\mathbf{Ru^{+}}$to $\mathbf{MV^{2+}}$:
  $\Delta G_{ET} = -e\,(-0.44\,V + 1.33\,V) = -0.89\,eV$
- Electron transfer from $\mathbf{Ru^{+}}$to $\mathbf{MV^{+}}$:
  $\Delta G_{ET} = -e\,(-0.83\,V + 1.33\,V) = -0.50\,eV$
- Electron transfer from $\mathbf{exTTF^{+}}$ to $\mathbf{PTZ^{+}}$:
  $\Delta G_{ET} = -e\,(0.68\,V - 0.05\,V) = -0.63\,eV$
- The energy of the final charge-accumulated state (following the red arrows in Scheme 5.4) with two MV^{+} formed therefore amounts to
  $E_{CA\text{-}state}$ = 2.10 eV - 0.37 eV - 0.61 eV - 0.26 eV + 2.10 eV - 0.37 eV - 0.61 eV - 0.63 eV = **1.35 eV**.

Bibliography

[1] Pausas, J. G.; Keeley, J. E. A Burning Story: The Role of Fire in the History of Life. *BioScience* **2009**, *59*, 593–601.

[2] *Key World Energy Statistics*; International Energy Agency, 2017.

[3] *World Energy Outlook 2017*; International Energy Agency, 2017.

[4] Balzani, V.; Credi, A.; Venturi, M. Photochemical Conversion of Solar Energy. *ChemSusChem* **2008**, *1*, 26–58.

[5] Zhou, H.; Fan, T.; Zhang, D. An Insight into Artificial Leaves for Sustainable Energy Inspired by Natural Photosynthesis. *ChemCatChem* **2011**, *3*, 513–528.

[6] Gust, D.; Moore, T. A.; Moore, A. L. Solar Fuels via Artificial Photosynthesis. *Accounts of Chemical Research* **2009**, *42*, 1890–1898.

[7] Tüysüz, H., Chan, C. K., Eds. *Solar Energy for Fuels*; Topics in Current Chemistry; Springer International Publishing: Cham, 2016; Vol. 371; pp 1–324.

[8] Hammarström, L. Accumulative Charge Separation for Solar Fuels Production: Coupling Light-Induced Single Electron Transfer to Multielectron Catalysis. *Accounts of Chemical Research* **2015**, *48*, 840–850.

[9] Kalyanasundaram, K.; Graetzel, M. Artificial photosynthesis: biomimetic approaches to solar energy conversion and storage. *Current Opinion in Biotechnology* **2010**, *21*, 298–310.

[10] Berardi, S.; Drouet, S.; Francas, L.; Gimbert-Surinach, C.; Guttentag, M.; Richmond, C.; Stoll, T.; Llobet, A. Molecular artificial photosynthesis. *Chem. Soc. Rev.* **2014**, *43*, 7501–7519.

[11] Kruse, O.; Rupprecht, J.; Mussgnug, J. H.; Dismukes, G. C.; Hankamer, B. Photosynthesis: a blueprint for solar energy capture and biohydrogen production technologies. *Photochemical & Photobiological Sciences* **2005**, *4*, 957–970.

[12] McConnell, I.; Li, G.; Brudvig, G. W. Energy Conversion in Natural and Artificial Photosynthesis. *Chemistry & Biology* **2010**, *17*, 434–447.

[13] Barber, J. Photosynthetic energy conversion: natural and artificial. *Chem. Soc. Rev.* **2009**, *38*, 185–196.

[14] Tommos, C.; Babcock, G. T. Oxygen Production in Nature: A Light-Driven Metalloradical Enzyme Process. *Accounts of Chemical Research* **1998**, *31*, 18–25.

[15] Barber, J. Photosystem II: the engine of life. *Quarterly Reviews of Biophysics* **2003**, *36*, 71–89.

[16] Ferreira, K. N. Architecture of the Photosynthetic Oxygen-Evolving Center. *Science* **2004**, *303*, 1831–1838.

[17] Kok, B.; Forbush, B.; McGloin, M. Cooperation of charges in photosynthetic O2 evolution - 1. A linear four step mechanism. *Photochemistry and Photobiology* **1970**, *11*, 457–475.

[18] Haumann, M. Photosynthetic O2 Formation Tracked by Time-Resolved X-ray Experiments. *Science* **2005**, *310*, 1019–1021.

[19] Dau, H.; Haumann, M. Eight steps preceding O-O bond formation in oxygenic photosynthesis - A basic reaction cycle of the Photosystem II manganese complex. *Biochimica et Biophysica Acta (BBA) - Bioenergetics* **2007**, *1767*, 472–483.

[20] O'Neil, M. P.; Niemczyk, M. P.; Svec, W. A.; Gosztola, D.; Gaines, G. L.; Wasielewski, M. R. Picosecond Optical Switching Based on Biphotonic Excitation of an Electron Donor-Acceptor-Donor Molecule. *Science* **1992**, *257*, 63–65.

[21] Imahori, H.; Hasegawa, M.; Taniguchi, S.; Aoki, M.; Okada, T.; Sakata, Y. Synthesis and Photophysical Properties of Porphyrin-Tetracyanoanthraquinodimethane-Porphyrin Triad: Photon-Dependent Molecular Switching. *Chemistry Letters* **1998**, *27*, 721–722.

[22] Kini, A. M.; Cowan, D. O.; Gerson, F.; Moeckel, R. New synthesis and properties of 11,11,12,12-tetracyano-9,10-anthraquinodimethane: an electron acceptor displaying a single-wave, two-electron reduction and a coproportionation pathway to the radical anion. *Journal of the American Chemical Society* **1985**, *107*, 556–562.

[23] Santos, J.; Illescas, B. M.; Martín, N.; Adrio, J.; Carretero, J. C.; Viruela, R.; Ortí, E.; Spänig, F.; Guldi, D. M. A Fully Conjugated TTF-π-TCAQ System: Synthesis, Structure, and Electronic Properties. *Chemistry - A European Journal* **2011**, *17*, 2957–2964.

[24] Konduri, R.; Ye, H.; MacDonnell, F. M.; Serroni, S.; Campagna, S.; Rajeshwar, K. Ruthenium Photocatalysts Capable of Reversibly Storing up to Four Electrons in a Single Acceptor Ligand: A Step Closer to Artificial Photosynthesis. *Angewandte Chemie International Edition* **2002**, *41*, 3185–3187.

[25] Wouters, K. L.; de Tacconi, N. R.; Konduri, R.; Lezna, R. O.; MacDonnell, F. M. Driving Multi-electron Reactions with Photons: Dinuclear Ruthenium Complexes

Capable of Stepwise and Concerted Multi-electron Reduction. *Photosynthesis Research* **2006**, *87*, 41–55.

[26] Karlsson, S.; Boixel, J.; Pellegrin, Y.; Blart, E.; Becker, H.-C.; Odobel, F.; Hammarström, L. Accumulative Charge Separation Inspired by Photosynthesis. *Journal of the American Chemical Society* **2010**, *132*, 17977–17979.

[27] Karlsson, S.; Boixel, J.; Pellegrin, Y.; Blart, E.; Becker, H.-C.; Odobel, F.; Hammarström, L. Accumulative electron transfer: Multiple charge separation in artificial photosynthesis. *Faraday Discuss.* **2012**, *155*, 233–252.

[28] Orazietti, M.; Kuss-Petermann, M.; Hamm, P.; Wenger, O. S. Light-Driven Electron Accumulation in a Molecular Pentad. *Angewandte Chemie International Edition* **2016**, *55*, 9407–9410.

[29] Kuss-Petermann, M.; Orazietti, M.; Neuburger, M.; Hamm, P.; Wenger, O. S. Intramolecular Light-Driven Accumulation of Reduction Equivalents by Proton-Coupled Electron Transfer. *Journal of the American Chemical Society* **2017**, *139*, 5225–5232.

[30] Kuss-Petermann, M.; Wenger, O. S. Exceptionally Long-Lived Photodriven Multi-Electron Storage without Sacrificial Reagents. *Chemistry - A European Journal* **2017**, *23*, 10808–10814.

[31] Nomrowski, J.; Wenger, O. S. Exploiting Potential Inversion for Photoinduced Multielectron Transfer and Accumulation of Redox Equivalents in a Molecular Heptad. *Journal of the American Chemical Society* **2018**, *140*, 5343–5346.

[32] Gosztola, D.; Niemczyk, M. P.; Svec, W.; Lukas, a. S.; Wasielewski, M. R. Excited doublet states of electrochemically generated aromatic imide and diimide radical anions. *Journal of Physical Chemistry A* **2000**, *104*, 6545–6551.

[33] Kaiser, C.; Schmiedel, A.; Holzapfel, M.; Lambert, C. Long-lived singlet and triplet charge separated states in small cyclophane-bridged triarylamine-naphthalene diimide dyads. *Journal of Physical Chemistry C* **2012**, *116*, 15265–15280.

[34] Asir, S.; Demir, A. S.; Icil, H. The synthesis of novel, unsymmetrically substituted, chiral naphthalene and perylene diimides: Photophysical, electrochemical, chiroptical and intramolecular charge transfer properties. *Dyes and Pigments* **2010**, *84*, 1–13.

[35] Kobaisi, M. A.; Bhosale, S. V.; Latham, K.; Raynor, A. M.; Bhosale, S. V. Functional Naphthalene Diimides: Synthesis, Properties, and Applications. *Chemical Reviews* **2016**, *116*, 11685–11796.

[36] Sakai, N.; Mareda, J.; Vauthey, E.; Matile, S. Core-substituted naphthalenediimides. *Chemical Communications* **2010**, *46*, 4225.

[37] Bhosale, S. V.; Jani, C. H.; Langford, S. J. Chemistry of naphthalene diimides. *Chem. Soc. Rev.* **2008**, *37*, 331–342.

[38] Pan, M.; Lin, X.-M.; Li, G.-B.; Su, C.-Y. Progress in the study of metal-organic materials applying naphthalene diimide (NDI) ligands. *Coordination Chemistry Reviews* **2011**, *255*, 1921–1936.

[39] Lambert, C.; Wagener, R.; Klein, J. H.; Grelaud, G.; Moos, M.; Schmiedel, A.; Holzapfel, M.; Bruhn, T. A photoinduced mixed-valence state in an organic bis-triarylamine mixed-valence compound with an iridium-metal-bridge. *Chemical Communications* **2014**, *50*, 11350.

[40] Zieschang, F.; Schreck, M. H.; Schmiedel, A.; Holzapfel, M.; Klein, J. H.; Walter, C.; Engels, B.; Lambert, C. Photoinduced Electron Transfer Dynamics in Triarylamine - Naphthalene Diimide Cascades. *Journal of Physical Chemistry C* **2014**, *118*, 27698–27714.

[41] Klein, J. H.; Sunderland, T. L.; Kaufmann, C.; Holzapfel, M.; Schmiedel, A.; Lambert, C. Stepwise versus pseudo-concerted two-electron-transfer in a triarylamine-iridium dipyrrin-naphthalene diimide triad. *Physical Chemistry Chemical Physics* **2013**, *15*, 16024.

[42] Taylor, A. J.; Davies, E. S.; Weinstein, J. a.; Sazanovich, I. V.; Bouganov, O. V.; Tikhomirov, S. a.; Towrie, M.; McMaster, J.; Garner, C. D. Ultrafast Intramolecular Charge Separation in a Donor-Acceptor Assembly Comprising Bis(η5-cyclopentadienyl)molybdenum Coordinated to an Ene-1,2-dithiolate-naphthalenetetracarboxylicdiimide Ligand. *Inorganic Chemistry* **2012**, *51*, 13181–13194.

[43] Sazanovich, I. V.; Best, J.; Scattergood, P. A.; Towrie, M.; Tikhomirov, S. A.; Bouganov, O. V.; Meijer, A. J. H. M.; Weinstein, J. A. Ultrafast photoinduced charge transport in Pt(II) donor-acceptor assembly bearing naphthalimide electron acceptor and phenothiazine electron donor. *Phys. Chem. Chem. Phys.* **2014**, *16*, 25775–25788.

[44] Mendes Marinho, S.; Ha-Thi, M.-H.; Pham, V.-T.; Quaranta, A.; Pino, T.; Lefumeux, C.; Chamaillé, T.; Leibl, W.; Aukauloo, A. Time-Resolved Interception of Multiple-Charge Accumulation in a Sensitizer-Acceptor Dyad. *Angewandte Chemie International Edition* **2017**, *56*, 15936–15940.

[45] NCCR Molecular Systems Engineering. `http://www.nccr-mse.ch`.

[46] Gebicki, J.; Marcinek, A.; Zielonka, J. Transient Species in the Stepwise Interconversion of NADH and NAD+. *Accounts of Chemical Research* **2004**, *37*, 379–386.

[47] Wang, X.; Saba, T.; Yiu, H. H.; Howe, R. F.; Anderson, J. A.; Shi, J. Cofactor

NAD(P)H Regeneration Inspired by Heterogeneous Pathways. *Chem* **2017**, *2*, 621–654.

[48] Vuorilehto, K.; Lütz, S.; Wandrey, C. Indirect electrochemical reduction of nicotinamide coenzymes. *Bioelectrochemistry* **2004**, *65*, 1–7.

[49] McSkimming, A.; Colbran, S. B. The coordination chemistry of organo-hydride donors: new prospects for efficient multi-electron reduction. *Chemical Society Reviews* **2013**, *42*, 5439–5488.

[50] Lauterbach, L.; Lenz, O.; Vincent, K. A. H2-driven cofactor regeneration with NAD(P)+-reducing hydrogenases. *FEBS Journal* **2013**, *280*, 3058–3068.

[51] Nam, D. H.; Park, C. B. Visible Light-Driven NADH Regeneration Sensitized by Proflavine for Biocatalysis. *ChemBioChem* **2012**, *13*, 1278–1282.

[52] van Esch, J. H.; Hoffmann, M. a. M.; Nolte, R. J. M. Reduction of Nicotinamides, Flavins, and Manganese Porphyrins by Formate, Catalyzed by Membrane-Bound Rhodium Complexes. *The Journal of Organic Chemistry* **1995**, *60*, 1599–1610.

[53] Hildebrand, F.; Kohlmann, C.; Franz, A.; Lütz, S. Synthesis, characterization and application of new rhodium complexes for indirect electrochemical cofactor regeneration. *Advanced Synthesis and Catalysis* **2008**, *350*, 909–918.

[54] Hollmann, F.; Arends, I. W. C. E.; Buehler, K. Biocatalytic Redox Reactions for Organic Synthesis: Nonconventional Regeneration Methods. *ChemCatChem* **2010**, *2*, 762–782.

[55] Steckhan, E. In *Electrochemistry V*; Steckhan, E., Ed.; Springer Berlin Heidelberg: Berlin, Heidelberg, 1994; pp 83–111.

[56] Steckhan, E.; Herrmann, S.; Ruppert, R.; Dietz, E.; Frede, M.; Spika, E. Analytical study of a series of substituted (2,2'-bipyridyl) (pentamethylcyclopentadienyl)rhodium and -iridium complexes with regard to their effectiveness as redox catalysts for the indirect electrochemical and chemical reduction of NAD(P)+. *Organometallics* **1991**, *10*, 1568–1577.

[57] Oppelt, K. T.; Gasiorowski, J.; Egbe, D. A. M.; Kollender, J. P.; Himmelsbach, M.; Hassel, A. W.; Sariciftci, N. S.; Knör, G. Rhodium-Coordinated Poly(arylene-ethynylene)alt-Poly(arylene-vinylene) Copolymer Acting as Photocatalyst for Visible-Light-Powered NAD+/NADH Reduction. *Journal of the American Chemical Society* **2014**, *136*, 12721–12729.

[58] Ryu, J.; Nam, D. H.; Lee, S. H.; Park, C. B. Biocatalytic Photosynthesis with Water as an Electron Donor. *Chemistry - A European Journal* **2014**, *20*, 12020–12025.

[59] Kim, J. H.; Lee, S. H.; Lee, J. S.; Lee, M.; Park, C. B. Zn-containing porphyrin

as a biomimetic light-harvesting molecule for biocatalyzed artificial photosynthesis. *Chemical Communications* **2011**, *47*, 10227.

[60] Lo, H. C.; Leiva, C.; Buriez, O.; Kerr, J. B.; Olmstead, M. M.; Fish, R. H. Bioorganometallic Chemistry. 13. Regioselective Reduction of NAD+ Models, 1-Benzylnicotinamde Triflate and β-Nicotinamide Ribose-5'-methyl Phosphate, with in Situ Generated [Cp*Rh(Bpy)H]+: Structure-Activity Relationships, Kinetics, and Mechanistic Aspect. *Inorganic Chemistry* **2001**, *40*, 6705–6716.

[61] Ghosh, T.; Slanina, T.; König, B. Visible light photocatalytic reduction of aldehydes by Rh(III)-H: a detailed mechanistic study. *Chemical Science* **2015**, *6*, 2027–2034.

[62] Wu, H.; Tian, C.; Song, X.; Liu, C.; Yang, D.; Jiang, Z. Methods for the regeneration of nicotinamide coenzymes. *Green Chemistry* **2013**, *15*, 1773.

[63] Quinto, T.; Köhler, V.; Ward, T. R. Recent Trends in Biomimetic NADH Regeneration. *Topics in Catalysis* **2014**, *57*, 321–331.

[64] Lee, S. H.; Kim, J. H.; Park, C. B. Coupling Photocatalysis and Redox Biocatalysis Toward Biocatalyzed Artificial Photosynthesis. *Chemistry - A European Journal* **2013**, *19*, 4392–4406.

[65] Choudhury, S.; Baeg, J.-O.; Park, N.-J.; Yadav, R. K. A Photocatalyst/Enzyme Couple That Uses Solar Energy in the Asymmetric Reduction of Acetophenones. *Angewandte Chemie International Edition* **2012**, *51*, 11624–11628.

[66] Song, N.; Zhang, M.-T.; Binstead, R. A.; Fang, Z.; Meyer, T. J. Multiple Pathways in the Oxidation of a NADH Analogue. *Inorganic Chemistry* **2014**, *53*, 4100–4105.

[67] Fukuzumi, S.; Inada, O.; Suenobu, T. Mechanisms of Electron-Transfer Oxidation of NADH Analogues and Chemiluminescence. Detection of the Keto and Enol Radical Cations. *Journal of the American Chemical Society* **2003**, *125*, 4808–4816.

[68] Oppelt, K. T.; Wöß, E.; Stiftinger, M.; Schöfberger, W.; Buchberger, W.; Knör, G. Photocatalytic Reduction of Artificial and Natural Nucleotide Co-factors with a Chlorophyll-Like Tin-Dihydroporphyrin Sensitizer. *Inorganic Chemistry* **2013**, *52*, 11910–11922.

[69] Mengele, A. K.; Seibold, G. M.; Eikmanns, B. J.; Rau, S. Coupling Molecular Photocatalysis to Enzymatic Conversion. *ChemCatChem* **2017**, *9*, 4369–4376.

[70] Damian, A.; Maloo, K.; Omanovic, S. Direct electrochemical regeneration of NADH on Au, Cu and Pt-Au electrodes. *Chemical and Biochemical Engineering Quarterly* **2007**, *21*, 21–32.

[71] Bresnahan, W.; Elving, P. Spectrophotometric investigation of products formed following the initial one-electron electrochemical reduction of nicotinamide adenine

dinucleotide (NAD+). *Biochimica et Biophysica Acta (BBA) - General Subjects* **1981**, *678*, 151–156.

[72] Fukuzumi, S. Artificial photosynthetic systems for production of hydrogen. *Current Opinion in Chemical Biology* **2015**, *25*, 18–26.

[73] Kölle, U.; Kang, B.-S.; Infelta, P.; Comte, P.; Grätzel, M. Elektrochemische und pulsradiolytische Reduktion von (Pentamethylcyclopentadienyl)(polypyridyl)rhodium-Komplexen. *Chemische Berichte* **1989**, *122*, 1869–1880.

[74] Kölle, U.; Grätzel, M. Metallorganische Rhodium(III)-Komplexe als Homogenkatalysatoren für die Photoreduktion von Protonen zu Wasserstoff an kolloidalem TiO2. *Angewandte Chemie* **1987**, *99*, 572–574.

[75] Fukuzumi, S.; Inada, O.; Satoh, N.; Suenobu, T.; Imahori, H. Significant Enhancement of Electron Transfer Reduction of NAD+ Analogues by Complexation with Scandium Ion and the Detection of the Radical Intermediate-Scandium Ion Complex. *Journal of the American Chemical Society* **2002**, *124*, 9181–9188.

[76] Mengele, A. K.; Rau, S. Product Selectivity in Homogeneous Artificial Photosynthesis Using [(bpy)Rh(Cp*)X]n+ -Based Catalysts. *Inorganics* **2017**, *5*, 35.

[77] Prier, C. K.; Rankic, D. A.; MacMillan, D. W. C. Visible Light Photoredox Catalysis with Transition Metal Complexes: Applications in Organic Synthesis. *Chemical Reviews* **2013**, *113*, 5322–5363.

[78] Klippenstein, J.; Arya, P.; Wayner, D. D. M. Relative bond dissociation energies for some NADH model compounds from hydride transfer/electron transfer equilibria in acetonitrile. *The Journal of Organic Chemistry* **1991**, *56*, 6736–6737.

[79] Fukuzumi, S.; Koumitsu, S.; Hironaka, K.; Tanaka, T. Energetic comparison between photoinduced electron-transfer reactions from NADH model compounds to organic and inorganic oxidants and hydride-transfer reactions from NADH model compounds to p-benzoquinone derivatives. *Journal of the American Chemical Society* **1987**, *109*, 305–316.

[80] Ruppert, R.; Herrmann, S.; Steckhan, E. Efficient indirect electrochemical in-situ regeneration of NADH: electrochemically driven enzymatic reduction of pyruvate catalyzed by D-LDH. *Tetrahedron Letters* **1987**, *28*, 6583–6586.

[81] Pellegrin, Y.; Odobel, F. Sacrificial electron donor reagents for solar fuel production. *Comptes Rendus Chimie* **2017**, *20*, 283–295.

[82] Skaisgirski, M.; Guo, X.; Wenger, O. S. Electron Accumulation on Naphthalene Diimide Photosensitized by [Ru(2,2'-Bipyridine)3]2+. *Inorganic Chemistry* **2017**, *56*, 2432–2439.

[83] Cline, E. D.; Adamson, S. E.; Bernhard, S. Homogeneous Catalytic System for Pho-

toinduced Hydrogen Production Utilizing Iridium and Rhodium Complexes. *Inorganic Chemistry* **2008**, *47*, 10378–10388.

[84] Summers, P. A.; Dawson, J.; Ghiotto, F.; Hanson-Heine, M. W. D.; Vuong, K. Q.; Stephen Davies, E.; Sun, X.-Z.; Besley, N. A.; McMaster, J.; George, M. W.; Schröder, M. Photochemical Dihydrogen Production Using an Analogue of the Active Site of [NiFe] Hydrogenase. *Inorganic Chemistry* **2014**, *53*, 4430–4439.

[85] Probst, B.; Rodenberg, A.; Guttentag, M.; Hamm, P.; Alberto, R. A Highly Stable Rhenium-Cobalt System for Photocatalytic H2 Production: Unraveling the Performance-Limiting Steps. *Inorganic Chemistry* **2010**, *49*, 6453–6460.

[86] Ilic, S.; Pandey Kadel, U.; Basdogan, Y.; Keith, J. A.; Glusac, K. D. Thermodynamic Hydricities of Biomimetic Organic Hydride Donors. *Journal of the American Chemical Society* **2018**, *140*, 4569–4579.

[87] Shen, G.-B.; Xia, K.; Li, X.-T.; Li, J.-L.; Fu, Y.-H.; Yuan, L.; Zhu, X.-Q. Prediction of Kinetic Isotope Effects for Various Hydride Transfer Reactions Using a New Kinetic Model. *The Journal of Physical Chemistry A* **2016**, *120*, 1779–1799.

[88] Whitten, D. G. Photoinduced electron transfer reactions of metal complexes in solution. *Accounts of Chemical Research* **1980**, *13*, 83–90.

[89] DeLaive, P. J.; Foreman, T. K.; Giannotti, C.; Whitten, D. G. Photoinduced electron transfer reactions of transition-metal complexes with amines. Mechanistic studies of alternate pathways to back electron transfer. *Journal of the American Chemical Society* **1980**, *102*, 5627–5631.

[90] Zhu, X. Q.; Mu, Y. Y.; Li, X. T. What are the differences between ascorbic acid and NADH as hydride and electron sources in vivo on thermodynamics, kinetics, and mechanism? *Journal of Physical Chemistry B* **2011**, *115*, 14794–14811.

[91] Warren, J. J.; Mayer, J. M. Tuning of the thermochemical and kinetic properties of ascorbate by its local environment: Solution chemistry and biochemical implications. *Journal of the American Chemical Society* **2010**, *132*, 7784–7793.

[92] Bachmann, C.; Probst, B.; Guttentag, M.; Alberto, R. Ascorbate as an electron relay between an irreversible electron donor and Ru(II) or Re(I) photosensitizers. *Chemical Communications* **2014**, *50*, 6737.

[93] Marcus, R.; Sutin, N. Electron transfers in chemistry and biology. *Biochimica et Biophysica Acta (BBA) - Reviews on Bioenergetics* **1985**, *811*, 265–322.

[94] Fox, L. S.; Kozik, M.; Winkler, J. R.; Gray, H. B. Gaussian Free-Energy Dependence of Electron-Transfer Rates in Iridium Complexes. *Science* **1990**, *247*, 1069–1071.

[95] Evans, D. H. One-Electron and Two-Electron Transfers in Electrochemistry and Homogeneous Solution Reactions. *Chemical Reviews* **2008**, *108*, 2113–2144.

[96] Macías-Ruvalcaba, N. A.; Telo, J. P.; Evans, D. H. Studies of the electrochemical reduction of some dinitroaromatics. *Journal of Electroanalytical Chemistry* **2007**, *600*, 294–302.

[97] Evans, D. H.; Juusola, P. M.; Minkkinen, P. O.; Olsen, C. E.; Søtofte, I.; Francis, G. W.; Szúnyog, J.; Långström, B. The Kinetic Burden of Potential Inversion in Two-Electron Electrochemical Reactions. *Acta Chemica Scandinavica* **1998**, *52*, 194–197.

[98] Evans, D. H.; Hu, K. Inverted potentials in two-electron processes in organic electrochemistry. *Journal of the Chemical Society, Faraday Transactions* **1996**, *92*, 3983.

[99] Evans, D. H.; Lehmann, M. W.; Burghart, A.; Little, R. D.; Silvestri, G.; Tallec, A.; Shono, T.; Toftlund, H. Two-Electron Reactions in Organic and Organometallic Electrochemistry. *Acta Chemica Scandinavica* **1999**, *53*, 765–774.

[100] Macías-Ruvalcaba, N. A.; Evans, D. H. Study of the Effects of Ion Pairing and Activity Coefficients on the Separation in Standard Potentials for Two-Step Reduction of Dinitroaromatics. *The Journal of Physical Chemistry B* **2005**, *109*, 14642–14647.

[101] Amriou, S.; Wang, C.; Batsanov, A. S.; Bryce, M. R.; Perepichka, D. F.; Ortí, E.; Viruela, R.; Vidal-Gancedo, J.; Rovira, C. The Interplay of Inverted Redox Potentials and Aromaticity in the Oxidized States of New π-Electron Donors: 9-(1,3-Dithiol-2-ylidene)fluorene and 9-(1,3-Dithiol-2-ylidene)thioxanthene Derivatives. *Chemistry - A European Journal* **2006**, *12*, 3389–3400.

[102] Kraiya, C.; Evans, D. H. Investigation of potential inversion in the reduction of 9,10-dinitroanthracene and 3,6-dinitrodurene. *Journal of Electroanalytical Chemistry* **2004**, *565*, 29–35.

[103] Nishiumi, T.; Chimoto, Y.; Hagiwara, Y.; Higuchi, M.; Yamamoto, K. First Redox Polymer Bearing One-Step Successive Two-Electron-Transfer Process Based on Redox Potential Inversion. *Macromolecules* **2004**, *37*, 2661–2664.

[104] Lehmann, M. W.; Singh, P.; Evans, D. H. Potential inversion in the reduction of trans-2,3-dinitro-2-butene. *Journal of Electroanalytical Chemistry* **2003**, *549*, 137–143.

[105] Ludwig, K.; Quintanilla, M.; Speiser, B.; Stauß, A. Two-electon-transfer redox systems. *Journal of Electroanalytical Chemistry* **2002**, *531*, 9–18.

[106] Saito, G.; Hirate, S.; Nishimura, K.; Yamochi, H. Nature of the strong electron donor 1,3,6,8-tetrakis(dimethylamino)pyrene and ionicity of its charge transfer complexes. *Journal of Materials Chemistry* **2001**, *11*, 723–735.

[107] Wolff, J. J.; Zietsch, A.; Nuber, B.; Gredel, F.; Speiser, B.; Würde, M. Hex-

aaminobenzene derivatives: synthesis and unusual oxidation behavior. *The Journal of organic chemistry* **2001**, *66*, 2769–77.

[108] Carlier, R.; Hapiot, P.; Lorcy, D.; Robert, A.; Tallec, A. Electrosynthesis and redox behavior of vinylogous TTF displaying strong conformational changes associated with electron transfers. *Electrochimica Acta* **2001**, *46*, 3269–3277.

[109] Bellec, N.; Boubekeur, K.; Carlier, R.; Hapiot, P.; Lorcy, D.; Tallec, A. Controlling the Conformation Changes Associated to Electron Transfer Steps through Chemical Substitution: Intriguing Redox Behavior of Substituted Vinylogous TTF. *The Journal of Physical Chemistry A* **2000**, *104*, 9750–9759.

[110] Dümmling, S.; Speiser, B.; Kuhn, N.; Weyers, G.; Motevalli, M.; Murase, H.; Shono, T.; Toftlund, H. Two-Electron-Transfer Redox Systems. Part 3. Electrochemical Reduction of N,N'-Dialkyl-4,5-dimethylimidazolium-2-dithiocarboxylates to 1,1-Dithiolate Dianions in THF. Steric Modulation of Potential Ordering by Substituents. *Acta Chemica Scandinavica* **1999**, *53*, 876–886.

[111] Speiser, B.; Würde, M.; Maichle-Mössmer, C. Electrochemical Oxidation of Hexakis(dimethylamino)benzene. *Chemistry - A European Journal* **1998**, *4*, 222–233.

[112] Moore, A. J.; Bryce, M. R. Generation and Trapping of Phosphorus Stabilized 4,5-Ethylenedithio-1,3-dithiol-2-ide Carbanions: Synthesis of Ethylenedithio-1,3-dithiafulvalenes. *Synthesis* **1991**, *1991*, 26–28.

[113] Bryce, M. R.; Coffin, M. A.; Hursthouse, M. B.; Karaulov, A.; Müllen, K.; Scheich, H. Synthesis, x-ray crystal structure and multistage redox properties of a severely-distorted tetrathiafulvalene donor. *Tetrahedron Letters* **1991**, *32*, 6029–6032.

[114] Salbeck, J.; Schöberl, U.; Rapp, K. M.; Daub, J. Structural Effects Determining the Reductive Electron Transfer Chemistry of 2.5-Disubstituted Furans - One and 'Two-electron' Transfer Behaviour Investigated by Cyclic Voltammetry and UV/VIS/NIR-Spectroelectrochemistry. *Zeitschrift für Physikalische Chemie* **1991**, *171*, 191–212.

[115] Yamashita, Y.; Kobayashi, Y.; Miyashi, T. p-Quinodimethane Analogues of Tetrathiafulvalene. *Angewandte Chemie International Edition in English* **1989**, *28*, 1052–1053.

[116] Aumüller, A.; Hünig, S. Mehrstufige, reversible Redoxsysteme, XXXVI. 11,11,12,12-Tetracyan-9,10-anthrachinodimethan (TCNAQ) und seine Derivate: Synthese und Redoxeigenschaften. *Liebigs Annalen der Chemie* **1984**, *1984*, 618–621.

[117] Brunetti, F. G.; López, J. L.; Atienza, C.; Martín, N. π-Extended TTF: a versatile molecule for organic electronics. *Journal of Materials Chemistry* **2012**, *22*, 4188.

[118] Illescas, B. M.; Santos, J.; Díaz, M. C.; Martín, N.; Atienza, C. M.; Guldi, D. M. Supramolecular threaded complexes from fullerene-crown ether and π-extended TTF derivatives. *European Journal of Organic Chemistry* **2007**, 5027–5037.

[119] Bendikov, M.; Wudl, F.; Perepichka, D. F. Tetrathiafulvalenes, Oligoacenenes, and Their Buckminsterfullerene Derivatives: The Brick and Mortar of Organic Electronics. *Chemical Reviews* **2004**, *104*, 4891–4946.

[120] Christensen, C. a.; Batsanov, A. S.; Bryce, M. R. Thiolated π-Extended Tetrathiafulvalenes: Versatile Multifunctional π-Systems. *The Journal of Organic Chemistry* **2007**, *72*, 1301–1308.

[121] Gruhn, N. E.; Macías-Ruvalcaba, N. A.; Evans, D. H. Studies of Potential Inversion in an Extended Tetrathiafulvalene. *Langmuir* **2006**, *22*, 10683–10688.

[122] Martín, N.; Sánchez, L.; Seoane, C.; Ortí, E.; Viruela, P. M.; Viruela, R. Synthesis, Properties, and Theoretical Characterization of Largely π-Extended Tetrathiafulvalene Derivatives with Quinonoid Structures. *The Journal of Organic Chemistry* **1998**, *63*, 1268–1279.

[123] Hachem, H.; Vacher, A.; Dorcet, V.; Lorcy, D. How the Anchoring Site on Two Extended Tetrathiafulvalenes Impacts the Electronic Communication through a Bis(acetylide)ruthenium Linker. *Organometallics* **2017**, *36*, 2208–2217.

[124] Díaz, M. C.; Illescas, B. M.; Seoane, C.; Martín, N. Synthesis and Electron-Donor Ability of the First Conjugated π-Extended Tetrathiafulvalene Dimers. *The Journal of Organic Chemistry* **2004**, *69*, 4492–4499.

[125] Martín, N.; Pérez, I.; Sánchez, L.; Seoane, C. Highly Conjugated π-Electron Donor and π-Electron Acceptor Dimers with p -Quinodimethane Structures. *The Journal of Organic Chemistry* **1997**, *62*, 870–877.

[126] Guldi, D. M.; Sánchez, L.; Martín, N. Formation and Characterization of the π-Radical Cation and Dication of π-Extended Tetrathiafulvalene Materials. *The Journal of Physical Chemistry B* **2001**, *105*, 7139–7144.

[127] Jones, A. E.; Christensen, C. A.; Perepichka, D. F.; Batsanov, A. S.; Beeby, A.; Low, P. J.; Bryce, M. R.; Parker, A. W. Photochemistry of the pi-extended 9,10-bis(1,3-dithiol-2-ylidene)-9,10-dihydroanthracene system: generation and characterisation of the radical cation, dication, and derived products. *Chemistry - A European Journal* **2001**, *7*, 973–8.

[128] Gómez, R.; Seoane, C.; Segura, J. L. The first two decades of a versatile electron acceptor building block: 11,11,12,12-tetracyano-9,10-anthraquinodimethane (TCAQ). *Chemical Society Reviews* **2007**, *36*, 1305.

[129] Bureš, F.; Schweizer, W. B.; Boudon, C.; Gisselbrecht, J.-P.; Gross, M.; Diederich, F.

New Push-Pull Chromophores Featuring TCAQ (11,11,12,12-Tetracyano-9,10-anthraquinodimethane) and Other Dicyanovinyl Acceptors. *European Journal of Organic Chemistry* **2008**, *2008*, 994–1004.

[130] Murschell, A. E.; Kan, W. H.; Thangadurai, V.; Sutherland, T. C. Anthraquinone derivatives as electron-acceptors with liquid crystalline properties. *Physical Chemistry Chemical Physics* **2012**, *14*, 4626.

[131] Macías-Ruvalcaba, N. A.; Evans, D. H. Studies of Potential Inversion in the Electrochemical Reduction of 11,11,12,12-Tetracyano-9,10-anthraquinodimethane and 2,3,5,6-Tetramethyl-7,7,8,8-tetracyano-1,4-benzoquinodimethane. *The Journal of Physical Chemistry B* **2006**, *110*, 5155–5160.

[132] Illescas, B. M.; Martin, N. [60]Fullerene Adducts with Improved Electron Acceptor Properties. *The Journal of Organic Chemistry* **2000**, *65*, 5986–5995.

[133] Isoda, K.; Yasuda, T.; Kato, T. Dipole-driven self-assembly of redox-active mesogenic tetracyanoanthraquinodimethanes. *Journal of Materials Chemistry* **2008**, *18*, 4522.

[134] Walther, M. E.; Wenger, O. S. Hole Tunneling and Hopping in a Ru(bpy)32+-Phenothiazine Dyad with a Bridge Derived from oligo-p-Phenylene. *Inorganic Chemistry* **2011**, *50*, 10901–10907.

[135] Schmidt, H. C.; Guo, X.; Richard, P. U.; Neuburger, M.; Palivan, C. G.; Wenger, O. S. Mixed-Valent Molecular Triple Deckers. *Angewandte Chemie International Edition* **2018**, 1–5.

[136] Wagner, E.; Filipek, S.; Kalinowski, M. K. Visible absorption spectra of the phenothiazine radical cation and its 10-substituted derivatives. *Monatshefte für Chemie Chemical Monthly* **1988**, *119-119*, 929–932.

[137] Homnick, P. J.; Tinkham, J. S.; Devaughn, R.; Lahti, P. M. Engineering Frontier Energy Levels in Donor-Acceptor Fluoren-9-ylidene Malononitriles versus Fluorenones. *The Journal of Physical Chemistry A* **2014**, *118*, 475–486.

[138] Wong, W.-Y.; Lu, G.-L.; Choi, K.-H.; Lin, Z. Functionalization of 9-(Dicyanomethylene)fluorene Derivatives with Substituted Acetylenes. *European Journal of Organic Chemistry* **2003**, *2003*, 365–373.

[139] Pavlishchuk, V. V.; Addison, A. W. Conversion constants for redox potentials measured versus different reference electrodes in acetonitrile solutions at 25 C. *Inorganica Chimica Acta* **2000**, *298*, 97–102.

[140] Boixel, J.; Blart, E.; Pellegrin, Y.; Odobel, F.; Perin, N.; Chiorboli, C.; Fracasso, S.; Ravaglia, M.; Scandola, F. Hole-Transfer Dyads and Triads Based on Perylene

Monoimide, Quaterthiophene, and Extended Tetrathiafulvalene. *Chemistry - A European Journal* **2010**, *16*, 9140–9153.

[141] Benniston, A. C.; Allen, B. D.; Harriman, A.; Llarena, I.; Rostron, J. P.; Stewart, B. Accessing molecular memory via a disulfide switch. *New J. Chem.* **2009**, *33*, 417–427.

[142] Hall, G. B.; Kottani, R.; Felton, G. A. N.; Yamamoto, T.; Evans, D. H.; Glass, R. S.; Lichtenberger, D. L. Intramolecular Electron Transfer in Bipyridinium Disulfides. *Journal of the American Chemical Society* **2014**, *136*, 4012–4018.

[143] Elgrishi, N.; Rountree, K. J.; McCarthy, B. D.; Rountree, E. S.; Eisenhart, T. T.; Dempsey, J. L. A Practical Beginner's Guide to Cyclic Voltammetry. *Journal of Chemical Education* **2018**, *95*, 197–206.

[144] Thomas, D.; Rasheed, Z.; Jagan, J. S.; Kumar, K. G. Study of kinetic parameters and development of a voltammetric sensor for the determination of butylated hydroxyanisole (BHA) in oil samples. *Journal of Food Science and Technology* **2015**, *52*, 6719–6726.

[145] Christensen, C. A.; Batsanov, A. S.; Bryce, M. R. Extreme Conformational Constraints in π-Extended Tetrathiafulvalenes: Unusual Topologies and Redox Behavior of Doubly and Triply Bridged Cyclophanes. *Journal of the American Chemical Society* **2006**, *128*, 10484–10490.

[146] Takano, Y.; Herranz, M. Á.; Martín, N.; de Miguel Rojas, G.; Guldi, D. M.; Kareev, I. E.; Strauss, S. H.; Boltalina, O. V.; Tsuchiya, T.; Akasaka, T. Electron Donor-Acceptor Interactions in Regioselectively Synthesized exTTF2-C70(CF3)10 Dyads. *Chemistry - A European Journal* **2010**, *16*, 5343–5353.

[147] Martin, N.; Sánchez, L.; Herranz, M. Á.; Illescas, B.; Guldi, D. M. Electronic Communication in Tetrathiafulvalene (TTF)/C60 Systems: Toward Molecular Solar Energy Conversion Materials? *Accounts of Chemical Research* **2007**, *40*, 1015–1024.

[148] Herranz, M. Á.; Illescas, B.; Martin, N.; Luo, C.; Guldi, D. M. Donor/Acceptor Fulleropyrrolidine Triads. *The Journal of Organic Chemistry* **2000**, *65*, 5728–5738.

[149] Martín, N.; Sánchez, L.; Guldi, D. M. Stabilisation of charge-separated states via gain of aromaticity and planarity of the donor moiety in C60-based dyads. *Chemical Communications* **2000**, 113–114.

[150] Thompson, D. W.; Ito, A.; Meyer, T. J. [Ru(bpy)3]2+* and other remarkable metal-to-ligand charge transfer (MLCT) excited states. *Pure and Applied Chemistry* **2013**, *85*, 1257–1305.

[151] Lomoth, R.; Häupl, T.; Johansson, O.; Hammarström, L. Redox-Switchable Direc-

tion of Photoinduced Electron Transfer in an Ru(bpy)32+-Viologen Dyad. *Chemistry - A European Journal* **2002**, *8*, 102–110.

[152] Heath, G. A.; Yellowlees, L. J.; Braterman, P. S. Spectro-electrochemical studies on tris-bipyridyl ruthenium complexes; ultra-violet, visible, and near-infrared spectra of the series [Ru(bipyridyl)3]2+/1+/0/1-. *Journal of the Chemical Society, Chemical Communications* **1981**, 287.

[153] Kalyanasundaram, K. Photophysics, photochemistry and solar energy conversion with tris(bipyridyl)ruthenium(II) and its analogues. *Coordination Chemistry Reviews* **1982**, *46*, 159–244.

[154] Tran, T.-T.; Ha-Thi, M.-H.; Pino, T.; Quaranta, A.; Lefumeux, C.; Leibl, W.; Aukauloo, A. Snapshots of Light Induced Accumulation of Two Charges on Methylviologen using a Sequential Nanosecond Pump-Pump Photoexcitation. *The Journal of Physical Chemistry Letters* **2018**, *9*, 1086–1091.

[155] Duan, L.; Xu, Y.; Zhang, P.; Wang, M.; Sun, L. Visible Light-Driven Water Oxidation by a Molecular Ruthenium Catalyst in Homogeneous System. *Inorganic Chemistry* **2010**, *49*, 209–215.

[156] Mills, A.; Valenzuela, M. A. The photo-oxidation of water by sodium persulfate, and other electron acceptors, sensitised by TiO2. *Journal of Photochemistry and Photobiology A: Chemistry* **2004**, *165*, 25–34.

[157] Henbest, K.; Douglas, P.; Garley, M. S.; Mills, A. Persulphate quenching of the excited state of ruthenium(II) tris-bipyridyl dication: thermal reactions. *Journal of Photochemistry and Photobiology A: Chemistry* **1994**, *80*, 299–305.

[158] Gómez, R.; Segura, J. L.; Martín, N. Synthesis of an optically active electron-acceptor tetracyanoanthraquinodimethane (TCAQ) main-chain polyester. *Tetrahedron Letters* **2006**, *47*, 6445–6448.

[159] Estrada, L. A.; Francés-Monerris, A.; Schapiro, I.; Olivucci, M.; Roca-Sanjuán, D. Mechanism of excited state deactivation of indan-1-ylidene and fluoren-9-ylidene malononitriles. *Physical Chemistry Chemical Physics* **2016**, *18*, 32786–32795.

[160] Wong, W.-Y.; Choi, K.-H.; Lu, G.-L.; Shi, J.-X.; Lai, P.-Y.; Chan, S.-M.; Lin, Z. Binuclear Gold(I) and Mercury(II) Derivatives of Diethynylfluorenes. *Organometallics* **2001**, *20*, 5446–5454.

[161] Ortí, E.; Viruela, R.; Viruela, P. M. Influence of Benzoannulation on the Molecular and Electronic Structures of Tetracyanoquinodimethanes. *The Journal of Physical Chemistry* **1996**, *100*, 6138–6146.

[162] Ortí, E.; Viruela, R.; Viruela, P. M. A theoretical study of the molecular and elec-

tronic structure of benzoannulated tetracyanoquinodimethanes. *J. Mater. Chem.* **1995**, *5*, 1697–1705.

[163] Creutz, C.; Sutin, N. Electron-transfer reactions of excited states. Reductive quenching of the tris(2,2'-bipyridine)ruthenium(II) luminescence. *Inorganic Chemistry* **1976**, *15*, 496–499.

[164] Yoshimura, A.; Hoffman, M. Z.; Sun, H. An evaluation of the excited state absorption spectrum of Ru(bpy)32+ in aqueous and acetonitrile solutions. *Journal of Photochemistry and Photobiology A: Chemistry* **1993**, *70*, 29–33.

[165] Creutz, C.; Chou, M.; Netzel, T. L.; Okumura, M.; Sutin, N. Lifetimes, spectra, and quenching of the excited states of polypyridine complexes of iron(II), ruthenium(II), and osmium(II). *Journal of the American Chemical Society* **1980**, *102*, 1309–1319.

[166] Caspar, J. V.; Kober, E. M.; Sullivan, B. P.; Meyer, T. J. Application of the energy gap law to the decay of charge-transfer excited states. *Journal of the American Chemical Society* **1982**, *104*, 630–632.

[167] Schlicke, B.; Belser, P.; De Cola, L.; Sabbioni, E.; Balzani, V. Photonic Wires of Nanometric Dimensions. Electronic Energy Transfer in Rigid Rodlike Ru(bpy)32 - (ph)n - Os(bpy)32+ Compounds (ph = 1,4-Phenylene; n = 3, 5, 7). *Journal of the American Chemical Society* **1999**, *121*, 4207–4214.

[168] Montalti, M.; Credi, A.; Prodi, L.; Teresa Gandolfi, M. *Handbook of Photochemistry, Third Edition*; CRC Press: Bosa Roca, 2006.

[169] Lehnert, W. Verbesserte Variante der Knoevenagel-Kondensation mit TiCl4/THF/Pyridin(I). Alkyliden- und Arylidenmalonester bei 0-25 C. *Tetrahedron Letters* **1970**, *11*, 4723–4724.

[170] Lehnert, W. Knoevenagel-Kondensationen mit TiCl4/Base - V1. 3-Alkyliden- und 3-Aryliden-2,4-pentandione aus Aldehyden und Acetylaceton. *Synthesis* **1974**, *1974*, 667–669.

[171] Zakeeruddin, S. M.; Nazeeruddin, M. K.; Humphry-Baker, R.; Grätzel, M.; Shklover, V. Stepwise Assembly of Tris-Heteroleptic Polypyridyl Complexes of Ruthenium(II). *Inorganic Chemistry* **1998**, *37*, 5251–5259.

[172] Huang, W.; Han, C. D. Synthesis and Intramolecular Charge-Transfer Interactions of a Donor-Acceptor Type Polymer Containing Ferrocene and TCNAQ Moieties. *Macromolecules* **2012**, *45*, 4425–4428.

[173] Pasini, D. The Click Reaction as an Efficient Tool for the Construction of Macrocyclic Structures. *Molecules* **2013**, *18*, 9512–9530.

[174] Hein, C. D.; Liu, X.-M.; Wang, D. Click Chemistry, A Powerful Tool for Pharmaceutical Sciences. *Pharmaceutical Research* **2008**, *25*, 2216–2230.

[175] Fulmer, G. R.; Miller, A. J. M.; Sherden, N. H.; Gottlieb, H. E.; Nudelman, A.; Stoltz, B. M.; Bercaw, J. E.; Goldberg, K. I. NMR Chemical Shifts of Trace Impurities: Common Laboratory Solvents, Organics, and Gases in Deuterated Solvents Relevant to the Organometallic Chemist. *Organometallics* **2010**, *29*, 2176–2179.

[176] Kuss-Petermann, M.; Wenger, O. S. Increasing Electron-Transfer Rates with Increasing Donor-Acceptor Distance. *Angewandte Chemie International Edition* **2016**, *55*, 815–819.

[177] Mössinger, D.; Jester, S.-S.; Sigmund, E.; Müller, U.; Höger, S. Defined Oligo(p-phenylene-butadiynylene) Rods. *Macromolecules* **2009**, *42*, 7974–7978.

[178] Lin, R. Y.-Y.; Wu, F.-L.; Li, C.-T.; Chen, P.-Y.; Ho, K.-C.; Lin, J. T. High-Performance Aqueous/Organic Dye-Sensitized Solar Cells Based on Sensitizers Containing Triethylene Oxide Methyl Ether. *ChemSusChem* **2015**, *8*, 2503–2513.

[179] Hanss, D.; Wenger, O. S. Conformational Effects on Long-Range Electron Transfer: Comparison of Oligo-p-phenylene and Oligo-p-xylene Bridges. *European Journal of Inorganic Chemistry* **2009**, *2009*, 3778–3790.

[180] Kuss-Petermann, M.; Wolf, H.; Stalke, D.; Wenger, O. S. Influence of Donor-Acceptor Distance Variation on Photoinduced Electron and Proton Transfer in Rhenium(I)-Phenol Dyads. *Journal of the American Chemical Society* **2012**, *134*, 12844–12854.

[181] Do, T. T.; Pham, H. D.; Manzhos, S.; Bell, J. M.; Sonar, P. Molecular Engineering Strategy for High Efficiency Fullerene-Free Organic Solar Cells Using Conjugated 1,8-Naphthalimide and Fluorenone Building Blocks. *ACS Applied Materials & Interfaces* **2017**, *9*, 16967–16976.

[182] Alston, J.; Kobayashi, S.; Younts, T.; Poler, J. Synthesis and characterization of rigid +2 and +3 heteroleptic dinuclear ruthenium(II) complexes. *Polyhedron* **2010**, *29*, 2696–2702.

[183] Toyama, M.; Inoue, K.-i.; Iwamatsu, S.; Nagao, N. Syntheses and Crystal Structures of Mono(2,2'-bipyridine)dichlorobis(dimethyl sulfoxide-S)ruthenium(II) Complexes, [RuCl2(bpy)(dmso-S)2]. *Bulletin of the Chemical Society of Japan* **2006**, *79*, 1525–1534.